PROTEIN TRANSPORT IN CILIA: ASSEMBLY OF INTRAFLAGELLAR TRANSPORT TRAINS AND TUBULIN TRANSPORT

by

JENNA LYNNE WINGFIELD

(Under the Direction of Karl F. Lechtreck)

ABSTRACT

Cilia are thin microtubule-based organelles, which act in cell sensing and movement. Cilia are gated from the cell body and devoid of ribosomes; thus, they rely on large bi-directional protein complexes, termed intraflagellar transport (IFT) trains to move material from the cell body into cilia. IFT trains are composed of repeats of IFT-A, IFT-B, kinesin-II (anterograde motor), and IFT-dynein (retrograde motor). Anterograde trains emerge from a pool of IFT proteins at the cilia base, traffic to the ciliary tip, remodel into retrograde trains and then return to the base. How these trains assemble at the base and remodel at the tip is poorly understood. Here, we use single-particle microscopy on fluorescently-tagged IFT proteins, representing different parts of the train, to reveal how these processes occur. Using different photobleaching approaches at the cilia base, we found that trains assemble in a stepwise fashion with IFT-A recruiting to the base first followed by IFT-B, kinesin-II, and lastly dynein and other cargos. Additionally, while IFT trains continuously cycle through cilia, only a portion of IFT-B is immediately reused on trains; IFT-A, dynein, and kinesin enter the cell body pool after cycling through cilia. Next, we utilized similar photobleaching techniques with single- and two-color imaging on fluorescent protein-tagged IFT proteins, and focused on the ciliary tip. We found that IFT-A, IFT-B, and IFT-dynein remain associated during train fragmentation. We postulate that fragmentation of anterograde

trains at the tip releases IFT dynein from inhibitory contacts with IFT-B leading to its activation on the smaller fragments and initiating retrograde IFT.

Lastly, we analyzed how tubulin binds to IFT for import into cilia. We identified that when a strain lacking the CH domain of IFT54 (ΔCH-IFT54) was combined with strains defective in the establish IFT81/74 tubulin binding site (IFT81-5E and ΔN-IFT74), the moderate ciliogenesis defects of the single mutants are aggravated with many cells failing to assemble cilia. Analysis of the *ift54-2* ΔCH-IFT54 *ift81-1* CH5E-IFT81 double mutant revealed normal IFT but reduced frequency of tubulin transport. These observations suggest that the CH-domain of IFT54 participates in ciliary tubulin transport, likely via and a tripartite domain.

INDEX WORDS: Cilia, Intraflagellar Transport, Tubulin, *Chlamydomonas reinhardtii*

PROTEIN TRANSPORT IN CILIA: ASSEMBLY OF INTRAFLAGELLAR TRANSPORT TRAINS AND TUBULIN TRANSPORT

by

JENNA LYNNE WINGFIELD

B.S., Christopher Newport University, 2015

A Dissertation Submitted to the Graduate Faculty of The University of Georgia in Partial Fulfillment of the Requirements for the Degree

DOCTOR OF PHILOSOPHY

ATHENS, GEORGIA

2020

PROTEIN TRANSPORT IN CILIA: ASSEMBLY OF INTRAFLAGELLAR TRANSPORT TRAINS AND TUBULIN TRANSPORT

by

JENNA LYNNE WINGFIELD

Major Professor:	Karl F. Lechtreck
Committee:	Jacek Gaertig Daichi Kamiyama Jonathan Eggenschwiler

Electronic Version Approved:

Ron Walcott
Interim Dean of the Graduate School
The University of Georgia
May 2020

DEDICATION

To those who wonder

ACKNOWLEDGEMENTS

I would like to first acknowledge Karl Lechtreck, my wonderful mentor, for making this dissertation possible. Your never-ending enthusiasm and passion for both science and life are infectious; it has made coming into work every day something I look forward to. Your openness to new ideas, opportunities, and experiences has empowered me to be a more confident person and scientist. I would also like to acknowledge the rest of my committee, Jacek, Daichi, and Jonathan. Your feedback and guidance helped make this dissertation possible. Thank you.

To my dearest lab mates. Aaron, your oddness is what made me feel like I could find a home in the lab. Peiwei, your patience, curiosity, and kindness will be missed. Ilaria! I honestly could not have done this without you! You are the cloning queen, a fabulous potter, and a fantastic friend. Dipna, the way you looked at me when I did weird things helped me know I always kept you on your toes. Jin, thank you for all the wasps, cockroaches, and mosquitoes that you killed. I'm sure you saved me from getting malaria a time or two. Gui, you were such a tremendous help and a kind face in my last year, thanks for keeping us fit in lab. Kewei, I'm already missing our walks home. Your stubbornness to get scientific answers helped invigorate me in my last year, you are awesome.

To my family and friends, thank you for supporting me along the way. Jennie, Rachel, Hannah, and Alexis; you are all incredibly inspiring women who helped me make unforgettable memories here in Athens. Denisse, Leandra, Paige, and Jessie, you all were just a call of encouragement away, thank you for being there. Dexter, thank you for being a kind a supportive partner in my last year. Here's to our next journey together. Mom and Dad, you let me follow my passions. Dr. Joyce Taylor, your instantiable thirst for learning and teaching is absolutely inspiring. This is for you.

TABLE OF CONTENTS

Page

CHAPTER 1

INTRODUCTION AND LITERATURE REVIEW

1.1 CILIA

Cilia are slender microtubule-based organelles that protrude from the cell body into the surrounding environment, functioning in both cell motility and sensation. Cilia were first identified by Antony van Leeuwenhoek in 1675, noting protozoa moved very nimbly by tiny feet, thus recognizing them as the first organelle (Satir, 1995). A little over a century later, Otto Müller termed these tiny feet cilia (Latin for eyelash), a term we now use as synonymous for eukaryotic flagella (Müller and Fabricius, 1786). Due to the nature of their discovery, the motility role of cilia has long been known, but their sensory role was only uncovered in the late 1990s (Beales and Jackson, 2012). Since then, the cilia field has grown substantially. Researchers now work on not just motile cilia but also primary and nodal cilia. The various types of cilia and their key functions are described below.

Motile, primary, and nodal cilia are all thin cellular extension which are differentiated based on the structure of their microtubular axoneme. Motile cilia have a canonical 9+2 arrangement, which means their scaffold or axoneme is composed of nine microtubule doublets with two microtubule singlets in the center (Fig. 1A,b). Their axonemes are decorated with dynein arms and radial spokes and which allow them to beat with a whip-like waveform (Gudis and Cohen, 2010). Perhaps the most well-known cilia are the tails of sperm, which propel the gametes towards the egg. Motile cilia also function in the female reproductive tract where multiciliated cells line the fallopian tubes and push the egg towards the uterine cavity (Lehti and

Sironen, 2017; Raidt et al., 2015). Cilia in our airways move mucus and debris out of the lungs (Peabody et al., 2018). Furthermore, cilia move the cerebrospinal fluid in brain ventricles, bringing nutrients to various regions of the brain (Banizs et al., 2005; Eichele et al., 2020). Cilia also help single-cell organisms, like the biflagellate alga *Chlamydomonas reinhardtii*, used in this dissertation, move towards and away from nutrient sources and mate. In addition to their role in motility, motile cilia also participate in cell sensing and signaling (Bloodgood, 2010). For example, cilia in the lungs beat faster when ligands bind to bitter taste receptors on cilia, helping expel noxious substances from the lungs (Shah et al., 2009). While there are many other examples of the chemo- and mechano-sensory roles of motile cilia, these roles are better characterized in primary cilia (see Bloodgood (2010)).

Primary cilia, or nonmotile cilia, have a 9+0 microtubule arrangement, which lack dynein arms and other mechanical accessories entirely. Primary cilia are much more prevalent than motile cilia in our bodies as they exist on nearly every cell and are proposed to act as an antenna, protruding into the environment to send and receive signal easily (Hua and Ferland, 2018). The outer segments of the rod and cones in our eyes are modified primary cilia which require constant maintenance in order to participate in photoreception (Khanna, 2015). Olfactory sensory neurons are equipped with multiple primary cilia at their apical end (Jenkins et al., 2009). Olfactory cilia are enriched with GPCRs which act as odorant receptors, enabling us smell and aid in our sense of taste (Jenkins et al., 2009). Besides the sensing of light and odor by structurally specialized sensory cilia in the eye and nose, non-motile cilia participate in several signaling pathways including Hedgehog (Hh) (Corbit et al., 2005; Haycraft et al., 2005; Huangfu et al., 2003; Pazour et al., 2000), Wnt (Wallingford and Mitchell, 2011), Notch (Liu et al., 2019; Stasiulewicz et al., 2015), Receptor Tyrosine Kinase (RTKs) (Christensen et al., 2012), Hippo

(Habbig et al., 2011), TGF-β signaling (Clement et al., 2013; Mönnich et al., 2018) and GPCR signaling (Berbari et al., 2008). Ciliary sensing and signaling rely on membrane-embedded receptors that cycle through the cilium during signaling. Thus, it is important to understand how cells establish, maintain and adjust the specific receptor, and ion channel composition of the ciliary membrane.

Nodal cilia are another variety of cilia that have a 9+0 arrangement; however, they do possess dynein arms attached to the axonemes that allow them to beat in a twirling fashion, generating a leftward flow (Okada et al., 1999). Nodal cilia exist only for a short time in development within the embryonic node when the organism does not possess a defined left and right side. The original hypothesis was that nodal cilia function in producing a flow that moves an unknown morphogen to the left side of the organism, thereby establishing left-right asymmetry (Hirokawa et al., 2009). However, there is also evidence that the flow itself may elicit a mechanosensory response in the immotile cilia on one side of the node, triggering downstream effects that define the left and right sides (Hirokawa et al., 2009). While it is not known precisely how nodal cilia function, it is clear that their absence leads to left-right patterning defects (Wagner and Yost, 2000).

Due to the prevalence and diversity of cilia in our body, cilia disorders collectively termed ciliopathies, result in a plethora of disease etiologies. Complete lack of cilia is embryonic lethal (Huangfu et al., 2003; Liu et al., 2005). Defects in the dynein arms or other aspects of the motility machinery can lead to infertility, hydrocephaly, and most commonly, primary cilia dyskinesia (PCD), cystic fibrosis (CF), and chronic obstructive pulmonary disease (Banizs et al., 2005; Eichele et al., 2020; Peabody et al., 2018; Raidt et al., 2015). Defects in proper gating of the cilia or protein trafficking within the cilium result in an array of developmental and

degenerative disorders. These range from Bardet-Biedl syndrome (BBS), a genetically heterogenous recessive mendelian disorder characterized primarily by polydactyly, genital malformation, retinal degeneration, morbid obesity and kidney anomalies; to congenital heart disease (Koefoed et al., 2014). Recent studies are also uncovering the importance of cilia in regulating the cell cycle as lack of cilia cause certain cancers (Peixoto et al., 2020). In summary, properly functioning cilia are critical to both our development and our health as adults. Understanding how cilia are built and maintained is imperative not just for their relevance to human health, and but also understanding cell function in general.

1.2 INTRAFLAGELLAR TRANSPORT

Cilia assembly poses unique challenges to the cell as an organelle. While the ciliary membrane is continuous with that of the cell body, proteins from the cell body are excluded from the cilium by a protein gate called the transition zone (Gonçalves and Pelletier, 2017) (Fig. 1Ac). Additionally, cilia are devoid of ribosomes, meaning all proteins must be synthesized within the cell body and then be imported into the organelle. Proteomic studies revealed the presence of ~1000 distinct proteins in cilia, many of which are highly enriched inside the organelle compared to their concentration in the cell body (Pazour et al., 2005). Thus, ciliary assembly depends on intraflagellar transport (IFT), a protein shuttle dedicated to cilia that selects proteins within the cell body, traffics them across the transition zone, and deposits them in within cilia, generally near the tip. Nearly every cilium, in every organism, requires IFT for assembly, with *Plasmodium falciparum* and *Drosophila* sperm as the identified exceptions (Avidor-Reiss et al., 2004; Han et al., 2003; Sarpal et al., 2003).

The IFT apparatus consists of the IFT particle proteins and the IFT motors, which together form into repetitive multi-megadalton arrays (termed IFT trains) that move up and down cilia between the axonemal doublet microtubules and the ciliary membrane. The IFT motors are heterotrimeric kinesin-2, used for anterograde transport to the flagellar tip and IFT-dynein, utilized for retrograde transport back to the cell body (Kozminski et al., 1995; Piperno et al., 1998) (Fig. 1.2). The IFT particles comprise of 22 distinct IFT proteins, organized into three biochemically stable subcomplexes (IFT-A: IFT43, IFT121, IFT122, IFT139, IFT140 and IFT144; IFT-B2: IFT22, IFT25, IFT27, IFT46, IFT54, IFT56, IFT70, IFT74, IFT81 and IFT88, and IFT-B2: IFT20, IFT38, IFT54, IFT57, IFT80 and IFT172) (Cole et al., 1998b; Taschner and Lorentzen, 2016) (Fig 1.1A). The BBSome is a controversial third component of IFT trains. In most systems, BBSomes move on IFT trains through cilia and the BBSome can thus be considered an additional IFT subcomplex (Blacque et al., 2004; Lechtreck et al., 2009; Liew et al., 2014; Williams et al., 2014). However, while mutations in IFT components typically result in the loss or shortening of cilia, the effect of *bbs* mutations on cilia size and ultrastructure is often negligible (Nachury, 2018). In some cases, structural defects of cilia do occur, i.e., the cilia-like outer segments of photoreceptor cells in *Bbs4*$^{-/-}$ mice initially form normally but then degenerate over time and the composition of the ciliary membrane declines (Datta et al., 2015; Hsu et al., 2017; Mykytyn et al., 2004). Thus, it is widely accepted that the BBSome is mostly dispensable for cilia assembly but performs critical roles as an IFT cargo adaptor for the retrograde export of ciliary membrane proteins (Liew et al., 2014; Liu and Lechtreck, 2018).

IFT trains appear as electron-dense zigzag lines, located between the ciliary membrane and microtubules by standard electron microscopy (EM) (Rogowski et al., 2013). Cryo-EM and advancements in electron tomography have enabled researchers to identify structural differences

in anterograde and retrograde and define the location of the complexes on anterograde trains (Jordan et al., 2018; Stepanek and Pigino, 2016). Using correlative fluorescence and three-dimensional electron microscopy, Stepanek and Pigino (2016) identified anterograde trains as ~200–300 nm in length; retrograde trains are about the same length but less structured (Jordan et al., 2018; Stepanek and Pigino, 2016). Anterograde trains tend to stall inside cilia and then assume an extended configuration with a length of ~700 nm (Dentler, 2005; Pedersen et al., 2006; Stepanek and Pigino, 2016; Vannuccini et al., 2016). By using in situ cryo-electron tomography Jordan and colleagues characterized the structure of anterograde trains in Chlamydomonas had three distinct polymer-like repeats of ~6nm, 11nm, and 18nm (Jordan et al., 2018). They took advantage of *Chlamydomonas* mutants, which either lacked IFT-A or IFT dynein and then assigned these repeats identities of IFT-B, IFT-A, and IFT dynein, respectively. After assigning these identities, they determined the ratio for dynein: IFT-B: IFT-A is 2:8:4. Additionally, they found that IFT-B sits closest to the microtubule doublets with IFT-A and dynein riding on top (Fig. 1.2B). Importantly, they noted that dynein sits in autoinhibited configuration with crossed stalks and the microtubule-binding domains on the side of the train facing away from the microtubule tracks (Fig. 1.2B) (Jordan et al., 2018). They proposed both the configuration and orientation of dynein on anterograde trains help ensure the highly processive nature of IFT.

Toropova and colleagues obtained a higher resolution cryo-EM structure of the recombinantly expressed human IFT dynein complex (Toropova et al., 2019). Interestingly, in addition to finding the purified complexes naturally dimerized into the autoinhibited conformation, they found that two intermediate chains (nonmotor subunits: WDR34 and WDR60) of the complex force an asymmetric kink in the structure of two identical dynein-2

heavy chains; removal of these intermediate chains relieved the autoinhibited conformation and enabled its motility. The kinked dynein complex matched the periodicity of the dyneins on the Chlamydomonas anterograde trains. By fitting their structure into the *in situ* structure from (Jordan et al., 2018), they found the kinked structure also fits well on top of IFT-B, spanning over 7-8 IFT-B repeats. Furthermore, they noted contacts between adjacent dyneins, which imply the docking of one dynein provides additional binding sites of another IFT-dynein, ensuring cooperative assembly (Toropova et al., 2019). These findings suggest that IFT-B periodicity on anterograde trains is established before the addition of dynein, that if WDR34 and WDR60 are bound to dynein heavy chains, dynein will not be activated, and dynein-dynein interactions may also aid in keeping anterograde trains processive.

Anterograde trains appear to keep their uniform structure until they reach the ciliary tip. The ciliary tip is a hot spot in the cilium: it is the location for axonemal assembly (Marshall and Rosenbaum, 2001; Qin et al., 2004a), for disassembly (Ishikawa and Marshall, 2011), for pickup of signaling proteins (Liew et al., 2014), and for dynein activation (Jordan et al., 2018). In order for all these processes to occur, anterograde trains must deposit cargo, retrieve cargoes, release autoinhibited dynein and form into retrograde trains at the tip. Two elegant, live imaging studies have begun to address how these processes occur. By using single-molecule imaging on four different *C.elegans* strains, each expressing a fluorescent tagged-protein representative of IFT-A, IFT-B, IFT-dynein, and OSM-3 (one of the *C. elegans* anterograde motors), they found that IFT-B pauses at the tip while the rest of the train immediately undergoes retrograde traffic once it reaches the tip (Mijalkovic et al., 2018). They propose that IFT fragments into at least IFT-A, IFT-B, IFT-dynein, and OSM-3 before reforming into retrograde trains. However, *C. elegans* has two anterograde motors and requires the BBSome to keep IFT-A and IFT-B together in

transport, therefore making its trafficking, and likely remodeling, distinct from other organisms. Another study examined three different *Chlamydomonas* strains with fluorescently-tagged proteins representative of kinesin, dynein and IFT-B. By utilizing a novel photobleaching approach which allowed them to analyze the behavior of single anterograde train they made several interesting findings. First they discovered that at the tip, dynein and the IFT-B subunit, IFT27, fragment and mix with material at the tip to form several retrograde trains (Chien et al., 2017a). They also noted that the kinesin subunit KAP, separates from trains at the tip and slowly diffuses back to the base; this could provide a mechanism ensuring kinesin is not active on retrograde trains. While they do show evidence for anterograde train fragmentation, they do not provide evidence for IFT-B and dynein separating from each other and they have no evidence of what happens to IFT-A. Therefore, the extent that IFT trains fragment and what train remodeling entails is still largely unknown.

Before trains can traffic within the cilium, they must first be assembled. Train assembly likely occurs at the base of the cilia, or around the basal bodies (Fig. 1.1). More than 90% of the total amount of the IFT proteins are present in the cell body with an unknown portion pooling near each basal body; and IFT trains emerge from this basal body-associated pool of IFT proteins (Ahmed et al., 2008; Deane et al., 2001; Richey and Qin, 2012b). In contrast to the distinct structure of ciliary IFT trains, the pool of IFT proteins surrounding the basal bodies appears amorphous and IFT trains are only seen near the distal end of basal bodies (Rogowski et al., 2013). The hierarchy by which IFT proteins are recruited to the basal body has been explored using IFT and basal body mutants, most of which lack flagella (Richey and Qin, 2012b). IFT52, an IFT-B protein for example, is required for the accumulation of IFT46, another IFT-B protein at the flagellar base (Lv et al., 2017a). IFT-A proteins (e.g., IFT139) still accumulate at the base

of *ift74-1* mutants (an IFT-B mutant), but their entry into the flagellum is diminished (Brown et al., 2015). Furthermore, IFT particle proteins still enter cilia in the IFT dynein mutant *d1blic*, suggesting that the retrograde motor is dispensable for train assembly (Hou et al., 2004; Reck et al., 2016). The core IFT-B1 protein IFT52 has been observed associates to the transitional fibers of the basal bodies (Fig. 1Ad) (Deane et al., 2001). The mutant *bld-2* cells lack the transitional fibers, (Fig. 1Ad) and kinesin-2 fails to gather near the basal bodies suggesting the transitional fibers are necessary for motor recruitment (Richey and Qin, 2012b). However, how the higher-order IFT trains are built near the basal bodies is only developing and is further explored in this dissertation.

1.3 TUBULIN TRANSPORT

At the base, anterograde IFT trains are loaded with the various cargoes required to build the cilium. One of the major cargoes IFT brings in is that of the scaffold itself, tubulin. In *Chlamydomonas reinhardtii,* this requires ~350,000 tubulin dimers to be imported and assembled into the axoneme in the ~60 minutes it takes to build a cilium (Kubo et al., 2016b). Previous studies have determined that IFT trains accomplish this task by being heavily loaded with tubulin while cilia grow but essentially devoid of tubulin in non-growing cilia; revealing that cells regulate tubulin loading onto IFT trains (Craft et al., 2015a). Additionally, a short flagella mutant (*shf2*) and a long flagella mutant (*lf2-1*) have impaired regulation of tubulin loading: in *shf2*, IFT trains stop carrying tubulin before cilia reach their appropriate length; in *lf2-1*, IFT trains continuously carry tubulin, even when cilia have reached beyond the wild-type length (Craft et al., 2015a). These data suggest that the regulation of tubulin transport into cilia likely contributes to establishing the specific length of cilia, which is critical for its motility and

sensory functions. In order to understand how tubulin transport is regulated, we must first identify which IFT proteins directly participate in tubulin transport.

Currently, two IFT-B proteins, IFT81 and IFT74 are thought to be the main tubulin binding site on IFT. IFT81 binds the globular interface of tubulin dimers via its calponin homology (CH) domain and IFT74 binds the acidic E-hook on beta tubulin via basic residues on its N-terminal tail (Bhogaraju et al., 2013). In *Chlamydomonas*, single mutants in each of these tubulin binding domains (*ift74-2* ΔN-IFT74 and *ift81-1* CH5E-IFT81) assemble almost full-length cilia but at a reduced rate and have decreased rates of tubulin transport, while the double IFT81/74N mutant lacks cilia but for short stumps; suggesting IFT81/74 forms the major tubulin binding site on IFT trains (Kubo et al., 2016). Nevertheless, the fact that the single CH5E-IFT81 and ΔN-IFT74 mutants still form near wild type flagella is surprising because IFT81 and IFT74 alone bind only weakly to tubulin *in vitro*; IFT81 alone has a 16μM K_d while IFT81/74 binds with 0.9μM K_d affinity (Bhogaraju et al., 2013). Additionally, *Drosophila* and several other organisms do not have homologs to IFT81 or IFT74 and *C.elegans* mutants in IFT81 and IFT74 still grow sensory cilia, suggesting another IFT protein(s) contributes to tubulin transport by IFT in these organisms (Cole and Snell, 2009; Kobayashi et al., 2007; van Dam et al., 2013). Besides IFT81, CH domains are present on IFT57, IFT54, and IFT38 (qilin) (Taschner et al., 2016c). Only the CH-domain of IFT54 has been shown to bind tubulin dimers and microtubules, with a 3μM binding affinity *in vitro,* raising the question whether IFT54 contributes to tubulin transport and ciliogenesis (Taschner et al., 2016c). Furthermore, mutations in the CH domain of IFT54 result in human ciliopathies (Bizet et al., 2015). Zhu and colleagues showed rescue of an *ift54-1* loss-of-function mutant by CH-deficient IFT54 (ΔCH-IFT54) suggesting that the CH of IFT54 is

dispensable for ciliogenesis (Zhu et al., 2017c). However, given the data on the IFT74 and IFT81 mutants, IFT54 may contribute to tubulin transport with IFT81N/74N.

1.4 OVERVIEW OF DISSERTATION

Understanding the mechanisms behind how cilia are built and maintained is important both for their relevance in human health and elucidating general cellular functions. In this dissertation, we explore how IFT trains assemble at the ciliary base, whether or not IFT components are recycled, to what degree trains fragment at the ciliary tip, and further characterize the IFT-tubulin binding site. Bringing understanding to these processes can help inform key questions in the field, such as how cargo loading is regulated and how dynein is activated at the ciliary tip.

In Chapter 2 of this dissertation, we will describe how IFT trains assembled at the base in and whether the constantly cycling trains are composed of recycled or *de novo* material. Utilizing photobleaching techniques on fluorescence protein-tagged IFT proteins in *Chlamydomonas reinhardtii* we identified that while IFT-A and motor proteins that cycle through the cilium and disperse back into the cell body, a portion of IFT-B proteins from retrograde trains will re-enter the pool and be reused directly in anterograde trains indicating a 'semi-open' system. We made similar observations in *Tetrahymena thermophila* and IMCD3 cells, suggesting that IFT trains are largely composed of *de novo* materials. FRAP analysis of the basal body pools revealed that IFT trains are built with IFT-A arriving at the basal bodies first, followed by IFT-B and kinesin. IFT dynein and tubulin cargoes are loaded briefly before the trains commence anterograde transport. We conclude IFT trains in multiple stages of assembly, line up at the basal body pools for successive release into the cilium upon formation.

In Chapter 3, we follow IFT trains to the tip and study how anterograde trains remodel into retrograde trains. We utilized single- and two-color *in vivo* imaging of eight distinct fluorescent protein-tagged IFT and motor proteins to visualize single and multiple fluorescent trains at the tip. Our findings indicate that IFT-A, IFT-B, and IFT-dynein all dwell at the ciliary tip for ~2 seconds before undergoing retrograde transport. Furthermore, fragmentation entails anterograde trains breaking into 'train-cars,' which maintain IFT-A, IFT-B, and IFT-dynein contacts. We propose association of IFT-A, IFT-B, and IFT dynein at the tip could prevent a build-up of IFT components at the tip by maintaining the stoichiometry of the component of anterograde IFT trains during the formation of retrograde trains.

In Chapter 4, we explore how IFT trains carry the main structural component of the axoneme, tubulin. By using a novel IFT54 strain that lacks its CH domain (ΔCH-IFT54), in combination with a strain with an incapacitated IFT81-CH (IFT81-5E) or a strain lacking the head domain of IFT74 (ΔN-IFT74), we find the moderate ciliogenesis defects of the respective single mutants are aggravated; with many cells failing to assemble cilia. Thus, impairment of tubulin-binding in any of the three IFT54/74/81 protein, results in more severe ciliogenesis defect. In-depth analysis of the few cilia of the *ift54-2* ΔCH-IFT54 *ift81-1* CH5E-IFT81 double mutant revealed that while IFT appeared normal, the frequency of tubulin transport was reduced. Further, an IFT81 construct carrying the CH domain of IFT54 instead of its own was able to partially rescue the more attenuated cilia phenotype of a novel *ift81* ΔCH-IFT81 mutant strain, indicating that the CH domains of IFT81 and IFT54 perform a similar role in IFT and ciliary assembly. Taken together, these observations suggest that the CH-domain of IFT54 participates in ciliary tubulin transport and likely forms a tripartite tubulin-binding site with IFT81/74.

Lastly, in Chapter 5, we summarize the work completed in this dissertation. Additionally, we discuss how regulation of a tripartite tubulin-binding site might be achieved.

1.5 FIGURES

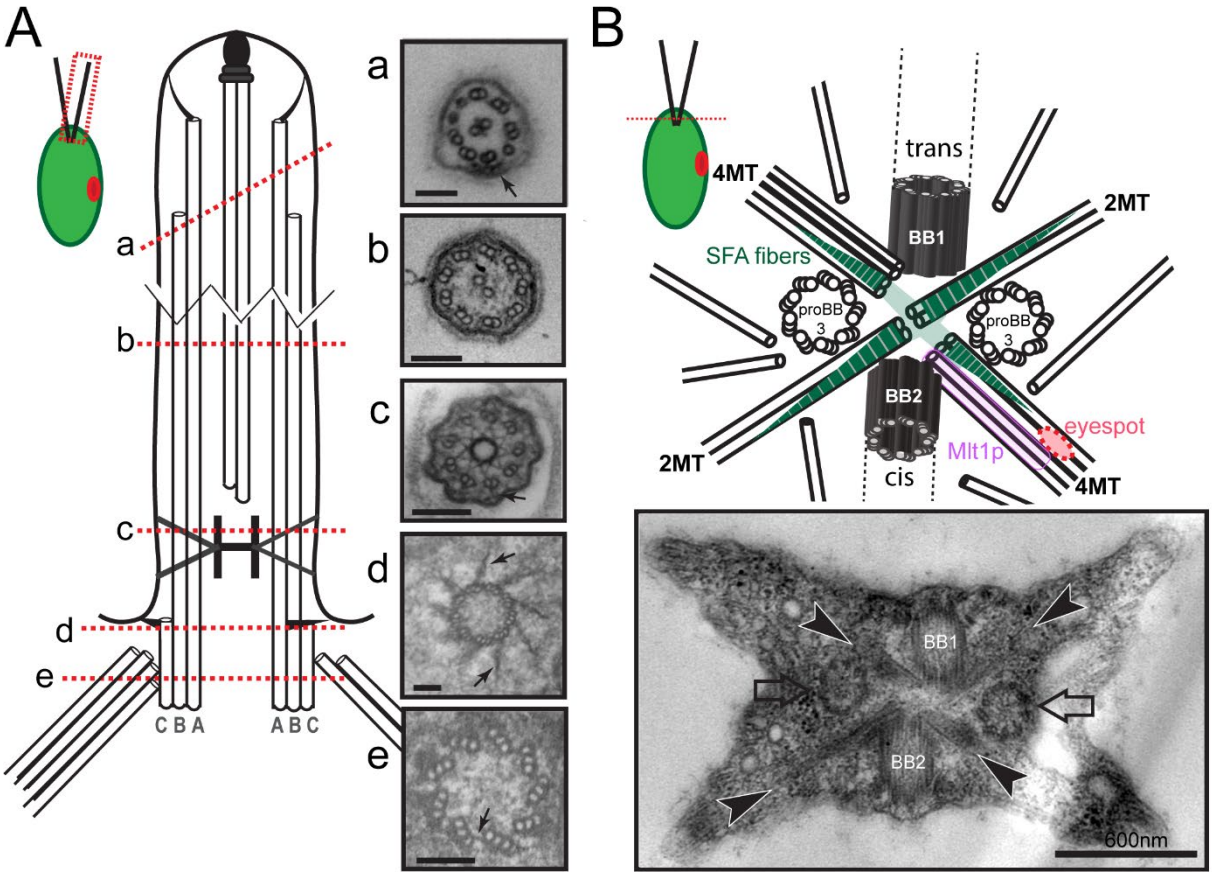

Figure 1.1 Structure of *C. reinhardtii* flagella and flagellar basal apparatus (modified from Wingfield and Lechtreck, 2018).

A) Cell overview. The dashed red box indicates the region shown in detail. Schematic drawing of a longitudinal section of a flagellum; the A-, B-, and C-tubules of the basal body are indicated. Red-dashed lines indicate the planes of the TEM cross-sections **(a–e)**. **a)** Flagellar tip with a mixture of singlet and doublet microtubules indicative for an oblique section. Arrow points to an IFT train. **b)** 9 + 2 axoneme surrounded by the plasma membrane and glycocalyx. **c)** Transition zone (TZ) with stellate structure, which appears as an H-shaped structure in longitudinal sections. The arrow marks a Y-linker. **d)** The distal end of the basal body with the transitional

fibers (arrows) connecting the triplets to the plasma membrane. **e)** Triplet microtubules of the basal body. Arrow: A-C linker. Scale bars = 100 nm. **B)** Cell overview, the red dashed line designates the plane of the cross-section. Top: Drawing of the flagellar basal apparatus with the flagella-bearing mother (BB1) and daughter (BB2) basal bodies, the probasal bodies (proBB3) and the microtubular roots consisting of 2 (2MT) or 4 microtubules (4MT). Green striated triangles: SFA fibers. The four fibers are interconnected as indicated by the green shaded area. The 4-stranded root of the daughter basal body connects to the eyespot; it is associated with Mlt1 protein, which participates in eyespot positioning. Bottom: TEM section of the flagellar basal apparatus. Arrows, probasal bodies; arrowheads, microtubular roots.

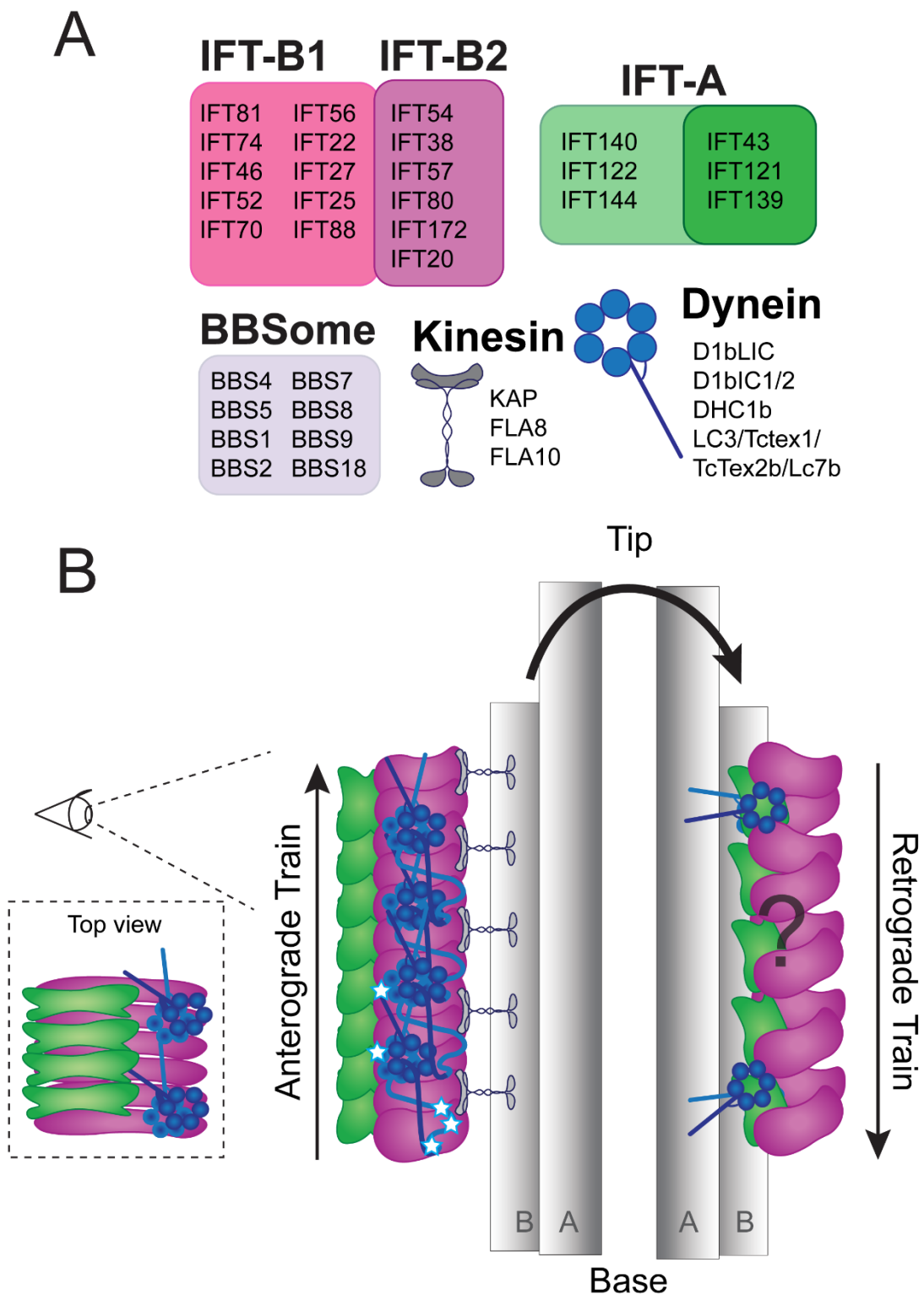

Figure 1.2 Composition and structure of IFT trains.

A) Cartoon representation of IFT subunits, IFT-A (core and peripheral), IFT-B1, and IFT-B2. An IFT cargo adaptor, the BBSome [not shown in B], and the IFT motors, kinesin-II and IFT dynein. The proteins that comprise each of the complexes are listed below the complex name. **B)** Cartoon representation of an anterograde train and retrograde train based on (Jordan et al., 2018) and (Toropova et al., 2019). Complexes and motors are colored as in A. Jordan et al. (2018) identified a 2:6:4 stoichiometry for dynein: IFT-B: IFT-A on anterograde trains; with IFT-A and inactive dynein riding on top of IFT-B. Toropova et al. (2019) found that inactive dynein makes five inhibitory contacts with IFT-B; shown as stars on a representative dynein. IFT-A and IFT-B could not be distinguished on retrograde trains indicated with-?. Active, uncrossed dyneins were able to be identified on retrograde trains (Jordan et al., 2018). The A-tubule and B-tubule are labeled in grey.

1.6 REFERENCES

Ahmed, N.T., C. Gao, B.F. Lucker, D.G. Cole, and D.R. Mitchell. 2008. ODA16 aids axonemal outer row dynein assembly through an interaction with the intraflagellar transport machinery. *The Journal of cell biology*. 183:313-322.

Avidor-Reiss, T., A.M. Maer, E. Koundakjian, A. Polyanovsky, T. Keil, S. Subramaniam, and C.S. Zuker. 2004. Decoding cilia function: defining specialized genes required for compartmentalized cilia biogenesis. *Cell*. 117:527-539.

Banizs, B., M.M. Pike, C.L. Millican, W.B. Ferguson, P. Komlosi, J. Sheetz, P.D. Bell, E.M. Schwiebert, and B.K. Yoder. 2005. Dysfunctional cilia lead to altered ependyma and choroid plexus function, and result in the formation of hydrocephalus. *Development (Cambridge, England)*. 132:5329-5339.

Beales, P., and P.K. Jackson. 2012. Cilia - the prodigal organelle. *Cilia*. 1:1-1.

Berbari, N.F., J.S. Lewis, G.A. Bishop, C.C. Askwith, and K. Mykytyn. 2008. Bardet-Biedl syndrome proteins are required for the localization of G protein-coupled receptors to primary cilia. *Proceedings of the National Academy of Sciences of the United States of America*. 105:4242-4246.

Bhogaraju, S., L. Cajanek, C. Fort, T. Blisnick, K. Weber, M. Taschner, N. Mizuno, S. Lamla, P. Bastin, E.A. Nigg, and E. Lorentzen. 2013. Molecular basis of tubulin transport within the cilium by IFT74 and IFT81. *Science*. 341:1009-1012.

Bizet, A.A., A. Becker-Heck, R. Ryan, K. Weber, E. Filhol, P. Krug, J. Halbritter, M. Delous, M.-C. Lasbennes, B. Linghu, E.J. Oakeley, M. Zarhrate, P. Nitschké, M. Garfa-Traore, F. Serluca, F. Yang, T. Bouwmeester, L. Pinson, E. Cassuto, P. Dubot, N.A.S. Elshakhs, J.A. Sahel, R. Salomon, I.A. Drummond, M.-C. Gubler, C. Antignac, S. Chibout, J.D. Szustakowski, F. Hildebrandt, E. Lorentzen, A.W. Sailer, A. Benmerah, P. Saint-Mezard, and S. Saunier. 2015. Mutations in TRAF3IP1/IFT54 reveal a new role for IFT proteins in microtubule stabilization. *Nature Communications*. 6:8666.

Blacque, O.E., M.J. Reardon, C. Li, J. McCarthy, M.R. Mahjoub, S.J. Ansley, J.L. Badano, A.K. Mah, P.L. Beales, W.S. Davidson, R.C. Johnsen, M. Audeh, R.H.A. Plasterk, D.L. Baillie, N. Katsanis, L.M. Quarmby, S.R. Wicks, and M.R. Leroux. 2004. Loss of C. elegans BBS-7 and BBS-8 protein function results in cilia defects and compromised intraflagellar transport. *Genes & development*. 18:1630-1642.

Bloodgood, R.A. 2010. Sensory reception is an attribute of both primary cilia and motile cilia. 123:505-509.

Brown, J.M., D.A. Cochran, B. Craige, T. Kubo, and G.B. Witman. 2015. Assembly of IFT trains at the ciliary base depends on IFT74. *Current biology : CB*. 25:1583-1593.

Chien, A., S.M. Shih, R. Bower, D. Tritschler, M.E. Porter, and A. Yildiz. 2017. Dynamics of the IFT machinery at the ciliary tip. *eLife*. 6:e28606.

Christensen, S.T., C.A. Clement, P. Satir, and L.B. Pedersen. 2012. Primary cilia and coordination of receptor tyrosine kinase (RTK) signalling. *The Journal of pathology*. 226:172-184.

Clement, C.A., K.D. Ajbro, K. Koefoed, M.L. Vestergaard, I.R. Veland, M.P. Henriques de Jesus, L.B. Pedersen, A. Benmerah, C.Y. Andersen, L.A. Larsen, and S.T. Christensen. 2013. TGF-beta signaling is associated with endocytosis at the pocket region of the primary cilium. *Cell reports*. 3:1806-1814.

Cole, D.G., D.R. Diener, A.L. Himelblau, P.L. Beech, J.C. Fuster, and J.L. Rosenbaum. 1998. Chlamydomonas Kinesin-II–dependent Intraflagellar Transport (IFT): IFT Particles Contain Proteins Required for Ciliary Assembly in Caenorhabditis elegans Sensory Neurons. *The Journal of cell biology*. 141:993-1008.

Cole, D.G., and W.J. Snell. 2009. SnapShot: Intraflagellar transport. *Cell*. 137:784-784.e781.

Corbit, K.C., P. Aanstad, V. Singla, A.R. Norman, D.Y. Stainier, and J.F. Reiter. 2005. Vertebrate Smoothened functions at the primary cilium. *Nature*. 437:1018-1021.

Craft, J.M., J.A. Harris, S. Hyman, P. Kner, and K.F. Lechtreck. 2015. Tubulin transport by IFT is upregulated during ciliary growth by a cilium-autonomous mechanism. *The Journal of cell biology*. 208:223.

Datta, P., C. Allamargot, J.S. Hudson, E.K. Andersen, S. Bhattarai, A.V. Drack, V.C. Sheffield, and S. Seo. 2015. Accumulation of non-outer segment proteins in the outer segment underlies photoreceptor degeneration in Bardet-Biedl syndrome. *Proceedings of the National Academy of Sciences of the United States of America*. 112:E4400-4409.

Deane, J.A., D.G. Cole, E.S. Seeley, D.R. Diener, and J.L. Rosenbaum. 2001. Localization of intraflagellar transport protein IFT52 identifies basal body transitional fibers as the docking site for IFT particles. *Current biology : CB*. 11:1586-1590.

Dentler, W. 2005. Intraflagellar transport (IFT) during assembly and disassembly of Chlamydomonas flagella. *The Journal of cell biology*. 170:649-659.

Eichele, G., E. Bodenschatz, Z. Ditte, A.K. Gunther, S. Kapoor, Y. Wang, and C. Westendorf. 2020. Cilia-driven flows in the brain third ventricle. *Philosophical transactions of the Royal Society of London. Series B, Biological sciences*. 375:20190154.

Gonçalves, J., and L. Pelletier. 2017. The Ciliary Transition Zone: Finding the Pieces and Assembling the Gate. *Mol Cells*. 40:243-253.

Gudis, D.A., and N.A. Cohen. 2010. Cilia dysfunction. *Otolaryngologic clinics of North America*. 43:461-472, vii.

Habbig, S., M.P. Bartram, R.U. Muller, R. Schwarz, N. Andriopoulos, S. Chen, J.G. Sagmuller, M. Hoehne, V. Burst, M.C. Liebau, H.C. Reinhardt, T. Benzing, and B. Schermer. 2011. NPHP4, a cilia-associated protein, negatively regulates the Hippo pathway. *The Journal of cell biology*. 193:633-642.

Han, Y.G., B.H. Kwok, and M.J. Kernan. 2003. Intraflagellar transport is required in Drosophila to differentiate sensory cilia but not sperm. *Current biology : CB*. 13:1679-1686.

Haycraft, C.J., B. Banizs, Y. Aydin-Son, Q. Zhang, E.J. Michaud, and B.K. Yoder. 2005. Gli2 and Gli3 localize to cilia and require the intraflagellar transport protein polaris for processing and function. *PLoS genetics*. 1:e53.

Hirokawa, N., Y. Tanaka, and Y. Okada. 2009. Left-right determination: involvement of molecular motor KIF3, cilia, and nodal flow. *Cold Spring Harb Perspect Biol*. 1:a000802-a000802.

Hou, Y., G.J. Pazour, and G.B. Witman. 2004. A dynein light intermediate chain, D1bLIC, is required for retrograde intraflagellar transport. *Mol Biol Cell*. 15:4382-4394.

Hsu, Y., J.E. Garrison, G. Kim, A.R. Schmitz, C.C. Searby, Q. Zhang, P. Datta, D.Y. Nishimura, S. Seo, and V.C. Sheffield. 2017. BBSome function is required for both the morphogenesis and maintenance of the photoreceptor outer segment. *PLoS genetics*. 13:e1007057-e1007057.

Hua, K., and R.J. Ferland. 2018. Primary cilia proteins: ciliary and extraciliary sites and functions. *Cellular and molecular life sciences : CMLS*. 75:1521-1540.

Huangfu, D., A. Liu, A.S. Rakeman, N.S. Murcia, L. Niswander, and K.V. Anderson. 2003. Hedgehog signalling in the mouse requires intraflagellar transport proteins. *Nature*. 426:83-87.

Ishikawa, H., and W.F. Marshall. 2011. Ciliogenesis: building the cell's antenna. *Nature Reviews Molecular Cell Biology*. 12:222-234.

Jenkins, P.M., D.P. McEwen, and J.R. Martens. 2009. Olfactory cilia: linking sensory cilia function and human disease. *Chem Senses*. 34:451-464.

Jordan, M.A., D.R. Diener, L. Stepanek, and G. Pigino. 2018. The cryo-EM structure of intraflagellar transport trains reveals how dynein is inactivated to ensure unidirectional anterograde movement in cilia. *Nat Cell Biol*. 20:1250-1255.

Khanna, H. 2015. Photoreceptor Sensory Cilium: Traversing the Ciliary Gate. *Cells*. 4:674-686.

Kobayashi, T., K. Gengyo-Ando, T. Ishihara, I. Katsura, and S. Mitani. 2007. IFT-81 and IFT-74 are required for intraflagellar transport in C. elegans. *Genes to cells : devoted to molecular & cellular mechanisms*. 12:593-602.

Koefoed, K., I.R. Veland, L.B. Pedersen, L.A. Larsen, and S.T. Christensen. 2014. Cilia and coordination of signaling networks during heart development. *Organogenesis*. 10:108-125.

Kozminski, K.G., P.L. Beech, and J.L. Rosenbaum. 1995. The Chlamydomonas kinesin-like protein FLA10 is involved in motility associated with the flagellar membrane. *The Journal of cell biology*. 131:1517-1527.

Kubo, T., J.M. Brown, K. Bellve, B. Craige, J.M. Craft, K. Fogarty, K.F. Lechtreck, and G.B. Witman. 2016. Together, the IFT81 and IFT74 N-termini form the main module for intraflagellar transport of tubulin. *Journal of cell science*. 129:2106-2119.

Lechtreck, K.F., E.C. Johnson, T. Sakai, D. Cochran, B.A. Ballif, J. Rush, G.J. Pazour, M. Ikebe, and G.B. Witman. 2009. The Chlamydomonas reinhardtii BBSome is an IFT cargo required for export of specific signaling proteins from flagella. *The Journal of cell biology*. 187:1117-1132.

Lehti, M.S., and A. Sironen. 2017. Formation and function of sperm tail structures in association with sperm motility defects†. *Biology of Reproduction*. 97:522-536.

Liew, G.M., F. Ye, A.R. Nager, J.P. Murphy, J.S. Lee, M. Aguiar, D.K. Breslow, S.P. Gygi, and M.V. Nachury. 2014. The intraflagellar transport protein IFT27 promotes BBSome exit from cilia through the GTPase ARL6/BBS3. *Dev Cell*. 31:265-278.

Liu, A., B. Wang, and L.A. Niswander. 2005. Mouse intraflagellar transport proteins regulate both the activator and repressor functions of Gli transcription factors. *Development (Cambridge, England)*. 132:3103-3111.

Liu, P., and K.F. Lechtreck. 2018. The Bardet-Biedl syndrome protein complex is an adapter expanding the cargo range of intraflagellar transport trains for ciliary export. *Proceedings of the National Academy of Sciences of the United States of America*. 115:E934-e943.

Liu, Z., H. Tu, Y. Kang, Y. Xue, D. Ma, C. Zhao, H. Li, L. Wang, and F. Liu. 2019. Primary cilia regulate hematopoietic stem and progenitor cell specification through Notch signaling in zebrafish. *Nature Communications*. 10:1839.

Lv, B., L. Wan, M. Taschner, X. Cheng, E. Lorentzen, and K. Huang. 2017. Intraflagellar transport protein IFT52 recruits IFT46 to the basal body and flagella. *Journal of cell science*. 130:1662-1674.

Marshall, W.F., and J.L. Rosenbaum. 2001. Intraflagellar transport balances continuous turnover of outer doublet microtubules: implications for flagellar length control. *The Journal of cell biology*. 155:405-414.

Mijalkovic, J., J. van Krugten, F. Oswald, S. Acar, and E.J.G. Peterman. 2018. Single-Molecule Turnarounds of Intraflagellar Transport at the C. elegans Ciliary Tip. *Cell reports*. 25:1701-1707.e1702.

Mönnich, M., L. Borgeskov, L. Breslin, L. Jakobsen, M. Rogowski, C. Doganli, J.M. Schrøder, J.B. Mogensen, L. Blinkenkjær, and L.M.J.C.r. Harder. 2018. CEP128 localizes to the subdistal appendages of the mother centriole and regulates TGF-β/BMP signaling at the primary cilium. 22:2584-2592.

Müller, O.F., and O. Fabricius. 1786. Animalcula infusoria fluviatilia et marina que detexit, systematice descripsit et ad vivum delineari curavit Otho Fridericus Müller sistit opus hoc posthumum quod cum tabulis Aeneis L. in lucem tradit vidua ejus nobilissima cura Othonis Fabricii. Typis N. Mölleri, Hauniae :.

Mykytyn, K., R.F. Mullins, M. Andrews, A.P. Chiang, R.E. Swiderski, B. Yang, T. Braun, T. Casavant, E.M. Stone, and V.C. Sheffield. 2004. Bardet-Biedl syndrome type 4 (BBS4)-null mice implicate Bbs4 in flagella formation but not global cilia assembly. *Proceedings of the National Academy of Sciences of the United States of America*. 101:8664-8669.

Nachury, M.V.J.C.o.i.c.b. 2018. The molecular machines that traffic signaling receptors into and out of cilia. 51:124-131.

Okada, Y., S. Nonaka, Y. Tanaka, Y. Saijoh, H. Hamada, and N. Hirokawa. 1999. Abnormal Nodal Flow Precedes Situs Inversus in iv and inv mice. *Molecular Cell*. 4:459-468.

Pazour, G.J., N. Agrin, J. Leszyk, and G.B. Witman. 2005. Proteomic analysis of a eukaryotic cilium. *The Journal of cell biology*. 170:103-113.

Pazour, G.J., B.L. Dickert, Y. Vucica, E.S. Seeley, J.L. Rosenbaum, G.B. Witman, and D.G. Cole. 2000. Chlamydomonas IFT88 and its mouse homologue, polycystic kidney disease gene tg737, are required for assembly of cilia and flagella. *The Journal of cell biology*. 151:709-718.

Peabody, J.E., R.-J. Shei, B.M. Bermingham, S.E. Phillips, B. Turner, S.M. Rowe, and G.M. Solomon. 2018. Seeing cilia: imaging modalities for ciliary motion and clinical connections. *Am J Physiol Lung Cell Mol Physiol*. 314:L909-L921.

Pedersen, L.B., S. Geimer, and J.L. Rosenbaum. 2006. Dissecting the Molecular Mechanisms of Intraflagellar Transport in Chlamydomonas. *Current Biology*. 16:450-459.

Peixoto, E., S. Richard, K. Pant, A. Biswas, and S.A. Gradilone. 2020. The primary cilium: Its role as a tumor suppressor organelle. *Biochemical Pharmacology*. 175:113906.

Piperno, G., E. Siuda, S. Henderson, M. Segil, H. Vaananen, and M. Sassaroli. 1998. Distinct mutants of retrograde intraflagellar transport (IFT) share similar morphological and molecular defects. *The Journal of cell biology*. 143:1591-1601.

Qin, H., D.R. Diener, S. Geimer, D.G. Cole, and J.L. Rosenbaum. 2004. Intraflagellar transport (IFT) cargo: IFT transports flagellar precursors to the tip and turnover products to the cell body. *The Journal of cell biology*. 164:255-266.

Raidt, J., C. Werner, T. Menchen, G.W. Dougherty, H. Olbrich, N.T. Loges, R. Schmitz, P. Pennekamp, and H. Omran. 2015. Ciliary function and motor protein composition of human fallopian tubes. *Human Reproduction*. 30:2871-2880.

Reck, J., A.M. Schauer, K. VanderWaal Mills, R. Bower, D. Tritschler, C.A. Perrone, and M.E. Porter. 2016. The role of the dynein light intermediate chain in retrograde IFT and flagellar function in Chlamydomonas. *Mol Biol Cell*. 27:2404-2422.

Richey, E.A., and H. Qin. 2012. Dissecting the sequential assembly and localization of intraflagellar transport particle complex B in Chlamydomonas. *PLoS One*. 7:e43118-e43118.

Rogowski, M., D. Scholz, and S. Geimer. 2013. Electron microscopy of flagella, primary cilia, and intraflagellar transport in flat-embedded cells. *Methods in enzymology*. 524:243-263.

Rosenbaum, J.L., and F.M. Child. 1967. Flagellar regeneration in protozoan flagellates. *The Journal of cell biology*. 34:345-364.

Sarpal, R., S.V. Todi, E. Sivan-Loukianova, S. Shirolikar, N. Subramanian, E.C. Raff, J.W. Erickson, K. Ray, and D.F. Eberl. 2003. Drosophila KAP interacts with the kinesin II motor subunit KLP64D to assemble chordotonal sensory cilia, but not sperm tails. *Current biology : CB*. 13:1687-1696.

Satir, P. 1995. Landmarks in cilia research from Leeuwenhoek to us. *Cell motility and the cytoskeleton*. 32:90-94.

Shah, A.S., Y. Ben-Shahar, T.O. Moninger, J.N. Kline, and M.J. Welsh. 2009. Motile Cilia of Human Airway Epithelia Are Chemosensory. 325:1131-1134.

Stasiulewicz, M., S.D. Gray, I. Mastromina, J.C. Silva, M. Björklund, P.A. Seymour, D. Booth, C. Thompson, R.J. Green, E.A. Hall, P. Serup, and J.K. Dale. 2015. A conserved role for Notch signaling in priming the cellular response to Shh through ciliary localisation of the key Shh transducer Smo. 142:2291-2303.

Stepanek, L., and G. Pigino. 2016. Microtubule doublets are double-track railways for intraflagellar transport trains. *Science*. 352:721-724.

Taschner, M., A. Lorentzen, A. Mourao, T. Collins, G.M. Freke, D. Moulding, J. Basquin, D. Jenkins, and E. Lorentzen. 2018. Crystal structure of intraflagellar transport protein 80 reveals a homo-dimer required for ciliogenesis. *eLife*. 7.

Taschner, M., and E. Lorentzen. 2016. The Intraflagellar Transport Machinery. *Cold Spring Harb Perspect Biol*. 8.

Taschner, M., K. Weber, A. Mourão, M. Vetter, M. Awasthi, M. Stiegler, S. Bhogaraju, and E. Lorentzen. 2016. Intraflagellar transport proteins 172, 80, 57, 54, 38, and 20 form a stable tubulin-binding IFT-B2 complex. *The EMBO Journal*. 35:773-790.

Toropova, K., R. Zalyte, A.G. Mukhopadhyay, M. Mladenov, A.P. Carter, and A.J. Roberts. 2019. Structure of the dynein-2 complex and its assembly with intraflagellar transport trains. *Nature Structural & Molecular Biology*. 26:823-829.

van Dam, T.J., M.J. Townsend, M. Turk, A. Schlessinger, A. Sali, M.C. Field, and M.A. Huynen. 2013. Evolution of modular intraflagellar transport from a coatomer-like progenitor. *Proceedings of the National Academy of Sciences of the United States of America*. 110:6943-6948.

Vannuccini, E., E. Paccagnini, F. Cantele, M. Gentile, D. Dini, F. Fino, D. Diener, C. Mencarelli, and P. Lupetti. 2016. Two classes of short intraflagellar transport train with different 3D structures are present in Chlamydomonas flagella. *Journal of cell science*. 129:2064-2074.

Wagner, M.K., and H.J. Yost. 2000. Left–right development: The roles of nodal cilia. *Current Biology*. 10:R149-R151.

Wallingford, J.B., and B. Mitchell. 2011. Strange as it may seem: the many links between Wnt signaling, planar cell polarity, and cilia. *Genes & development*. 25:201-213.
Wingfield, J.L., and K.-F. Lechtreck. 2018. Chlamydomonas Basal Bodies as Flagella Organizing Centers. *Cells*. 7:79.
Williams, C.L., J.C. McIntyre, S.R. Norris, P.M. Jenkins, L. Zhang, Q. Pei, K. Verhey, and J.R. Martens. 2014. Direct evidence for BBSome-associated intraflagellar transport reveals distinct properties of native mammalian cilia. *Nat Commun*. 5:5813.
Zhu, X., Y. Liang, F. Gao, and J. Pan. 2017. IFT54 regulates IFT20 stability but is not essential for tubulin transport during ciliogenesis. *Cellular and molecular life sciences : CMLS*. 74:3425-3437.

CHAPTER 2

IFT TRAINS IN DIFFERENT STAGES OF ASSEMBLY QUEUE AT THE CILIARY BASE FOR CONSECUTIVE RELEASE INTO THE CILIUM[1]

[1] Wingfield, J.L., I. Mengoni, H. Bomberger, Y.Y. Jiang, J.D. Walsh, J.M. Brown, T. Picariello, D.A. Cochran, B. Zhu, J. Pan, J. Eggenschwiler, J. Gaertig, G.B. Witman, P. Kner, and K. Lechtreck. 2017. IFT trains in different stages of assembly queue at the ciliary base for consecutive release into the cilium. *eLife*. 6:e26609. Reprinted here with permission of the publisher via the Creative Commons Attribution License (https://creativecommons.org/licenses/by/4.0/).

2.1 ABSTRACT

Intraflagellar transport (IFT) trains, multimegadalton assemblies of IFT proteins and motors, traffic proteins in cilia. To study how trains assemble, we employed fluorescence protein-tagged IFT proteins in Chlamydomonas reinhardtii. IFT-A and motor proteins are recruited from the cell body to the basal body pool, assembled into trains, move through the cilium, and disperse back into the cell body. In contrast to this 'open' system, IFT-B proteins from retrograde trains reenter the pool and a portion is reused directly in anterograde trains indicating a 'semi-open' system. Similar IFT systems were also observed in Tetrahymena thermophila and IMCD3 cells. FRAP analysis indicated that IFT proteins and motors of a given train are sequentially recruited to the basal bodies. IFT dynein and tubulin cargoes are loaded briefly before the trains depart. We conclude that the pool contains IFT trains in multiple stages of assembly queuing for successive release into the cilium upon completion.

2.2 INTRODUCTION

The assembly of most cilia and flagella (terms used interchangeably) depends on bidirectional intraflagellar transport (IFT) (Rosenbaum and Witman, 2002). Anterograde IFT trains move from the ciliary base to the tip powered by kinesin-2; in retrograde IFT, the trains return to the cell body employing IFT dynein. The IFT trains transport proteins in and out of cilia to support ciliary assembly, maintenance, and signaling (for review: (Lechtreck, 2015)). They are composed of IFT motors and IFT particles, the latter consisting of 22 conserved IFT proteins organized into biochemically stable IFT-A, IFT-B1 and IFT-B2 subcomplexes each consisting of equimolar amounts of 6, 10 and 6 proteins, respectively (Cole et al., 1998; Katoh et al., 2016; Taschner et al., 2012; Taschner et al., 2016). At the ultrastructural level, the trains possess a

periodic substructure presumably resulting from the 22-subunit IFT particles (Pigino et al., 2009; Stepanek and Pigino, 2016; Vannuccini et al., 2016). Numerous protein-protein interactions within the IFT particle have been identified and a 15-subunit IFT-B complex has been assembled from recombinant proteins (Hirano et al., 2017; Taschner et al., 2016). The oligomerization of purified IFT complexes to the size of trains observed in vivo under cell free conditions has not yet been reported. In summary, our knowledge on how trains assemble is limited.

Western blot analyses showed that 90% or more of the IFT proteins reside in the cell body, a portion of which is concentrated around the basal bodies forming an IFT pool (Ahmed et al., 2008; Deane et al., 2001; Richey and Qin, 2012). The IFT trains emerge from the basal body pool (bb-pool) and enter into the cilia in a kinesin-2 dependent manner (Kozminski et al., 1995). In contrast to the discrete IFT trains observed inside cilia, the IFT bb-pool appears to be amorphous at the ultrastructural level, i.e., bona fide IFT trains with their characteristic zigzag structure are visible only near the distal end of the basal bodies (Rogowski et al., 2013). IFT-B loss-of-function mutants often fail to assemble cilia presumably due to impaired IFT train formation. In such mutants, the stability of the remaining IFT proteins and their spatial distribution in the bb-pool are altered (see for example: (Hou et al., 2007; Lv et al., 2017; Richey and Qin, 2012)). Studies on such mutants clarify the interdependence among IFT proteins during subcomplex assembly and recruitment into the bb-pool. They are, however, less suited to determine the dynamics of IFT proteins in the bb-pool during the assembly of functional IFT trains. In a pioneering study, Buisson et al. (2012) used GFP-tagged IFT52 and fluorescence recovery after photobleaching (FRAP) to study the assembly of IFT trains in *Trypanosoma brucei* (Buisson et al., 2012). After photobleaching of the bb-pool, anterograde traffic of fluorescent IFT trains was transiently interrupted, indicative of bleached trains exiting the bb-

pool. The pool signal recovered partially and anterograde IFT traffic resumed albeit with reduced signal strength suggesting that photobleached proteins in the bb-pool mix with unbleached IFT proteins supposedly derived from retrograde trains. This led to the proposal of a closed IFT system in which the IFT proteins perpetually cycle between the flagellum and the bb-pool with limited exchange of proteins between the flagellum-basal body entity and the rest of the cell body.

Here, we used a collection of eight fluorescent protein (FP)-tagged IFT proteins to study the assembly of IFT trains in C. reinhardtii, which allows for high quality imaging of protein traffic inside flagella by total internal reflection fluorescence (TIRF) microscopy (Engel et al., 2009; Lechtreck, 2013; Lechtreck, 2016). Our analysis revealed a largely open IFT system in which proteins are continuously recruited from the cell body to the basal bodies, assembled into trains, and released back into the cell body after traveling through the cilium. Bleaching of the bb-pool was followed by a temporal gap in fluorescence anterograde IFT traffic of several seconds before unbleached trains reentered the cilium. Notably, the duration of this gap differed among the IFT proteins analyzed suggesting that IFT-A, IFT-B, and finally the motor proteins are sequentially recruited into assembling trains. Our data indicate a high temporospatial organization of the IFT bb-pool with IFT trains in various stages of assembly queuing near the basal bodies for sequential release into the cilium.

RESULTS

2.3 IFT proteins occupy distinct regions of the basal body pool.

To analyze the dynamics of IFT proteins in the pool surrounding each of the two flagella-bearing basal bodies of Chlamydomonas reinhardtii, we employed strains expressing fluorescent protein

(FP)-tagged IFT particle and motor proteins (Fig. 2.1A). IFT27 was expressed in a wild-type strain and KAP-GFP was expressed in fla3, which has a mutant KAP of reduced function (Mueller et al., 2005; Qin et al., 2007). The other proteins were expressed in loss-of-function mutants and rescued the corresponding flagella assembly phenotypes (Fig. 2.1A, B). The transgenic strains had normal or nearly normal length flagella and displayed IFT traffic with mostly wild-type IFT velocities and anterograde frequencies (~ 1/s); retrograde frequencies were more variable which we attribute mostly to the weaker signals of retrograde trains (Fig. 2.1A-D). Trajectories representing retrograde traffic of KAP-GFP, which in C. reinhardtii mostly dissociates from IFT trains at the tip, were faint and infrequent. For our experiments, we selected cells displaying frequent IFT traffic avoiding cells with stationary IFT proteins accumulated inside the flagella (Stepanek and Pigino, 2016). To image IFT proteins in the basal body pool, the incident angle of the laser beam was increased to allow for a deeper penetration of the light into the specimen. The various FP-tagged IFT proteins were present in dot-, colon-, or dumbbell-shaped regions near each basal body; most of them also showed weak X-shaped signals representing the microtubular flagellar roots (Fig. 2.1A). Focal series from the flagella down into the cell body revealed that most of KAP-GFP was close to the distal end of the basal bodies followed by accumulations of the tagged IFT-B proteins; the IFT-A proteins and D1bLIC were concentrated deeper in the cell (not shown; (Brown et al., 2015)). The IFT140-sfGFP signals were more peripheral than those of most IFT-B proteins. Within the limitations of the technique used, live cell imaging confirms and extends pervious observations on fixed cells indicating that different IFT proteins inhabit non-identical spatial domains within the bb-pool (Hou et al., 2007).

2.4 IFT proteins in the basal body pool exchange at different rates.

A focused laser beam in epi-illumination was used to photobleach one of the two IFT pools at the flagellar base (Figs. 2.2A, 2.2-figure supplement 1A-C). The IFT bb-pool signals of all eight FP-tagged IFT particle and motor proteins recovered on average within 3 to 10 s (Fig. 2.2B). To quantify the degree and rate of recovery, we normalized the signal intensity of the bleached experimental bb-pool for fluorescence loss encountered by the unbleached control bb-pool due to the continuous TIRF illumination (Fig. 2.2C, D). Signal recovery typically exceeded 60% of the prebleach strength and often complete recovery to the level of the control bb-pool was observed (Fig. 2.2C). Recovery of the signal was also observed after repeated bleaching of the bb-pool indicating that the size of one IFT bb-pool is small as compared to the total cellular supply of IFT proteins (Figs. 2.2D, 2.2-figure supplement 1D, E). While the KAP-GFP signal recovered in less than 4 s, IFT43-YFP, IFT20-FP and NG-IFT54 required ~9s to reach maximum recovery (Fig. 2.2E). In conclusion, IFT proteins in the bb-pool exchange at different rates.

2.5 The dispatched IFT-A and motor proteins do not return to the basal body pool.

The unbleached proteins causing the recovery of a bleached bb-pool could either be derived from retrograde IFT or newly recruited from the cell body (referred to here as the “cell body pool” or cb-pool). To determine which source resupplies the IFT bb-pool, we used a fluorescence loss in photobleaching (FLIP) approach by placing a focused laser beam near the tip of one flagellum preventing the return of unbleached IFT proteins to the basal body via retrograde IFT (Fig. 2.3A). The duty ratio of the bleaching laser was set to 100-200 ms on and 400-900 ms off and in many experiments, images were only recorded while the bleaching laser was off to eliminate over-exposed frames (compare Figs. 2.3B, C, F and 2.3-figure supplement 1A). TIRF imaging at

the flagella level identified fluorescent retrograde IFT trains in the control flagellum but not in the experimental flagellum (Figs. 2.3B, 2.3-figure supplement 1A). Focusing onto the basal bodies, the fluorescence intensity of the bb-pool attached to the experimental flagellum was determined and normalized for general fluorescence loss using the control basal body. For the IFT-B proteins IFT20-NG, IFT46-YFP, and NG-IFT54 the signal intensity of the experimental basal body decreased significantly during FLIP illumination (Fig. 2.3C, D, F, G). The fluorescence loss was substantially lower for the tagged IFT27, motor protein subunits, and in particular IFT-A proteins (Figs. 2.3E – G, 2.3-figure supplement 1D). A pronounced fluorescence loss occurred predominately during the first 10-20s of FLIP and some unbleached IFT-B proteins were present in the experimental bb-pool even in prolonged FLIP experiments (>30 s; Figs. 2.3C, D, 2.3-figure supplement 1B). For the NG-IFT54 bb-pool, this plateau was reached after ~15 s (STD 4.4s, n=14; Fig. 2.3-figure supplement 1F) of FLIP illumination when the normalized signal strength of the experimental basal body was reduced to ~52% (STD 9.2%, n=14; Fig. 2.3-figure supplement 1G) of its initial level. After switching off the FLIP laser, the basal body signal recovered and retrograde IFT recommenced (Fig. 2.3-figure supplement 1A, C). We conclude that most of IFT27 and the tested IFT-A and motor subunits do not reenter the bb-pool whereas IFT20/46/54 re-enter to the bb-pool after returning from the cilium.

2.6 Anterograde trains are largely assembled from proteins freshly recruited to the basal bodies.

The above experiments raise the question whether the IFT-B proteins returning via retrograde IFT into the bb-pool will be released with a delay into the cb-pool or reused directly in subsequent anterograde IFT trains without first cycling through the cb-pool. In the latter scenario, the signal strength of anterograde traffic should decrease progressively as the return of

unbleached protein from the flagellum to the bb-pool is prevented. However, anterograde IFT trains containing unbleached IFT20/46/54 continued to enter the experimental flagella even after prolonged (>60s) FLIP illumination with a frequency comparable to anterograde IFT in the control flagellum (Figs. 2.3C, 2.3-figure supplement 1A). The signal strength of such trains, however, was generally below those in the control flagellum indicating that these trains contain both bleached proteins derived from retrograde trains and unbleached proteins recruited from the cell body. The signal strength of such trains could provide a measure of how much bleached and unbleached IFT-B protein was used for their assembly. A precise quantification is impeded because signal strength is affected by the absence of retrograde traffic and progressive loss of signal from stationary IFT in the experimental flagellum. To adjust for these shortcomings, we first analyzed the IFT-A protein IFT43-YFP, whose bb-pool signal is not affected in the FLIP assay (Fig. 2.3F, G, 2.3-figure supplement 1D). The signal strength of trains exiting the experimental bb-pool under FLIP illumination was ~10% below those in the control flagellum (n=8, 4 – 7 IFT trains were measured in each cilium). A similar comparison for NG-IFT54 showed a 40% intensity decrease of trains in the experimental flagellum compared to trains in the control flagellum (n=11; 4 – 8 measurements per cilium). trains. With the qualification that IFT20/46/54 are partly salvaged, we conclude that C. reinhardtii possess a largely open IFT system, in which proteins are recruited from the cb-pool to the basal bodies, assembled into trains, and travel once through the flagellum before being disassembled and released back into the cell body pool.

When FLIP bleaching at one ciliary tip of a given cell was continued for several minutes the signal of IFT trains progressively diminished in both cilia (Fig. 2.3-figure supplement 2). After ~6 - 9 minutes of FLIP, IFT traffic diminished indicating that the entire cellular IFT pool

was near exhaustion. Sporadic residual IFT traffic allowed for the observation of individual trains presumably containing only one or a few copies of unbleached NG-IFT54 (Fig. 2.3-figure supplement 2C). Unbleached NG-IFT54 was evenly distributed between the two flagella. In control cells imaged for similar periods of time without being directly hit by the FLIP laser, dense IFT traffic albeit of reduced intensity persisted (Fig. 2.3-figure supplement 2D). The data suggest that NG-IFT54 returning to the cb-pool will eventually be reused and that bleached and unbleached proteins mix in the cb-pool and are stochastically recruited to the basal body pools.

2.7 Half of the NG-IFT54 is derived from retrograde trains.

The above data indicate that the bb-pool consists in parts of disassembling IFT-B complexes. The approach of bleaching trains only at the tip still allows unbleached retrograde trains *en route* and IFT proteins transiently stationary along the length of the cilium to return to the bb-pool. To determine the dynamics of the disassembling IFT-B bb-pool, we moved the focused laser beam from the flagellar tip to the base bleaching almost the entire NG-IFT54 population in the experimental flagellum (Fig. 2.3-figure supplement 3A). This approach offers a clear onset and an extended period during which only bleached trains return to the bb-pool. After the bleaching step, the signal strength of the experimental bb-pool declined by 52% (STD 8.5%, n=6) over a period of 5.8 s (STD 0.9 s, n = 6) before reaching a plateau (Fig. 2.3-figure supplement 3B-D). Thus, ~50% of the NG-IFT54 in the bb-pool is derived from retrograde trains. The first unbleached retrograde train returned after 10.9 s (STD 1.8 s, n=22) to the experimental basal body (Fig. 2.3-figure supplement 3B, C). Concomitantly with the return of unbleached NG-IFT54 via retrograde traffic, the bb-pool recovered in strength on average in 16.6 s after the bleaching step (STD 2.4s, n=6) to levels of the control basal body (Fig. 2.3-figure supplement

2.3B-D). The data suggest that NG-IFT54 entering the bb-pool by retrograde traffic remains for ~6 s in the pool before its release into the cell body or reuse in anterograde trains. In similar experiments using KAP-GFP or the IFT-A protein IFT43-YFP, the signal strength of the bb-pool attached to the experimental flagellum remained essentially unaltered indicating that these proteins are released into the cb-pool upon return from the cilium (n=4 and 5, respectively; Fig. 2.3-figure supplement 3E-H).

2.8 Mammalian IMCD3 cells and Tetrahymena thermophila have open IFT systems

In contrast to our data on *C. reinhardtii*, observations made in *Trypanosoma brucei* indicated a closed IFT system in which proteins move back and forth between the bb-pool and flagellum with negligible exchange with the cb-pool during the duration of the experiment (Buisson et al., 2012). To determine the prevalence of open and closed systems, primary cilia of IMCD cells expressing IFT88-YFP and motile cilia of the ciliate *Tetrahymena thermophila* expressing GFP-Dyf-1 (IFT70) were analyzed (Fig. 2.4).

In primary cilia of IMCD cells, IFT88-YFP moved in typical anterograde IFT trains but was also present in stationary aggregates resulting in a high background (Fig. 2.4A,B). After photobleaching of the entire cilium including its bb-pool, the basal body signal recovered to 60 – 95% within 16.8 s (STD 7.2 s, n = 11, normalized using the cilium of a neighboring unbleached cell; Fig. 2.4A, C); the first unbleached IFT trains entered the cilia after an average of 18.1 s (STD 9.5 s, n= 39, Fig. 2.4B). The data reveal that IFT88-YFP in IMCD cells is continuously recruited from the cell body to the basal bodies and assembled into IFT trains.

T. thermophila possesses ~800 cilia; these mobile cells were immobilized by compression between the cover glass and slide allowing us to image IFT as visualized by the

expression of GFP-Dyf-1 (IFT70) in a null background (Dave et al., 2009; Jiang et al., 2015). After bleaching of a single cilium with its bb-pool, the recovery of the basal body signal became quickly apparent and reached a maximum of 74 % (STD 25%, n = 10) of the prebleach value in 29 s (STD 8s, n = 10, Fig. 2.4D-F); unbleached anterograde trains were observed after 17.1 s (STD 8 s, n = 20) and the ciliary signal recovered partially indicating a continuous recruitment of cell body IFT70-GFP to the basal bodies for assembly into IFT trains. In summary, FRAP analysis indicates open and semi-open IFT systems in all three cell types.

2.9 IFT trains exit the pool from distinct sites.

To determine the size of the IFT bb-pool in *C. reinhardtii*, we focused on NG-IFT54 and KAP-GFP, which due to their distal position on the basal body often allowed for simultaneous imaging of the bb-pool and departing trains (Fig. 2.5). The departure of an IFT train resulted in a transient reduction of signal strength at the bb-pool of ~16.1% (STD 7.2%, n=18) for KAP-GFP, and 12.7% (STD 5.8, n=20) for NG-IFT54 (Fig. 2.5A-C). Similarly, the arrival of a train increased the NG-IFT54 bb-pool signal by up to 25% (Fig. 2.5C). In this analysis we focused on bright trains allowing for a clear correlation between train trajectories and fluorescence loss in the bb-pool. Bright trains alternated with dimmer trains (Ludington et al., 2013), which changed the bb-pool signal by an estimated 5 – 10%. The data reveal that the departure (or arrival) of a single IFT train appreciably affects the strength of the bb-pool suggesting that the amount of IFT protein in the bb-pool is equivalent to a number of IFT trains in the upper single or lower double digits. NG-IFT54 trains, which could be best studied due to their bright and stable signal, exited the bb-pool at distinct sites resulting in a local depletion of the bb-pool (Fig. 2.5D). Kymograms obtained by scanning along two or three distinct lines parallel to the basal body-flagellum axis of

a given cell were merged to visualize the exit of trains from distinct sites of the bb-pool and their journey along the flagellum (Fig. 2.5E-I). While no particular pattern was observed, the data nevertheless indicate that consecutive trains are often released from distinct sites of the bb-pool.

2.10 IFT proteins are recruited and assembled sequentially into anterograde trains.

To determine the time required for the assembly of anterograde IFT trains, we measured the interval between the bleaching of one bb-pool and the departure of the first unbleached train into the attached flagellum (Fig. 2.6A). The untreated basal body and its flagellum served as a crucial control because exceedingly strong or long laser pluses disturbed IFT traffic in both flagella (not shown). Typically, bleaching of the bb-pool was followed by an interruption in the traffic of fluorescent anterograde IFT in the experimental flagellum; we refer to this period as the gap. After the gap anterograde traffic recommenced with prebleach or almost prebleach intensity and frequency (Fig. 2.6B). Infrequent "early bird" IFT trains could result from incomplete bleaching of the bb-pool; a limited replacement of bleached protein in the assembling trains with unbleached proteins from the surroundings is also possible. Occasionally, we also observed retrograde trains apparently making a U-turn near the ciliary base (not shown).

The presence of a distinct gap after bleaching of the bb-pool suggests that IFT trains containing the bleached proteins exit the bb-pool before new trains assembled from unbleached proteins emerge. The duration of the gap varied considerably for the different IFT proteins analyzed and ranged from ~7 s for IFT140-sfGFP to ~2.5 s for D1bLIC-GFP (Fig. 2.6C). The differences in the duration of the gap between each of the two IFT-A, -B1, and -B2 proteins as well as those between the IFT-A and -B2 proteins were not significant while those between IFT-A and -B1 and the motors were. The observation suggests that distinct IFT proteins need

different time spans to transition through the bb-pool from recruitment to release via anterograde IFT.

To substantiate this observation, we generated a strain (*fla3* KAP-GFP *ift140* IFT140-mCherry) expressing KAP-GFP and IFT140-mCherry in the corresponding *fla3 ift140* double mutant background (Fig. 2.7A). We then analyzed the duration of the gap between bleaching of the bb-pool and release of the first unbleached KAP-GFP and IFT140-mC trains into the attached flagellum (Fig. 2.7B). In most experiments (42 of 49), trains labeled only with KAP-GFP reappeared before trains marked by both KAP-GFP and IFT140-mCherry; in the remaining experiments both markers were present in the first postbleach train (data not shown). In the two-color experiments, the average duration of the gaps between bleaching of the bb-pool and the discharge of the first unbleached KAP or IFT140 trains were similar to those determined in the single-tag strains (Fig. 2.7C). The distinct properties of the two proteins were also apparent in two-color FRAP analysis of the bb-pool: The KAP-GFP signal was restored significantly before that of IFT140-mCherry (n=3, Fig. 2.7D, E). The data indicate that IFT140-sfGFP is recruited early during the assembly of a given IFT train while KAP-GFP is added later (Fig. 2.7-figure supplement 1). In a similar analysis using a strain expressing NG-IFT54 (IFT-B2) and IFT140-mCherry (IFT-A), the post-bleach trains mostly contained both fluorescent IFT-proteins (13 of 15 experiments; in two experiments the first train contained NG-IFT54 but not IFT140-mC; not shown). We propose that IFT trains are assembled by sequential addition of distinct IFT proteins/subcomplexes and that trains in different states of assembly are lined up in the bb-pool to be successively dispatched into the flagellum upon completion.

2.11 Tubulin binds briefly before the departure of IFT trains into the cilium.

IFT trains transport axonemal proteins into flagella but it remains unclear when and where cargo proteins attach to the trains (Craft et al., 2015b; Qin et al., 2004b; Wren et al., 2013b). Axonemal cargoes could already bind to IFT complexes in the cb-pool (e.g., on post-Golgi vesicles) or later during train assembly in the bb-pool (Wood and Rosenbaum, 2014). The above described approach of determining the duration of the gap in anterograde traffic after bleaching of the bb-pool has the potential to discriminate between these possibilities: If a cargo binds to IFT already prior to the recruitment to the bb-pool the gap should be in the range of that determined for the IFT proteins; shorter gaps would indicate loading at a later stage of train assembly. A prerequisite for this approach is a dense and regular cargo traffic as it has been reported for sfGFP-tubulin, which during flagellar regeneration enters cilia with an anterograde frequency of ~20/minute with higher frequencies during early regeneration (Craft et al., 2015b). Cells expressing sfGFP-α-tubulin at ~10% of the endogenous α-tubulin were first deflagellated by a pH shock and allowed to initiate flagellar regeneration for >20 minutes. sfGFP-tubulin already incorporated into the flagella was photobleached until IFT traffic of sfGFP-tubulin became visible (Fig. 2.8A). Then, one basal body region was photobleached using the microtubular roots to position the beam (Fig. 8B). sfGFP-tubulin traffic into the attached flagellum resumed almost immediately (Fig. 2.8C, D). In detail, the gap between the bleach and the first sfGFP-tubulin trajectory was 1.9 s (STD 1.7s, n=25) for the experimental flagellum and 2.1 s (STD 1.6s, n=25) for the control flagellum; the difference was not significant (2-tailed t-test p= 0.74). To ensure proper bleaching of sfGFP-tubulin near the flagellar base, we used an extended laser beam with a diameter of ~2 μm. sfGFP-tubulin traffic into the flagella resumed after on average 2.5s (STD 1.5 s, n = 22). Notably, a similar short gap was also observed for

D1bLIC, a subunit of IFT dynein, which is transported as a cargo on anterograde trains. Based on these data, we propose that sfGFP-tubulin and IFT dynein associate to IFT trains at the flagellar base briefly before departure into the cilium.

2.12 DISCUSSION

We used *in vivo* imaging in *C. reinhardtii* to study the assembly of IFT trains. IFT trains were first observed using DIC microscopy as birefringent particles moving up and down the flagella (Kozminski et al., 1993). Using GFP-tagged proteins, discrete IFT trains traveling inside cilia were observed of various organisms (Besschetnova et al., 2009; Mueller et al., 2005; Orozco et al., 1999; Williams et al., 2014). Correlative light-electron microscopy identified IFT trains at as electron opaque arrays with a repetitive ultrastructural moving between the ciliary membrane and the axoneme (Kozminski et al., 1995; Stepanek and Pigino, 2016). The pool of IFT proteins surrounding the basal bodies apparently lacks the well-defined ultrastructure of the trains moving inside cilia (Rogowski et al., 2013). Based on the brightness of signals representing immunostained or FP-tagged IFT proteins, the bb-pool is several times the size of a single train. Due to this crowded situation, imaging of individual IFT trains from their inception to release into the cilium has not been achieved. Here, we used *in vivo* imaging and photobleaching to study the assembly of IFT trains. Our two main conclusions are that the IFT system is largely open with proteins constantly exchanging between the basal body-flagellum compartment and the cell body and that the bb-pool consists of a queue of IFT trains in different stages of construction.

The IFT system is open

IFT trains perpetually enter and exit the flagellum but the source of IFT proteins in the bb-pool and the fate of the IFT proteins returning to the pool are less clear. Two not mutually exclusive models have been proposed: A closed IFT system in which retrograde trains are remodeled in the bb-pool and reused in anterograde traffic and an open IFT system in which proteins are recruited to the bb-pool, move as trains through the cilium, and disperse back into the cb-pool (Buisson et al., 2012). Photobleaching of FP-tagged IFT proteins allows us to distinguish between these models. In a closed system, fluorescent anterograde traffic should quickly cease when the return of unbleached proteins to the flagellar base is prevented by photobleaching. In contrast, fluorescent anterograde traffic will continue in an open system until the entire cellular pool of the protein in question is bleached. Our data in *C. reinhardtii* revealed a largely open system for the IFT-B protein IFT27-GFP and the tested IFT-A and motor subunits and semi-open systems for the IFT-B proteins IFT20/46/54, where portions of the retrograde trains are reused in the assembly of anterograde trains (Fig. 2.8E). FRAP analysis of one IFT-B protein each indicates that open or semi-open IFT systems are also in place in *T. thermophila* and IMCD cells.

In contrast, a closed IFT system was proposed for the IFT-B protein IFT52 in *T. brucei* (Buisson et al., 2012). Similar to our observations on *C. reinhardtii*, IFT-B proteins, bleaching of the IFT52-GFP bb-pool in *T. brucei* was followed by a gap in anterograde traffic and IFT52-GFP from retrograde trains reentered the bb-pool. However, when anterograde IFT resumed the signal intensity of the trains was markedly below that of trains prior to the bleaching step and the total recovery of the bb-pool reached only ~50% of the prebleach intensity suggesting that the bleached proteins continue to cycle within the flagellum-basal body domain while an exchange with the cb-pool is negligible within the time span of the experiment. Possible reasons for the

disparities between *C. reinhardtii* and *T. brucei* range from differences in the experimental set-up to fundamental differences in IFT. For example, in a semi-open system as described for the IFT-B proteins, the ratio between new recruitment from the cb-pool and reusage of proteins derived from retrograde trains could be different between species with *T. brucei* favoring reusage. To study IFT52 dynamics in *T. brucei,* the bb-pool was photobleached. This technique cannot distinguish whether the unbleached proteins in postbleach trains are derived from retrograde trains or recruited from the cb-pool. In contrast, the observation of stable fluorescent IFT traffic after prolonged bleaching of retrograde IFT clearly indicates that unbleached proteins are continuously recruited from the cell body for incorporation into IFT trains. Single molecule imaging showed that kinesin-2 and IFT dynein returning from cilia in *C. elegans* diffuse briefly near the base to turn around and re-enter the cilium supporting a closed IFT system (Mijalkovic et al., 2017; Prevo et al., 2015). While our data do not exclude that some motors remain in the basal body-cilium compartment for several rounds of IFT, the bulk of the motor subunits KAP-GFP and D1bLIC-GFP in anterograde trains of *C. reinhardtii* is recruited from the cb-pool (see Fig. 2.3-figure supplement 3G, H for KAP-GFP). In their mature state, *C. elegans* cilia possess altered basal bodies and lack the transitional fibers, two structures that are likely to be critical for the recruitment of IFT proteins from the cb-pool to the ciliary base; these changes in could favor a more closed IFT system (Nechipurenko et al., 2017). Future studies using a range of imaging approaches and organisms are needed to evaluate the prevalence of closed and open IFT systems.

Temporal and spatial organization of the IFT pool

Comparison of the *in vivo* signals of eight FP-tagged proteins revealed differences with respect to their distribution along the basal body axis and their distance to the basal bodies

confirming previous observations based on antibody staining (Brown et al., 2015; Hou et al., 2007; Richey and Qin, 2012a). It appears that different IFT proteins occupy distinct territories indicating that the bb-pool contains IFT subcomplexes or individual proteins rather than entire IFT particles. Super-resolution imaging is likely to provide a clearer image of IFT protein territories within the bb-pool. Our data also indicate a functional compartmentalization of the bb-pool into assembling anterograde trains and disassembling IFT-B complexes.

The FRAP pattern of anterograde traffic after bleaching of the IFT bb-pool further informs on the assembly of IFT trains. Bleaching of the bb-pool is typically followed by a marked gap in IFT traffic during which no visible or only a few dim anterograde IFT trains enter the flagellum. A distinct gap in IFT traffic was also observed for IFT52-GFP in *T. brucei* (Buisson et al., 2012). The presence of a gap indicates that bleached trains exit the bb-pool ahead of trains assembled later from unbleached proteins. Based on these data, we propose that the IFT trains queue in the bb-pool to be released in order with newly assembling trains added to the end of the queue.

The length of the postbleach gap varied between the IFT proteins analyzed. A short gap, as it was observed for the KAP and D1bLIC, indicates recruitment of a given subunit shortly before the train exits the bb-pool; conversely, a long gap as observed for the IFT-A and IFT-B2 subunits, indicates that a protein was recruited early during train assembly. The data imply that the bb-pool should contain more IFT-A proteins (in equivalents of IFT trains) than KAP. The use of different FPs, the distinct spatial distribution of IFT protein in the bb-pool, and the expected small scale of the expected differences prevented us from comparing the amounts of the different IFT proteins in the pool. The post-bleach gaps were similar for proteins within each subcomplex suggesting that IFT proteins at the flagellar base are organized into subcomplexes,

rather than entire IFT particles. In detail, the data suggest that during the assembly of a given train IFT-A and B2 are recruited first, followed by addition of B1, and finally binding of the anterograde motor as visualized by KAP-GFP.

The sequential arrival of IFT subcomplexes in the bb-pool does not necessarily indicate that the recruitment of a late arriving subcomplexes depends on the presence of the earlier arriving ones. Knock-out of the IFT-A core protein IFT144, for example, prevents the assembly of functional IFT-A complexes but IFT-B proteins still enter cilia and accumulate at the tip due to the lack of retrograde traffic (Hirano et al., 2017). Thus, the sequential recruitment of IFT subcomplexes into the pool does not automatically reflect the interdependence during train assembly. We consider it more likely that IFT subcomplexes are recruited independently of each other and line up in (spatially) separated queues to be then combined into trains. To summarize, our data indicate a functional, spatial, and temporal organization of the IFT basal body pool.

Tubulin is loaded briefly before the IFT trains enter the cilium

It has been suggested that axonemal proteins including tubulin and radial spoke subunits already associate to IFT proteins on IFT-coated post-Golgi vesicles and remain in this association during the arrival at the ciliary base, vesicle fusion with the plasma membrane, train formation, and transport into the cilium (Wood and Rosenbaum, 2014). To gain insights into the timing and location of cargo loading, we used sfGFP-tubulin, which due to its high frequency of transport by IFT is well suited for our photobleaching approach (Craft et al., 2015). The calponin-homology (CH) domain of IFT81 and the N-terminal domain of IFT74 bind tubulin in vitro, and cilia assembly is impaired in C. reinhardtii strains carrying mutations in both domains indicating that the IFT81/74 module is the dominant tubulin binding site of IFT (Bhogaraju et al.,

2013; Kubo et al., 2016; Taschner et al., 2016; Zhu et al., 2017b). While these two proteins were not analyzed here, we consider it unlikely that pre-formed IFT81/74/tubulin complexes are incorporated into trains shortly before departure because IFT81 and IFT74 are core structural components of the IFT-B1 complex (Lucker et al., 2005; Taschner et al., 2014). If IFT-B1 proteins were already bound to tubulin at the time of their recruitment and incorporation into the trains, the gap in tubulin traffic after bleaching of the bb-pool should correspond in duration to that of the IFT-B1 proteins. However, the gap in sfGFP-tubulin traffic was actually shorter than that of KAP or any IFT particle protein studied here. The data indicate that tubulin loading occurs in the basal bodies pool and briefly before the trains move into the cilium. Axonemal cargoes are mostly released from IFT trains at the ciliary tip where IFT trains partially disassemble to reorganize for retrograde traffic (Bower et al., 2013; Craft et al., 2015; Johnson and Rosenbaum, 1992; Lechtreck et al., 2013; Wren et al., 2013). We speculate that cargo binding and unloading could be linked to train assembly and disassembly.

A model for the stepwise assembly of IFT trains

A critical role in train assembly can be attributed to the transitional fibers (TFs), which link the basal body triplets to the plasma membrane. C. elegans mutants in the TF protein Dyf-19 have severely reduced amounts of IFT proteins and IFT traffic inside cilia (Wei et al., 2013). The IFT-B1 protein IFT52 is associated with the TFs and the TFs are required to recruit kinesin-2, but not the IFT particle proteins, into the bb-pool (Cole et al., 1998; Deane et al., 2001). The entry of IFT proteins into the cilium depends on kinesin-2 (Kozminski et al., 1995), the binding of kinesin-2 to IFT is regulated by phosphorylation (Liang et al., 2014), and we show here that the addition of kinesin-2 is a late step of train assembly.

The longest average gap in IFT traffic was ~9s for the IFT-A/B2 proteins. In C. reinhardtii, IFT trains exit the bb-pool with a frequency of ~1/s suggesting that one train is completed each second and that ~9 trains in different stages of assembly are in the pool at a given time. This value fits with our estimates of the bb-pool size based on the fluorescence loss or gain upon departure/arrival of a single train. In a speculative model, each of the nine basal body triplets with its associated structures could assist to assemble one IFT train. The nascent trains move upwards along the triplet blades combining with additional IFT subcomplexes. Then, they will associate with kinesin-2 at the TFs, which will pull the nascent train upwards and into the cilium, compressing and concentrating the IFT material between the microtubules and the membrane. Once a position is vacated by a departing train, the assembly of a new train is initiated near the proximal end of the basal body (Fig. 2.8F).

2.13 FIGURES

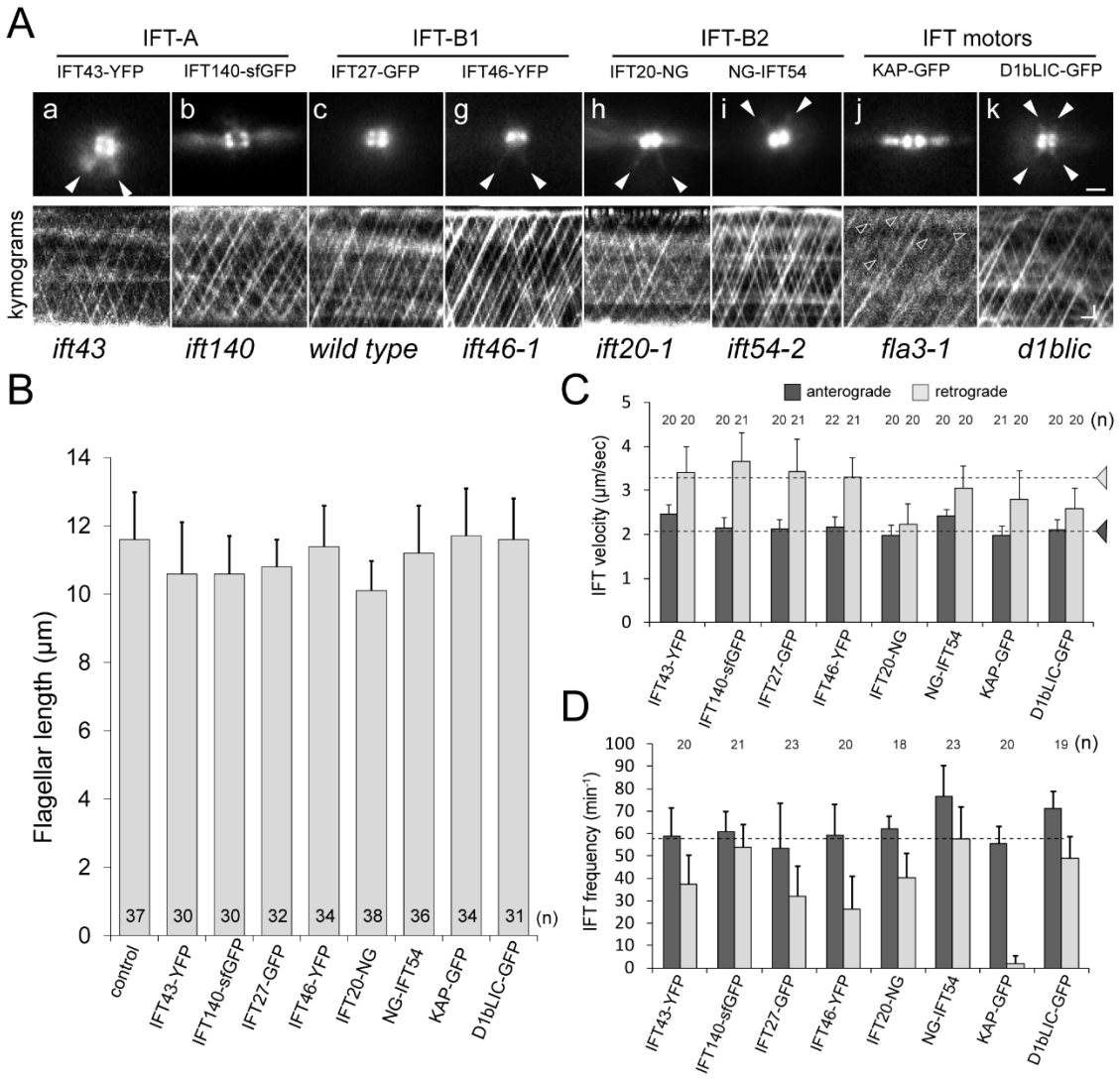

Figure 2.1 IFT proteins are concentrated at the flagellar base

A) top: Still images from live cells showing the distribution of FP-tagged IFT proteins in the basal body pool. Arrowheads: IFT proteins along the microtubular roots. To enhance clarity, 10-frame image averages are shown. Bar = 1 µm. bottom: Kymograms showing the trajectories of IFT trains inside flagella. Anterograde traffic results in trajectories running from the bottom left to the top right; retrograde traffic is presented by lines running from the top left to the bottom right. The genetic background of the strains is indicated. Bars = 1µm 1s. **B)** Flagellar length of

the strains expressing FP-tagged IFT proteins. The standard deviation and the number of measurements are indicated. Strain CC-620 was used as a control. **C)** Velocity of anterograde and retrograde IFT traffic in the rescue strains. Note the reduction in retrograde velocity of IFT20-NG. Dashed lines indicate the velocities of anterograde and retrograde trains as determined by DIC microscopy based of Reck et al. (2015). **D)** Frequency of IFT traffic. While the anterograde frequency was close to 1 train/s for all strains, retrograde frequencies were lower and *more variable than reported for IFT in C. reinhardtii*. The usage of fast bleaching fluorescent proteins (i.e., YFP) and the low laser intensity used here to allow for long-term imaging could have prevented the detection of weaker trains. The standard deviation is indicated.

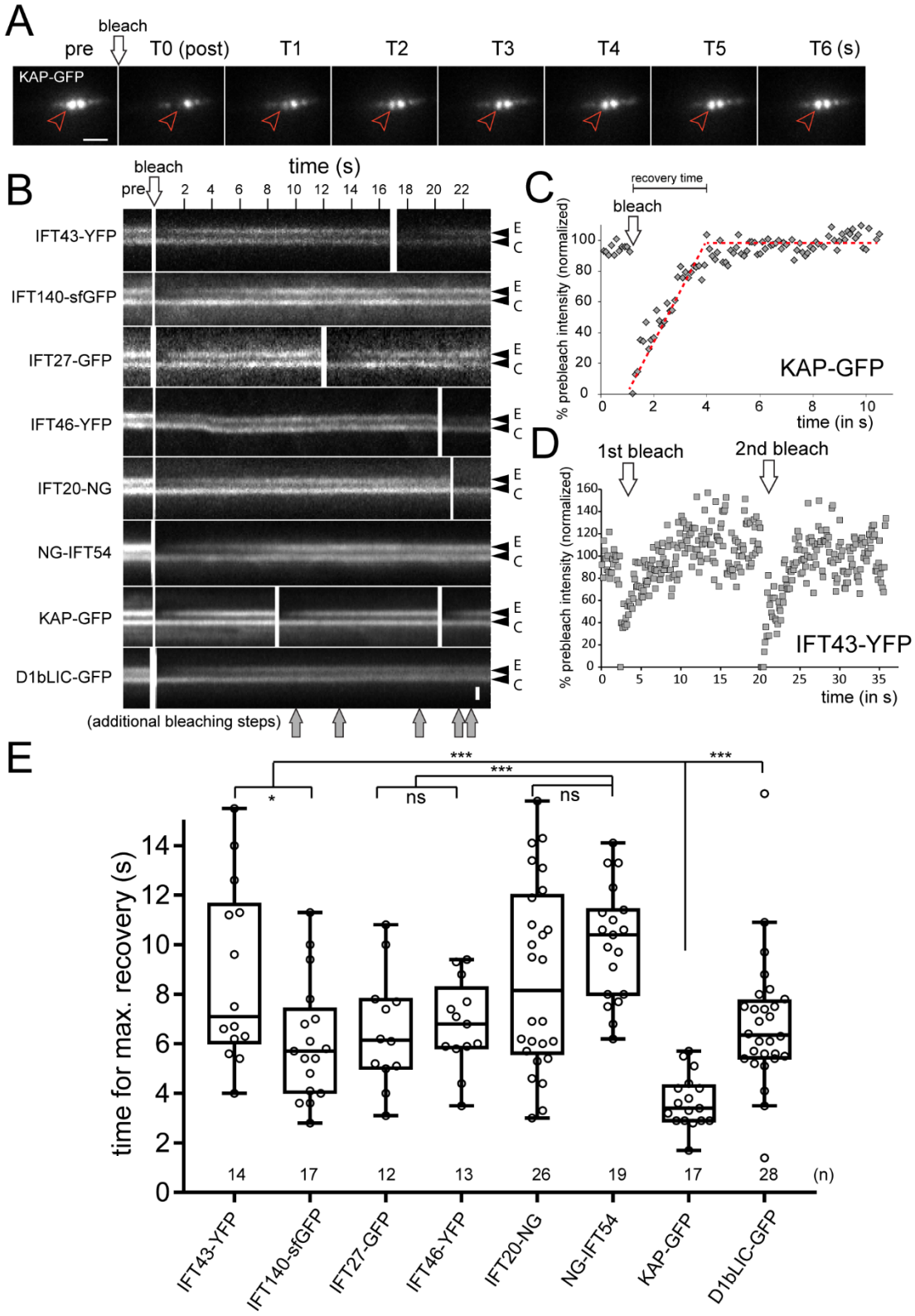

Figure 2.2 IFT proteins in the pool are exchanged at distinct rates

A) Series of still images showing a cell expressing KAP-GFP before (pre) and immediately after bleaching of one of the two IFT bb-pools surrounding the flagellar basal bodies (arrowhead; T0), and during recovery (in s). Bar = 2 µm. **B)** Kymograms from FRAP experiments after bleaching of one IFT bb-pool followed by signal recovery; repeated bleaching was used in some experiments (arrows, bottom). The experimental (E) and control (C) pool are indicated. Bar= 1 µm. **C, D)** Quantitative analysis of FRAP for KAP-GFP (C) and IFT43-YFP (D) after bleaching of the experimental basal body; data are normalized for the unbleached basal body. The time needed for recovery was determined manually by determining the point of interception of lines along the slope during recovery and the plateau of the recovered signal (red dashed lines). **E)** Box plot comparing FRAP times for the FP-tagged IFT proteins. The individual measurements, the median, and the quadrants are indicated. The number of measurements (n)and the result of a paired T-test are indicated. ns, not significant ($P>0.05$); *, $P\leq0.05$; **, $P\leq0.01$; ***, $P\leq0.001$.

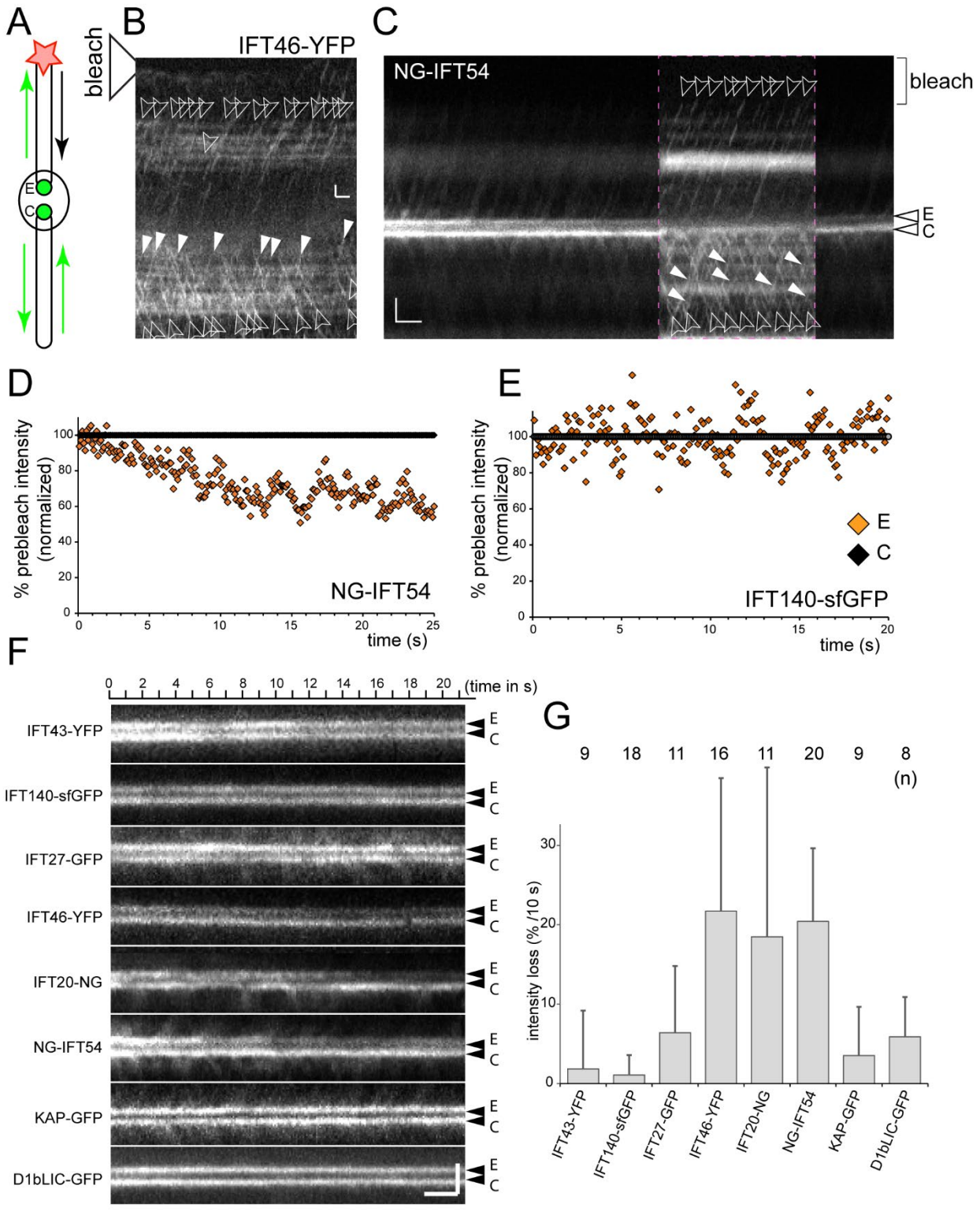
A
B
bleach
IFT46-YFP
C
NG-IFT54
bleach
E
C
D
% prebleach intensity (normalized)
NG-IFT54
time (s)
E
% prebleach intensity (normalized)
E
C
IFT140-sfGFP
time (s)
F
(time in s)
IFT43-YFP
IFT140-sfGFP
IFT27-GFP
IFT46-YFP
IFT20-NG
NG-IFT54
KAP-GFP
D1bLIC-GFP
G
9 18 11 16 11 20 9 8
(n)
intensity loss (% /10 s)
IFT43-YFP
IFT140-sfGFP
IFT27-GFP
IFT46-YFP
IFT20-NG
NG-IFT54
KAP-GFP
D1bLIC-GFP

Figure 2.3 IFT-B, but not IFT-A or motor proteins, return to the basal body pool

A) Schematic presentation of the FLIP assay to analyze the return of IFT proteins from the flagella to the bb-pool. The star indicates the laser beam positioned at the tip of the experimental (E) flagellum. **B)** FLIP bleaching at the tip of the E flagellum prevented the return of unbleached IFT46-YFP via retrograde IFT; note retrograde tracks in the control (C) flagellum (full arrowheads). See Fig. 2.3-figure supplement 1A for a more detailed analysis of IFT traffic under FLIP illumination. Bar = 1 μm 1 s. **C)** Kymogram of a FLIP experiment of an NG-IFT54 cell. FLIP illumination decreased the signal of the E basal body. Unbleached anterograde trains (open arrowheads) continue to enter the E cilium in the absence of retrograde traffic (open arrowheads). To better visualize IFT traffic the focus level was changed during part of the recording (dashed square). Bar = 2 μm 2 s. **D, E)** Quantitative analysis of FLIP of the E basal body from an NG-IFT54 and an IFT140-sfGFP cells; the data are normalized for the control (C) basal body. **F)** Kymograms of FLIP experiments using the IFT-FP strains. The experimental (E; top) and control (C) pool are indicated. Bars = 2 μm 2s. **G)** Bar graph showing the average loss of signal of the E basal body during the first 10 s of FLIP illumination. The standard deviation and the number of cells analyzed are indicated. See Fig. 2.3 – figure supplement 1E for a box plot presentation of the data.

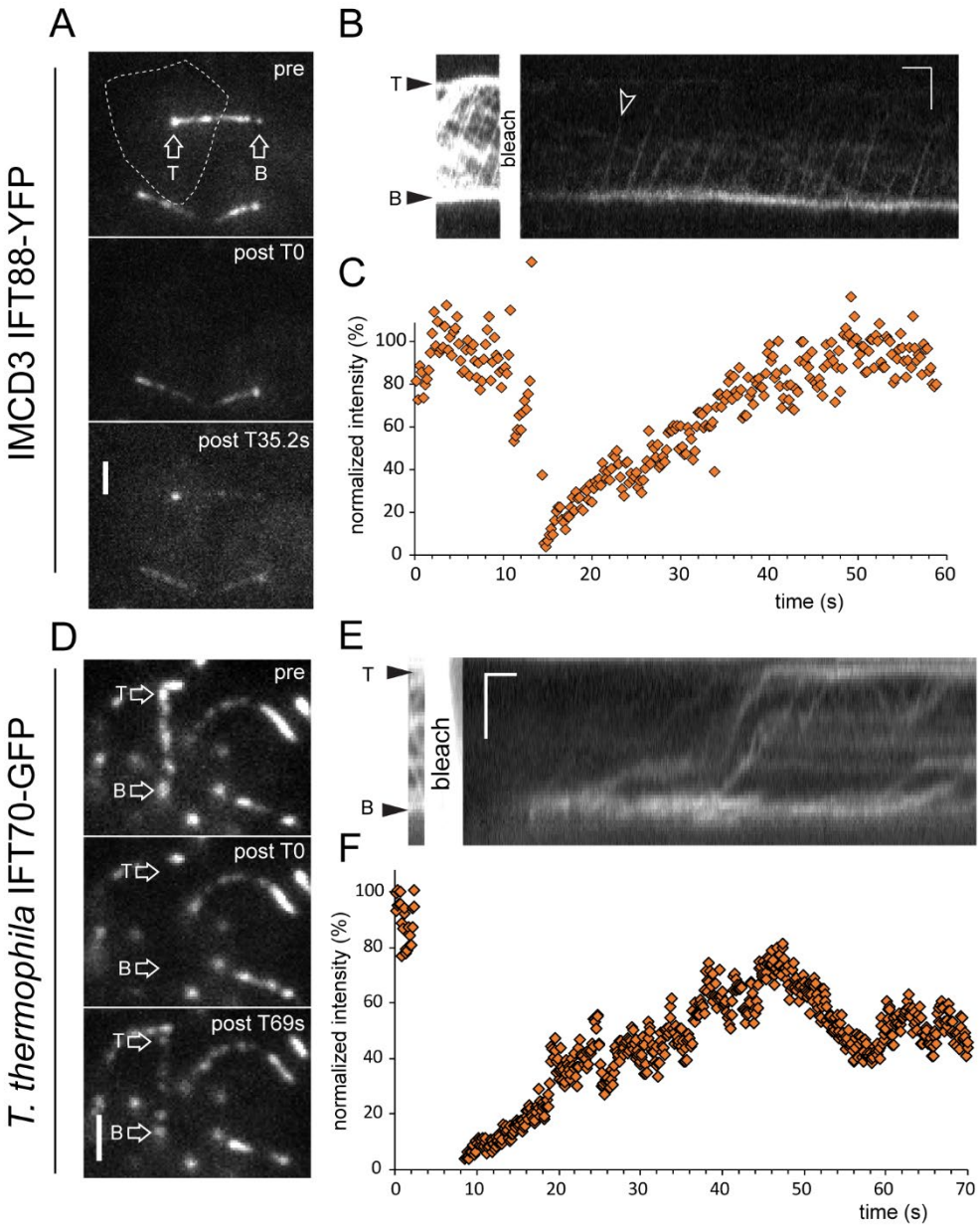

Figure 2.4 IMCD cells and T. thermophila have open IFT systems

A) Still images of an IMCD cell expressing IFT88-YFP before (pre), immediately after photobleaching of the entire cilium plus basal body (post), and during recovery. The dotted line marks the cell boundaries. Bar = 1 µm. **B)** Corresponding kymogram (Bar = 2µm 5s) and **(C)** quantitative analysis of the signal at the basal body. **D)** Still images showing a detail of the cortex of a T. thermophila cell expressing IFT70-GFP before (pre), immediately after

photobleaching of the entire cilium plus basal body (post), and during recovery. Bar = 1µm. **E)** Corresponding kymogram (Bar = 2µm 5s) and **(F)** quantitative analysis of the signal at the basal body.

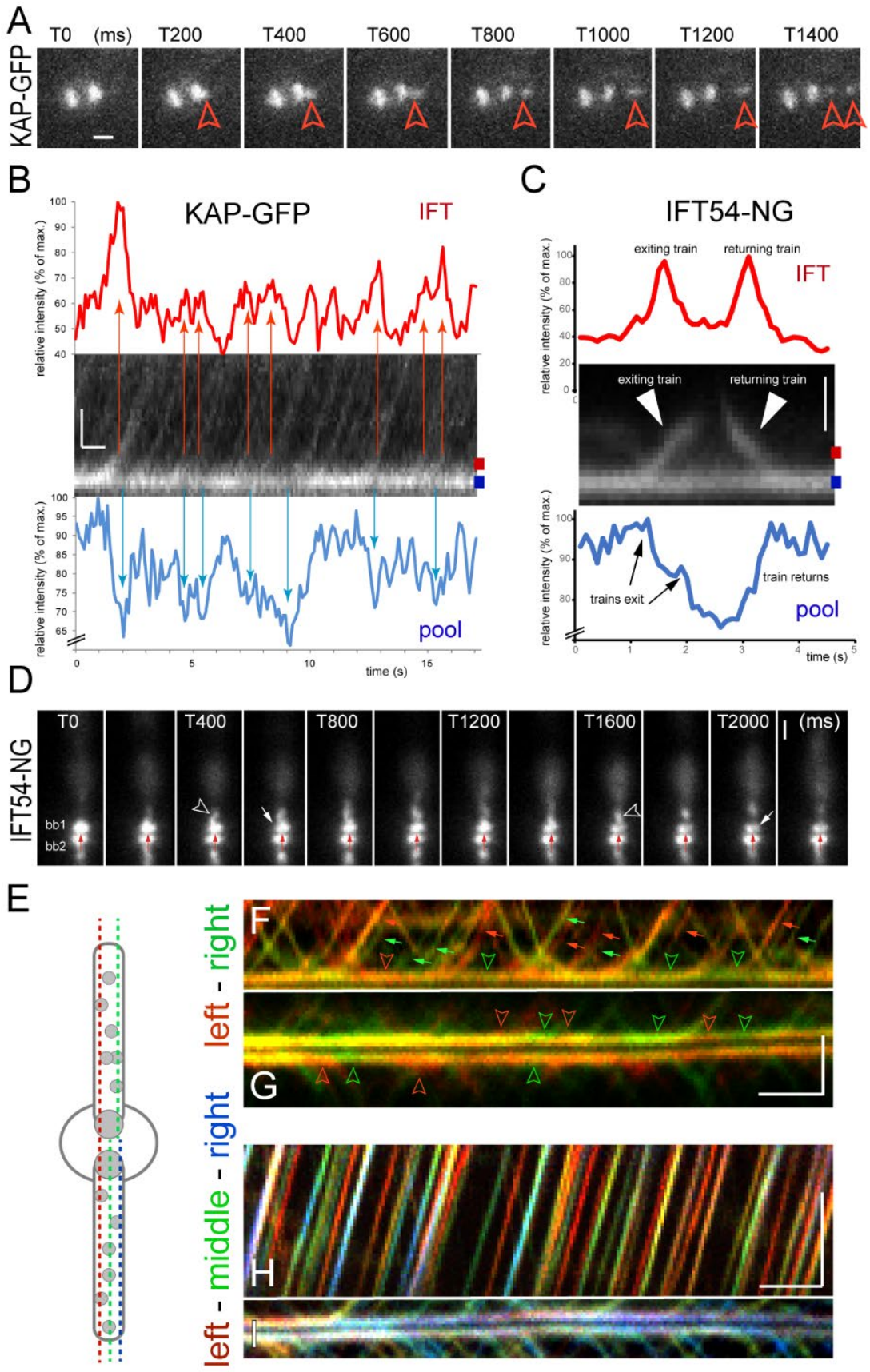
A
T0 (ms)
T200
T400
T600
T800
T1000
T1200
T1400
KAP-GFP
B
KAP-GFP
IFT
relative intensity (% of max.)
pool
time (s)
C
IFT54-NG
exiting train
returning train
IFT
trains exit
train returns
pool
D
IFT54-NG
T0
T400
T800
T1200
T1600
T2000
(ms)
bb1
bb2
E
F
G
H
I
left - right
left - middle - right

Figure 2.5 The basal body pool contains IFT proteins equivalent to several IFT trains

A) Series of still images from a cell expressing KAP-GFP showing the departure of an IFT train (red arrowhead). The intensity of the bb-pool decreases concomitantly with the departure of the train. Bar = 1 μm; the time points in ms are indicated. **B)** Kymogram showing the bb-pool and proximal regions of one flagellum of a cell expressing KAP-GFP. Intensity profiles (in percent of the maximum intensity) for the bb-pool (blue) and flagellum (red) depict the correlation between the exit of IFT trains (red arrows) and a transient decrease of fluorescence in the pool (blue arrows); the positions of the lines used to generate the intensity profiles are indicated. Bars = 1s 1μm. **C)** Kymogram and its analysis as described in B but for NG-IFT54. Bar = 1 μm. **D)** Series of still images from a cell expressing NG-IFT54 showing two IFT trains departing from the upper basal body (bb1; arrowheads). The first train departs from the left (T400) side of the bb-pool while the second train exits the pool at the right side causing a local loss of fluorescence in the pool. The red arrow near bb2 serves as a fiduciary marker. Bar = 1μm. **E)** Schematic presentation of the position of the lines used to generate the kymograms shown in F – I. **F, G)** Merged kymograms showing the two sides of the bb-pool and cilium in red and green. Note the alternation of predominantly red and green trains (small arrows) and red and green areas (open arrowheads) in the bb-pool indicative for a transient reduction of NG-IFT54 in one side of the pool. Bars = 2s 2μm. **H, I)** as in F and G, but showing the left, middle, and right positions of the pool and cilium in red, green, and blue respectively. Bars = 2s 2μm.

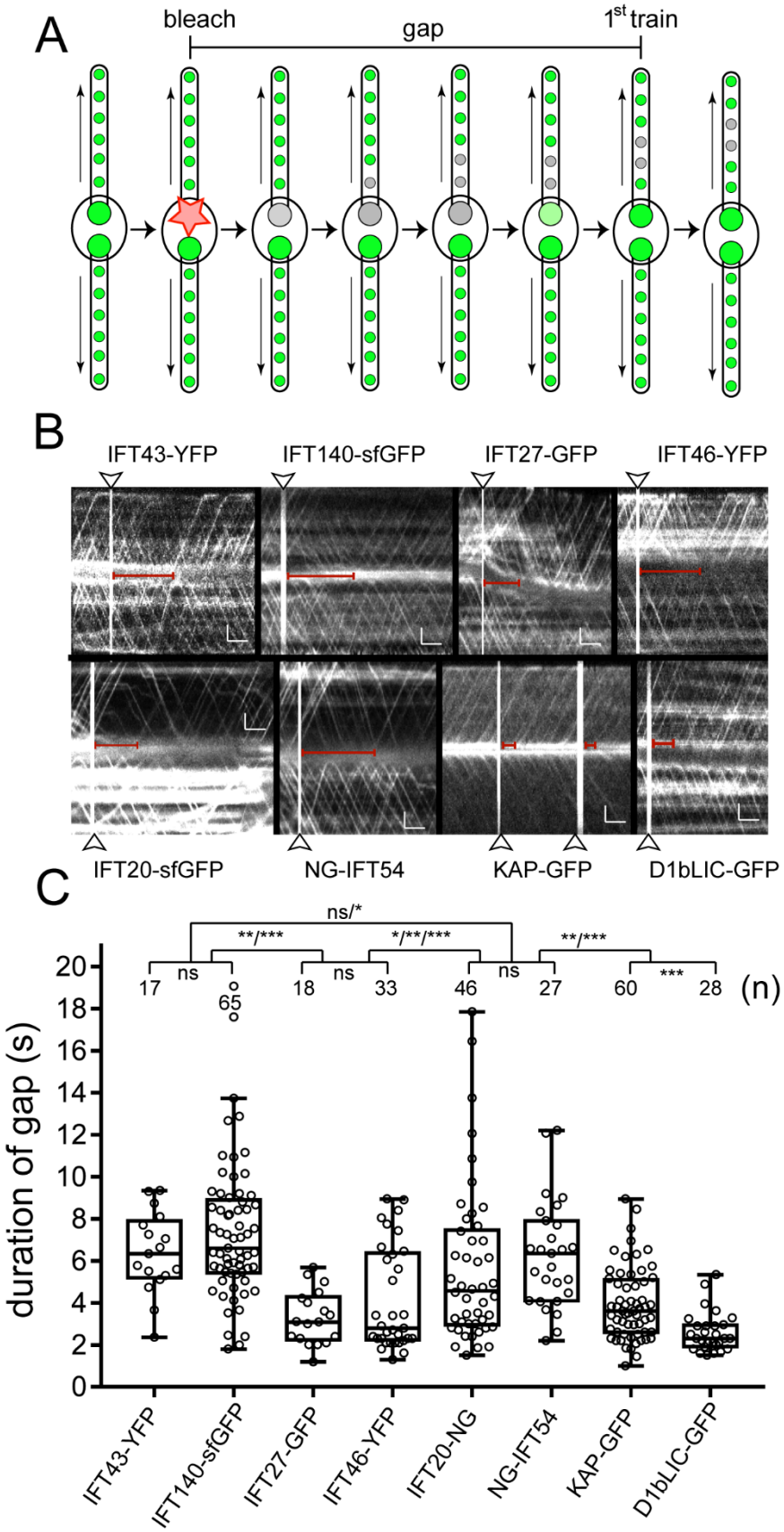
A
bleach
gap
1st train
B
IFT43-YFP
IFT140-sfGFP
IFT27-GFP
IFT46-YFP
IFT20-sfGFP
NG-IFT54
KAP-GFP
D1bLIC-GFP
C
ns/*
/*
*/**/***
/*
ns
ns
ns
***
17
65
18
33
46
27
60
28
(n)
duration of gap (s)
0
2
4
6
8
10
12
14
16
18
20
IFT43-YFP
IFT140-sfGFP
IFT27-GFP
IFT46-YFP
IFT20-NG
NG-IFT54
KAP-GFP
D1bLIC-GFP

Figure 2.6 Bleaching of the basal body pool is followed by a gap in IFT traffic

A) Schematic presentation of the gap assay to determine the interval between bleaching of the bb-pool (bleach, indicated by the star) and recommencement of anterograde IFT traffic (1st train). **B)** Representative gap analysis for the eight FP-tagged IFT proteins. Arrowheads mark the bleaching steps; the red bars indicate the gap between the bleach and the dispatch of the first unbleached IFT train. Bars = 2s 2μm. **C)** Quantitative analysis of the gap data. The standard deviation, number of gaps analyzed, and the results of a paired T-test are indicated. ns, not significant ($P>0.05$); *, $P\leq0.05$; **, $P\leq0.01$; ***, $P\leq0.001$.

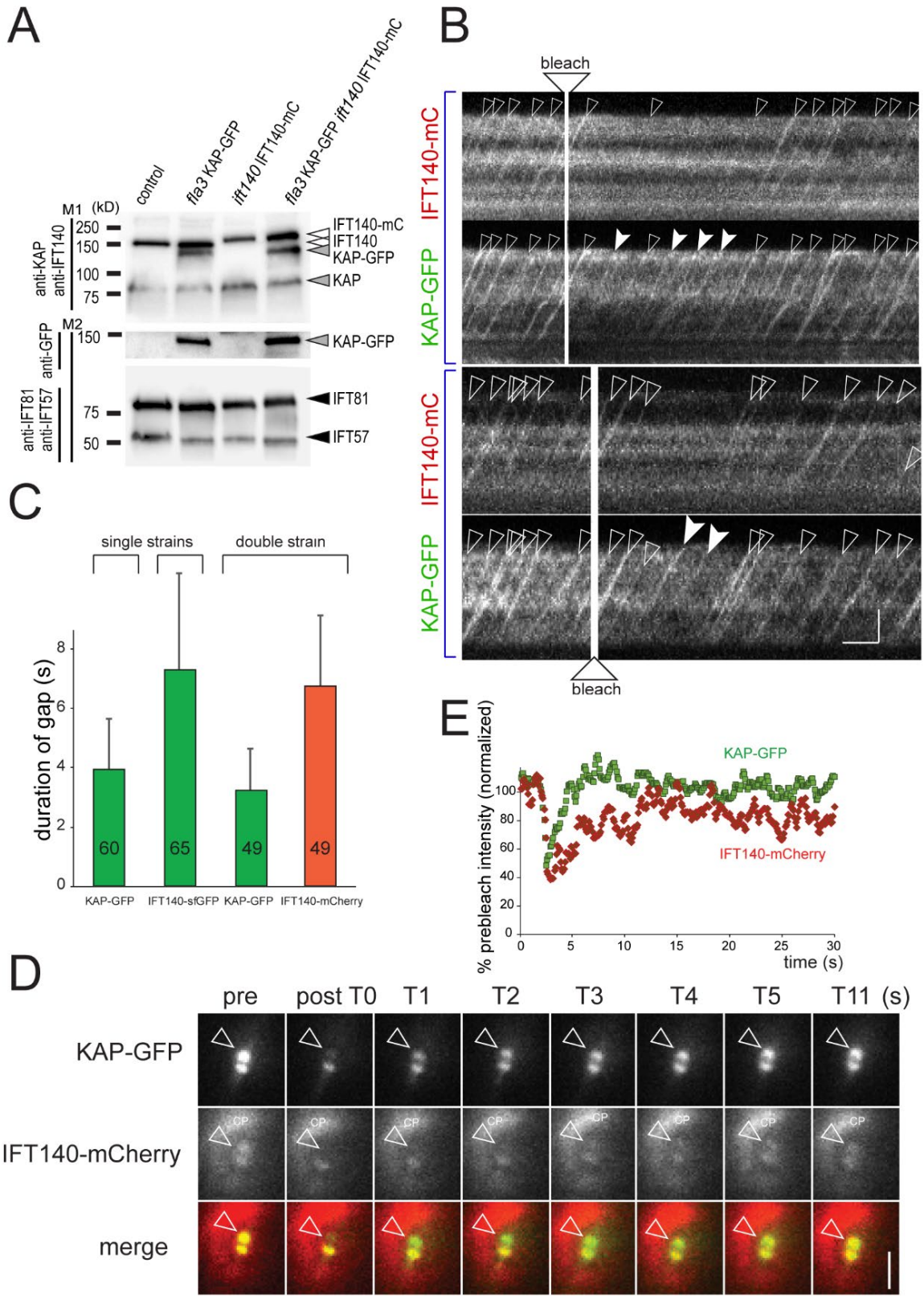

Figure 2.7 IFT140 is recruited early, KAP is recruited late during IFT train assembly.

A) Western blot analysis of the flagellar "membrane + matrix" fraction of a control (G1), the KAP-GFP, the IFT140-mC, and the KAP-GFP IFT140-mC strains; note that KAP-GFP was expressed in the fla3 which has a mutated endogenous KAP of reduced function. Two membranes (M1 and M2) loaded with the same amount of sample were stained with a mix of anti-KAP and anti-IFT140 (M1) or of IFT81 and IFT57 as loading controls (M2), the latter membrane was subsequently stained with anti-GFP. Molecular weight markers are indicated (in kD). **B)** Two examples showing the recommencement of IFT traffic after photobleaching of the basal body in cells expressing KAP-GFP and IFT140-mCherry. Trains containing only unbleached KAP-GFP (filled arrowheads) appeared before trains containing both unbleached IFT140-mCherry and unbleached KAP-GFP (open arrowheads). Bars = 2s 2µm. **C)** Histogram comparing the duration of the gap after bleaching of the bb-pool for strains expressing KAP-GFP, IFT140-sfGFP, or KAP-GFP and IFT140-mCherry. **D)** FRAP analysis of the bb-pool in a cell expressing KAP-GFP and IFT140-mCherry. Note that the KAP-GFP signal recovered before the IFT140-mCherry signal. CP, chloroplast. **E)** Quantification of the KAP-GFP and the IFT140-mCherry signals of the experiment depicted in C. Data are normalized for the signal strength of the control basal body pool.

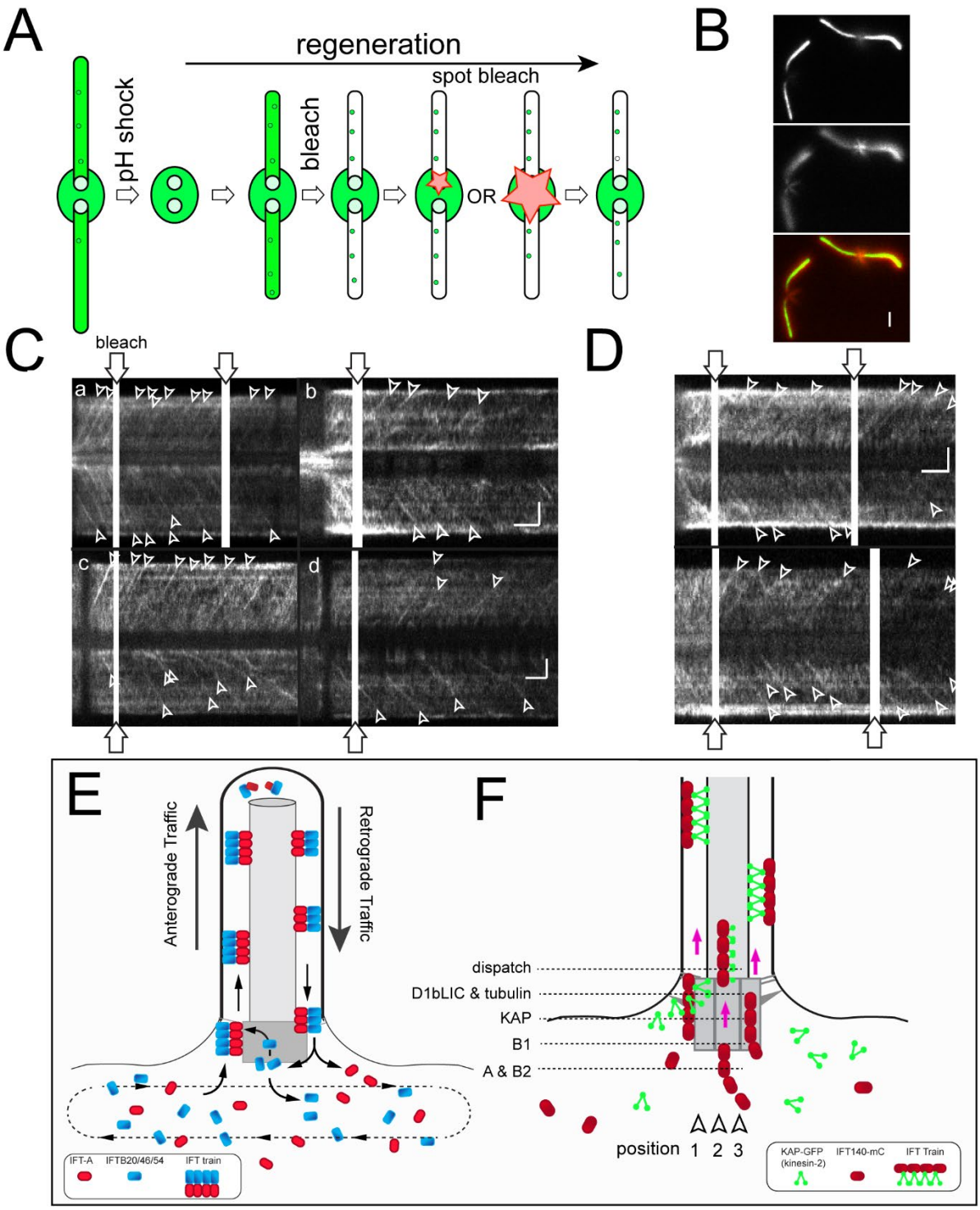

Figure 2.8 Tubulin is loaded briefly before IFT trains enter the cilium

A) Schematic presentation of the experimental design used to determine the gap in anterograde traffic of sfGFP-tubulin after photobleaching of the basal body. Cells were deflagellated by a pH

shock, allowed to initiate regeneration, and mounted for TIRF analysis. Then, the two flagella were partially bleached, followed by spot bleaching of either one or both basal body pools (for the latter the size of the laser beam was extended to ~2 um), and TIRF analysis of tubulin traffic. **B)** Two images from a focal series showing the flagella and the microtubular root; the latter were used to position the cells with respect to the laser beam. The two images are displayed in red and green in the merged image. Bar = 2µm. **C)** Gallery of kymograms from experiments in which one of the two basal body pools was bleached. The bleached basal body is oriented to the top. Bars = 2s 2µm (in d for a, c, d; in b for b). **D)** Gallery of kymograms in which both basal body pools were bleached. In C and D, trajectories indicating IFT of tubulin are indicated by arrowheads. Bars = 2s 2µm. **E)** Schematic presentation of the open IFT system. IFT-A proteins (and IFT27 and the motors) are recruited to the pool, cycle once through the flagellum, and return into the cell body pool. IFT-B proteins return to the bb-pool to be either reused in subsequent IFT trains or released into the cell body pool. IFT proteins mix in the cb-pool and are randomly re-deployed into IFT trains. **F)** Model of the temporal-spatial organization of IFT proteins in the basal body pool. We propose that IFT trains assemble in distinct positions near the basal body from which they are sequentially released into the cilium upon completion. Assembly commences with the arrival of IFT-A complexes which then combine with the other IFT-subcomplexes and motors as they move toward the distal end of the basal body. For simplicity, only IFT-A and kinesin-2 are depicted. See also Fig. 2.7-figure supplement 1.

2.14 SUPPLEMENTARY MATERIALS

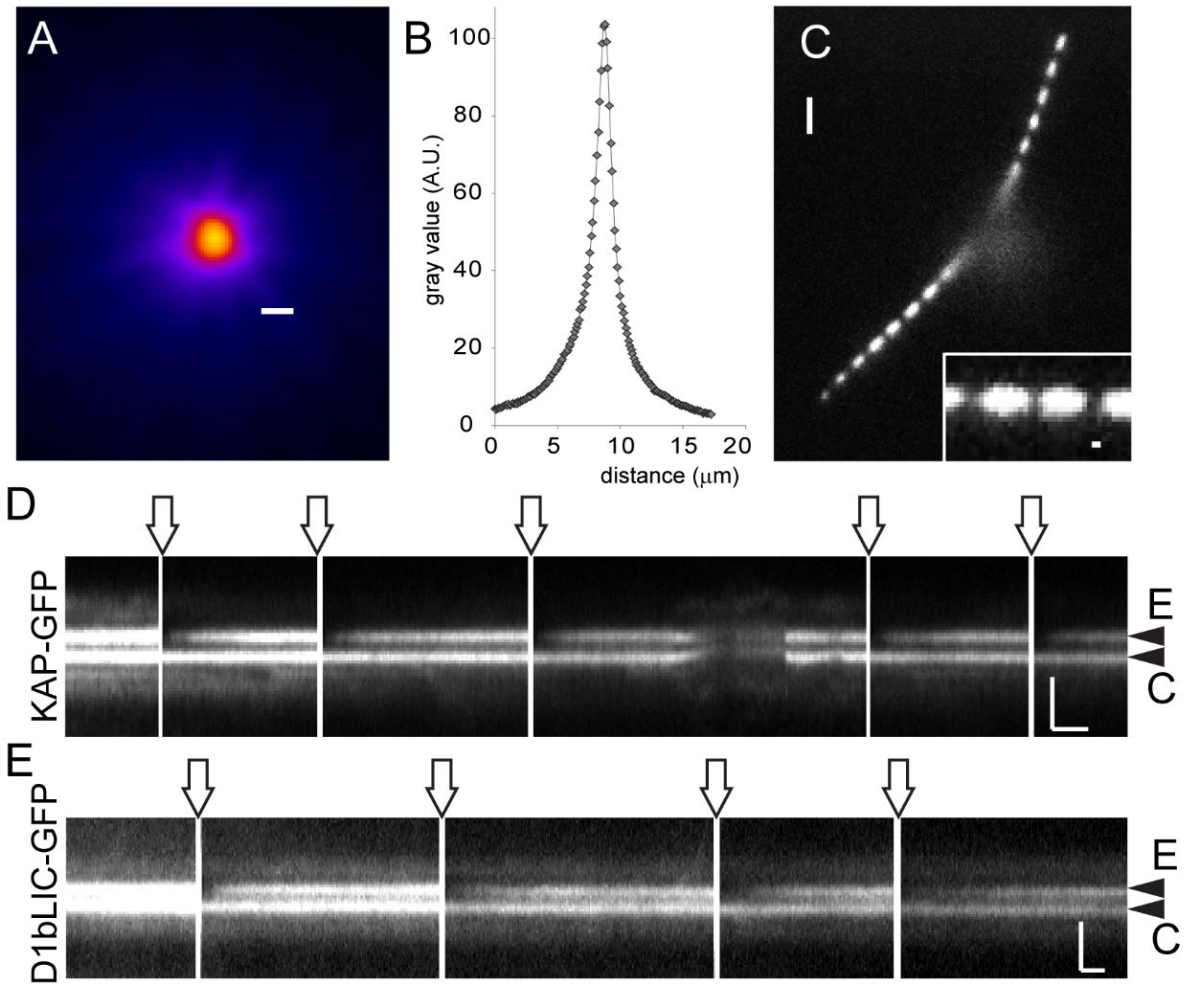

Figure 2.2-figure supplement 1 Rapid and local photobleaching using a focused laser beam

A) Heat map of a focused laser beam as visualized using fluorescent polystyrene beads. Bar = 1 μm. **B)** Intensity profile of a focused laser beam. **C)** Spot bleaching of the flagella of a cell expressing sfGFP-alpha-tubulin. Insert: detail of a spot bleached flagellum. Bar = 2μm and 0.2μm (insert). **D)** Kymogram depicting repeated photobleaching (arrows) and recovery of one basal body (E) of a KAP-GFP cell; C indicates the unbleached control basal body. Proper focus was lost for a part of the recording. Bars = 2s 2μm. **E)** as D, but for a D1bLIC-GFP cell. Bars = 2s 2μm.

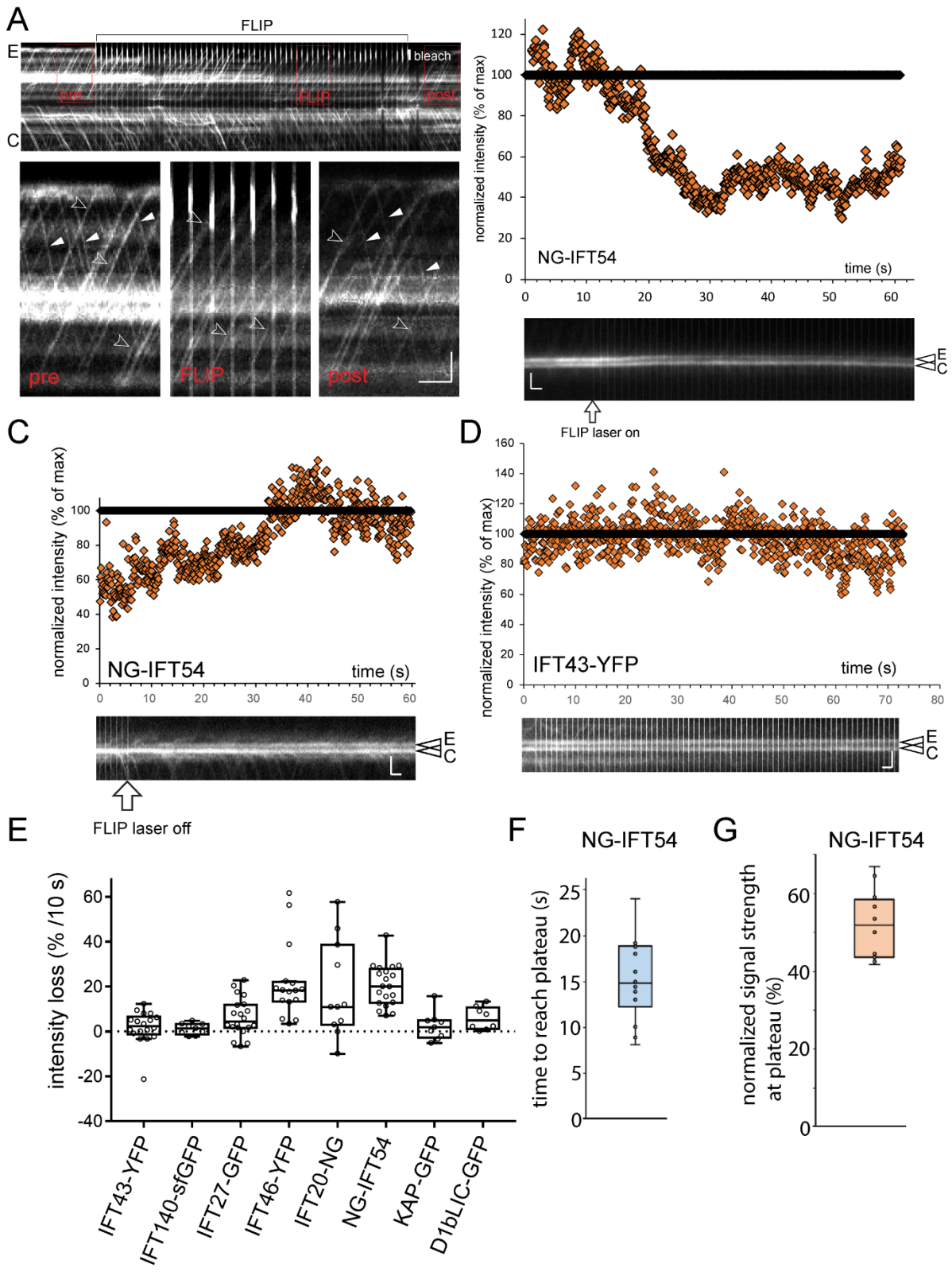
A
FLIP
E
C
bleach
pre
FLIP
post
pre
FLIP
post
normalized intensity (% of max)
NG-IFT54
time (s)
FLIP laser on
C
normalized intensity (% of max)
NG-IFT54
time (s)
FLIP laser off
D
normalized intensity (% of max)
IFT43-YFP
time (s)
E
intensity loss (% /10 s)
IFT43-YFP
IFT140-sfGFP
IFT27-GFP
IFT46-YFP
IFT20-NG
NG-IFT54
KAP-GFP
D1bLIC-GFP
F
NG-IFT54
time to reach plateau (s)
G
NG-IFT54
normalized signal strength at plateau (%)

Figure 2.3-figure supplement 1: FLIP illumination prevents return of unbleached proteins to the ciliary base

A) Kymogram showing NG-IFT54 traffic before (pre), during (FLIP), and after (post) illuminating the tip of the experimental flagellum (E) with a focused laser beam. The position of the laser beam is indicated (white bar, bleach). The three boxed areas are shown in detail in the bottom row. Open arrowheads: anterograde trains; full arrowheads, retrograde trains. Bars = 2s 2μm. **B, C)** Kymograms (bottom) and scatter plots of the signal intensity showing the loss of NG-IFT54 from the experimental pool during FLIP illumination (B) and recovery of the signal when the FLIP laser is turn off (C). **D)** As in B but for IFT43-YFP. Bars (B-D) = 2s 2μm.
E) Summary of the FLIP experiments as shown in Fig. 2.3G but presented as a box plot.
F) Box plot showing the time of FLIP illumination required to reach a plateau for NG-IFT54.
G) Box plot showing the normalized signal intensity of NG-IFT54 at the experimental basal body after FLIP illumination.

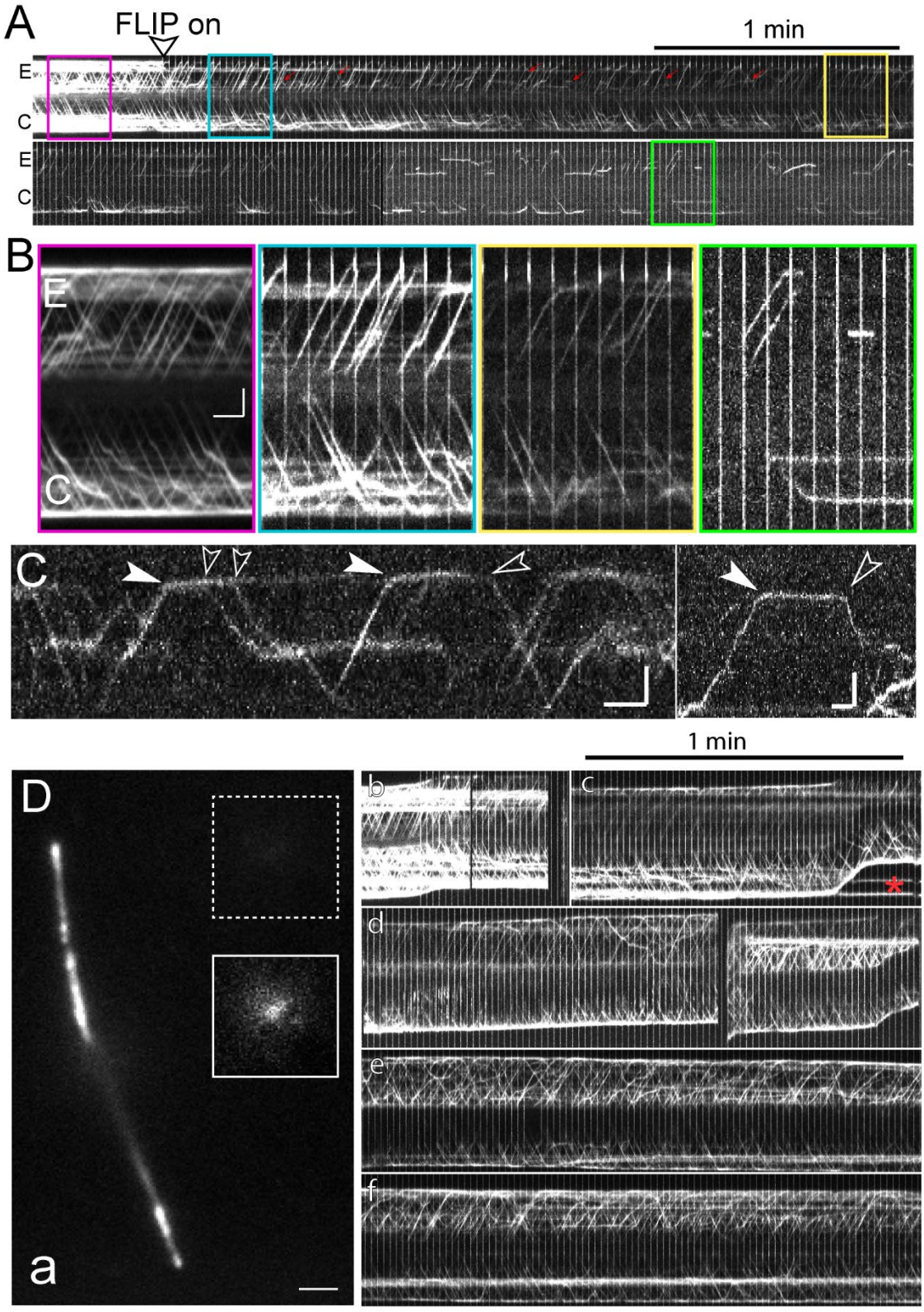
A
FLIP on
1 min
E
C
E
C
B
E
C
C
1 min
D
a
b
c
d
e
f

Figure 2.3-figure supplement 2: Bleaching of the entire NG-IFT54 protein pool

A) Kymograms of a given cell during prolonged FLIP bleaching of one ciliary tip (E). The start of the FLIP illumination is marked by an arrowhead. While most retrograde trains in the experimental flagellum were bleached, occasionally retrograde trains originating subdistally either from stationary NG-IFT54 or anterograde trains turning around early were present (red arrows). **B)** Blow-ups of the boxed areas of the kymograms shown in A. Red, prebleach; blue, briefly after onset of the bleaching; yellow, ~2.5 minutes of FLIP, and green, after ~8 minutes of FLIP. Note the absence of retrograde traffic from the E flagellum. Bars = 2s 2µm.

C) Kymograms obtained after prolonged FLIP illumination showing the arrival (filled arrowheads) and departure (open arrowheads) of individual IFT trains at the ciliary tip. Bars = 2s 2µm. **D)** Still image (a) and kymograms (b-f) from a control recording in which the bleaching laser was not aimed at the cilia tip. a) This frame was recorded while the spot bleaching laser was on. The position of the spot bleaching laser is marked by the red circle. Bar = 2µm. b-f) Kymograms showing continuous IFT traffic in both cilia of the cell shown in a; the kymogram is shown in segments due to movements of the cell. Red star: Vesicles containing NG-IFT54 shed from the ciliary tip. Bar = 1 minute.

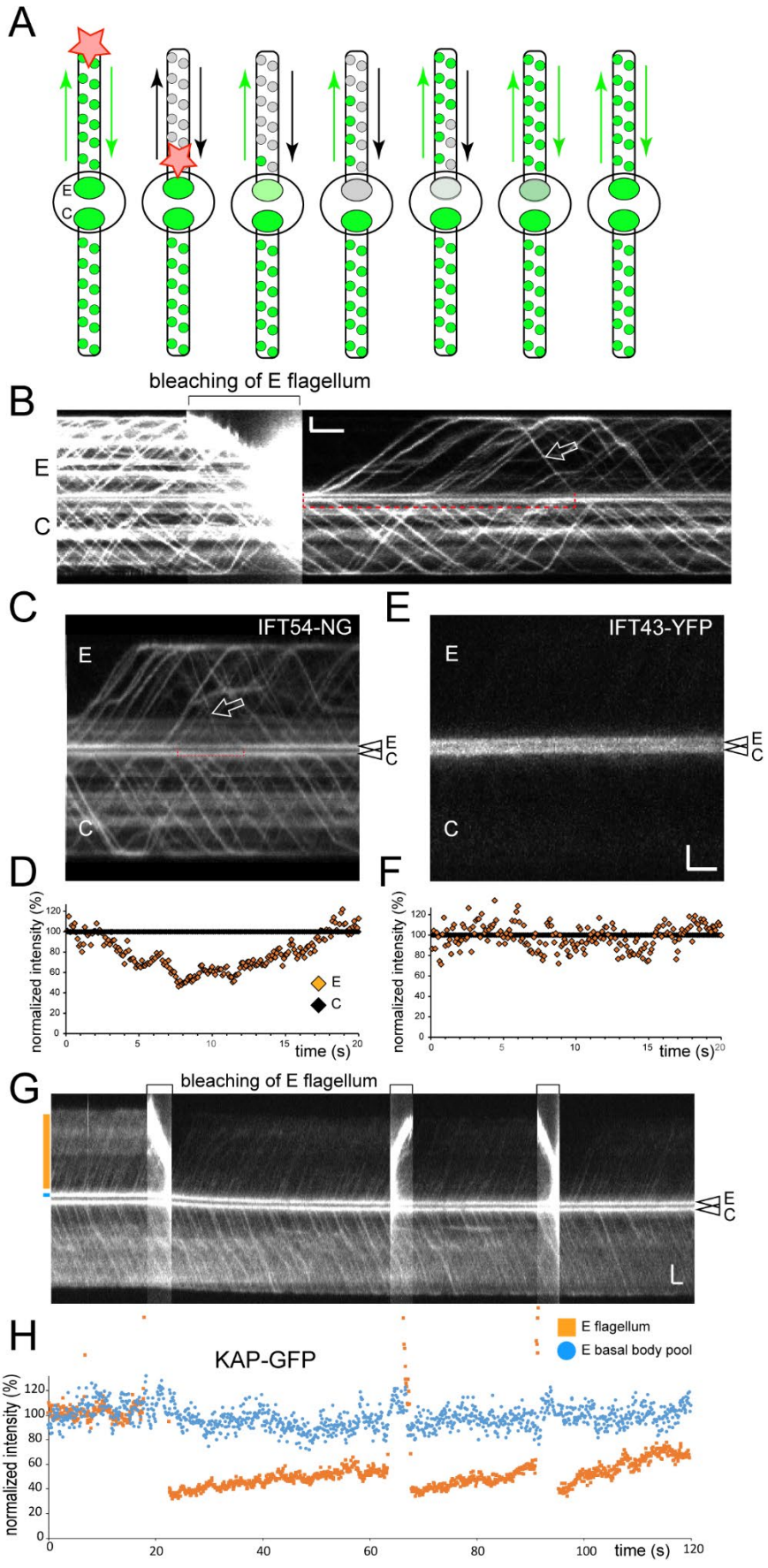
A
E
C
B
bleaching of E flagellum
E
C
C
IFT54-NG
E
C
E
E
IFT43-YFP
E
C
D
normalized intensity (%)
time (s)
E
C
F
normalized intensity (%)
time (s)
G
bleaching of E flagellum
E
C
L
H
KAP-GFP
E flagellum
E basal body pool
normalized intensity (%)
time (s)

Figure 2.3-figure supplement 3: A portion of the pool consists of disassembling IFT-B complexes

A) Schematic presentation of total flagella FLIP in which the entire experimental flagellum (E) was bleached by moving a focused laser beam along the flagellum. **B)** Kymogram before, during, and after bleaching of NG-IFT54 in the experimental flagellum. Open arrow, first unbleached retrograde train after the bleach. The red bracket indicated the time span during which no unbleached NG-IFT54 returned to the pool; note the decrease in the signal strength of the pool. Bars = 2s 2µm. **C)** as B, but only depicting the time after the bleaching step. The bracket indicates the trough in the pool signal prior to the return of unbleached NG-IFT54 by retrograde traffic. **D)** Quantification of the pool signal corresponding to the kymogram in C. E (orange), experimental basal body. **E, F)** as C and D but for a cell expressing IFT43-YFP. Because the pool of IFT43-YFP is deeper inside the cell, imaging of the pool and IFT traffic in the same focal plane was mostly unfeasible. Bars (for C and E): 2s 2µm. **G)** Kymogram before, during, and after bleaching of KAP-GFP in the experimental flagellum; the bleaching step was repeated thrice as indicated by brackets. Orange and blue boxes indicate the positions of the lines used for signal quantification. Bars = 2s 2µm. **H)** Quantification of the pool signal corresponding to the kymogram in G. The blue markers indicate the pool signal; the orange ones the flagellar signal of the experimental flagellum. Note that the strength of the pool signal is unaffected by repeated bleaching of the associated flagellum. Due to the presence of diffusing KAP-GFP in flagella, the flagellar signal recovers only incompletely.

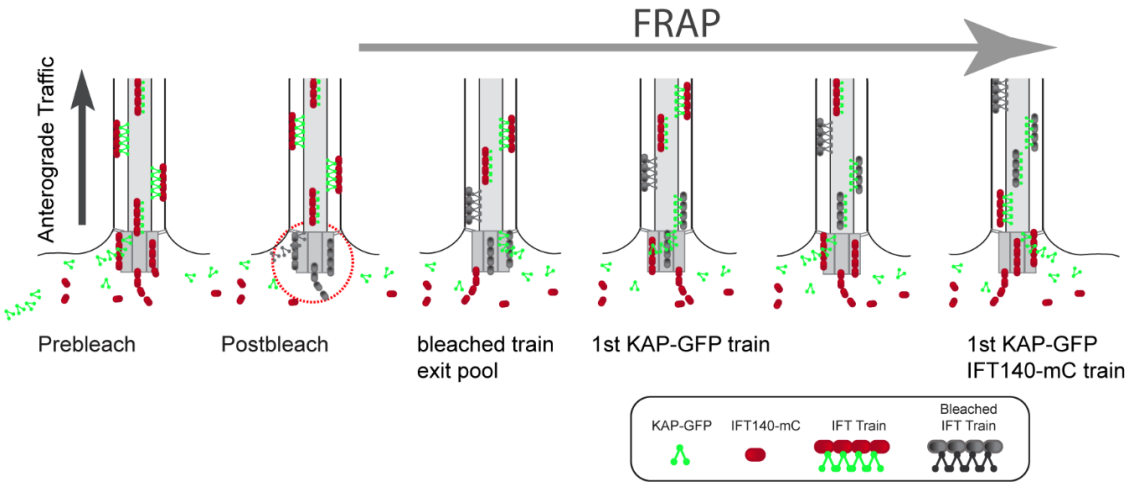

Figure 2.7 - figure supplement 1: Model of the temporal and spatial organization of IFT proteins in the basal body pool.

Schematic drawings showing how the difference in the postbleach gap in anterograde IFT traffic can be explained by sequential recruiting of proteins into the pool. For simplicity, only KAP and IFT140 are shown. In the proposed model, IFT-A complexes of a given train are recruited early into the bb-pool to be later combined with kinesin-2 motors, which afterwards arrived in the pool.

2.15 MATERIAL AND METHODS

Strains and culture conditions

The IFT20-FP (sfGFP or NG), IFT27-GFP, IFT43-YFP, KAP-GFP (CC-4296), and D1bLIC-GFP (CC-4488) strains were previously described; the corresponding strain numbers of the Chlamydomonas Resource Center (RRID:SCR_014960) are added in brackets when available. (Lechtreck et al., 2009; Lv et al., 2017b; Mueller et al., 2005; Qin et al., 2007a; Reck et al., 2016; Zhu et al., 2017b). KAP-GFP was expressed in the hypomorphic mutant *fla3* and IFT27-GFP was expressed in wild-type cells. The bald *ift46-1* mutant (CC-4375) has been previously described and was rescued by expressing IFT46-YFP (Hou et al., 2007; Lv et al., 2017b). The novel *ift54* and *ift140 C. reinhardtii* mutants lacked flagella and were obtained by insertional mutagenesis using *aph7*, and *NIA1*, respectively, as selectable markers. PCR was used to confirm the insertions and specific antibodies confirmed the loss of the wild-type proteins; details of the mutant strains will be reported in upcoming publications from the Lechtreck and Witman laboratories, respectively. A DNA fragment encompassing the coding region of IFT54 was amplified from genomic DNA and cloned downstream of NG into pBR25, which allows for selection on zeocin; the construct rescued the flagella-less phenotype of *ift54-2*. The *ift140* mutant was rescued using a construct consisting of the aphVIII selectable marker gene and the genomic region of IFT140 fused at its C-terminus to either sfGFP or mCherry codon-adapted for *C. reinhardtii*. The IFT140-sfGFP and –mCherry strains were grown in TAP medium, all other strains were maintained in modified M medium with a light/dark cycle of 14:10 h. The *fla3* KAP-GFP *ift140* IFT140-mCherry strain was obtained by mating the *fla3* KAP-GFP and the *ift140* IFT140-mCherry strains. Motile progeny was analyzed by TIRF microcopy and the strains expressing KAP-GFP and IFT140-mC were analyzed by Western blotting using

antibodies to C. reinhardtii KAP (Invitrogen, Carlsbad, CA) and IFT140 (Picariello et al., in preparation). *Tetrahymena thermophila* expressing GFP-Dyf1p/IFT70 have been previously described (Dave et al., 2009). Briefly, the *GFP-Dyf1* cassette was inserted into the nonessential *BTU1* locus of a correspond knock-out strain; the cells were grown in SPP medium. A mIMCD3 cell line (RRID:CVCL_0429) stably expressing IFT88::YFP was a gift from Dr. Jagesh Shah (Harvard Medical School); cells were cultured as described (Besschetnova et al., 2009).

TIRF microscopy

For TIRF imaging, we used Eclipse Ti-U microscope (Nikon) equipped with 60× NA1.49 TIRF objective and through-the-objective TIRF illumination provided by a 40-mW 488-nm and a 75-mW 561-nm diode laser (Spectraphysics) as previously described (Lechtreck, 2013). The excitation lasers were cleaned up with a Nikon GFP/mCherry TIRF filter and the emission was separated using an Image Splitting Device (Photometrics DualView2 with filter cube 11-EM). Images were mostly recorded at 10 fps using an iXON3 (Andor) and the NIS-Elements Advanced Research software (Nikon); μManager (https://micro-manager.org/) was used to record some FLIP experiments.

To obtain a focused laser beam, the 488-nm laser beam was split using a 488nm zero-order half-wave plate and a broad band polarized beam splitter; one of the beams was used for TIRF illumination. The other beam was expanded using a 3x beam expander, focused using 200 mm plano-convex lens and a 35 mm plano-convex lens and recombined with the TIRF laser beam using polarized beam splitter (all parts from Thorlabs Inc.). A motorized mirror connected to a joystick (Newfocus) was used to move the bleaching laser and the size of the laser spot was altered manually by moving the 35-mm lens. For FLIP experiments, the shutter and shutter driver (Uniblitz) for the bleaching laser were controlled via an Arduino Uno device and a

custom-written macro for μ-Manager (see Supplementary methods). The FLIP experiments were recorded using either μ-Manger, which allowed us to prevent the acquisition of frames while the shutter was open or Nikon Elements; in the latter, the camera continued to record while the bleaching laser shutter was open resulting in over-exposed frames. FIJI (National Institutes of Health) was used to generate kymograms and quantify signals. Excel was used for statistical analysis; the kinetics of fluorescence recovery was determined manually based on the Excel scatter plots (see Fig. 2.2C as an example). Adobe Photoshop was used to adjust image contrast and brightness, and figures were prepared in Adobe Illustrator. SigmaPlot in Tukey setting was used to prepare the box plots.

Observation chambers for *C. reinhardtii* were constructed by applying a ring of vacuum grease or petroleum jelly to a 24 x 60 mm No. 1.5 coverslip; 10 μl of cell suspension were applied and allowed to settle for ~1 minute. Then, the chamber was closed by inverting a 22 × 22 mm no. 1.5 cover glass with ~5-10 μl of 5 mM Hepes, pH 7.3, 5 mM EGTA onto the larger coverslip. Cells were imaged through the large cover glass at room temperature.

TIRF microscopy of *T. thermophila* was performed as previously described (Jiang et al., 2015) with following modifications: Cells were washed and resuspended in Tris HCL buffer, pH 7.5, mixed in a 10:1 ratio with 20 μM $NiCl_2$ and applied to a 22x22 mm No. 1.5 cover glass. Nickel inhibits axonemal dyneins facilitating imaging of IFT (Jiang et al., 2015). A thin coat of petroleum jelly matching the outline of the cover glass was applied to a glass slide and inverted onto the cover glass. For *in vivo* imaging of IMCD cells expressing IFT88-YFP, the cells were grown under a transwell cup (Corning, Corning NY), switched to phenol red-free CO_2 independent medium with 25mM HEPES (Gibco), and placed directly on a 22x60 mm No. 1.5 cover glass (Ott and Lippincott-Schwartz, 2012).

FRAP and FLIP analysis of the basal body pool, IFT traffic, and tubulin transport

For FRAP analysis of the IFT bb-pool, kymograms were generated from videos showing the cells before, during and after the application of a brief laser pulse to bleach the experimental basal body. Grayscale profiles were plotted along lines covering the basal body signals, the data were converted to an Excel sheet, and the fluorescence of the experimental basal body was calculated in % of the intensity of the control basal body in a frame-by-frame manner. The recovery time and intensity were determined manually as shown in Fig. 2.2C. In IMCD cells and *T. thermophila*, basal bodies with the attached cilium were bleached completely by moving the focused laser beam along the length of the cilium. To determine the rate of signal loss in FLIP experiments, we used the slope of a trendline added in Excel to the frames representing the initial 10 - 25 s of the experiment. For the gap analysis, a fiduciary mark on the monitor was used to position the cell so that one basal body was targeted by the laser spot; the focus level was adjusted to the level of the flagella, the recording was started, and a laser pulse of <100 ms to ~600 ms was applied. Cells which moved prior to the bleaching step or which did not resume regular IFT traffic after the bleaching step were ignored.

To analyze tubulin transport, cells expressing sfGFP-α-tubulin were washed and resuspended in M media, deflagellated by pH shock, transferred to fresh M medium, and allowed to regrow cilia under constant light with agitation (Craft et al., 2015b; Lefebvre, 1995)). To delay the onset on regeneration, cells were kept on ice until needed. In stored cells, regeneration was initiated by diluting the cells with room temperature M media and incubation as above. For photobleaching of sfGFP-α-tubulin already present in the axoneme, the intensity of the 488-nm laser was increased from <1% to ~10% for 4–12 s.

To analyze the signal intensity of IFT trains, a line partially covering the trajectory was placed on kymograms in ImageJ and the grey value was obtained.

2.16 REFERENCES

Ahmed, N.T., C. Gao, B.F. Lucker, D.G. Cole, and D.R. Mitchell. 2008. ODA16 aids axonemal outer row dynein assembly through an interaction with the intraflagellar transport machinery. *The Journal of cell biology*. 183:313-322.

Avidor-Reiss, T., A.M. Maer, E. Koundakjian, A. Polyanovsky, T. Keil, S. Subramaniam, and C.S. Zuker. 2004. Decoding cilia function: defining specialized genes required for compartmentalized cilia biogenesis. *Cell*. 117:527-539.

Banizs, B., M.M. Pike, C.L. Millican, W.B. Ferguson, P. Komlosi, J. Sheetz, P.D. Bell, E.M. Schwiebert, and B.K. Yoder. 2005. Dysfunctional cilia lead to altered ependyma and choroid plexus function, and result in the formation of hydrocephalus. *Development (Cambridge, England)*. 132:5329-5339.

Beales, P., and P.K. Jackson. 2012. Cilia - the prodigal organelle. *Cilia*. 1:1-1.

Berbari, N.F., J.S. Lewis, G.A. Bishop, C.C. Askwith, and K. Mykytyn. 2008. Bardet-Biedl syndrome proteins are required for the localization of G protein-coupled receptors to primary cilia. *Proceedings of the National Academy of Sciences of the United States of America*. 105:4242-4246.

Besschetnova, T.Y., B. Roy, and J.V. Shah. 2009. Imaging intraflagellar transport in mammalian primary cilia. *Methods Cell Biol*. 93:331-346.

Bhogaraju, S., L. Cajanek, C. Fort, T. Blisnick, K. Weber, M. Taschner, N. Mizuno, S. Lamla, P. Bastin, E.A. Nigg, and E. Lorentzen. 2013. Molecular basis of tubulin transport within the cilium by IFT74 and IFT81. *Science*. 341:1009-1012.

Bizet, A.A., A. Becker-Heck, R. Ryan, K. Weber, E. Filhol, P. Krug, J. Halbritter, M. Delous, M.-C. Lasbennes, B. Linghu, E.J. Oakeley, M. Zarhrate, P. Nitschké, M. Garfa-Traore, F. Serluca, F. Yang, T. Bouwmeester, L. Pinson, E. Cassuto, P. Dubot, N.A.S. Elshakhs, J.A. Sahel, R. Salomon, I.A. Drummond, M.-C. Gubler, C. Antignac, S. Chibout, J.D. Szustakowski, F. Hildebrandt, E. Lorentzen, A.W. Sailer, A. Benmerah, P. Saint-Mezard, and S. Saunier. 2015. Mutations in TRAF3IP1/IFT54 reveal a new role for IFT proteins in microtubule stabilization. *Nature Communications*. 6:8666.

Blacque, O.E., M.J. Reardon, C. Li, J. McCarthy, M.R. Mahjoub, S.J. Ansley, J.L. Badano, A.K. Mah, P.L. Beales, W.S. Davidson, R.C. Johnsen, M. Audeh, R.H.A. Plasterk, D.L. Baillie, N. Katsanis, L.M. Quarmby, S.R. Wicks, and M.R. Leroux. 2004. Loss of C. elegans BBS-7 and BBS-8 protein function results in cilia defects and compromised intraflagellar transport. *Genes & development*. 18:1630-1642.

Bloodgood, R.A. 2010. Sensory reception is an attribute of both primary cilia and motile cilia. 123:505-509.

Brown, J.M., D.A. Cochran, B. Craige, T. Kubo, and G.B. Witman. 2015. Assembly of IFT trains at the ciliary base depends on IFT74. *Current biology : CB*. 25:1583-1593.

Buisson, J., N. Chenouard, T. Lagache, T. Blisnick, J.C. Olivo-Marin, and P. Bastin. 2012. Intraflagellar transport proteins cycle between the flagellum and its base. *J Cell Sci*.

Chien, A., S.M. Shih, R. Bower, D. Tritschler, M.E. Porter, and A. Yildiz. 2017. Dynamics of the IFT machinery at the ciliary tip. *eLife*. 6:e28606.

Christensen, S.T., C.A. Clement, P. Satir, and L.B. Pedersen. 2012. Primary cilia and coordination of receptor tyrosine kinase (RTK) signalling. *The Journal of pathology*. 226:172-184.

Clement, C.A., K.D. Ajbro, K. Koefoed, M.L. Vestergaard, I.R. Veland, M.P. Henriques de Jesus, L.B. Pedersen, A. Benmerah, C.Y. Andersen, L.A. Larsen, and S.T. Christensen. 2013. TGF-beta signaling is associated with endocytosis at the pocket region of the primary cilium. *Cell reports*. 3:1806-1814.

Cole, D.G., D.R. Diener, A.L. Himelblau, P.L. Beech, J.C. Fuster, and J.L. Rosenbaum. 1998. Chlamydomonas Kinesin-II–dependent Intraflagellar Transport (IFT): IFT Particles Contain Proteins Required for Ciliary Assembly in Caenorhabditis elegans Sensory Neurons. *The Journal of cell biology*. 141:993-1008.

Cole, D.G., and W.J. Snell. 2009. SnapShot: Intraflagellar transport. *Cell*. 137:784-784.e781.

Corbit, K.C., P. Aanstad, V. Singla, A.R. Norman, D.Y. Stainier, and J.F. Reiter. 2005. Vertebrate Smoothened functions at the primary cilium. *Nature*. 437:1018-1021.

Craft, J.M., J.A. Harris, S. Hyman, P. Kner, and K.F. Lechtreck. 2015a. Tubulin transport by IFT is upregulated during ciliary growth by a cilium-autonomous mechanism. *The Journal of cell biology*. 208:223.

Craft, J.M., J.A. Harris, S. Hyman, P. Kner, and K.F. Lechtreck. 2015b. Tubulin transport by IFT is upregulated during ciliary growth by a cilium-autonomous mechanism. *J Cell Biol*. 208:223-237.

Datta, P., C. Allamargot, J.S. Hudson, E.K. Andersen, S. Bhattarai, A.V. Drack, V.C. Sheffield, and S. Seo. 2015. Accumulation of non-outer segment proteins in the outer segment underlies photoreceptor degeneration in Bardet-Biedl syndrome. *Proceedings of the National Academy of Sciences of the United States of America*. 112:E4400-4409.

Dave, D., D. Wloga, N. Sharma, and J. Gaertig. 2009. DYF-1 Is required for assembly of the axoneme in Tetrahymena thermophila. *Eukaryot Cell*. 8:1397-1406.

Deane, J.A., D.G. Cole, E.S. Seeley, D.R. Diener, and J.L. Rosenbaum. 2001. Localization of intraflagellar transport protein IFT52 identifies basal body transitional fibers as the docking site for IFT particles. *Current biology : CB*. 11:1586-1590.

Dentler, W. 2005. Intraflagellar transport (IFT) during assembly and disassembly of Chlamydomonas flagella. *The Journal of cell biology*. 170:649-659.

Eichele, G., E. Bodenschatz, Z. Ditte, A.K. Gunther, S. Kapoor, Y. Wang, and C. Westendorf. 2020. Cilia-driven flows in the brain third ventricle. *Philosophical transactions of the Royal Society of London. Series B, Biological sciences*. 375:20190154.

Gonçalves, J., and L. Pelletier. 2017. The Ciliary Transition Zone: Finding the Pieces and Assembling the Gate. *Mol Cells*. 40:243-253.

Gudis, D.A., and N.A. Cohen. 2010. Cilia dysfunction. *Otolaryngologic clinics of North America*. 43:461-472, vii.

Habbig, S., M.P. Bartram, R.U. Muller, R. Schwarz, N. Andriopoulos, S. Chen, J.G. Sagmuller, M. Hoehne, V. Burst, M.C. Liebau, H.C. Reinhardt, T. Benzing, and B. Schermer. 2011. NPHP4, a cilia-associated protein, negatively regulates the Hippo pathway. *The Journal of cell biology*. 193:633-642.

Han, Y.G., B.H. Kwok, and M.J. Kernan. 2003. Intraflagellar transport is required in Drosophila to differentiate sensory cilia but not sperm. *Current biology : CB*. 13:1679-1686.

Haycraft, C.J., B. Banizs, Y. Aydin-Son, Q. Zhang, E.J. Michaud, and B.K. Yoder. 2005. Gli2 and Gli3 localize to cilia and require the intraflagellar transport protein polaris for processing and function. *PLoS genetics*. 1:e53.

Hirano, T., Y. Katoh, and K. Nakayama. 2017. Intraflagellar transport-A complex mediates ciliary entry and retrograde trafficking of ciliary G protein-coupled receptors. *Mol Biol Cell*. 28:429-439.

Hirokawa, N., Y. Tanaka, and Y. Okada. 2009. Left-right determination: involvement of molecular motor KIF3, cilia, and nodal flow. *Cold Spring Harb Perspect Biol*. 1:a000802-a000802.

Hou, Y., G.J. Pazour, and G.B. Witman. 2004. A dynein light intermediate chain, D1bLIC, is required for retrograde intraflagellar transport. *Mol Biol Cell*. 15:4382-4394.

Hou, Y., H. Qin, J.A. Follit, G.J. Pazour, J.L. Rosenbaum, and G.B. Witman. 2007. Functional analysis of an individual IFT protein: IFT46 is required for transport of outer dynein arms into flagella. *The Journal of cell biology*. 176:653-665.

Hsu, Y., J.E. Garrison, G. Kim, A.R. Schmitz, C.C. Searby, Q. Zhang, P. Datta, D.Y. Nishimura, S. Seo, and V.C. Sheffield. 2017. BBSome function is required for both the morphogenesis and maintenance of the photoreceptor outer segment. *PLoS genetics*. 13:e1007057-e1007057.

Hua, K., and R.J. Ferland. 2018. Primary cilia proteins: ciliary and extraciliary sites and functions. *Cellular and molecular life sciences : CMLS*. 75:1521-1540.

Huangfu, D., A. Liu, A.S. Rakeman, N.S. Murcia, L. Niswander, and K.V. Anderson. 2003. Hedgehog signalling in the mouse requires intraflagellar transport proteins. *Nature*. 426:83-87.

Ishikawa, H., and W.F. Marshall. 2011. Ciliogenesis: building the cell's antenna. *Nature Reviews Molecular Cell Biology*. 12:222-234.

Jenkins, P.M., D.P. McEwen, and J.R. Martens. 2009. Olfactory cilia: linking sensory cilia function and human disease. *Chem Senses*. 34:451-464.

Jiang, Y.Y., K. Lechtreck, and J. Gaertig. 2015. Total internal reflection fluorescence microscopy of intraflagellar transport in Tetrahymena thermophila. *Methods Cell Biol*. 127:445-456.

Jordan, M.A., D.R. Diener, L. Stepanek, and G. Pigino. 2018. The cryo-EM structure of intraflagellar transport trains reveals how dynein is inactivated to ensure unidirectional anterograde movement in cilia. *Nat Cell Biol*. 20:1250-1255.

Khanna, H. 2015. Photoreceptor Sensory Cilium: Traversing the Ciliary Gate. *Cells*. 4:674-686.

Kobayashi, T., K. Gengyo-Ando, T. Ishihara, I. Katsura, and S. Mitani. 2007. IFT-81 and IFT-74 are required for intraflagellar transport in C. elegans. *Genes to cells : devoted to molecular & cellular mechanisms*. 12:593-602.

Koefoed, K., I.R. Veland, L.B. Pedersen, L.A. Larsen, and S.T. Christensen. 2014. Cilia and coordination of signaling networks during heart development. *Organogenesis*. 10:108-125.

Kozminski, K.G., P.L. Beech, and J.L. Rosenbaum. 1995. The Chlamydomonas kinesin-like protein FLA10 is involved in motility associated with the flagellar membrane. *The Journal of cell biology*. 131:1517-1527.

Kozminski, K.G., K.A. Johnson, P. Forscher, and J.L. Rosenbaum. 1993. A motility in the eukaryotic flagellum unrelated to flagellar beating. *Proc Natl Acad Sci U S A*. 90:5519-5523.

Kubo, T., J.M. Brown, K. Bellve, B. Craige, J.M. Craft, K. Fogarty, K.F. Lechtreck, and G.B. Witman. 2016. Together, the IFT81 and IFT74 N-termini form the main module for intraflagellar transport of tubulin. *Journal of cell science*. 129:2106-2119.

Lechtreck, K.F., E.C. Johnson, T. Sakai, D. Cochran, B.A. Ballif, J. Rush, G.J. Pazour, M. Ikebe, and G.B. Witman. 2009. The Chlamydomonas reinhardtii BBSome is an IFT cargo required for export of specific signaling proteins from flagella. *The Journal of cell biology*. 187:1117-1132.

Lefebvre, P.A. 1995. Flagellar amputation and regeneration in Chlamydomonas. *Methods Cell Biol*. 47:3-7.

Lehti, M.S., and A. Sironen. 2017. Formation and function of sperm tail structures in association with sperm motility defects†. *Biology of Reproduction*. 97:522-536.

Liew, G.M., F. Ye, A.R. Nager, J.P. Murphy, J.S. Lee, M. Aguiar, D.K. Breslow, S.P. Gygi, and M.V. Nachury. 2014. The intraflagellar transport protein IFT27 promotes BBSome exit from cilia through the GTPase ARL6/BBS3. *Dev Cell*. 31:265-278.

Liu, A., B. Wang, and L.A. Niswander. 2005. Mouse intraflagellar transport proteins regulate both the activator and repressor functions of Gli transcription factors. *Development (Cambridge, England)*. 132:3103-3111.

Liu, P., and K.F. Lechtreck. 2018. The Bardet-Biedl syndrome protein complex is an adapter expanding the cargo range of intraflagellar transport trains for ciliary export. *Proceedings of the National Academy of Sciences of the United States of America*. 115:E934-e943.

Liu, Z., H. Tu, Y. Kang, Y. Xue, D. Ma, C. Zhao, H. Li, L. Wang, and F. Liu. 2019. Primary cilia regulate hematopoietic stem and progenitor cell specification through Notch signaling in zebrafish. *Nature Communications*. 10:1839.

Ludington, W.B., K.A. Wemmer, K.F. Lechtreck, G.B. Witman, and W.F. Marshall. 2013. Avalanche-like behavior in ciliary import. *Proc Natl Acad Sci U S A*. 110:3925-3930.

Lv, B., L. Wan, M. Taschner, X. Cheng, E. Lorentzen, and K. Huang. 2017a. Intraflagellar transport protein IFT52 recruits IFT46 to the basal body and flagella. *Journal of cell science*. 130:1662-1674.

Lv, B., L. Wan, M. Taschner, X. Cheng, E. Lorentzen, and K. Huang. 2017b. Intraflagellar transport protein IFT52 recruits IFT46 to the basal body and flagella. *J Cell Sci*.

Marshall, W.F., and J.L. Rosenbaum. 2001. Intraflagellar transport balances continuous turnover of outer doublet microtubules: implications for flagellar length control. *The Journal of cell biology*. 155:405-414.

Mijalkovic, J., B. Prevo, F. Oswald, P. Mangeol, and E.J. Peterman. 2017. Ensemble and single-molecule dynamics of IFT dynein in Caenorhabditis elegans cilia. *Nat Commun*. 8:14591.

Mijalkovic, J., J. van Krugten, F. Oswald, S. Acar, and E.J.G. Peterman. 2018. Single-Molecule Turnarounds of Intraflagellar Transport at the C. elegans Ciliary Tip. *Cell reports*. 25:1701-1707.e1702.

Mönnich, M., L. Borgeskov, L. Breslin, L. Jakobsen, M. Rogowski, C. Doganli, J.M. Schrøder, J.B. Mogensen, L. Blinkenkjær, and L.M.J.C.r. Harder. 2018. CEP128 localizes to the subdistal appendages of the mother centriole and regulates TGF-β/BMP signaling at the primary cilium. 22:2584-2592.

Mueller, J., C.A. Perrone, R. Bower, D.G. Cole, and M.E. Porter. 2005. The FLA3 KAP subunit is required for localization of kinesin-2 to the site of flagellar assembly and processive anterograde intraflagellar transport. *Mol Biol Cell*. 16:1341-1354.

Müller, O.F., and O. Fabricius. 1786. Animalcula infusoria fluviatilia et marina que detexit, systematice descripsit et ad vivum delineari curavit Otho Fridericus Müller sistit opus hoc posthumum quod cum tabulis Aeneis L. in lucem tradit vidua ejus nobilissima cura Othonis Fabricii. Typis N. Mölleri, Hauniae :.

Mykytyn, K., R.F. Mullins, M. Andrews, A.P. Chiang, R.E. Swiderski, B. Yang, T. Braun, T. Casavant, E.M. Stone, and V.C. Sheffield. 2004. Bardet-Biedl syndrome type 4 (BBS4)-null mice implicate Bbs4 in flagella formation but not global cilia assembly. *Proceedings of the National Academy of Sciences of the United States of America*. 101:8664-8669.

Nachury, M.V.J.C.o.i.c.b. 2018. The molecular machines that traffic signaling receptors into and out of cilia. 51:124-131.

Nechipurenko, I.V., C. Berciu, P. Sengupta, and D. Nicastro. 2017. Centriolar remodeling underlies basal body maturation during ciliogenesis in Caenorhabditis elegans. *Elife*. 6.

Okada, Y., S. Nonaka, Y. Tanaka, Y. Saijoh, H. Hamada, and N. Hirokawa. 1999. Abnormal Nodal Flow Precedes Situs Inversus in iv and inv mice. *Molecular Cell*. 4:459-468.

Orozco, J.T., K.P. Wedaman, D. Signor, H. Brown, L. Rose, and J.M. Scholey. 1999. Movement of motor and cargo along cilia. *Nature*. 398:674.

Ott, C., and J. Lippincott-Schwartz. 2012. Visualization of live primary cilia dynamics using fluorescence microscopy. *Curr Protoc Cell Biol*. Chapter 4:Unit 4 26.

Pazour, G.J., N. Agrin, J. Leszyk, and G.B. Witman. 2005. Proteomic analysis of a eukaryotic cilium. *The Journal of cell biology*. 170:103-113.

Pazour, G.J., B.L. Dickert, Y. Vucica, E.S. Seeley, J.L. Rosenbaum, G.B. Witman, and D.G. Cole. 2000. Chlamydomonas IFT88 and its mouse homologue, polycystic kidney disease gene tg737, are required for assembly of cilia and flagella. *The Journal of cell biology*. 151:709-718.

Peabody, J.E., R.-J. Shei, B.M. Bermingham, S.E. Phillips, B. Turner, S.M. Rowe, and G.M. Solomon. 2018. Seeing cilia: imaging modalities for ciliary motion and clinical connections. *Am J Physiol Lung Cell Mol Physiol*. 314:L909-L921.

Pedersen, L.B., S. Geimer, and J.L. Rosenbaum. 2006. Dissecting the Molecular Mechanisms of Intraflagellar Transport in Chlamydomonas. *Current Biology*. 16:450-459.

Peixoto, E., S. Richard, K. Pant, A. Biswas, and S.A. Gradilone. 2020. The primary cilium: Its role as a tumor suppressor organelle. *Biochemical Pharmacology*. 175:113906.

Piperno, G., E. Siuda, S. Henderson, M. Segil, H. Vaananen, and M. Sassaroli. 1998. Distinct mutants of retrograde intraflagellar transport (IFT) share similar morphological and molecular defects. *The Journal of cell biology*. 143:1591-1601.

Prevo, B., P. Mangeol, F. Oswald, J.M. Scholey, and E.J. Peterman. 2015. Functional differentiation of cooperating kinesin-2 motors orchestrates cargo import and transport in C. elegans cilia. *Nat Cell Biol*. 17:1536-1545.

Qin, H., D.R. Diener, S. Geimer, D.G. Cole, and J.L. Rosenbaum. 2004a. Intraflagellar transport (IFT) cargo: IFT transports flagellar precursors to the tip and turnover products to the cell body. *The Journal of cell biology*. 164:255-266.

Qin, H., D.R. Diener, S. Geimer, D.G. Cole, and J.L. Rosenbaum. 2004b. Intraflagellar transport (IFT) cargo: IFT transports flagellar precursors to the tip and turnover products to the cell body. *The Journal of cell biology*. 164:255-266.

Qin, H., Z. Wang, D. Diener, and J. Rosenbaum. 2007. Intraflagellar transport protein 27 is a small G protein involved in cell-cycle control. *Curr Biol*. 17:193-202.

Raidt, J., C. Werner, T. Menchen, G.W. Dougherty, H. Olbrich, N.T. Loges, R. Schmitz, P. Pennekamp, and H. Omran. 2015. Ciliary function and motor protein composition of human fallopian tubes. *Human Reproduction*. 30:2871-2880.

Reck, J., A.M. Schauer, K. VanderWaal Mills, R. Bower, D. Tritschler, C.A. Perrone, and M.E. Porter. 2016. The role of the dynein light intermediate chain in retrograde IFT and flagellar function in Chlamydomonas. *Mol Biol Cell*. 27:2404-2422.

Richey, E.A., and H. Qin. 2012a. Dissecting the sequential assembly and localization of intraflagellar transport particle complex B in Chlamydomonas. *PLoS One*. 7:e43118.

Richey, E.A., and H. Qin. 2012b. Dissecting the sequential assembly and localization of intraflagellar transport particle complex B in Chlamydomonas. *PLoS One*. 7:e43118-e43118.

Rogowski, M., D. Scholz, and S. Geimer. 2013. Electron microscopy of flagella, primary cilia, and intraflagellar transport in flat-embedded cells. *Methods in enzymology*. 524:243-263.

Rosenbaum, J.L., and F.M. Child. 1967. Flagellar regeneration in protozoan flagellates. *The Journal of cell biology*. 34:345-364.

Sarpal, R., S.V. Todi, E. Sivan-Loukianova, S. Shirolikar, N. Subramanian, E.C. Raff, J.W. Erickson, K. Ray, and D.F. Eberl. 2003. Drosophila KAP interacts with the kinesin II motor subunit KLP64D to assemble chordotonal sensory cilia, but not sperm tails. *Current biology : CB*. 13:1687-1696.

Satir, P. 1995. Landmarks in cilia research from Leeuwenhoek to us. *Cell motility and the cytoskeleton*. 32:90-94.

Shah, A.S., Y. Ben-Shahar, T.O. Moninger, J.N. Kline, and M.J. Welsh. 2009. Motile Cilia of Human Airway Epithelia Are Chemosensory. 325:1131-1134.

Stasiulewicz, M., S.D. Gray, I. Mastromina, J.C. Silva, M. Björklund, P.A. Seymour, D. Booth, C. Thompson, R.J. Green, E.A. Hall, P. Serup, and J.K. Dale. 2015. A conserved role for Notch signaling in priming the cellular response to Shh through ciliary localisation of the key Shh transducer Smo. 142:2291-2303.

Stepanek, L., and G. Pigino. 2016. Microtubule doublets are double-track railways for intraflagellar transport trains. *Science*. 352:721-724.

Taschner, M., A. Lorentzen, A. Mourao, T. Collins, G.M. Freke, D. Moulding, J. Basquin, D. Jenkins, and E. Lorentzen. 2018. Crystal structure of intraflagellar transport protein 80 reveals a homo-dimer required for ciliogenesis. *eLife*. 7.

Taschner, M., and E. Lorentzen. 2016. The Intraflagellar Transport Machinery. *Cold Spring Harb Perspect Biol*. 8.

Taschner, M., K. Weber, A. Mourão, M. Vetter, M. Awasthi, M. Stiegler, S. Bhogaraju, and E. Lorentzen. 2016. Intraflagellar transport proteins 172, 80, 57, 54, 38, and 20 form a stable tubulin-binding IFT-B2 complex. *The EMBO Journal*. 35:773-790.

Toropova, K., R. Zalyte, A.G. Mukhopadhyay, M. Mladenov, A.P. Carter, and A.J. Roberts. 2019. Structure of the dynein-2 complex and its assembly with intraflagellar transport trains. *Nature Structural & Molecular Biology*. 26:823-829.

van Dam, T.J., M.J. Townsend, M. Turk, A. Schlessinger, A. Sali, M.C. Field, and M.A. Huynen. 2013. Evolution of modular intraflagellar transport from a coatomer-like progenitor. *Proceedings of the National Academy of Sciences of the United States of America*. 110:6943-6948.

Vannuccini, E., E. Paccagnini, F. Cantele, M. Gentile, D. Dini, F. Fino, D. Diener, C. Mencarelli, and P. Lupetti. 2016. Two classes of short intraflagellar transport train with different 3D structures are present in Chlamydomonas flagella. *Journal of cell science*. 129:2064-2074.

Wagner, M.K., and H.J. Yost. 2000. Left–right development: The roles of nodal cilia. *Current Biology*. 10:R149-R151.
Wallingford, J.B., and B. Mitchell. 2011. Strange as it may seem: the many links between Wnt signaling, planar cell polarity, and cilia. *Genes & development*. 25:201-213.
Williams, C.L., J.C. McIntyre, S.R. Norris, P.M. Jenkins, L. Zhang, Q. Pei, K. Verhey, and J.R. Martens. 2014. Direct evidence for BBSome-associated intraflagellar transport reveals distinct properties of native mammalian cilia. *Nat Commun*. 5:5813.
Wingfield, J.L., I. Mengoni, H. Bomberger, Y.Y. Jiang, J.D. Walsh, J.M. Brown, T. Picariello, D.A. Cochran, B. Zhu, J. Pan, J. Eggenschwiler, J. Gaertig, G.B. Witman, P. Kner, and K. Lechtreck. 2017. IFT trains in different stages of assembly queue at the ciliary base for consecutive release into the cilium. *eLife*. 6.
Wood, C.R., and J.L. Rosenbaum. 2014. Proteins of the ciliary axoneme are found on cytoplasmic membrane vesicles during growth of cilia. *Curr Biol*. 24:1114-1120.
Wren, K.N., J.M. Craft, D. Tritschler, A. Schauer, D.K. Patel, E.F. Smith, M.E. Porter, P. Kner, and K.F. Lechtreck. 2013. A differential cargo-loading model of ciliary length regulation by IFT. *Curr Biol*. 23:2463-2471.
Zhu, B., X. Zhu, L. Wang, Y. Liang, Q. Feng, and J. Pan. 2017a. Functional exploration of the IFT-A complex in intraflagellar transport and ciliogenesis. *PLoS Genet*. 13:e1006627.
Zhu, X., Y. Liang, F. Gao, and J. Pan. 2017b. IFT54 regulates IFT20 stability but is not essential for tubulin transport during ciliogenesis. *Cellular and molecular life sciences : CMLS*. 74:3425-3437.

CHAPTER 3

A TRAIN FRAGMENTATION MODEL OF IFT TURNAROUND AT THE TIP[2]

[2] Wingfield, J.L., P. Liu, B. Mekkonnen, I. Mengoni, and K. Lechtreck. To be submitted to *eLife*.

3.1 ABSTRACT

Ciliary assembly depends on intraflagellar transport (IFT), a bidirectional motility of large protein carriers referred to as IFT trains. The trains consist of 22 IFT proteins organized into IFT-A, IFT-B1, and IFT-B2 subcomplexes and the IFT motors kinesin-2 and IFT dynein. At the ciliary base, multiple units of each subcomplex polymerize into trains and then move by anterograde IFT to the flagellar tip. At the tip, the trains are remodeled for retrograde IFT, a process that involves train fragmentation and the activation of IFT dynein. Here, we used *Chlamydomonas* to analyze the level of train fragmentation at the cilia tip, i.e., into "carts" encompassing IFT-A, IFT-B, and motor proteins, IFT subcomplexes, or individual IFT proteins. Single- and two-color *in vivo* imaging of eight distinct fluorescent protein-tagged IFT and motor proteins indicate that IFT-A, IFT-B, and IFT-dynein remain associated during fragmentation. We postulate that the fragmentation of the anterograde trains could release IFT dynein from inhibitory contacts with IFT-B leading to its activation on the smaller fragments and initiation of retrograde IFT. Lasting association of IFT-A, IFT-B, and IFT dynein at the tip could prevent a build-up of IFT components at the tip by maintaining the stoichiometry of the component of anterograde IFT trains during the formation of retrograde trains.

3.2 INTRODUCTION

Cilia are microtubule-based organelles that perform both sensory perception and motility roles for cells. Malformations in cilia cause a variety of diseases, termed ciliopathies, characterized by retinal degeneration, brain malformations, and renal disease (Waters and Beales, 2011). Therefore, the presence and maintenance of cilia are critical for human health. Cilia are built and sustained by conserved protein complexes termed intraflagellar transport (IFT)

trains. IFT trains are multi-megadalton complexes made of repeating units of IFT-A (6 proteins), IFT-B (16 proteins), IFT dynein, and kinesin-II (for review see (Taschner and Lorentzen, 2016)). These trains assemble at the ciliary base with IFT-A arriving first, then IFT-B, kinesin-II, and lastly dynein (Wingfield et al., 2017). Kinesin carries the trains to the tip with IFT dynein riding on the train as inactive cargo (Jordan et al., 2018; Kozminski et al., 1995). Once the trains reach the tip, the kinesin subunit KAP tends to dissociate from the train and diffuse back to the base, while the rest of the train undergoes remodeling (Chien et al., 2017a). Once dynein is activated, trains undergo retrograde trafficking back to the ciliary base (retrograde traffic) for disassembly or recycling (Iomini et al., 2001; Wingfield et al., 2017). While train assembly and disassembly has been examined at the ciliary base, it is not well understood at the ciliary tip. The ciliary tip is the site of IFT cargo delivery, ciliary assembly, disassembly, and signal detection and transduction (Craft et al., 2015a; Hunter et al., 2018; Qin et al., 2004a; Soares et al., 2019). Therefore, uncovering IFT remodeling could help us understand how these processes are regulated.

Nearly every model of IFT shows IFT-A, IFT-B, kinesin, and dynein separated at the ciliary tip, off of the axonemal tracks (Chien et al., 2017a; Cole and Snell, 2009; Dawson and House, 2010; Ishikawa and Marshall, 2011; Liang et al., 2014; Morga and Bastin, 2013; Nakayama and Katoh, 2018; Pedersen et al., 2006; Soares et al., 2019; Taschner and Lorentzen, 2016). These models suggest that an anterograde IFT train disassembles into these subunits before reassembling into retrograde trains in the ~2 seconds it resides at the tip (Pedersen et al., 2006). A recent study in Chlamydomonas discovered that at the tip, dynein and an IFT-B subunit, IFT27, fragment and mix with material at the tip to form several retrograde trains; but they do not provide evidence for IFT-A: IFT-B or even IFT-B: IFT-dynein separation (Chien et

al., 2017a). The former models fit well with *C.elegans* data showing IFT-B pauses while the rest of the train immediately undergoes retrograde traffic once it reaches the tip (Mijalkovic et al., 2018). However, *C. elegans* has two anterograde motors, therefore, making its trafficking, and likely remodeling, distinct from other organisms. Therefore, the degree of disassembly of an anterograde train undergoes at the ciliary tip is currently unknown. For example: Anterograde IFT trains could split into "carts" consisting of IFT-A, IFT-B, and IFT dynein, which then return together to the cilia base (Model 3.1a). Alternatively, trains could disassemble into individual IFT subcomplexes, as it is most commonly depicted in the literature (Model 3.1b). Another possibility is that IFT-A, IFT-B1, and IFT-B2 completely disassociate into their individual proteins, before reassembling into a retrograde train (Model 3.1c). Here we employ single- and two-color *in vivo* imaging of eight distinct fluorescent protein-tagged IFT and motor to distinguish between these mechanisms of fragmentation.

RESULTS

3.3 The size of the IFT protein pool at the tip is equivalent to approximately four anterograde trains.

To analyze how anterograde IFT trains reorganize at the cilia tip for retrograde travel, we employed *Chlamydomonas* strains expressing fluorescent protein-tagged versions of the IFT-A proteins IFT43 and IFT140, the IFT-B1 proteins IFT46, IFT81, and IFT74, the IFT-B2 protein IFT54, the BBSome subunit BBS4, and the IFT motor subunit D1bLIC (retrograde); all proteins were expressed to rescue the corresponding mutants (Table 3.1). We omitted KAP-GFP (a kinesin-II protein) from our analysis as it has been previously shown to dissociate from IFT at

the tip (Chien et al., 2017). For our analysis, we focused on cells with high-frequency IFT traffic and only small amounts of stationary IFT in the cilia.

In many systems, the ciliary tip appears brighter when FP-tagged IFT proteins are expressed or when cells are stained with antibodies to IFT proteins for immunofluorescence, indicating the presence of a pool of IFT proteins at the tip. To determine the size of this pool, we used a FRAP assay beaching FP-tagged IFT proteins in the tip region of cilia with a focused laser beam and analyzed the time and the number of arriving anterograde trains required to restore the signal at the tip (Fig. 3.1A). For these experiments, we focused on the IFT-A protein IFT140 and IFT-B protein IFT54 in an *ift54-2* mSc-IFT54 *ift140-1* IFT140-sfGFP double mutant double rescue strain (Fig. 3.1B). As expected, IFT140-sfGFP and mSc-IFT54 co-migrated during anterograde and retrograde IFT. After photobleaching the cilia tip, recovery of the tip signal plateaued on average in 3.5s for mSc-IFT54 and 3.6s for IFT140-sfGFP; during this time, an average of 4.1 anterograde trains, for mSc-IFT54 and 4.2 for IFT140-sfGFP, arrived at the tip (Fig. 3.1C-E). Since IFT140-sfGFP and the mSc-IFT54 signal recovered at the same pace and similar fluctuations in their signal were observed when trains departed the tip, these observations suggest a balance between the arrival and departure of actively moving IFT proteins at the tip.

Further, the data suggest that the ratio between IFT-A and IFT-B proteins of the anterograde trains in maintained in the pool and the assembly of retrograde trains (Fig. 3.1B). Also, retrograde trains exiting the pool caused a transient decrease of the signal at the tip by ~30% (Fig. 3.1G,H). Often, the signal at the tip reached pre-bleach intensity indicating a complete exchange of the bleached IFT proteins with unbleached ones derived from the arriving anterograde trains. However, in some experiments, the recovery after the initial bleaching step remained incomplete in comparison to the pre-bleach signal indicating the presence of stationary

or slow-exchanging IFT protein fraction at the tip. In both cases, signal recovery reached the same extent after each of several subsequent bleaching steps (data not shown). Taken together, the data indicate that the size of the IFT pool at the tip corresponds to approximately four anterograde train equivalents.

3.4 IFT-A and IFT-B proteins dwell for ~2 seconds at the ciliary tip.

The vast majority of IFT trains changed direction near the ciliary tip, but occasionally IFT trains or train fragments switched direction along the length of the cilia as previously observed by DIC microscopy (Dentler, 2005). Previous studies showed that D1bLIC and the IFT-B proteins IFT20 and IFT27 pause for ~ 2 s at the tip between the arrival by anterograde IFT and the onset of retrograde IFT (Chien et al., 2017a; Qin et al., 2007b; Reck et al., 2016; Wren et al., 2013a). To analyze if tip dwelling is a common feature of IFT proteins including those of the IFT-A subcomplex, we used a FRAP assay beaching the FP-tagged IFT proteins in the tip region of cilia with a focused laser beam and analyzed the time period between the arrival of the first unbleached train at the tip and the departure of the first unbleached retrograde train (Figs. 3.1A, 3.2A). For all FP-tagged IFT proteins analyzed, we observed a pause between their arrival at the tip and their departure toward the cilia base by retrograde. We term this time the, "minimum tip dwell time." The length of the pause varied somewhat for a given IFT protein between experiments (Fig. 3.2C) and, for the various strains analyzed, the average length of the pause ranged from ~1.3 s to ~2.3 s (Fig. 3.2B). Because additional anterograde trains arrived at the tip during this pause, it is unclear whether the first unbleached retrograde train is derived from the anterograde train that first arrived at the tip after the bleaching step, from subsequent trains or a mixture of both. However, the time range of the pauses observed with our approach is similar to

those reported previously for IFT-B proteins, including data based on the analysis of individual IFT trains (Chien et al., 2017b). The variability in the length of the pause recorded for the different FP-tagged IFT proteins could be caused by differences in the experimental conditions and in IFT in the rescue strains or represent distinct biological behaviors of the IFT proteins. Toward this end, we imaged a subset of FP-tagged IFT proteins at 15.5, 21, and 27 °C (Fig. 3.2-figure supplemental 1) and analyzed the velocity of IFT and the length of the pause at the tip, both of which showed a strong temperature dependency (Fig. 2-figure supplemental 1B,C). The retrograde velocity of IFT46-YFP, for example, increased from 1.6 μm/s at 16 °C to ~4 μm/s at 27 °C. Similarly, the length of the pause at the tip decreased from >4 s at 16 °C to ~ 2s at 27 °C for the IFT proteins analyzed. The values of the Q10 temperature coefficient ranged from ~1.6 to 2.7, which is close to the value of two observed for many enzymatic processes; somewhat higher values were typically for retrograde IFT and the pause at the tip. The data document a pronounced temperature sensitivity of *Chlamydomonas* IFT, similar to previous observations on IFT velocity and frequency in *Trypanosoma brucei* (Buisson et al., 2012). The data suggest that the variations in minimum tip dwell time are likely to be caused by variations in imaging conditions and probably between the rescue strain rather than indicating distinct tip dwell times of the different IFT proteins. We concluded that all IFT proteins pause at the tip and require at least ~1.5 s to transition from anterograde into retrograde trains

3.5 The BBSome is often released from IFT at the tip.

The BBSome is an octameric complex of BBS proteins that travels on IFT trains through the cilium and aids IFT with protein transport, in particular with protein export from cilia. In *Chlamydomonas*, BBS proteins are expendable for IFT traffic, substoichiometric to IFT proteins,

and only a subset of IFT trains carries BBS4-GFP when expressed in *bbs4* mutants at levels sufficient to rescue the non-phototactic phenotype of the mutant (Lechtreck et al., 2009). To examine the behavior of the BBSome at the ciliary tip, we expressed BBS4-mNG in the previously characterized *bbs4-1* mutant (Lechtreck et al., 2009). The low abundance of BBS4-mNG allowed us to image individual BBSomes at the tip without prior photobleaching. Similar to the IFT proteins, BBS4-mNG dwelled at the tip for 3.1s on average (Fig. 3.2-figure supplemental 3B,C). Often, the BBS4-mNG particles diffused in the tip region before commencing retrograde IFT (Fig. 3.2-figure supplemental 3B,a,c,d). This increased mobility at the tip distinguishes BBS4-mNG from the IFT proteins, which remained largely stationary during the pause (Fig. 3.2-figure supplemental 3A). These data suggest both that BBSomes often dissociate from IFT at the tip and that IFT particles are somehow secured from moving during the pause.

3.6 IFT proteins from one anterograde train are distributed onto several retrograde trains.

Previous studies revealed that IFT27 and D1bLIC of a given anterograde train return to the flagellar base in several different retrograde trains indicating that anterograde IFT trains fragment at the tip (Chien et al., 2017a). IFT27-GFP was expressed in wild-type cells also expressing endogenous IFT27, and data in mammalian cells suggest that IFT27 dissociates from the IFT-B complex at the ciliary tip raising the question whether IFT27-GFP is representative for other IFT proteins (Chien et al., 2017a). Also, Jordan et al. (2019) showed that IFT trains consist of individual layers of IFT-A, IFT-B, kinesin, and IFT-dynein rather than of particles with equimolar numbers of the subcomplexes. The layers have different periodicities, and it remains unclear how the different layers are affected during train remodeling. To answer this question, we used the PhotoGate approach to analyze the behavior of individual fluorescent IFT trains

within an otherwise bleached cilium. In brief, a focused laser beam is used to bleach the cilium of the strains expressing FP-tagged IFT43, IFT140, IFT54, and IFT81 and D1bLIC from the tip down (Fig. 3.3A) (Chien et al., 2017a). Once near the cilium's base, the bleaching laser is transiently blocked to allow one or a few unbleached IFT trains to enter the cilium and move to the tip. This laser beam is then set to blink, and its on/off ratio, size, and strength ensure that most IFT trains passing the beam are bleached, preventing the entry of unbleached IFT proteins into the distal cilium. For all IFT proteins analyzed, one anterograde train typically gave rise to several retrograde trains (Fig. 3.3C). After the arrival of a single fluorescent anterograde train, on average, 3.2 retrograde trains were detected departing from the tip for IFT140-sfGFP (SD 1.1, n=11) and mNG-IFT54 (SD 1.2, n=10), 4 retrograde trains for mNG-IFT81 (n=1), 2 for D1bLIC-GFP (n=4) and 1.1 for IFT43-YFP (n=28) (Fig. 3.3B,C). The low number of retrograde trains observed for IFT43-YFP could in parts result from the low photostability of YFP (2.5 times below that of mNeonGreen), causing most of the protein to be bleached while pausing at the tip (Fig. 3.3-figure supplemental 1B). When two or three fluorescent trains enter the cilium, the number of departing retrograde trains increased to 4.0 and 4.7, respectively (Fig. 3.3-figure supplemental 1A,B). However, as previously described for the other IFT-B proteins, the increase was sub-proportional to the number of anterograde trains suggesting that occasionally fragments derived from different anterograde trains combine into one retrograde train. While such events have not been directly observed, the scenario is supported by the ratio between the frequencies of anterograde and retrograde IFT (Fig. 3.3-figure supplemental 1C). We conclude that the IFT-A, IFT-B, and dynein motor layers of the anterograde IFT trains fragment with similar patterns, i.e., a similar number of breakage points. An exception is IFT43-YFP, which rarely produced multiple trains.

3.7 IFT-A and IFT-B remain associated during train remodeling.

FRAP and PhotoGate analyses of IFT trains at the ciliary tip revealed similar behaviors for all IFT proteins studied. However, the dwell times differed considerably for the IFT proteins analyzed. For example, the IFT-A protein IFT140-sfGFP dwelled on average for ~1.3 s, whereas ~2.1 s was determined for the IFT-B protein mSc-IFT54 (Fig. 3.1B). Since anterograde trains encompass both proteins, IFT140 from a given train would have to combine with IFT54 derived from an earlier train to explain the observations tentatively suggesting that these IFT proteins separate at the tip. However, such a scenario would also imply that the pool if IFT40-sfGFP is of a smaller size than that of mSc-IFT54, which was not observed. Also, the variations in minimal tip dwell time could reflect differences between the strains and/or the experimental conditions. To solve this conundrum, we generated an *ift140-1* IFT140-sfGFP *ift54-2* mSc-IFT54 strain to visualize IFT-A and B simultaneously (Fig. 3.1B). If IFT140-sfGFP indeed dwells for a shorter time than mSc-IFT54, the first retrograde train(s) released from the tip in the FRAP and PhotoGate assays should contain IFT140-sfGFP but not mSc-IFT54. However, both mSc-IFT54 and IFT140-sfGFP dwelled at the tip for ~2.5s (Fig. 3.4A,B), the merged kymographs show high levels of colocalization between IFTA-B as a train arrives and departs from the tip (Fig. 3.4A). The similarities between IFT-A and IFT-B at the tip can be easily visualized by kymographs where the red channel has been inverted on the green channel to show they are mirror images of each other (Fig. 3.4D). The tips of these flagella have a Pearson's correlation coefficient of 0.764, indicating a high amount of colocalization (Fig. 3.4D). Additionally, all of the first retrograde trains from this analysis carried both IFT-A and IFT-B (Fig. 3.4C). This suggests that at least one retrograde train has IFT-A: IFT-B material derived from the same anterograde train. To determine whether IFT-A and IFT-B stay together during fragmentation at the tip, we

performed the PhotoGate analysis outlined in Fig. 3.3A (Fig. 3.4E). Again, we saw that every retrograde train carried both IFTA- and IFTB (Fig. 3.4C). These data suggest IFT-A and IFT-B remain together during fragmentation. Nevertheless, these data could also mean IFT-A and IFT-B briefly separate at the tip but rejoining IFT trains at the exact same time with a similar ratio for retrograde transport. To distinguish between these interpretations, we examined the decay pattern of the IFT-A and IFT-B. If unbleached IFT-A and IFT-B separate from each other at the tip, they have a greater chance of recombining with different sized bleached trains. This would result in different decay patterns for IFT-A and IFT-B, *i.e.*, the first retrograde train of IFT140 might be bright followed by two dimmer trains while IFT54 might have a dim first train followed by a brighter second train and dimmer third train. However, this is not what we see; ~93% of the time we see that IFT140-sfGFP and mSc-IFT54 have identical decay patterns. Thus, suggesting IFT-A and IFT-B indeed remain together during the remodeling process.

Furthermore, an IFT-B1:B2 (*ift54-2* mSc-IFT54 *ift81-1* NG-IFT81) show similar patterns of colocalization in anterograde and retrograde transport (Fig. 3.4-figure supplemental 1). Therefore, we conclude that while IFT-A:A and IFT-B: -B junctions are broken at the ciliary tip, IFT-A: -B interactions remain intact during IFT turnaround.

3.8 IFT dynein and IFT-B remain associated during train remodeling

To further examine which parts of the trains separate from each other at the ciliary tip and which remain associated, we imaged tip dynamics in double-tagged IFT-B/Dynein strain. Visualizing both proteins simultaneously allows us to distinguish between results that are caused because of variations in a strain's background and real differences in protein behaviors. To visualize IFT-B and IFT dynein simultaneously, we generated a *d1blic* D1bLIC-GFP *ift54-2*

mSc-IFT54 strain (Fig. 3.5A). Next, we analyzed the minimum tip dwell time for both mSc-IFT54 and D1bLIC-GFP using the photobleaching technique of Fig. 1A (Fig. 3.5B). We saw both D1bLIC-GFP and mSc-IFT54 dwelled at the tip for ~1.5sec, suggesting they remain together in the first train (Fig. 3.5D). To determine whether D1bLIC and IFT-B stay together during fragmentation at the tip, we performed the PhotoGate analysis outlined in Fig. 3.3A (Fig. 3.5C). Interestingly, ~11% of the time we saw the first retrograde train only carried mSc-IFT54 and ~9% of the time, the first retrograde only carried D1bLIC-GFP (Fig. 3.5C,D). This small discrepancy is likely due to differences in the fluorophores' photostability rather than a biological principle. Together, these and the above data support that IFT-A, -B, and dynein remain together as train carts during IFT turnaround.

3.9 DISCUSSION

At the ciliary tip, IFT trains convert from highly ordered anterograde structures, consisting of distinct layers or IFT-A, IFT-B, and dynein, to more amorphous retrograde structures in the ~2 seconds they remain at the tip (Jordan et al., 2018). Based on models of IFT cycling in reviews and primary literature, the field assumes that IFT-A, IFT-B, dynein, and kinesin separate at the tip before remodeling and activating dynein for retrograde transport, despite little evidence for this. Here, to better understand IFT train remodeling, we performed *in vivo* imaging on IFT proteins in *Chlamydomonas*. We observed that the IFT proteins analyzed dwell at the tip for ~2s before undergoing retrograde trafficking. At the tip, trains fragment and the material from one anterograde train distributes onto several retrograde trains, confirming the observations of Chein et al. 2017, for not just IFT-B but IFT-A as well. Through imaging single train behavior in double-tagged strains, we determined the IFT-B subcomplexes, IFT-A, and

dynein remain together during the reorganization. Therefore, we propose that anterograde trains fragment into 'train cars' with IFT-A, -B and dynein still associated, but broken IFT-A: -A, IFT-B: -B junctions. These train cars mix with carts from other anterograde trains before undergoing retrograde transport, except IFT43, which may not mix with material from other anterograde trains. Our data best support a model where trains do not fully dissociate at the tip but undergo the remodeling proposed in Model 3.1A.

We observed that IFT-B2 and the IFT dynein mostly remain together during turnaround. In a small subset of experiments, D1bLIC began retrograde trafficking before the IFT54 derived from the same anterograde train and vice versa. If dynein regularly falls off retrograde trains and joins waiting trains at the tip, we would expect to see more instances of the first train fragment containing dynein but not IFT-B2. However, our data instead show an equal proportion of the first train fragment containing either Dynein or IFT-B. This is not supportive of a biological principle where dynein dissociates from anterograde train and activates to join an awaiting retrograde train.

IFT43 does appear to have a distinct behavior from the rest of the IFT proteins. Rather than mix with material at the tip, and have an irregular ratio or anterograde to retrograde we primarily see that for every one anterograde IFT43 train there is, one retrograde train forms. This may be related to its suggested function in train turnaround (Zhu et al., 2017a). In Zhu et al., the *ift43* mutant has and accumulation of both IFT-A and IFT-B at the ciliary tip, suggesting they can no longer turnaround transition to retrograde train. IFT139 KO cells also accumulate IFT-A and IFT-B at the tip, suggesting the peripheral IFT-A complex could coordinate train turnaround (Hirano et al., 2017). This could be achieved if the peripheral complex was a retrograde binding site for portions IFT dynein.

Potential mechanisms of Dynein activation and train remodeling

Dynein rides on anterograde trains with its heavy chains in an inactive zig-zag conformation (Jordan et al., 2018; Toropova et al., 2019). In this conformation, dynein makes five contact sites with IFT-B and other adjacent dyneins. This suggests that large trains, which would allow for these numerous contacts, inhibit the activation of dynein. By fragmenting, trains decrease in size, reduce the number of contacts, and thereby allow dynein to become active. This alone is likely insufficient for retrograde train formation but may be an important step. Why fragmentation occurs is still unknown. The microtubule tracks could be keeping the anterograde together, and as KAP is phosphorylated and the train runs off the track, the fragmentation could occur. Fragmentation may not only be important for dynein activation but also for releasing other large cargoes, like inner and outer dynein arms at the tip.

An alternative mechanism is that post-translational modifications, which release dynein chains that induce the inhibitory kink could free dynein from being in the inhibited conformation. The conformational change of dynein may then produce stress on the anterograde train, causing it to fragment. This would make dynein's activation similar to kinesin's inactivation, as at the tip, the KAP subunit get phosphorylated, which separates kinesin from the trains.

3.10 TABLE

Table 3.1 Chlamydomonas strains used in this study.

Subcomplex(es)	**Strain**	**Source**
IFT-A	*ift140-1* IFT140-sfGFP (or IFT140-MC)	Picariello et al. (2019a)
	ift43 IFT43-YFP	Zhu et al. (2017a)
IFT-B	*ift81-1* NG-IFT81	Novel strain
	ift74-2 mSc-IFT74	Novel strain
	ift46 IFT46-YFP	Lv et al. (2017a)
	ift54-2 NG-IFT54 (or mSc-IFT54 or Dendra-IFT54)	Wingfield et al. (2017) and Novel strains
BBSome	*bbs4*-1 BBS4-GFP	Lechtreck et al. (2009)
Dynein	*d1blic* D1bLIC-GFP	Reck et al. (2016)
IFT-A IFT-B2	*ift140-1* IFT140-sfGFP *ift54-2* mSc-IFT54	Novel Strain
IFT-B1 IFT-B2	*Ift81-1* NG-IFt81 *ift54-2* mSc-IFT54	Novel Strain
IFT-B2 IFT-Dynein	*ift54-2* mSc-IFT54 *d1blic* D1bLIC-GFP	Novel Strain

3.11 FIGURES

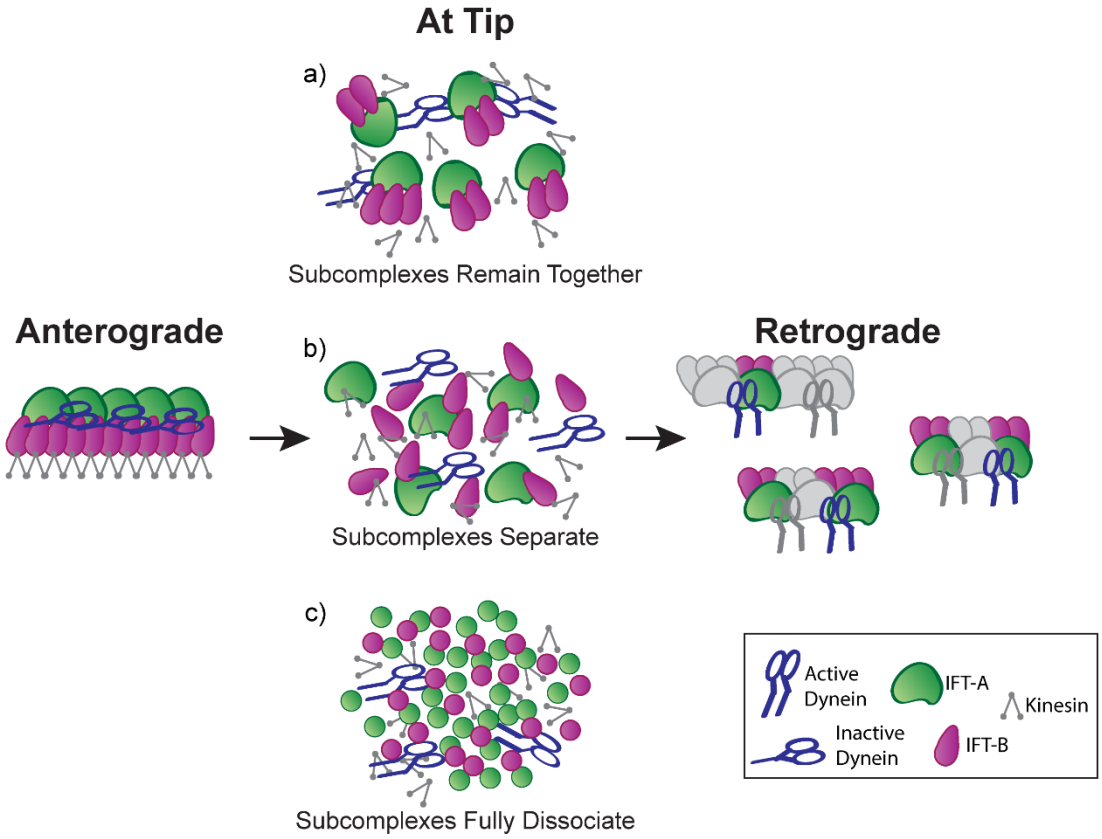

Model 3.1. Potential mechanisms of IFT train remodeling.

a) *Subcomplexes remain together:* IFT-A and IFT-B subcomplexes remain associated during the split of anterograde trains; trains could break, for example, at each of the IFT-A junctions. **b)** *Subcomplexes Separate:* Trains fragment into IFT-A, IFT-B, IFT dynein, and kinesin. **c)** *Subcomplexes Fully dissociate*: Anterograde IFT trains split into IFT-A and IFT-B, which fragment into their individual 22 proteins before recombining into a retrograde IFT train.

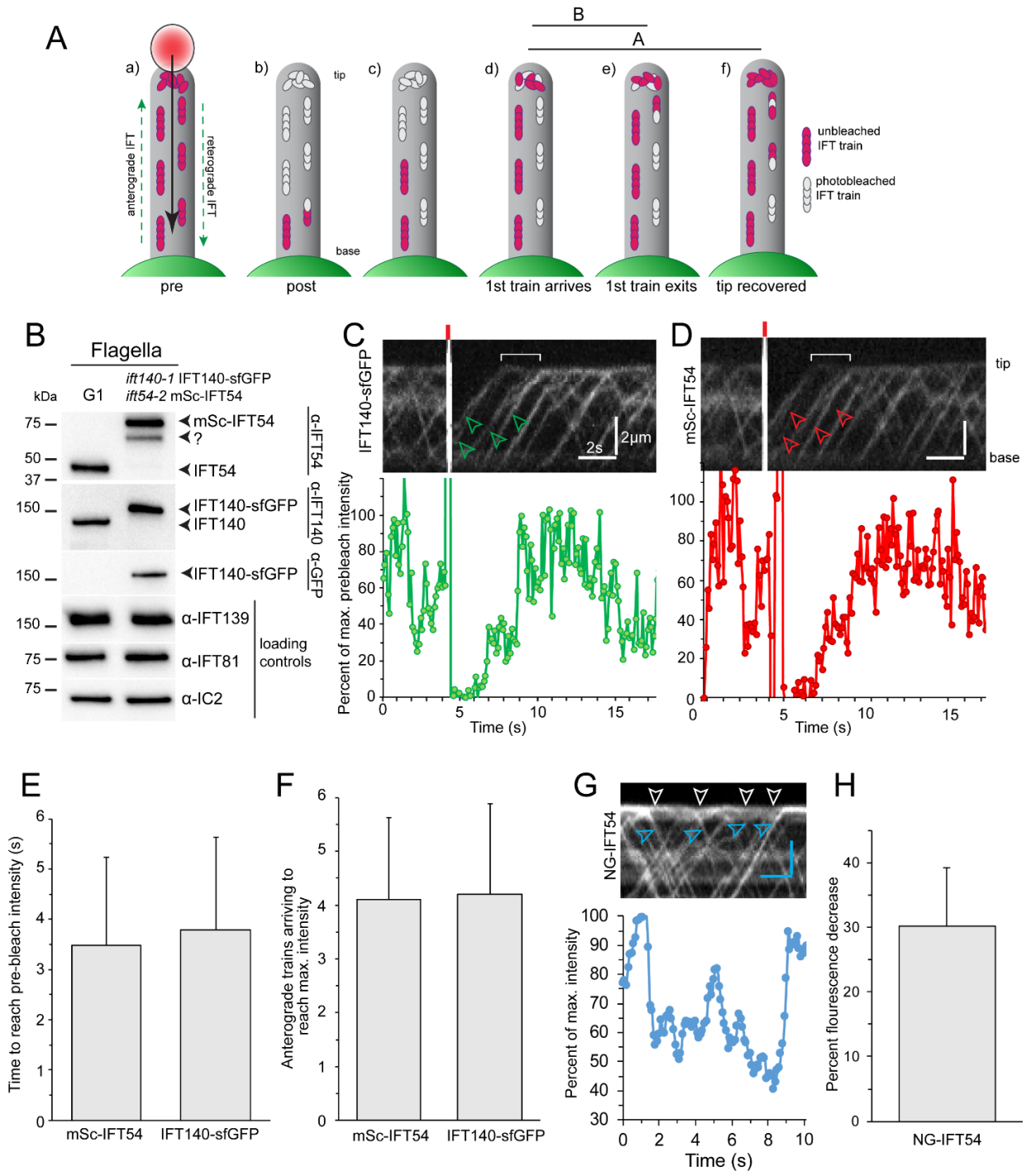

Figure 3.1. The size of the IFT protein pool at the tip is equivalent to approximately four anterograde trains.

A) Schematic of experimental technique. **a)** The bleaching laser was placed at the tip of the experimental flagellum and moved towards the base, photobleaching all trains in the flagellum

except those closest to the base. **b)** Florescent anterograde trains begin to enter the flagellum and fluorescent retrograde trains are exiting**. c)** Florescent anterograde trains continue to enter and photobleached retrograde trains exit. **d)** The first unbleached anterograde train arrives at the tip. **Line A:** how long it takes for the fluorescence intensity at the tip to recover; the number of trains it takes to replenish the pool can also be calculated during this time. This allows us to estimate the size of the IFT pool at the tip. **Line B:** the minimum tip dwell time for an anterograde train, i.e., time between arrival of the first unbleached anterograde train and the departure of the first unbleached retrograde train. This analysis was used in Figure 2. **e)** The first train containing unbleached material exits the tip on a retrograde train. **f)** The pool at the tip fully recovers florescence. **B)** Western blot of flagella from wild type (G1) and *ift140-1* IFT140-sfGFP *ift54-2* mSc-IFT54 flagella. ? band is most likely a degradation product of ble-mSc-IFT54. This strain was used for C-F. **C) top:** Kymograph of IFT140-sfGFP. Red bar= photobleaching step. White bracket=time to reach fluorescence recovery. Arrows mark anterograde trains contributing to fluorescence recovery. **bottom:** Quantitative analysis of the fluorescence intensity at the tip. bottom: Quantitative analysis of the fluorescence intensity at the tip. **D) top:** Kymograph of mSc-IFT54. Red bar=photobleaching step. White bracket=time to reach fluorescence recovery. Arrows mark anterograde trains contributing to fluorescence recovery. Scale bars correspond to 2µm, 2 sec. **bottom:** Quantitative analysis of the fluorescence intensity at the tip. **E)** Average time to reach full fluorescence recovery for IFT140-sfGFP and mSc-IFT54. **F)** Average number of anterograde trains arriving at the to reach full fluorescence recovery for IFT140-sfGFP and mSc-IFT54. **G) top:** Kymograph of a flagellum from *ift54-2* NG-IFT54. White arrows mark transient decreases in the fluorescence at the tip caused by retrograde trains exiting the tip (blue arrows). Scale bars correspond to 2µm, 2 sec. bottom: Quantitative analysis of the fluorescence

intensity at the tip. **H)** Average decrease in fluorescence at the tip caused by an exiting retrograde train for *ift54-2* NG-IFT54. Error bars indicate standard deviation.

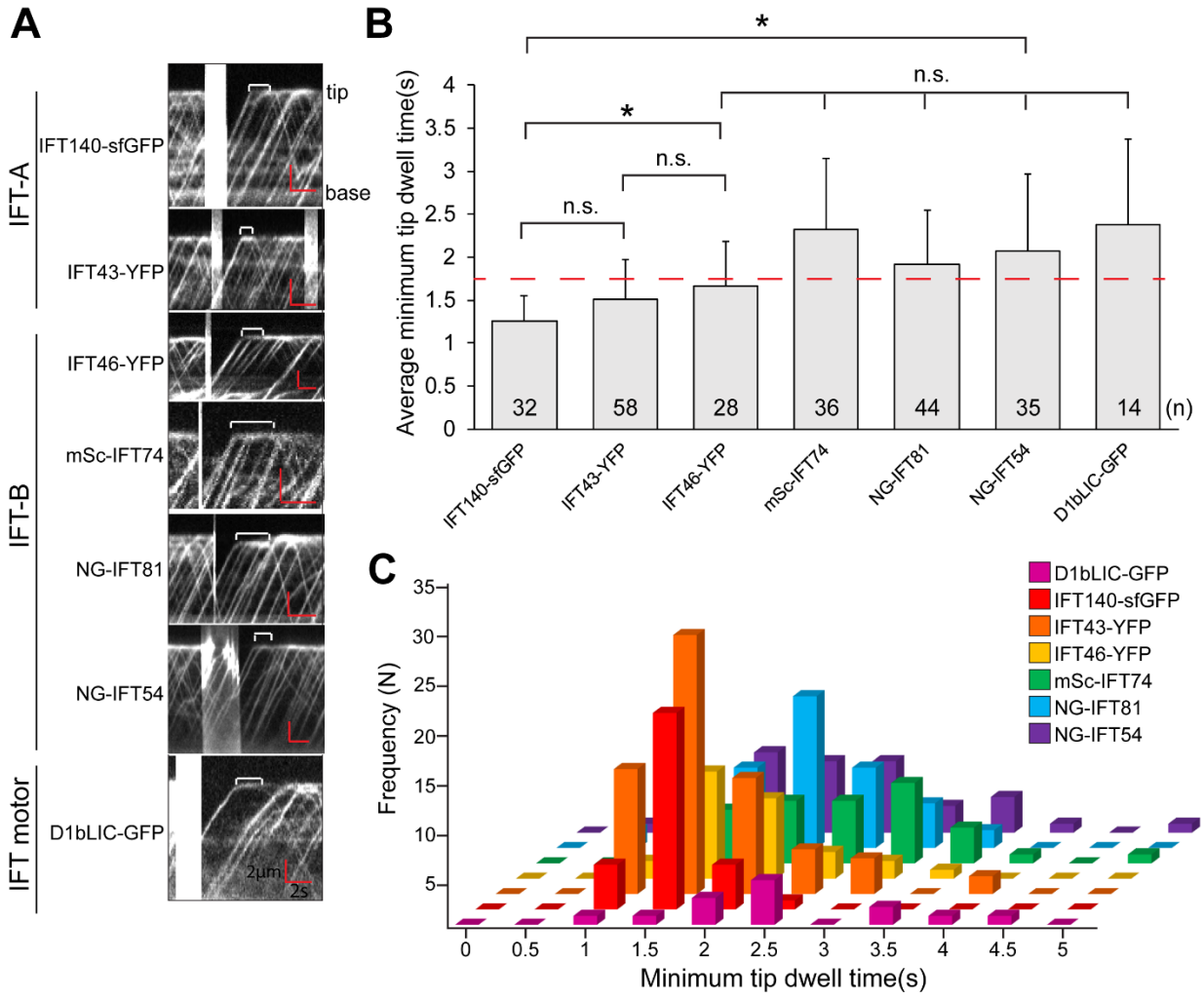

Figure 3.2. IFT-A, IFT-B, and IFT dynein proteins dwell for ~2 seconds at the ciliary tip. **A)** Gallery of kymographs from photobleaching experiment for each strain used in this study. For technique, see Figure 1A, line B. All tagged proteins were expressed in the corresponding mutant background and rescued the mutant phenotype, see Table 1. Red scale bars correspond to 2μm, 2sec. **B)** Average minimum tip dwell times for various tagged IFT proteins. Note that differences in the dwell times are likely to reflect differences between the strain and imaging conditions (i.e., temperature) rather than biologically significant differences between the IFT proteins. Red dotted line shows average dwell time of IFT at the tip (~1.87 sec). * p-value

<0.001. **C)** Distribution of minimum dwell times for the analyzed IFT proteins. Error bars represent standard deviation.

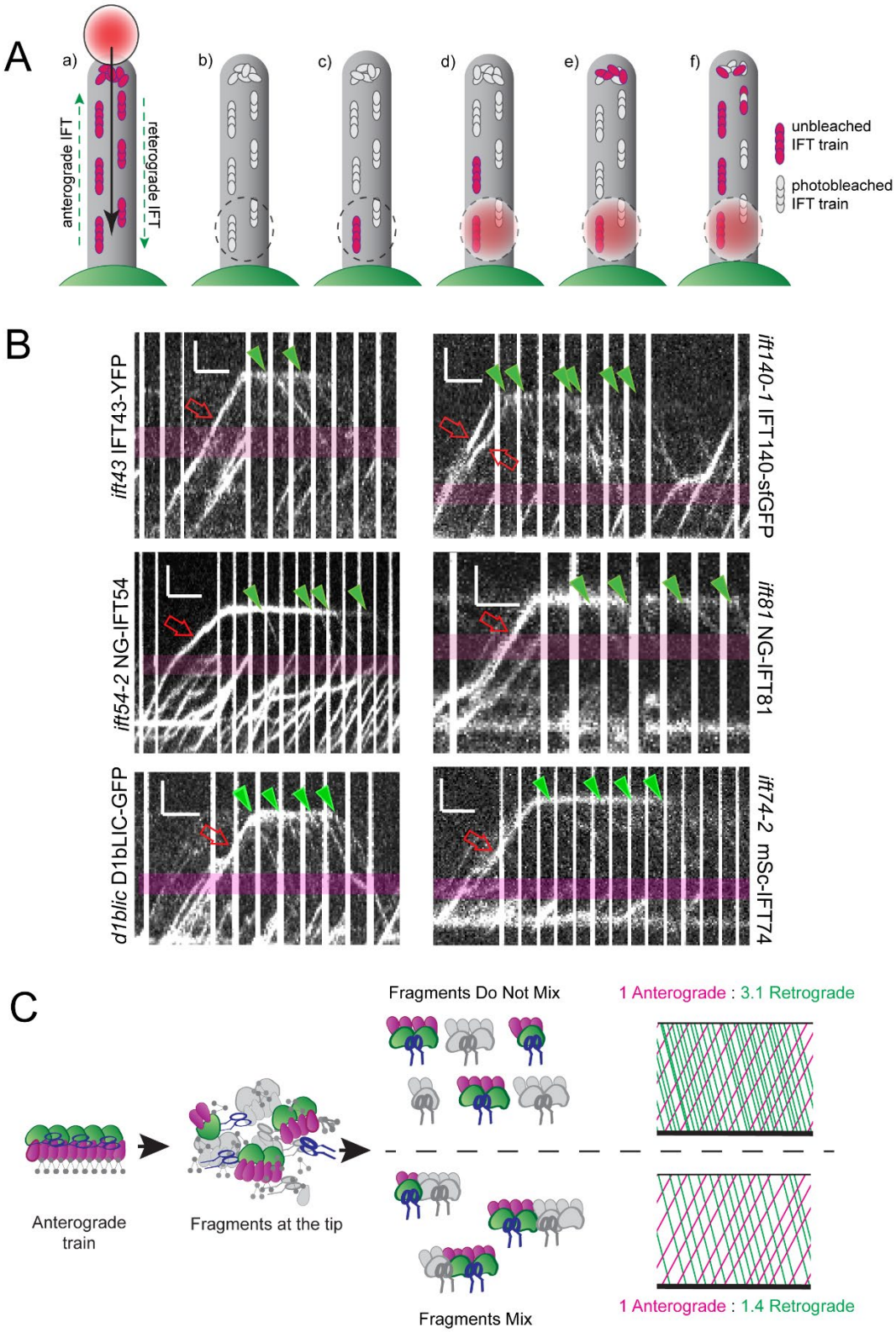

Figure 3.3. Fragmentation of individual IFT proteins at the tip.

A) Schematic of experimental technique [based off of Chien et al. 2017] **a)** The bleaching laser was placed at the tip of the experimental flagella and moved towards the base bleaching all tagged IFT proteins in the flagellum. **b)** The photobleaching laser was then positioned near the proximal end of the flagellum and blinked with 0.9 sec off and 0.1 sec on; this duty ratio bleaches all IFT trains entering the cilium. The position of the gating laser slightly varied between experiments and is designated by a magenta line in B. **c)** The bleaching laser was turned off to allow one unbleached train to enter the flagellum. In praxis, often more than one IFT train entered the cilium. **d)** The laser gate is closed again and the fate of the single unbleached train in the cilium is analyzed **(e-h)**. **B)** Gallery of kymographs of photobleaching experiment for the indicated strains. Red open arrows=anterograde trains. Green arrowheads=retrograde trains. Scale bars=2μm, 2sec. Sometimes multiple unbleached anterograde trains were let in at once. **C)** Model describing the interpretation of our results. Colored train material indicates florescent material. Grey train material corresponds to photobleached trains. On average, one anterograde train fragments into ~3.1 retrograde trains. If these train fragments undergo retrograde traffic as an autonomous unit then Chlamydomonas IFT would have a 1:3.1 anterograde track: retrograde track ratio. However, the established anterograde: retrograde ratio is 1:1.4, determined by both fluorescent imaging and DIC microscopy (Dentler, 2005; Iomini et al., 2001; Reck et al., 2016). These data indicate that retrograde trains are formed from multiple anterograde train fragments.

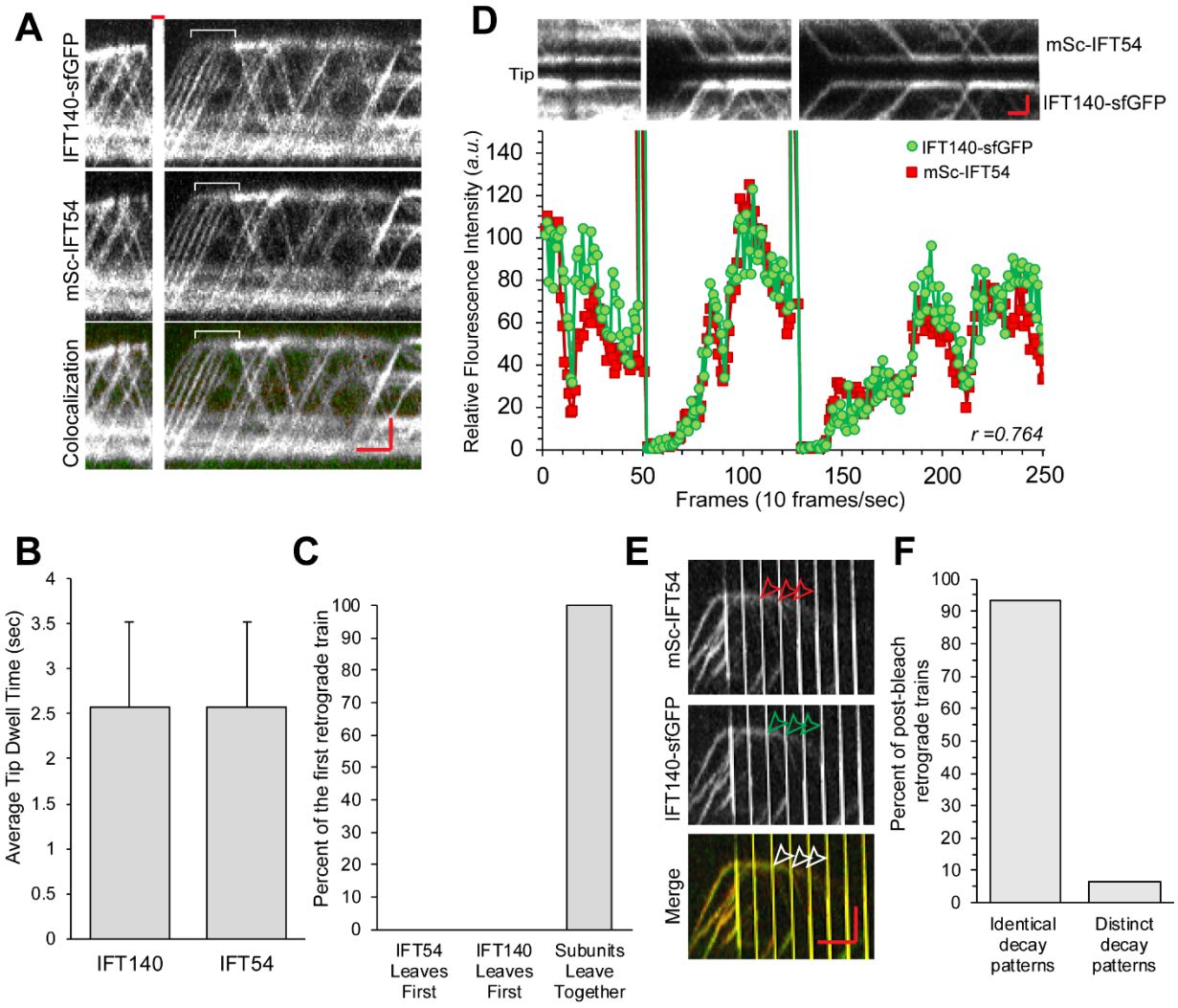

Figure 3.4. Analysis of an IFT-A IFT-B double tagged strain.

A) Kymograph from one flagellum of *ift140-1*IFT140-sfGFP *ift54-2* mSc-IFT54. White pixels in the colocalization represent where IFT140-sfGFP and mSc-IFT54 are above the Costes threshold. Brackets indicate minimum tip dwell time. Scale bars=2µm, 2sec. **B)** Quantification of the average tip dwell time and for IFT140 and IFT54. **C)** Quantification of how often IFT140 and IFT54 are seen in on the same first post-bleach retrograde train. **D)** top: Kymographs depicting the pool at the cilia tip and its recovery after photobleaching of mSc-IFT54 and IFT140-sfGFP; the mSc-IFT54 kymograph is displayed with the tip to the bottom to allow for an

easy comparison of signal strengths. Scale bars=1μm, 1sec. bottom: The relative florescence intensity of IFT140-sfGFP and mSc-IFT54 at the tip. Pearson correlation coefficient is 0.764 [*r* =1 means complete overlap *r* = 0 means no overlap] **E)** Kymographs from a laser gate experiment show that mSc-IFT54 and IFT140-sfGFP fragment together. Scale bars=2μm, 2sec. **F)** Quantification of the percentage of times mSc-IFT54 and IFT140-sfGFP had identical or distinct retrograde train decay patterns. Retrograde train decay patterns were determined by measuring the florescence intensity of retrograde trains from laser gate experiments. If the retrograde trains for IFT140-sfGFP and mSc-IFT54 had similar decay patterns; i.e. the first retrograde train was bright followed by dimmer 2nd and 3rd trains for both proteins IFT140 and IFT54, those post-bleach retrograde trains were classified as having identical decay patterns. If IFT140-sfGFP and mSc-IFT54 had different decay patterns they were classified as distinct.

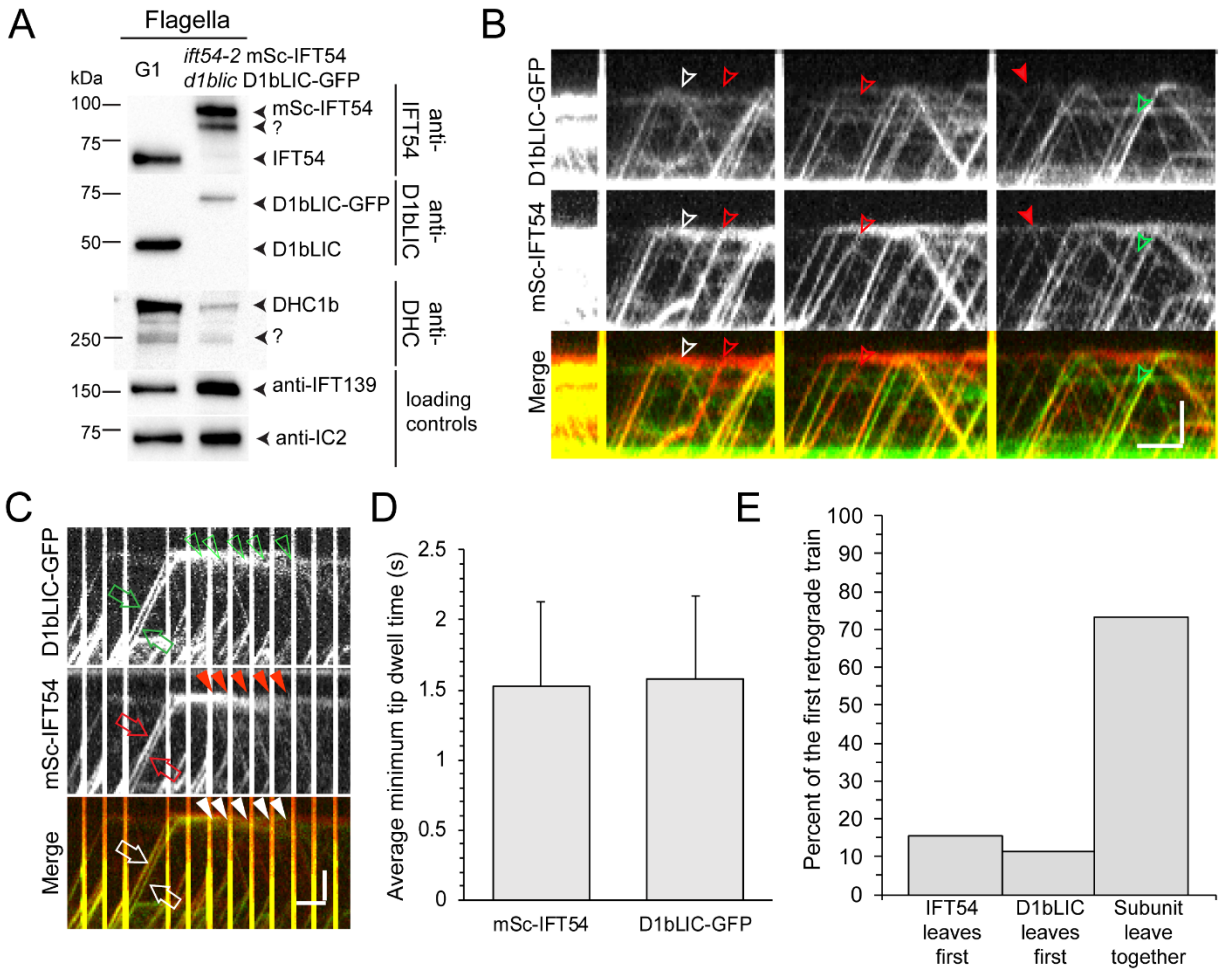

Figure 3.5. Analysis of an IFT-B and dynein double tagged strain.

A) Western blot of flagella from wild type (G1) and *d1blic* D1bLIC-GFP *ift54-2* mSc-IFT54 flagella. **B)** Kymograph obtained from the *d1blic* D1bLIC-GFP *ift54-2* mSc-IFT54 strain. After bleaching of the ciliary tip, retrograde trains lacking one of the two signals were observed occasionally (red filled arrowhead). However, in the vast majority of the experiments a separation between D1bLIC-GFP and mSc-IFT54 was not observed (white arrowhead points to one example of D1bLIC-GFP and mSc-IFT54 colocalizing on a retrograde train. Differences in the brightness and photo stability of mScarlet and GFP likely explain most of the observed apparent events of D1bLIC and IFT54 separation at the tip. D1bLIC-GFP is underrepresented or

absent from a subset of anterograde trains (red arrowheads). This is likely to result from the low expression level of D1bLIC-GFP (panel A). Scale bars=2µm, 2sec. **C)** Kymographs from a laser gate experiment show that both D1bLIC and IFT54 primarily fragment together. Open arrows=anterograde trains. Arrowheads=retrograde trains. Scale bars=2µm, 2sec. **D)** Quantification of the average tip dwell time and for D1bLIC and IFT54. **E)** The quantification of how often D1bLIC and IFT54 are seen in on the same retrograde train from laser gate experiments.

3.12 SUPPLEMENTARY FIGURES

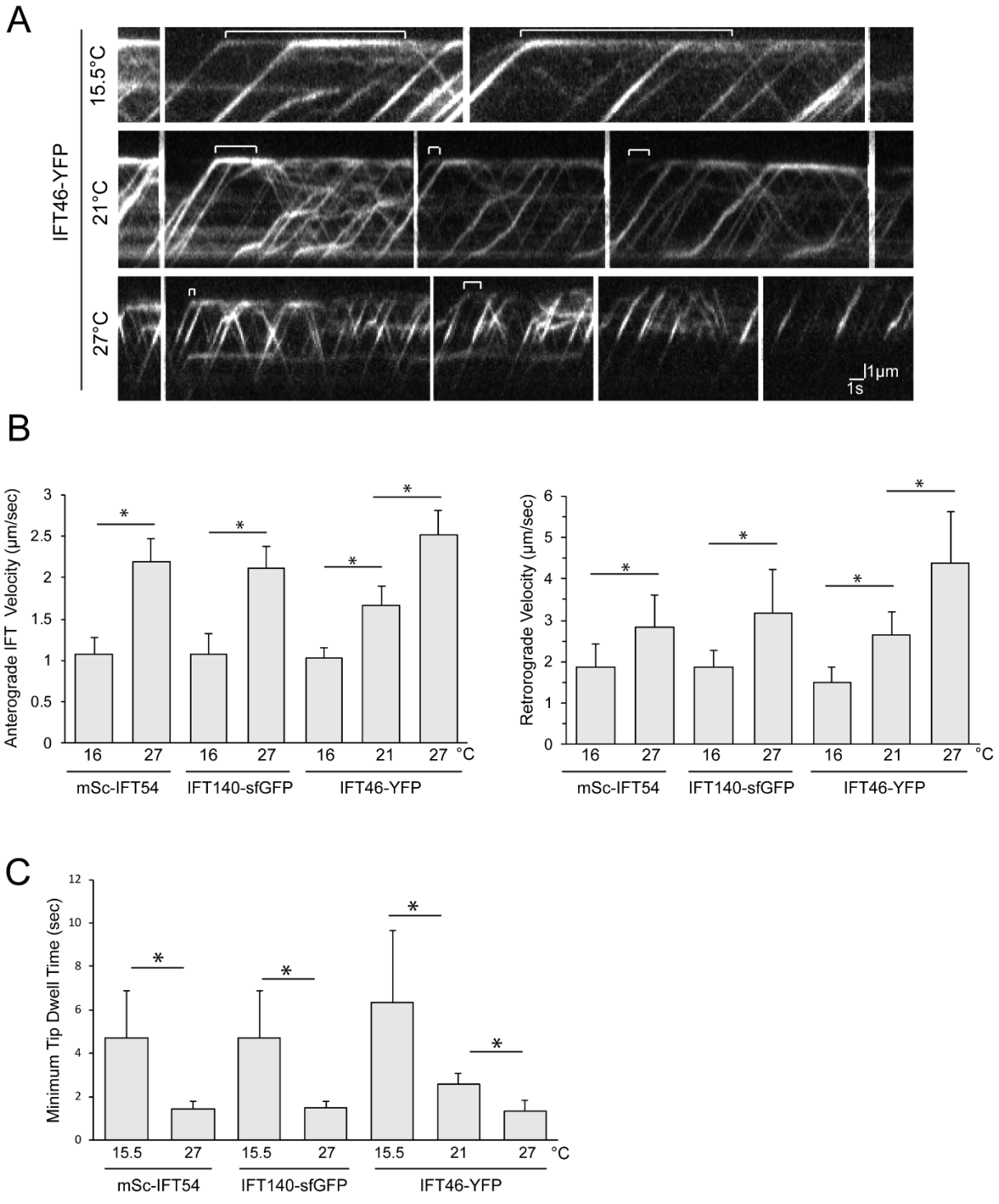

Figure 3.2-Figure Supplemental 1. Ambient temperature affects IFT velocity and minimum tip dwell time.

A) Representative kymographs of *ift46-1* IFT46-YFP taken at 15.5, 21, and 27 °C. White brackets indicate how the minimum tip dwell time was measured. **B)** The effect of temperature on anterograde and retrograde IFT velocities of mSc-IFT54, and IFT40-sfGFP imaged at 15.5 and 27 °C and IFT46-YFP imaged at 15.5, 21, and 27 °C. The established anterograde and retrograde velocities are ~2.0 μm/sec and ~3.5 μm/sec respectively (Dentler, 2005; Kozminski et al., 1995). **C)** The effect of temperature on the minimum tip dwell time of mS-IFT54 and IFT40-sfGFP imaged at 15.5 and 27 °C and IFT46-YFP imaged at 15.5, 21, and 27 °C. Error bars indicate standard deviation for B and C. * indicated a significant difference of <0.0001 or more.

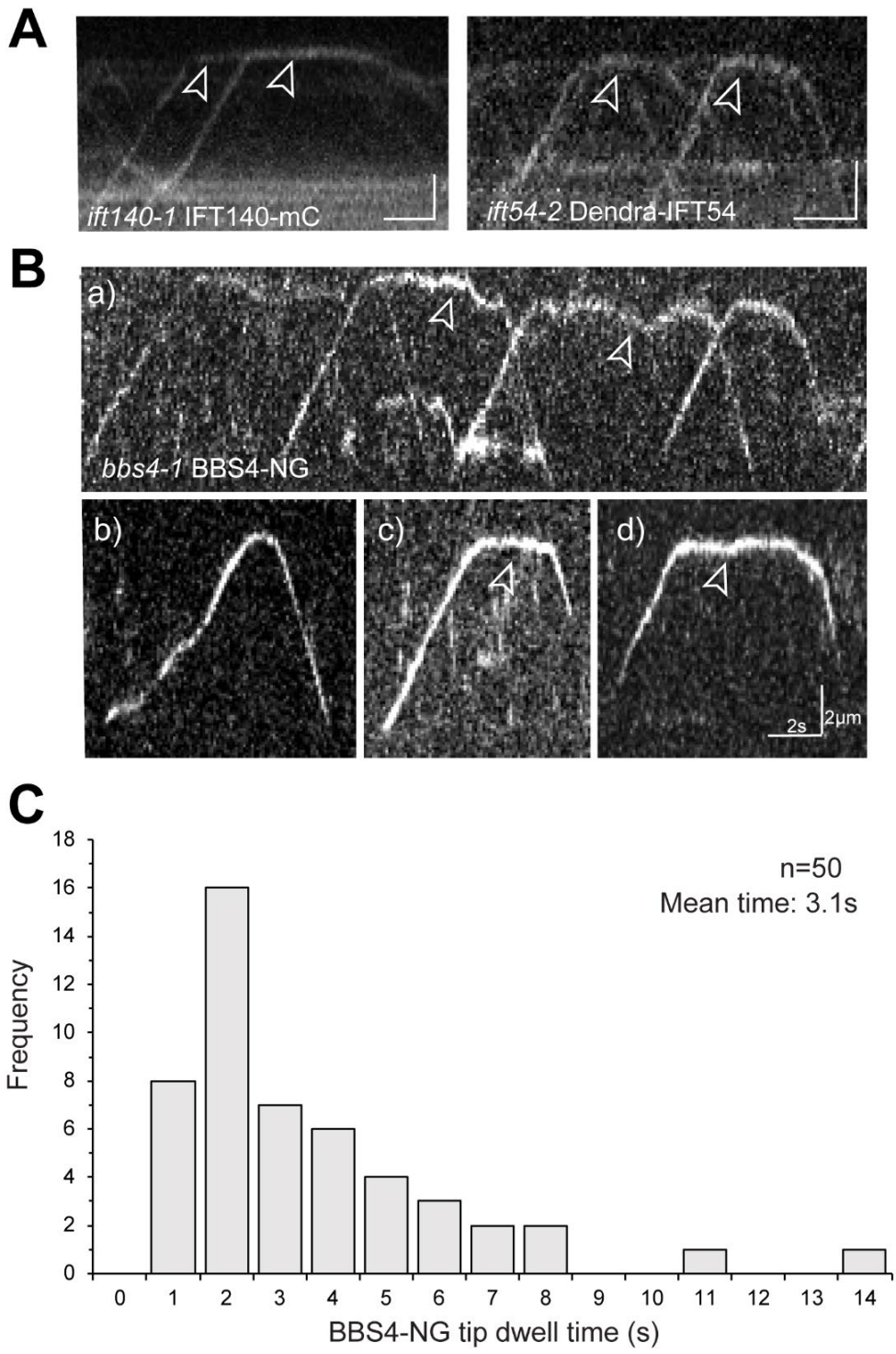

Figure 3.2-Figure Supplemental 2. BBSome dynamics at the tip.

A) Kymographs of single IFT particles at the tip for an IFT-A (IFT140) and an IFT-B (IFT54) protein showing stationary behavior at the ciliary tip. **B)** Kymographs characteristic of BBS4

behavior at the tip. White arrowheads point to shaky lines demonstrating diffusion. **a, c, d)** show instances of the BBSome pausing at the tip and diffusing before commencing retrograde traffic. Scale bar can be applied to all kymographs. **b)** A rare example of the BBSome catching a ride on a retrograde train almost as soon as it reaches the tip. **C)** The distribution of BBS4-NG dwell times at the flagella tip.

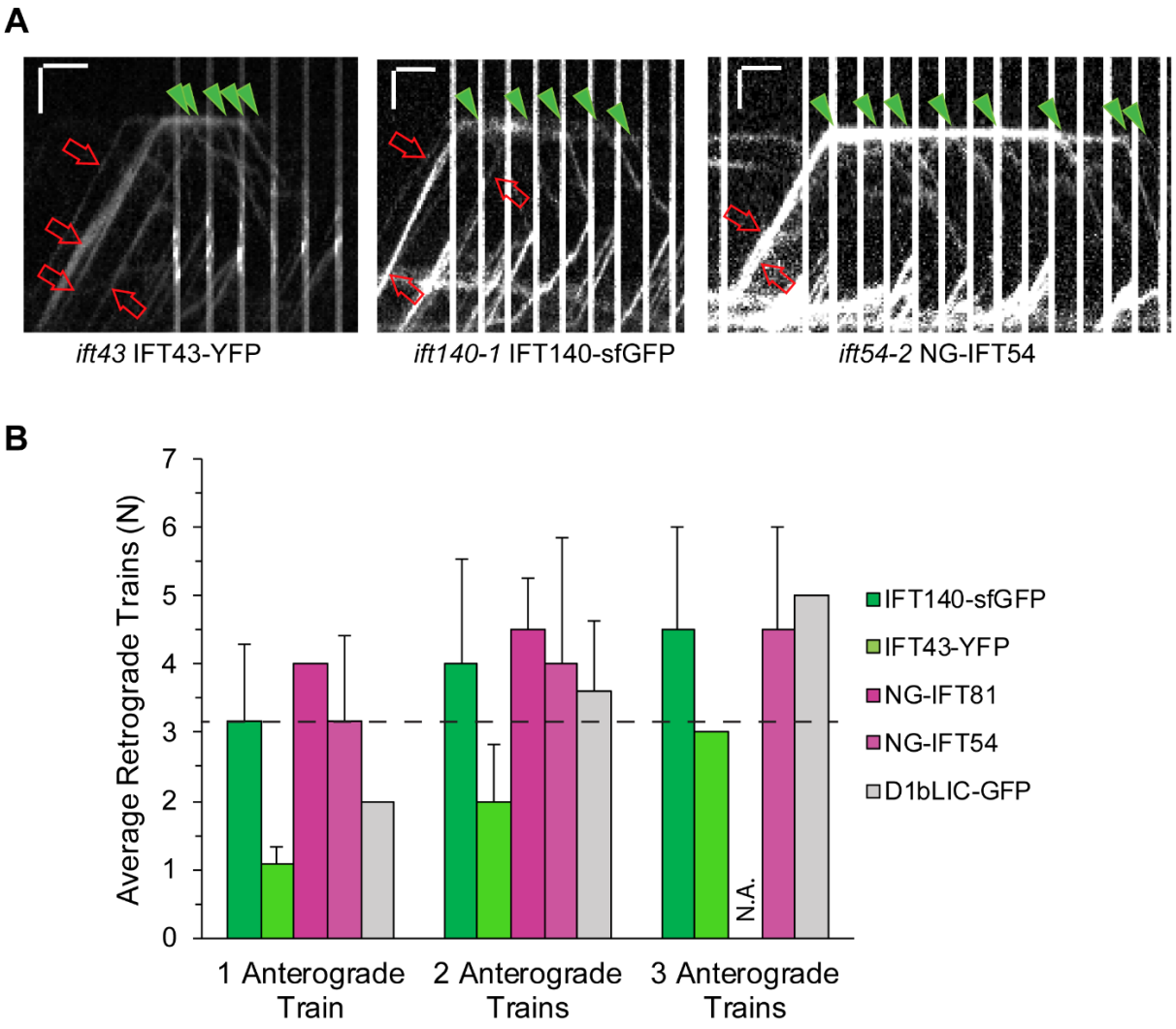

Figure 3.3-Figure Supplemental 1. Fragmentation of multiple anterograde trains at the tip.

A) Gallery of kymographs from two IFT-A proteins and one IFT-B proteins showing examples of multiple anterograde trains fragmenting into retrograde trains at the tip. Scale bars=2µm, 2sec.

B) Average number of retrograde trains derived from 1, 2 or 3 anterograde trains for the IFT proteins analyzed. The dotted line indicates the average number of retrograde trains formed by all protein (~3.1) . N.A. Indicates that that data was not collected.

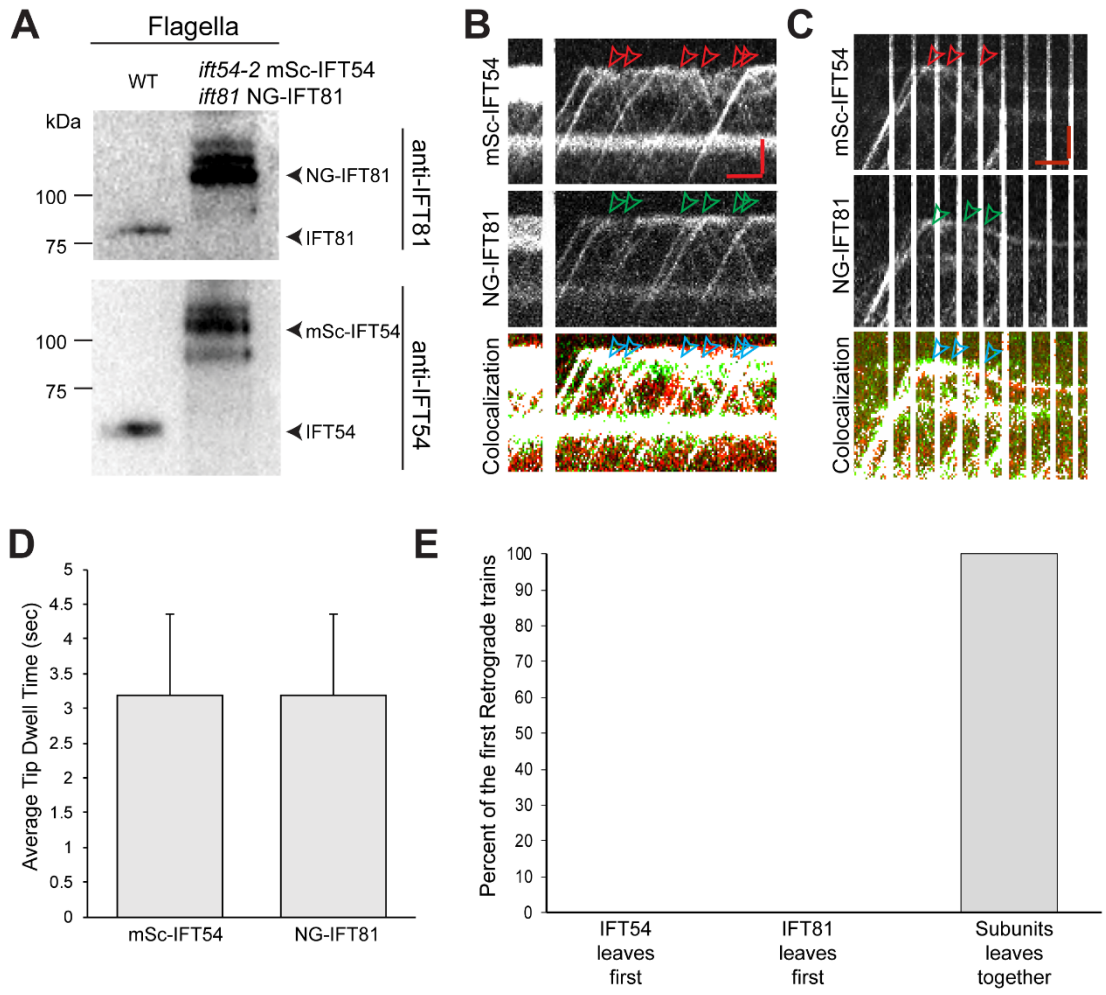

Figure 3.4-Figure Supplemental 1. IFT-B1 and IFT-B2 remain together during train remodeling.

A) Western blot of flagella from wildtype and *ift54-2* mSc-IFT54 *ift81* NG-IFT81 cells. **B)** Kymograph from one flagellum of *ift54-2* mSc-IFT54 *ift81* NG-IFT81 White pixels in the colocalization represent where mSc-IFT54 and NG-IFT81 are above the Costes threshold. Arrows mark retrograde trains departing from the tip. Scale bars=2µm, 2sec **C)** Kymographs from a laser gate experiment show that both IFT54 and IFT81 primarily fragment together. Arrowheads=retrograde trains. Scale bars=2µm, 2sec **D)** Quantification of the average tip dwell

time and for IFT54 and IFT81. **E)** The quantification of how often IFT54 and IFT81 are seen together on first post- bleach retrograde train.

3.13 METHODS

Strains and culture conditions

The IFT140-sfGFP, IFT43-YFP, IFT46-YFP, NG-IFT54, BBS4-(GFP and NG) and D1bLIC-GFP (CC-4488) strains were previously described; the corresponding strain numbers of the Chlamydomonas Resource Center (RRID:SCR_014960) are added in parenthesis when available (Lechtreck et al., 2009; Lv et al., 2017a; Picariello et al., 2014; Reck et al., 2016; Wingfield et al., 2017; Zhu et al., 2017a). The bald (lacking flagella) *ift140*-1 (CC-5490) and *ift46-1* (CC-4375), have been previously described and were rescued by expressing IFT140-sfGFP or IFT46-YFP, respectively (Hou et al., 2007; Lv et al., 2017b; Picariello et al., 2019b). The short flagella phenotype of *ift43* and *d1blic* (CC-4053) mutants have also been described previously and were rescued by expressing IFT43-YFP or D1bLIC-GFP respectively (Reck et al., 2016; Zhu et al., 2017a). The *bbs4-1* non-phototactic mutant was previously described and was rescued with BBS4-GFP or BBS4-NG (Lechtreck et al., 2009; Liu and Lechtreck, 2018). The bald *ift81-1* and *ift74-2* mutants have been previously described (Brown et al., 2015; Kubo et al., 2016b). *ift81-1* was rescued using a construct consisting of the aphVIII selectable marker gene and the genomic region of IFT81 fused at its N-terminus to NeonGreen codon-adapted for *C. reinhardtii*. *ift74-2* was rescued using a construct consisting of the aphVIII selectable marker gene and the genomic region of IFT74 fused at its N-terminus to mScarlet-I codon-adapted for *C. reinhardtii.* The *ift54-2* mutant lacked flagella and was obtained by insertional mutagenesis using the aph7" cassette in the Lechtreck Lab and was rescued using a construct consisting of the aphVIII(*ble*) selectable marker gene and the genomic region of IFT54 fused at its N-terminus to either mNeonGreen or mScarlet-I codon-adapted for *C. reinhardtii*. The tagged gene is and ble are separated by a 2A sequence which normally gets cleaved. Occasionally the 2A sequence will not

be cleaved, resulting in a portion if the tagged protein to appear heavier on a western blot. The *ift140-1* IFT140-sfGFP *ift54-2* mSc-IFT54 strain was obtained by mating the *ift140-1* IFT140-sfGFP and the *ift54-2* mSc-IFT54 strains. Motile progeny were analyzed by TIRF microcopy and the strains expressing IFT140-sfGFP and mSc-IFT54 were analyzed by Western blotting using antibodies to C. reinhardtii IFT140 (Picariello et al., 2019b) and IFT54 (Wingfield et al., in preparation). The *ift74-2* mSc-IFT74 *ift81-1* NG-IFT81 strain was obtained by mating the *ift74-2* mSc-IFT74 and the *ift81-1* NG-IFT81 strain. Motile progeny analyzed by TIRF microscopy and the strains expressing mSc-IFT74 and NG-IFT81 were analyzed by western blotting using antibodies to *C. reinhardtii* IFT74 (Qin et al., 2004a) and IFT81(Cole et al., 1998b). The *ift54-2* mSc-IFT54 *ift81-1* NG-IFT81 was generated by mating the *ift54-2* mSc-IFT54 and the *ift81-1* NG-IFT81 strain. Motile progeny analyzed by TIRF microscopy and the strains expressing mSc-IFT54 and NG-IFT81 were analyzed by western blotting using antibodies to *C. reinhardtii* IFT54 (Wingfield et al., in preparation) and IFT81(Cole et al., 1998b) The *d1blic* D1bLIC-GFP *ift54-2* mSc-IFT54 strain was obtained by mating the *d1blic* D1bLIC-GFP and the *ift54-2* mSc-IFT54 strains. Motile progeny were analyzed by TIRF microcopy and the strains expressing D1bLIC-GFP and mSc-IFT54 were analyzed by Western blotting using antibodies to *C. reinhardtii* D1bLIC (Perrone et al., 2003) and IFT54 (Wingfield et al., in preparation).

TIRF microscopy

For TIRF imaging, we used Eclipse Ti-U microscope (Nikon) equipped with 60× NA1.49 TIRF objective and through-the-objective TIRF illumination provided by a 40-mW 488-nm and a 75-mW 561-nm diode laser (Spectraphysics) as previously described (Lechtreck, 2013). The excitation lasers were cleaned up with a Nikon GFP/mCherry TIRF filter and the emission was

separated using an Image Splitting Device (Photometrics DualView2 with filter cube 11-EM). Images were mostly recorded at 10 fps using an iXON3 (Andor) and the NIS-Elements Advanced Research software (Nikon); μManager (https://micro-manager.org/) was used to record some FLIP experiments.

To obtain a focused laser beam, the 488-nm laser beam was split using a 488nm zero-order half-wave plate and a broad band polarized beam splitter; one of the beams was used for TIRF illumination. The other beam was expanded using a 3x beam expander, focused using 200 mm plano-convex lens and a 35 mm plano-convex lens and recombined with the TIRF laser beam using polarized beam splitter (all parts from Thorlabs Inc.). A motorized mirror connected to a joystick (Newfocus) was used to move the bleaching laser and the size of the laser spot was altered manually by moving the 35-mm lens. For PhotoGate experiments, the shutter and shutter driver (Uniblitz) for the bleaching laser were controlled via an Arduino Uno device and a custom-written macro for μ-Manager (see Supplementary methods). The PhotoGate experiments were recorded using either μ-Manger, which allowed us to prevent the acquisition of frames while the shutter was open or Nikon Elements; in the latter, the camera continued to record while the bleaching laser shutter was open resulting in over-exposed frames. FIJI (National Institutes of Health) was used to generate kymograms and quantify signals. Excel was used for statistical analysis. Adobe Photoshop was used to adjust image contrast and brightness, and figures were prepared in Adobe Illustrator.

Observation chambers for *C. reinhardtii* were constructed by applying a ring of vacuum grease or petroleum jelly to a 24 x 60 mm No. 1.5 coverslip; 10 μl of cell suspension were applied and allowed to settle for ~1 minute. Then, the chamber was closed by inverting a 22 × 22

mm no. 1.5 cover glass with ~5-10 µl of 5 mM HEPES, pH 7.3, 5 mM EGTA onto the larger coverslip. Cells were imaged through the large cover glass at room temperature.

FRAP analysis of the tip pool and IFT traffic

For FRAP analysis of the IFT bb-pool, kymograms were generated from videos showing the cells before, during and after the application of a brief laser pulse to bleach the experimental basal body. Grayscale profiles were plotted along lines covering the basal body signals, the data were converted to an Excel sheet, and the fluorescence of the experimental basal body was calculated in % of the intensity of the control basal body in a frame-by-frame manner. The recovery time and intensity were determined manually as shown in Fig. 1 Supplemental 2. For the gap analysis, a fiduciary mark on the monitor was used to position the cell so that one basal body was targeted by the laser spot; the focus level was adjusted to the level of the flagella, the recording was started, and a laser pulse of <100 ms to ~600 ms was applied. Cells which moved prior to the bleaching step or which did not resume regular IFT traffic after the bleaching step were ignored.

To analyze the signal intensity of IFT trains, a line partially covering the trajectory was placed on kymograms in ImageJ and the grey value was obtained.

3.14 REFERENCES

Brown, J.M., D.A. Cochran, B. Craige, T. Kubo, and G.B. Witman. 2015. Assembly of IFT trains at the ciliary base depends on IFT74. *Current biology : CB*. 25:1583-1593.

Buisson, J., N. Chenouard, T. Lagache, T. Blisnick, J.C. Olivo-Marin, and P. Bastin. 2012. Intraflagellar transport proteins cycle between the flagellum and its base. *J Cell Sci*.

Chien, A., S.M. Shih, R. Bower, D. Tritschler, M.E. Porter, and A. Yildiz. 2017. Dynamics of the IFT machinery at the ciliary tip. *eLife*. 6:e28606.

Cole, D.G., D.R. Diener, A.L. Himelblau, P.L. Beech, J.C. Fuster, and J.L. Rosenbaum. 1998. Chlamydomonas Kinesin-II–dependent Intraflagellar Transport (IFT): IFT Particles Contain Proteins Required for Ciliary Assembly in Caenorhabditis elegans Sensory Neurons. *The Journal of cell biology*. 141:993-1008.

Cole, D.G., and W.J. Snell. 2009. SnapShot: Intraflagellar transport. *Cell*. 137:784-784.e781.

Craft, J.M., J.A. Harris, S. Hyman, P. Kner, and K.F. Lechtreck. 2015. Tubulin transport by IFT is upregulated during ciliary growth by a cilium-autonomous mechanism. *The Journal of cell biology*. 208:223.

Dawson, S.C., and S.A. House. 2010. Life with eight flagella: flagellar assembly and division in Giardia. *Curr Opin Microbiol*. 13:480-490.

Dentler, W. 2005. Intraflagellar transport (IFT) during assembly and disassembly of Chlamydomonas flagella. *The Journal of cell biology*. 170:649-659.

Hirano, T., Y. Katoh, and K. Nakayama. 2017. Intraflagellar transport-A complex mediates ciliary entry and retrograde trafficking of ciliary G protein-coupled receptors. *Mol Biol Cell*. 28:429-439.

Hou, Y., H. Qin, J.A. Follit, G.J. Pazour, J.L. Rosenbaum, and G.B. Witman. 2007. Functional analysis of an individual IFT protein: IFT46 is required for transport of outer dynein arms into flagella. *J Cell Biol*. 176:653-665.

Hunter, E.L., K. Lechtreck, G. Fu, J. Hwang, H. Lin, A. Gokhale, L.M. Alford, B. Lewis, R. Yamamoto, R. Kamiya, F. Yang, D. Nicastro, S.K. Dutcher, M. Wirschell, and W.S. Sale. 2018. The IDA3 adapter, required for intraflagellar transport of I1 dynein, is regulated by ciliary length. *Mol Biol Cell*. 29:886-896.

Iomini, C., V. Babaev-Khaimov, M. Sassaroli, and G. Piperno. 2001. Protein particles in Chlamydomonas flagella undergo a transport cycle consisting of four phases. *The Journal of cell biology*. 153:13-24.

Ishikawa, H., and W.F. Marshall. 2011. Ciliogenesis: building the cell's antenna. *Nature Reviews Molecular Cell Biology*. 12:222-234.

Jordan, M.A., D.R. Diener, L. Stepanek, and G. Pigino. 2018. The cryo-EM structure of intraflagellar transport trains reveals how dynein is inactivated to ensure unidirectional anterograde movement in cilia. *Nat Cell Biol*. 20:1250-1255.

Kozminski, K.G., P.L. Beech, and J.L. Rosenbaum. 1995. The Chlamydomonas kinesin-like protein FLA10 is involved in motility associated with the flagellar membrane. *The Journal of cell biology*. 131:1517-1527.

Kubo, T., J.M. Brown, K. Bellve, B. Craige, J.M. Craft, K. Fogarty, K.F. Lechtreck, and G.B. Witman. 2016. Together, the IFT81 and IFT74 N-termini form the main module for intraflagellar transport of tubulin. *Journal of cell science*. 129:2106-2119.

Lechtreck, K.F., E.C. Johnson, T. Sakai, D. Cochran, B.A. Ballif, J. Rush, G.J. Pazour, M. Ikebe, and G.B. Witman. 2009. The Chlamydomonas reinhardtii BBSome is an IFT cargo

required for export of specific signaling proteins from flagella. *The Journal of cell biology*. 187:1117-1132.
Liang, Y., Y. Pang, Q. Wu, Z. Hu, X. Han, Y. Xu, H. Deng, and J. Pan. 2014. FLA8/KIF3B Phosphorylation Regulates Kinesin-II Interaction with IFT-B to Control IFT Entry and Turnaround. *Developmental Cell*. 30:585-597.
Liu, P., and K.F. Lechtreck. 2018. The Bardet-Biedl syndrome protein complex is an adapter expanding the cargo range of intraflagellar transport trains for ciliary export. *Proceedings of the National Academy of Sciences of the United States of America*. 115:E934-e943.
Lv, B., L. Wan, M. Taschner, X. Cheng, E. Lorentzen, and K. Huang. 2017. Intraflagellar transport protein IFT52 recruits IFT46 to the basal body and flagella. *Journal of cell science*. 130:1662-1674.
Mijalkovic, J., J. van Krugten, F. Oswald, S. Acar, and E.J.G. Peterman. 2018. Single-Molecule Turnarounds of Intraflagellar Transport at the C. elegans Ciliary Tip. *Cell Rep*. 25:1701-1707.e1702.
Morga, B., and P. Bastin. 2013. Getting to the heart of intraflagellar transport using Trypanosoma and Chlamydomonas models: the strength is in their differences. *Cilia*. 2:16.
Nakayama, K., and Y. Katoh. 2018. Ciliary protein trafficking mediated by IFT and BBSome complexes with the aid of kinesin-2 and dynein-2 motors. *J Biochem*. 163:155-164.
Pedersen, L.B., S. Geimer, and J.L. Rosenbaum. 2006. Dissecting the Molecular Mechanisms of Intraflagellar Transport in Chlamydomonas. *Current Biology*. 16:450-459.
Perrone, C.A., D. Tritschler, P. Taulman, R. Bower, B.K. Yoder, and M.E. Porter. 2003. A Novel Dynein Light Intermediate Chain Colocalizes with the Retrograde Motor for Intraflagellar Transport at Sites of Axoneme Assembly in Chlamydomonas and Mammalian Cells. *Mol Biol Cell*. 14:2041-2056.
Picariello, T., J.M. Brown, Y. Hou, G. Swank, D.A. Cochran, O.D. King, K. Lechtreck, G.J. Pazour, and G.B. Witman. 2019a. A global analysis of IFT-A function reveals specialization for transport of membrane-associated proteins into cilia. *Journal of cell science*. 132:jcs220749.
Picariello, T., J.M. Brown, Y. Hou, G. Swank, D.A. Cochran, O.D. King, K. Lechtreck, G.J. Pazour, and G.B. Witman. 2019b. A global analysis of IFT-A function reveals specialization for transport of membrane-associated proteins into cilia. *Journal of cell science*. 132.
Picariello, T., M.S. Valentine, J. Yano, and J. Van Houten. 2014. Reduction of meckelin leads to general loss of cilia, ciliary microtubule misalignment and distorted cell surface organization. *Cilia*. 3:2.
Qin, H., D.R. Diener, S. Geimer, D.G. Cole, and J.L. Rosenbaum. 2004. Intraflagellar transport (IFT) cargo: IFT transports flagellar precursors to the tip and turnover products to the cell body. *The Journal of cell biology*. 164:255-266.
Qin, H., Z. Wang, D. Diener, and J. Rosenbaum. 2007. Intraflagellar transport protein 27 is a small G protein involved in cell-cycle control. *Current biology : CB*. 17:193-202.
Reck, J., A.M. Schauer, K. VanderWaal Mills, R. Bower, D. Tritschler, C.A. Perrone, and M.E. Porter. 2016. The role of the dynein light intermediate chain in retrograde IFT and flagellar function in Chlamydomonas. *Mol Biol Cell*. 27:2404-2422.
Soares, H., B. Carmona, S. Nolasco, L. Viseu Melo, and J. Goncalves. 2019. Cilia Distal Domain: Diversity in Evolutionarily Conserved Structures. *Cells*. 8.

Taschner, M., and E. Lorentzen. 2016. The Intraflagellar Transport Machinery. *Cold Spring Harb Perspect Biol*. 8.

Toropova, K., R. Zalyte, A.G. Mukhopadhyay, M. Mladenov, A.P. Carter, and A.J. Roberts. 2019. Structure of the dynein-2 complex and its assembly with intraflagellar transport trains. *Nature Structural & Molecular Biology*. 26:823-829.

Waters, A.M., and P.L. Beales. 2011. Ciliopathies: an expanding disease spectrum. *Pediatric nephrology (Berlin, Germany)*. 26:1039-1056.

Wingfield, J.L., I. Mengoni, H. Bomberger, Y.Y. Jiang, J.D. Walsh, J.M. Brown, T. Picariello, D.A. Cochran, B. Zhu, J. Pan, J. Eggenschwiler, J. Gaertig, G.B. Witman, P. Kner, and K. Lechtreck. 2017. IFT trains in different stages of assembly queue at the ciliary base for consecutive release into the cilium. *Elife*. 6.

Wren, K.N., J.M. Craft, D. Tritschler, A. Schauer, D.K. Patel, E.F. Smith, M.E. Porter, P. Kner, and K.F. Lechtreck. 2013. A differential cargo-loading model of ciliary length regulation by IFT. *Current biology : CB*. 23:2463-2471.

Zhu, B., X. Zhu, L. Wang, Y. Liang, Q. Feng, and J. Pan. 2017. Functional exploration of the IFT-A complex in intraflagellar transport and ciliogenesis. *PLoS genetics*. 13:e1006627-e1006627.

CHAPTER 4

CHLAMYDOMONAS IFT54 PARTICIPATES IN CILIARY TUBULIN TRANSPORT[3]

[3] Wingfield, J.L., I. Mengoni, A. Christensen, T. Kubo, G. Witman, E. Lorentzen and K. Lechtreck. To be submitted to *Cytoskeleton*.

4.1 ABSTRACT

Intraflagellar transport (IFT) shuttles tubulin, the major structural protein of cilia and flagella, from the cell body into cilia to promote elongation. The IFT proteins, IFT81 and IFT74, form the main tubulin-binding module: IFT81 binds the dimer via its calponin homology (CH) domain and the basic N-terminal domain of IFT74 interacts with the acidic C-terminus of β-tubulin. The CH domain of IFT54 also binds microtubules and tubulin in vitro, raising the question of whether it contributes to ciliary tubulin transport (Taschner et al., 2016a). Here, we generated and novel IFT54 mutant, *ift54-2*, which lack cilia. *ift54-2* is fully rescued by a CH-deficient IFT54 (ΔCH-IFT54), confirming the finding of Zhu et al. (2017c) that this domain is dispensable for ciliogenesis in *Chlamydomonas*. However, when CH-less IFT54 is combined with either the incapacitated CH-domain of IFT81 (IFT81-5E) or the deletion of the head domain of IFT74 (ΔN-IFT74), the moderate ciliogenesis defects of the respective single mutants are intensified with many cells failing to assemble cilia. Thus, impairing the tubulin-binding capacity in any two of the three tubulin-binding domains of IFT54/74/81 results in a more severe ciliogenesis phenotype. To understand the underlying mechanism, we focused on the role of the IFT54/81 CH domains, which likely confer specificity for the binding of tubulin. In the remaining cilia of the *ift54-2* ΔCH-IFT54 *ift81-1* CH5E-IFT81 double mutant, IFT appeared normal while the frequency of tubulin transport was reduced. Further, an IFT81 construct carrying the CH domain of IFT54 instead of its own attenuated the short cilia phenotype of a novel *ift81* ΔCH-IFT81 mutant strain indicating that both CH domains perform a similar role in IFT and ciliary assembly. Together, our observations suggest that the CH-domain of IFT54 participates in ciliary tubulin transport.

4.2 INTRODUCTION

Cilia are microtubule-based organelles with motile and sensory functions. Ciliary assembly involves intraflagellar transport (IFT), a bidirectional motor protein-driven motility of IFT protein carriers (IFT trains) along the axonemal microtubules. One of the predominant cargoes of IFT is tubulin, the main structural protein of cilia and flagella (Craft et al., 2015a). In *Chlamydomonas reinhardtii,* ~350,000 tubulin dimers need to be moved from the cell body, their synthesis site, to the tip of a growing cilium to build a 12-μm long axoneme in ~60 minutes (Bhogaraju et al., 2014; Kubo et al., 2016b). Tubulin dimers apparently bind directly to the IFT trains by interacting with IFT81 and IFT74, which are part of the 10-subunits IFT-B1 subcomplex within the 16-subunits IFT-B particle. In detail, IFT81 binds the globular interface of the tubulin dimer via its N-terminal calponin homology (CH) domain, and IFT74 binds the acidic E-hook of β-tubulin via basic residues in its N-terminal head (Bhogaraju et al., 2013). Overexpression of truncated IFT81 lacking its CH domain negatively affected ciliogenesis in RPE cells; and expression of CH5E-IFT81, in which five lysines in the CH domain critical for tubulin-binding were altered to glutamates, failed to rescue the reduction in the percent of ciliated cells caused by IFT81 knock-down (Bhogaraju et al., 2013).

The availability of *ift74* and *ift81* null mutants in *Chlamydomonas* allowed for a more detailed analysis of their tubulin-binding domains and their role in cilia formation. While single mutants, lacking either the N-terminal domain of IFT74 (*ift74-2* ΔN-IFT74) or expressing the incapacitated/altered CH5E-IFT81 (*ift81-1* CH5E-IFT81) assemble almost full-length cilia, albeit, at a reduced speed, the *ift74-2* ΔN-IFT74 *ift81-1* CH5E-IFT81 double mutant lacks cilia but for short stumps (Kubo et al., 2016). The data suggest that the head domains of IFT81/74 together form the major tubulin-binding site of IFT in *Chlamydomonas*. However, apparent

homologues of *IFT81* or *IFT74* are absent from the genomes of *Drosophila* and several other organisms (Cole and Snell, 2009; Kobayashi et al., 2007; van Dam et al., 2013). Further, *in vitro* experiments with the N-terminal domains, show that IFT81N and IFT74N alone bind tubulin only weakly (i.e., 16μM K_d for IFT81 compared to 0.9μM K_d for the IFT81/74N module) (Bhogaraju et al., 2013). Thus, it is unclear how the CH5E-IFT81 and ΔN-IFT74 single mutants ensure tubulin transport sufficient to form flagella of near wild-type length. Similarly, *C. elegans ift-81* and *ift-74* loss-of-function mutants exhibit only weak anomalies in the formation of sensory cilia (Kobayashi et al., 2007). These data raise the question of whether other IFT proteins contribute to ciliary tubulin transport. Indeed, several other IFT-B proteins possess CH domains, but only that of IFT54 binds tubulin dimers and microtubules *in vitro* with a K_d of 3μM (Taschner et al., 2016c). However, Zhu and colleagues restored cilia formation in the *Chlamydomonas ift54-1* insertional mutant, which expresses only traces of the endogenous protein, by expressing a truncated IFT54 lacking its CH domain suggesting that the CH domain of IFT54 is dispensable for ciliogenesis in *Chlamydomonas* (Zhu et al., 2017c). Here, we rescued the flagella-less phenotype of a novel *ift54*-2 mutant using CH-deficient IFT54 (*ift54-2* ΔCH-IFT54) confirming that lack of this domain alone does not interfere with the assembly of full-length cilia. However, ciliogenesis was severely affected when the absence of the CH domain of IFT54 is combined with either the ΔN-IFT74 or CH5E-IFT81 mutation. The *ift54-2* ΔCH-IFT54 *ift74-2* ΔN-IFT74 and *ift54-2* ΔCH-IFT54 *ift81-1* CH5E-IFT81 double mutant strains showed normal IFT and reduced tubulin transport suggesting that the defects in ciliogenesis could result from a reduction in tubulin delivery rather than a general impairment of IFT. We conclude that the CH domain of IFT54 participates in tubulin transport by IFT in *Chlamydomonas*. We propose a partially redundant tripartite tubulin-binding site consisting of the CH domains of

IFT54 and IFT81 and the head domain of IFT74, in which any two of the three sites are sufficient to allow normal or near-normal cilia formation.

RESULTS

4.3 The CH-domain of IFT54 is not required for flagella assembly.

An insertional mutagenesis screen for *Chlamydomonas* motility mutants identified *ift54-2*, a novel mutant in the *IFT54* gene (Fig. 4.1A). Sequencing of the DNA flanking the insertion site revealed that the *aph7"* cassette was integrated at the beginning of exon 8 of *IFT54*, causing an infame sop codon after two codons. The mutated *ift54-2* gene is predicted to encode a protein of ~33 kD lacking the C-terminal coiled-coil (CC) of IFT54 (IFT54ΔCC), which is necessary for its interaction with IFT20 and incorporation into IFT particles (Figs. 4.1A, 4.2-figure supplemental 1A) (Taschner et al. EMBO)(Zhu et al., 2017c). To determine if *ift54-2* expresses a truncated IFT54, we raised a polyclonal antibody against IFT54$^{1-346}$. In control cells, the antibody recognized a band of ~57kD in Western blots, which represents IFT54 (Fig. 4.1 B). In immunofluorescence, the antibody stained the ciliary base as it is typical for IFT proteins (Fig. 4.1C). In the *ift54-2* cells, anti-IFT54 labeled a band of ~34kD, indicating that the mutant indeed expresses a truncated IFT54 protein; we refer to this protein as IFT54ΔCC (Fig. 1B). However, anti-IFT54 failed to stain the basal body region in *ift54-2* (Fig. 4.1C). Also, *ift54-2* cells lacked flagella and grew palmelloid, i.e., several cells together remaining encapsulated in the mother cell wall, as previously described for the *ift54-1* mutant (Zhu et al., 2017c) (Fig. 4.1D). We conclude that the *ift54-2* mutant expresses a dysfunctional protein, which is unable to support ciliary assembly.

To express IFT54, we amplified the coding region of the IFT54 gene from genomic DNA and cloned it into a derivative of the expression vector pBR25 (Rasala et al., 2013a). This vector contains a self-cleaving 2A sequence between the *BLE* selectable marker gene and *IFT54* (Fig. 4.1-figure supplemental 1). As previously reported, 2A based cleavage was variable and often incomplete, and in some of our preparations, the uncleaved sh-ble-IFT54 product is detected (Dai et al., 2018; Lechtreck et al., 2018). Stable nuclear transformation of *ift54-2* using a construct encoding full-length IFT54 restored full-length cilia confirming that the ciliogenesis defect of the mutant is caused by the lack of full-length IFT54 (Fig. 4.1 B, C). To test if the CH domain of IFT54 is required for ciliogenesis, we transformed *ift54-2* with a construct lacking the CH domain (ΔCH-IFT54) (Fig. 4.1A-C). The *ift54-2* ΔCH-IFT54 transformants were motile, had full-length cilia, and regrew cilia with wild-type kinetics after deciliation by a pH shock (Fig. 4.1 D-F). Like endogenous or transformed full-length IFT54, ΔCH-IFT54 was present near the basal bodies (Fig. 4.1C). The data confirm previous observations by Zhu et al. (2017c) showing that the CH domain of IFT54 is not required for ciliogenesis in cells that possess an otherwise wild-type IFT machinery.

To determine the distribution of the truncated IFT54ΔCC protein in the rescue cells, cilia were isolated from the *ift54-2* IFT54, the *ift54-2* ΔCH-IFT54, and as a control the previously described *ift54-1* 3xHA-ΔCH-IFT54, which lacks IFT54ΔCC (Zhu et al., 2017d); the cilia were separated into axonemes and a membrane+matrix fraction, loaded in a 1:1:1 ratio, and probed with anti-IFT54 (Fig. 4.1G). While IFT54ΔCC enters cilia, it is mostly found in the axonemal fraction but largely absent from the membrane+matrix, which contains the majority of the other IFT proteins tested, including full-length and ΔCH-IFT54. The data suggest that IFT54ΔCC binds to the axoneme likely via its CH-domain but is unable to interact with IFT trains.

4.4 Loss of the IFT54 CH domain exacerbates ciliary growth defects of mutants with a defective IFT81/74 tubulin-binding module.

In vitro and in vivo data indicate that the CH domain of IFT54 binds to microtubules and tubulin (Ling and Goeddel, 2000; Taschner et al., 2016a). Tubulin transport by IFT is critical for ciliary assembly, and the N-terminal domain of IFT74 or IFT81 together are thought to form the main tubulin-binding module of IFT (Bhogaraju et al., 2013; Kubo et al., 2016a). However, deletion or mutation of either of the two domains has only a limited effect on ciliary assembly and length. Thus, we wondered if the CH domain of IFT54 could make a cryptic contribution to tubulin transport by IFT, which is not apparent in the ΔCH-IFT54 single mutant. To test this idea, we crossed the *ift54-2* ΔCH-IFT54 with the previously described *ift81-1* CH5E-IFT81 mutants (Kubo et al., 2016b) and identified *ift54-2* ΔCH-IFT54 *ift81-1* CH5E-IFT81 double mutant strains (referred to as ΔCH54 CH5E81) using a combination of antibiotic selection, PCR and Western blotting (Figs. 4.2 A, -figure supplemental 2). From a mating between the *ift54-2* ΔCH-IFT54 and the previously characterized *ift74-2* ΔN-IFT74 strain (Brown et al., 2015) we obtained the bald *ift74-2* ΔN-IFT74 *ift54-2* strain, which we transformed with pBR25-ΔCH-IFT54 to generate *ift54-2* ΔCH-IFT54 *ift74-2* ΔN-IFT74 (referred to as ΔCH54 ΔN74).

The majority (80%) of ΔCH54 CH5E81 cells did not have cilia detectable by light microscopy (Fig. 4.2 C) Short flagella, often with bulbous tips, were present on ~20% of the cells, which mostly remained entrapped within the mother cell wall (Fig. 4.2 B,C,D). A failure to hatch from the mother cell wall is often observed for strains with paralyzed flagella (Huang et al., 1979). However, both ciliated ΔCH54 CH5E81 and the 54N/74N cells were motile and swam with reduced velocity, which is likely due to the short length of their cilia (Fig. 4.1-figure supplemental 1B,C). Accordingly, the axoneme of the ΔCH54 CH5E81 cells was of apparently

normal ultrastructure, as revealed by TEM. However, we noticed that many of the cilia of the double mutant terminated in a membranous tubule (Fig. 4.2 Da,c). Tips carrying such tubules are characteristics for ciliary stumps briefly after flagellar abscission (Lewin and Lee, 1985). Occasionally, we also observed membrane-enclosed fragments of the axoneme or cilia bluntly broken off above the transition zone (Fig. 4.2 Dd,f). These ultrastructural data suggest that the cilia of the ΔCH54 CH5E81 double mutant, for reasons unknown, might be less stable and prone to breakage and abscission. After cilia amputation by a pH shock, the ΔCH54 CH5E81 cells grow their flagella at a rate than of 0.06 μm/min, which is below that of either of the parental strains; even after 3 hours, the regenerated cilia remained below their average pre-deflagellation length (Fig. 4.2 E).

Similarly, the ΔCH54 ΔN74 double mutant grew mostly palmelloid (72% of the cells); the remainder of the cells built short cilia often with bulbous ends (Fig. 4.3B). With an average length of ~7 μm, the cilia of the ΔCH54 ΔN74 double mutant were shorter than those of each parental strain (i.e., ift54-2 ΔCH-54 and ift74-2 ΔN74; Fig. 4.3C). TEM analysis of ΔCH54 ΔN74 showed that short cilia appeared of normal ultrastructure but often terminated with an elongated blebbed membrane tube as described for the ΔCH54 CH5E81 (Fig. 4.3D). To summarize, ciliogenesis in the 54N/74N and ΔCH54 CH5E81 double mutants was more severely affected that in either parental strain. These observations suggest that the CH-domain of IFT54 contributes to ciliogenesis in situations when an intact 74N/81N module is absent.

4.5 IFT appears normal, and tubulin transport is reduced in the IFT81N/54N double mutant.

The reduction in ciliary length observed in the 54N/74N, and 54N/81N double mutants could be caused by general defects in IFT or a reduction in the transport specifically of tubulin (Craft et

al., 2015a; Kubo et al., 2016b; Picariello et al., 2019b). We focused our detailed analysis of ciliogenesis on the 81N/54N as the CH domains likely confer specificity for the binding of tubulin. To visualize IFT, we crossed sfGFP-IFT140 into the *ift54-2* ΔCH-IFT54 and *ift54-2* ΔCH-IFT54 *ift81-1* CH5E-IFT81 backgrounds and used TIRF microscopy to analyze IFT. The velocities and frequencies of anterograde and retrograde IFT in the 54N single and the 54N/81N double mutants were similar to those observed in the *ift140-1* sfGFP-IFT140 control strain (Fig. 4.4A-C). Thus, IFT appeared to be unaffected by the manipulations of the CH domains of IFT54/81.

To study the effect of the loss of the IFT54 CH domain on tubulin transport, we generated a 54N GFP-β-tubulin, an 81N GFP-β-tubulin, and an 81N/54N GFP-β-tubulin strain, by mating 81N/54N to a wild-type strain expressing GFP-β-tubulin (Fig. 4.4). Since tubulin transport is rarely observed in full-length cilia (Craft et al., 2015a), we measured tubulin transport frequencies in regenerating cilia of approximately half their steady-state length (Fig. 4.4D). The frequency of tubulin transport by anterograde IFT in the 81N/54N double mutant was significantly below that observed in the 54N and 81N parental strains (Fig. 4.4E). The data suggest that CH domain of IFT54 participates in tubulin transport by IFT in *Chlamydomonas* and that the ciliogenesis defects of the 81N/54N strain, and likely the 74/54N strain, are due to defects in tubulin transport.

4.6 The CH domains of IFT54 and IFT81 are partially exchangeable but bind to distinct sites on tubulin dimers.

Since CH domains of IFT54 and IFT81 both bind tubulin, we wondered if the CH of IFT54 can substitute for the CH domain of IFT81; we did not test the reverse exchange since the

loss of the CH of IFT54 has no discernible phenotype on its own (Taschner et al., 2016b). To test this, we replaced the CH domain of IFT81 with that of IFT54; the IFT54CH and ΔCH-IFT81 backbone were separated by a short flexible linker of 10 amino acids to allow for some movement of the IFT54CH (Fig. 4.5A). As a control for the resulting *ift81-1* IFT54CH-L-ΔCH-IFT81 strain, we used an *ift81* L-ΔCH-IFT81 strain, which has the linker but lacks a CH-domain, and an *ift81-1* IFT81CH-L-ΔCH-IFT81 strain, which has the IFT81 backbone and its original CH domain separated by the linker (Fig. 4.5A). Expression of the constructs and entry of the modified proteins into cilia was confirmed by probing ciliary extracts of each strain with anti-IFT81 (Fig. 4.5B).

The novel *ift81* L-ΔCH-IFT81 deletion strain had shorter cilia (~5μm) than the previously described *ift81* CH5E-IFT81 strain (~10μm), suggesting that the CH5E, despite being unable to bind tubulin in vitro, has some residual function in ciliogenesis (Fig. 5C). The average length of cilia in the *ift81-1* IFT54CH-L-ΔCH-IFT81 strain was below that of the *ift81-1* IFT81CH-L-ΔCH-IFT81 rescue but above that of the *ift81* L-ΔCH-IFT81 deletion strain. The *ift81-1* L-ΔCH-IFT81 strain regrew cilia slowly while the wild-type regeneration kinetics were observed for the *ift81-1* IFT81CH-L-ΔCH-IFT81 and the *ift81-1* IFT54CH-L-ΔCH-IFT81 strain. The velocity of IFT in the three linker strains was normal but for a slight reduction in the velocity of retrograde IFT in the *ift81* CH5E-IFT81. Taken together, the data show that the 54CH domain can partially replace the CH domain of IFT81, suggesting that both domains fulfill similar functions in ciliogenesis [data summarized in Fig. 4.5- figure supplemental 1].

While the overall ultrastructure of the CH domains of IFT54 and IFT81 is similar, they have distinct distributions of the charged residues that likely mediate the interaction with tubulin (Taschner et al., 2016b). To test whether the IFT54 and IFT81 CH domains interfere with each

other when binding to tubulin, we used an in vitro competition assay. A given amount of tubulin dimers and increasing amounts of the recombinant IFT54-CH were added to beads preloaded with IFT-B1 complexes encompassing the IFT81/74 site; then, the amount of tubulin bound to the beads was analyzed by SDS-PAGE and Coomassie staining (Fig. 4.5E). We reasoned that if the IFT54 and IFT81 CH compete for the same site on tubulin, exceeding amounts of the 54CH will block tubulin from interacting with the IFT-B1 complex. However, even a 50-fold excess of the IFT54-CH vs. the IFT81-CH did not reduce the amount of tubulin bound to the IFT-B1 complex (Fig. 4.5E). This suggests the CH domains of IFT54 and the IFT81 bind to distinct sites of the tubulin dimers. It seems therefore possible, that the two CH-domains interact with the same tubulin dimer during transport rather than forming two independent tubulin-binding sites. We thus propose that IFT54, IFT74, and IFT81 form a tripartite binding site for tubulin on the IFT trains (Fig. 4.5F).

4.7 DISCUSSION

The CH-domain of IFT54 participates in tubulin transport by IFT

The N-terminal domains of IFT74 and IFT81 are critical role for ciliary assembly in *Chlamydomonas* likely because together they form the main tubulin-binding site of IFT *(Bhogaraju et al., 2013; Kubo et al., 2016a)*. In addition to the IFT74/81 module, the CH domain of IFT54 binds to microtubules and tubulin in vitro, raising the question of whether it contributes to ciliary tubulin transport (Taschner et al., 2016a). The cilia-less phenotypes of the *ift54-1* and *ift54-2* mutants are fully rescued by a CH-deficient IFT54 (ΔCH-IFT54), revealing that this domain is dispensable for ciliogenesis in *Chlamydomonas* (this study and (Zhu et al., 2017d)). However, when CH-less IFT54 is combined with either the incapacitated CH-domain of IFT81

(IFT81-5E) or the deletion of the head domain of IFT74 (ΔN-IFT74), the moderate ciliogenesis defects of the respective single mutants are aggravated with many cells failing to assemble cilia. Thus, combinations of mutations or deletions in any two of the three tubulin-binding domains of IFT54/74/81 results in synthetic enhancement of the ciliogenesis phenotype. To understand the underlying mechanism, we focused on the role of the IFT54/81 CH domains, which likely confer specificity for the binding of tubulin. In the remaining cilia of the *ift54-2* ΔCH-IFT54 *ift81-1* CH5E-IFT81 double mutant, IFT appeared normal while the frequency of tubulin transport was reduced. Further, an IFT81 construct carrying the CH domain of IFT54 instead of its own attenuated the short cilia phenotype of a novel *ift81* ΔCH-IFT81 mutant strain indicating that both CH domains perform a similar role in IFT and ciliary assembly. Taken together, these observations suggest that the CH-domain of IFT54 participates in ciliary tubulin transport.

IFT54/74/81 likely from a tripartite tubulin-binding module

A comparison of how ciliogenesis is affected in the different mutants provides additional insights into the role of IFT54's CH domain in tubulin transport. In contrast to the IFT81-5E, ΔCH-IFT81, and ΔN-IFT74 single mutants, loss of the CH domain of IFT54 did not affect ciliary length and growth rate suggesting a minor contribution of this domain in cilia formation of cells possessing an intact IFT81/74 module. Indeed, ciliogenesis was most severely affected in the 81N/74N double mutant suggesting that tubulin transport based on IFT54's CH domain alone is insufficient for the formation of cilia. Thus, IFT54 could form an independent site with a low capacity to transport tubulin, whose role for ciliogenesis only becomes apparent when the main IFT74/81-based tubulin-binding site is affected. Alternatively, that head domains of IFT54/74/81 could form one tripartite tubulin-binding site, in which either two of the three

participating tubulin-binding domains are sufficient to maintain near normal cilia formation. The latter model could explain why ciliogenesis is only mildly affected in the IFT81-5E, ΔCH-IFT81, and ΔN-IFT74 single mutants, despite the low affinity of the IFT81 CH and the lack of selectivity of the IFT74 head domain for tubulin. The presence of one tripartite tubulin-binding module could also explain why cilia formation in *C. elegans* is only mildly affected by the loss of either IFT-74 or IFT-81. In species that lack either IFT74 or IFT81, IFT54/74 or IFT54/81 modules could ensure tubulin transport. Finally, IFT54 could have developed into the sole and self-sufficient tubulin-binding site of IFT in those species that lack both IFT74 and IFT81 homologues (van Dam et al., 2013).

Tubulin-binding by the IFT54/74/81 tripartite binding module

Our data are best explained by IFT54/74/81 forming a tripartite tubulin-binding site with a partial redundancy between the three tubulin-interacting head domains. As IFT74/81 are part of the IFT-B1 complex, whereas IFT54 is in the IFT-B2, a tripartite tubulin-binding site would require proximity between the head domain of IFT54 and the IFT81N/74N module in the IFT-B holo-complex. The head domain of IFT74 apparently binds the charged C-terminal E-hook of β-tubulin, but how precisely the two CH-domains interact with tubulin is currently unknown (Bhogaraju et al., 2013; Taschner et al., 2016a). CH domains undergo diverse interactions, including members that bind to actin filaments or microtubules. A well-studied example of the latter is the plus-end TIP end binding protein 1 (EB1). The CH of EB1 binds to the outside of the microtubule lattice at the interface between four tubulin dimers; however, it is unable to bind soluble α/β-tubulin dimers on its own (Slep and Vale, 2007; Zhang et al., 2015). Similar to EB1, the IFT81/74 module and the IFT54 CH densely decorate microtubules but bind only

comparatively weakly to soluble tubulin dimers. Our *in vitro* sedimentation assays indicate that the CH of IFT54 does not interfere with the binding of soluble tubulin by the IFT-B1 complex suggesting that IFT54 and the IFT81/74 module bind tubulin independently of each other. On the other hand, we show that substituting IFT81's CH with that of IFT54 partially rescues the ciliary assembly defect of ΔCH-IFT81 strain, suggesting related binding properties of the two CH domains. This raises the question of whether the two CH domains and the IFT74N indeed bind onto a single tubulin dimer or actually bind and stabilize a small tubulin oligomer. It has been suggested that several plus-end TIPs cooperate to form larger tubulin oligomers for delivery to the growing ends of microtubules (Slep and Vale, 2007). The IFT-B complex appears to dimerize via its IFT80 subunit, which could bring two IFT54/74/81 modules into proximity forming a more extended tubulin-binding patch (Taschner et al., 2018b). Together, our data raise the question of whether IFT54/74/81, rather than binding a single tubulin dimer, actually stabilizes and transports a tubulin oligomer.

4.8 FIGURES

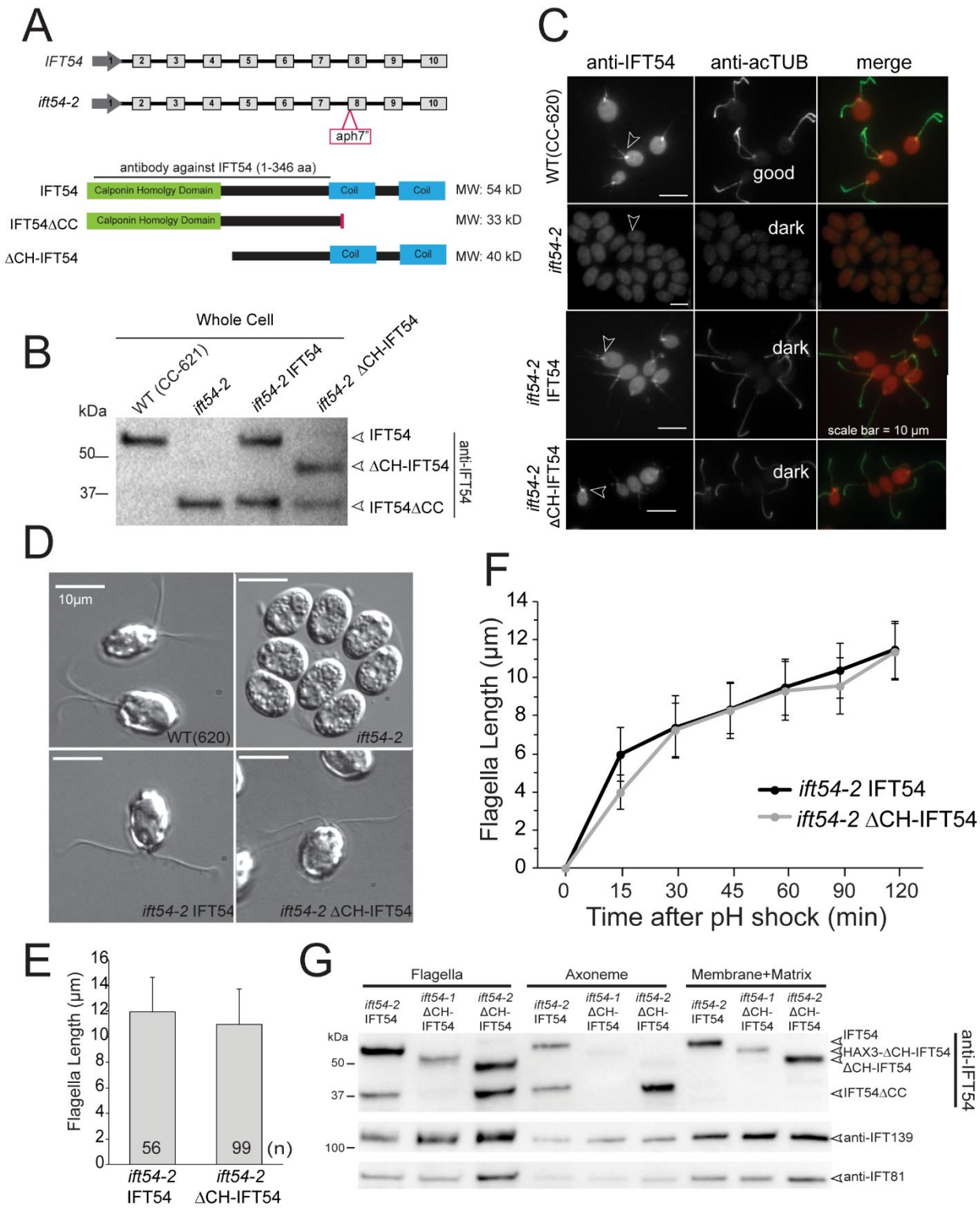
A
IFT54
ift54-2
aph7"
antibody against IFT54 (1-346 aa)
IFT54
Calponin Homolgy Domain
Coil
Coil
MW: 54 kD
IFT54ΔCC
Calponin Homolgy Domain
MW: 33 kD
ΔCH-IFT54
Coil
Coil
MW: 40 kD
B
Whole Cell
WT (CC-621)
ift54-2
ift54-2 IFT54
ift54-2 ΔCH-IFT54
kDa
50
37
IFT54
ΔCH-IFT54
IFT54ΔCC
anti-IFT54
C
anti-IFT54
anti-acTUB
merge
WT(CC-620)
good
ift54-2
dark
ift54-2 IFT54
dark
scale bar = 10 μm
ift54-2 ΔCH-IFT54
dark
D
10μm
WT(620)
ift54-2
ift54-2 IFT54
ift54-2 ΔCH-IFT54
E
Flagella Length (μm)
56
99
(n)
ift54-2 IFT54
ift54-2 ΔCH-IFT54
F
Flagella Length (μm)
Time after pH shock (min)
ift54-2 IFT54
ift54-2 ΔCH-IFT54
G
Flagella
Axoneme
Membrane+Matrix
ift54-2 IFT54
ift54-1 ΔCH-IFT54
ift54-2 ΔCH-IFT54
kDa
50
37
100
IFT54
HAX3-ΔCH-IFT54
ΔCH-IFT54
IFT54ΔCC
anti-IFT139
anti-IFT81
anti-IFT54

Figure 4.1 The CH domain of IFT54 is not required for flagella assembly.

A) Map of the *IFT54* gene and proteins encoded by wild-type and mutant genes and rescue constructs. The *ift54-2* mutant was made via insertional mutagenesis using *aph7*" as a selectable marker. The predicted molecular weight are on the right of each protein. **B)** Western blot of whole cell extracts from WT, *ift54-2*, *ift54-2* IFT54, and *ift54-2* ΔCH-IFT54 probed with a rabbit polyclonal antibody raised against recombinant IFT54 (1-346aa as shown in A. Note that the *ift54-2* mutant produces a truncated IFT54 protein (designated as IFT54ΔCC). **C)** Immunofluorescence of wild-type, *ift54-2*, *ift54-2* IFT54, and *ift54-2* ΔCH-IFT54 cells stained with anti-IFT54 (red) and anti-acetylated tubulin (green). Arrowheads show an accumulation of IFT54 at the basal bodies in wild-type, *ift54-2* IFT54, and *ift54-2* ΔCH-IFT54, which is absent in *ift54-2*. **D)** DIC images of a control (WT, CC-620), the *ift54-2* mutant, and the full-length *ift54-2* IFT54 and truncated *ift54-2* ΔCH-IFT54 rescue strains; both constructs fully restore flagellar assembly. Steady-state flagella length measurements of *ift54-2* IFT54 and *ift54-2* ΔCH-IFT54; these are comparable to wild-type and not significantly different by a two-tailed t-test. **E)** Steady-state flagella length measurements of *ift54-2* IFT54 and *ift54-2* ΔCH-IFT54; these are comparable to wild-type and not significantly different by a two-tailed t-test. **F)** Flagella regeneration proceeded with normal kinetics for both *ift54-2* IFT54 and *ift54-2* ΔCH-IFT54. n=50 or more flagella. Error bars represent standard deviation for all figures. **G)** Fractionated flagella from *ift54-2* IFT54, *ift54-1* ΔCH-IFT54, and *ift54-2* ΔCH-IFT54 probed with anti-IFT54 and loading controls (anti-IFT139, anti-IFT81). Like other IFT proteins, full-length IFT54 and ΔCH-IFT54 were primarily present in the membrane+matrix fraction while mutant ift54-ΔCC fractionated with the axoneme presumably binding the axoneme with its CH-domain.

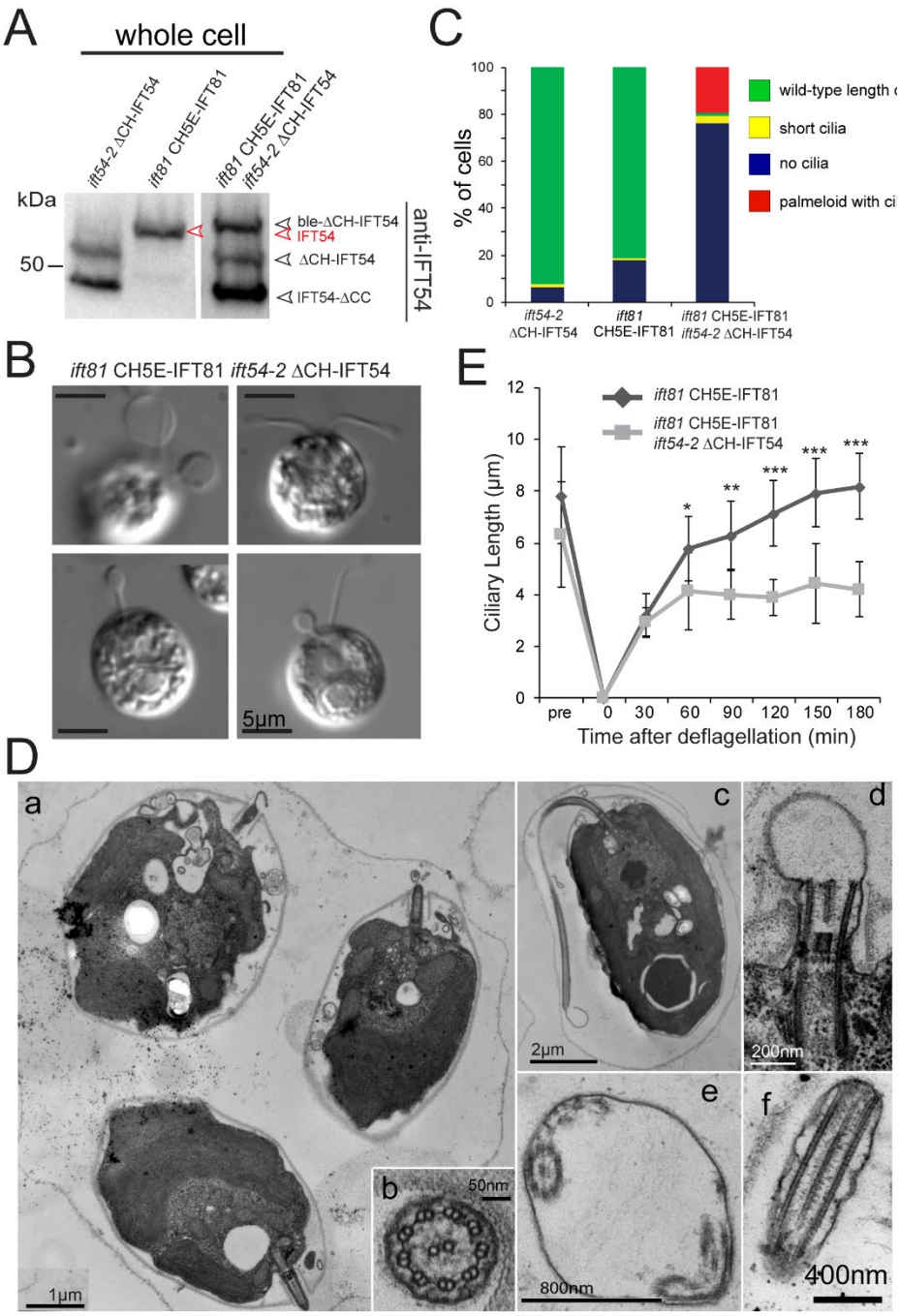

Figure 4.2 An ift54-2 ΔCH-IFT54 ift81-1 CH5E-IFT81 double mutant has impaired flagella growth and stability.

A) Western blot showing identification of *ift81* CH5E-IFT81 *ift54-2* ΔCH-IFT54 with the parental of *ift81* CH5E-IFT81 and *ift54-2* ΔCH-IFT54 strains. Note a background band from an

uncleaved ble-ΔCH-IFT54. **B)** DIC microscopy of *ift81* CH5E-IFT81 *ift54-2* ΔCH-IFT54. Note short and bulged flagella. **C)** Percent of cells with flagella in the parental *ift54-2* ΔCH-IFT54 and *ift81* CH5E-IFT81 single mutants and the *ift81* CH5E-IFT81 *ift54-2* ΔCH-IFT54 double mutant strains. N = 1,000 cells per strain. **D)** TEM on *ift54-2* ΔCH-IFT54 *ift81* CH5E-IFT81: a) Three cells inside mother cell wall with flagella stumps. b) Single cell with near full-length flagellum in mother cell wall; note abnormally extended flagellar tip. c) Flagella surrounded by membrane prior to abscission. d and e) Fragmented flagella in mother cell wall (cell wall not shown in d). f) cross-section through proximal flagella shows a normal axoneme. **E)** Flagella regeneration kinetics of i*ft81* CH5E-IFT81 and the *ift81* CH5E-IFT81 *ift54-2* ΔCH-IFT54 double mutant. Bars show standard deviation (*$p<0.05$,**$p<0.01$,***$p<0.001$).

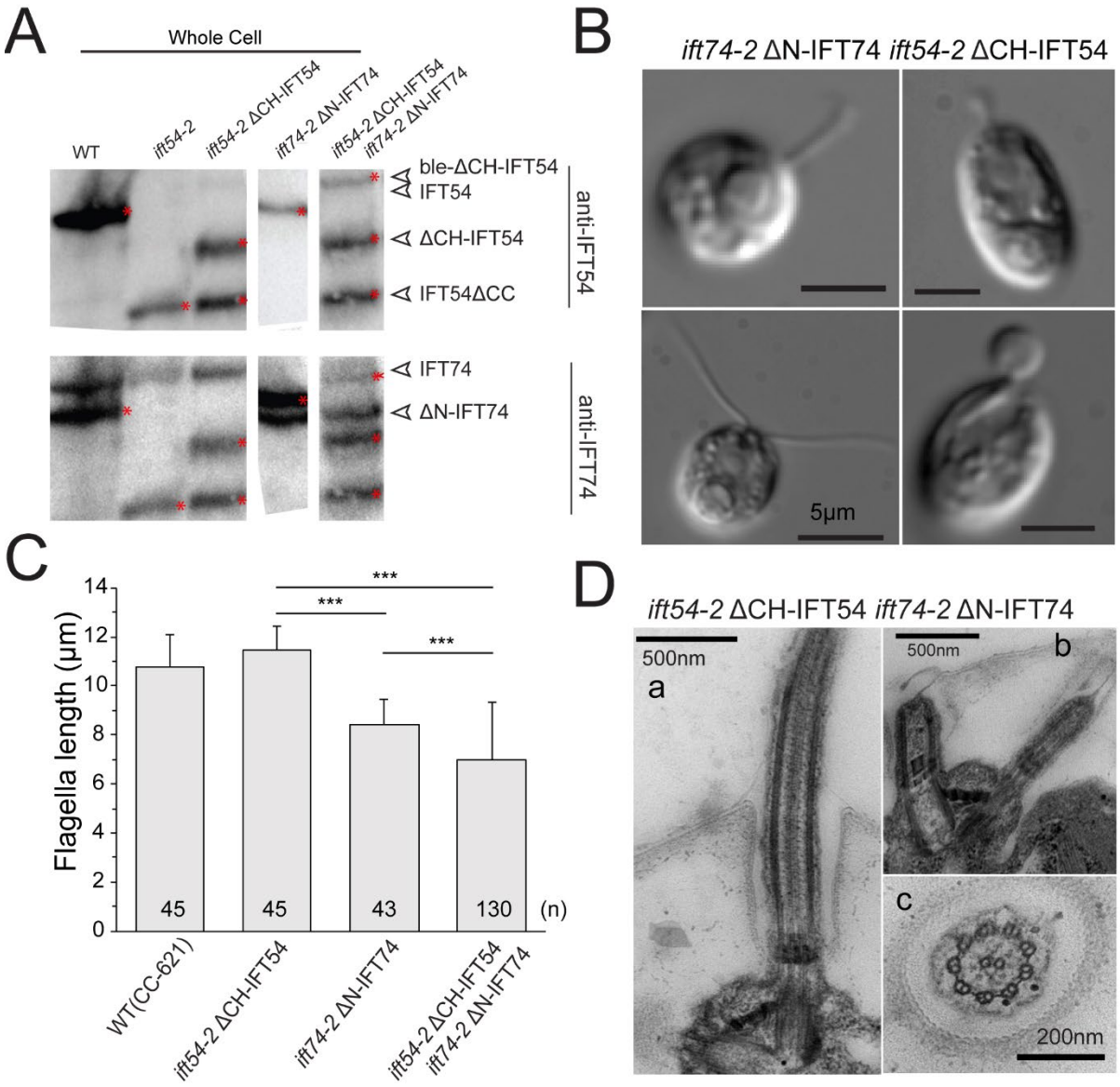

Figure 4.3 Ciliogenesis is affected with loss of the CH-domain of IFT54 is combined with head-less IFT74.

A) Western blot of the *ift54-2* ΔCH-IFT54 *ift74-2* ΔN-IFT74 double mutant. The blot was first probed with anti-IFT54 and then anti-IFT74. Red* note residual signal from anti-IFT54. **B)** DIC of *ift54-2* ΔCH-IFT54 *ift74-2* ΔN-IFT74 shows the cells to have short, bulbous flagella. **C)** Average flagella lengths of WT, *ift54-2* ΔCH-IFT54, *ift74-2* ΔN-IFT74, and *ift54-2* ΔCH-IFT54 *ift74-2* ΔN-IFT74. *ift74-2* ΔN-IFT74 had significantly shorter flagella than WT and *ift54-2* ΔCH-

IFT54. *ift54-2* ΔCH-IFT54 *ift74-2* ΔN-IFT74 had significantly shorter cilia than all other strains. **D)** TEM of *ift54-2* ΔCH-IFT54 *ift74-2* ΔN-IFT74 strains: **a)** longitudinal section through a flagellum reveals a normal axoneme. **b)** two short flagella on the same cell with membranous material at the distal end, a sign of recently excised flagella. **c)** cross section through a proximal region of the axoneme which appears wild-type.

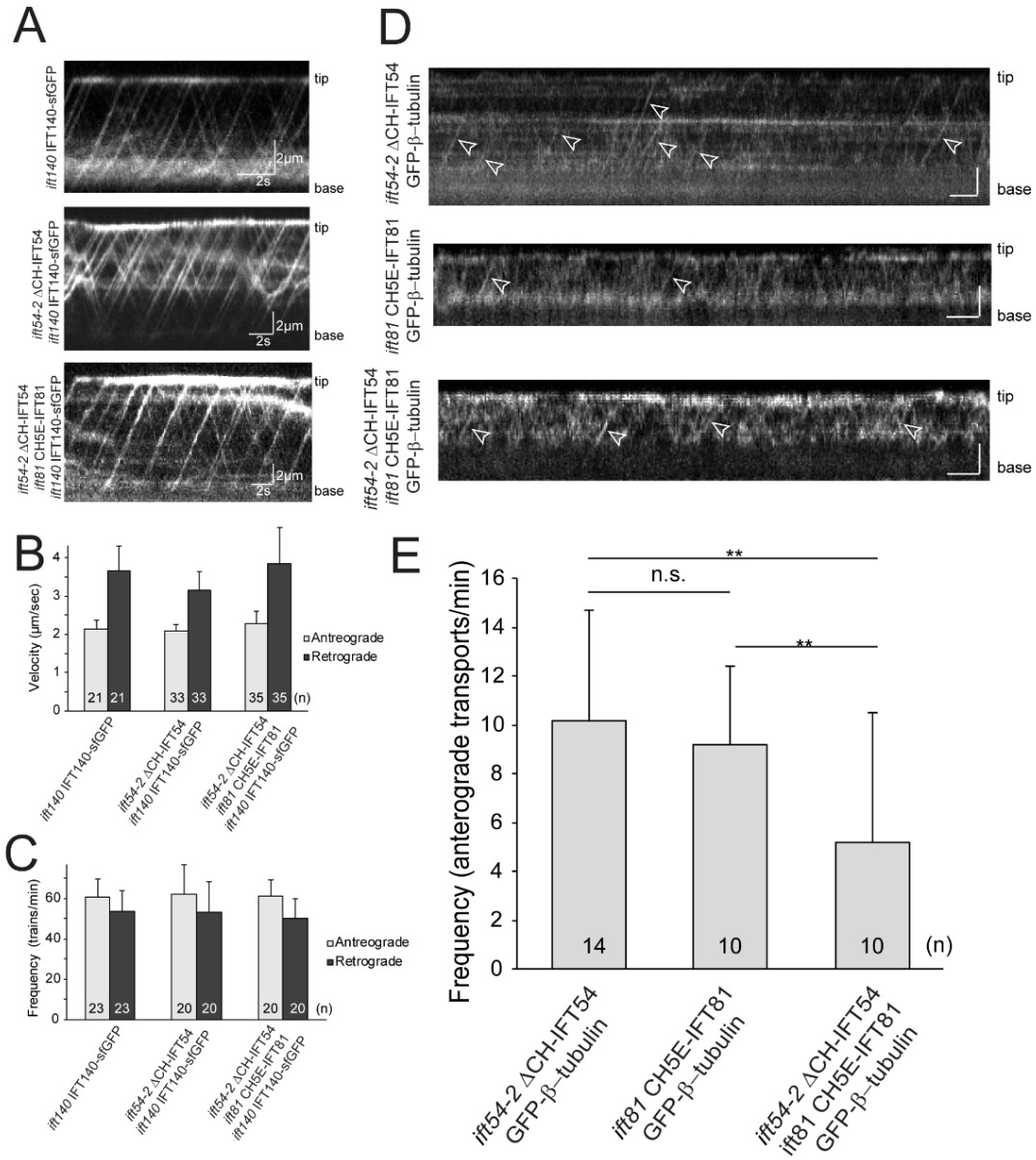

Figure 4.4 IFT velocity and frequency are normal while tubulin transport is reduced the ΔCH-54 CH5E-IFT81 double mutant.

A) Kymographs of *ift140* sfGFP-IFT140, *ift54-2* ΔCH-IFT54 *ift140* sfGFP-IFT140 and *ift54-2* ΔCH-IFT54 *ift81* 5E-IFT81 *ift140* sfGFP-IFT140. **B)** Velocity of anterograde and retrograde IFT trains in the *ift140* IFT140-sfGFP, *ift54-2* ΔCH-IFT54 *ift140* sfGFP-IFT140, and *ift54-2*

ΔCH-IFT54 *ift81* 5E-IFT81 *ift140* sfGFP-IFT140 reveals similar IFT velocities in all three strains. **C)** Number of anterograde and retrograde IFT trains per minute in the *ift140* IFT140-sfGFP, *ift54-2* ΔCH-IFT54 *ift140* sfGFP-IFT140, and *ift54-2* ΔCH-IFT54 *ift81* 5E-IFT81 *ift140* sfGFP-IFT140 reveals similar IFT frequencies in all three strains. Standard deviation bars shown. **D)** Kymographs of regenerating *ift54-2* ΔCH-IFT54 β-tubulin-GFP, *ift81* CH5E-IFT81 β-tubulin-GFP, and *ift54-2* ΔCH-IFT54 *ift*81 CH5E-IFT81 β-tubulin-GFP cells, following pH shock. Open white arrows point to IFT trafficking of tubulin, in one of the two flagella. **E)** Number of IFT trains carrying β-tubulin-GFP per minute in regenerating *ift54-2* ΔCH-IFT54 β-tubulin-GFP, *ift81* CH5E-IFT81 β-tubulin-GFP, and *ift54-2* ΔCH-IFT54 *ift81* CH5E-IFT81 β-tubulin-GFP cells, reveals significantly reduced tubulin transport frequencies in the IFT81/54 CH double mutant. Standard deviation bars shown. N.S. represents p-value>0.05. ** indicates p-value <0.05.

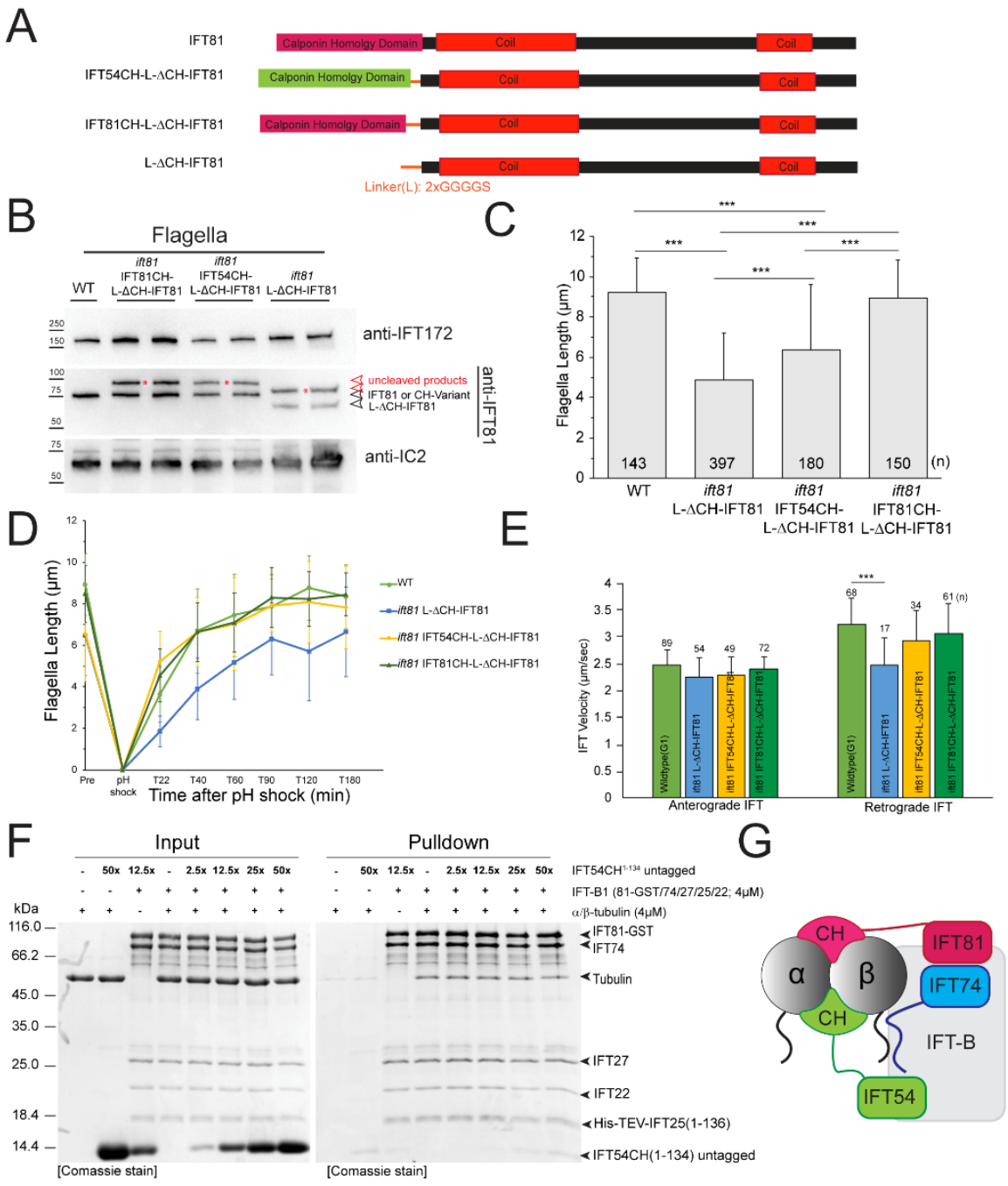

Figure 4.5 The CH domains of IFT54 and IFT81 are partially exchangeable but bind to distinct sites on tubulin dimers.

A) Schematics of the constructs used in B-E. **B)** Western blot of flagella extract probed with anti-IFT81 and the loading controls IFT-172 and anti-IC2. Protein samples for each of the ift81

X-CH-IFT81 strains were loaded in equivalent amounts in two adjacent lanes. The higher bands, marked by red arrows, in the ift81 X-CH-IFT81 lanes corresponds to an un-cleaved ble-2A-X-CH-IFT81 product. **C)** Steady-state flagella lengths of wild-type, *ift81* IFT81CH-L-ΔCH-IFT81, *ift81* IFT54CH-L-ΔCH-IFT81, *ift81* IFT81CH-L-ΔCH-IFT81 and *ift81* L-ΔCH-IFT81. *ift81* L-ΔCH-IFT81 has significantly shorter flagella than all other strains analyzed. *ift81* IFT54CH-L-ΔCH-IFT81 has shorter flagella than wild-type and *ift81* IFT81CH-L-ΔCH-IFT81 flagella. *** p-value<0.00001 **D)** Flagella regeneration kinetics of wild-type, *ift81* IFT81CH-L-ΔCH-IFT81, *ift81* IFT54CH-L-ΔCH-IFT81, *ift81* IFT81CH-L-ΔCH-IFT81 and *ift81* L-ΔCH-IFT81. *ift81* L-ΔCH-IFT81 has significantly slower flagella regeneration kinetics than all other strains analyzed. **E)** Anterograde and retrograde IFT velocity of wild-type, *ift81* IFT81CH-L-ΔCH-IFT81, *ift81* IFT54CH-L-ΔCH-IFT81, *ift81* IFT81CH-L-ΔCH-IFT81 and *ift81* L-ΔCH-IFT81. *ift81* L-ΔCH-IFT81 had significantly slower retrograde IFT velocity compared to the wild-type strain. *** p-value<0.00001. **F)** To determine if the CH domains of IFT54 and IFT81 bind the same location on tubulin dimers, a tubulin-binding assay was performed with varying amounts of untagged IFT54CH. GST beads were first incubated with GST-IFT81(in the IFT-B1 complex for stability). Then tubulin and IFT54CH was added simultaneously to the GST beads with IFT81 allowed to incubate for 1 hour at 4℃ (Input sample taken prior to incubation). GST beads and the associated proteins were spun down, washed and eluted with Glutathione. Eluates were loaded as Pulldown. Coomassie staining of SDS-Page gels indicate that IFT81 is able to bind to similar amounts of tubulin, even with 50X more IFT54CH. **G)** Model of the tripartite tubulin-binding domain.

4.9 FIGURE SUPPLEMENTALS

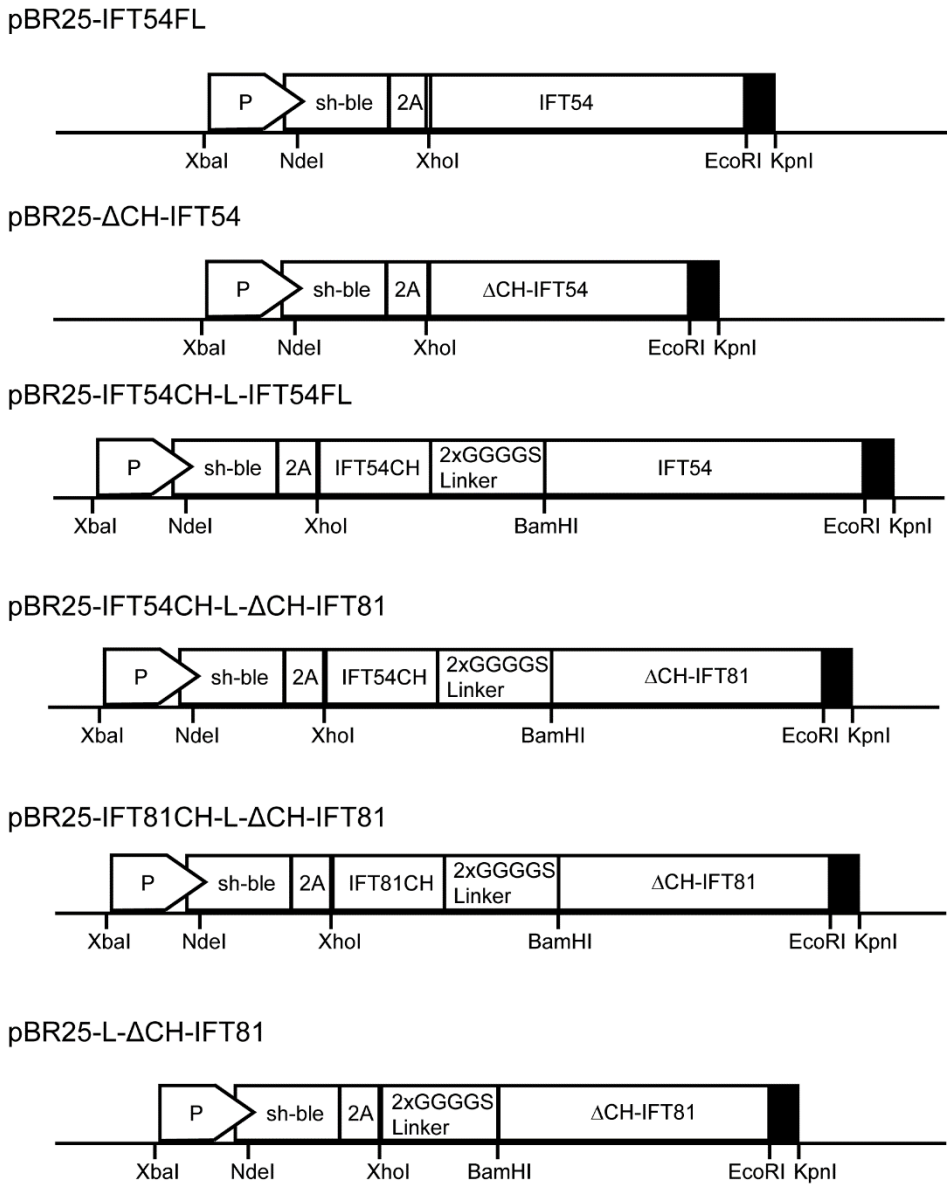

Figure 4.1-figure supplemental 1 Vector maps to express IFT54 and IFT81.

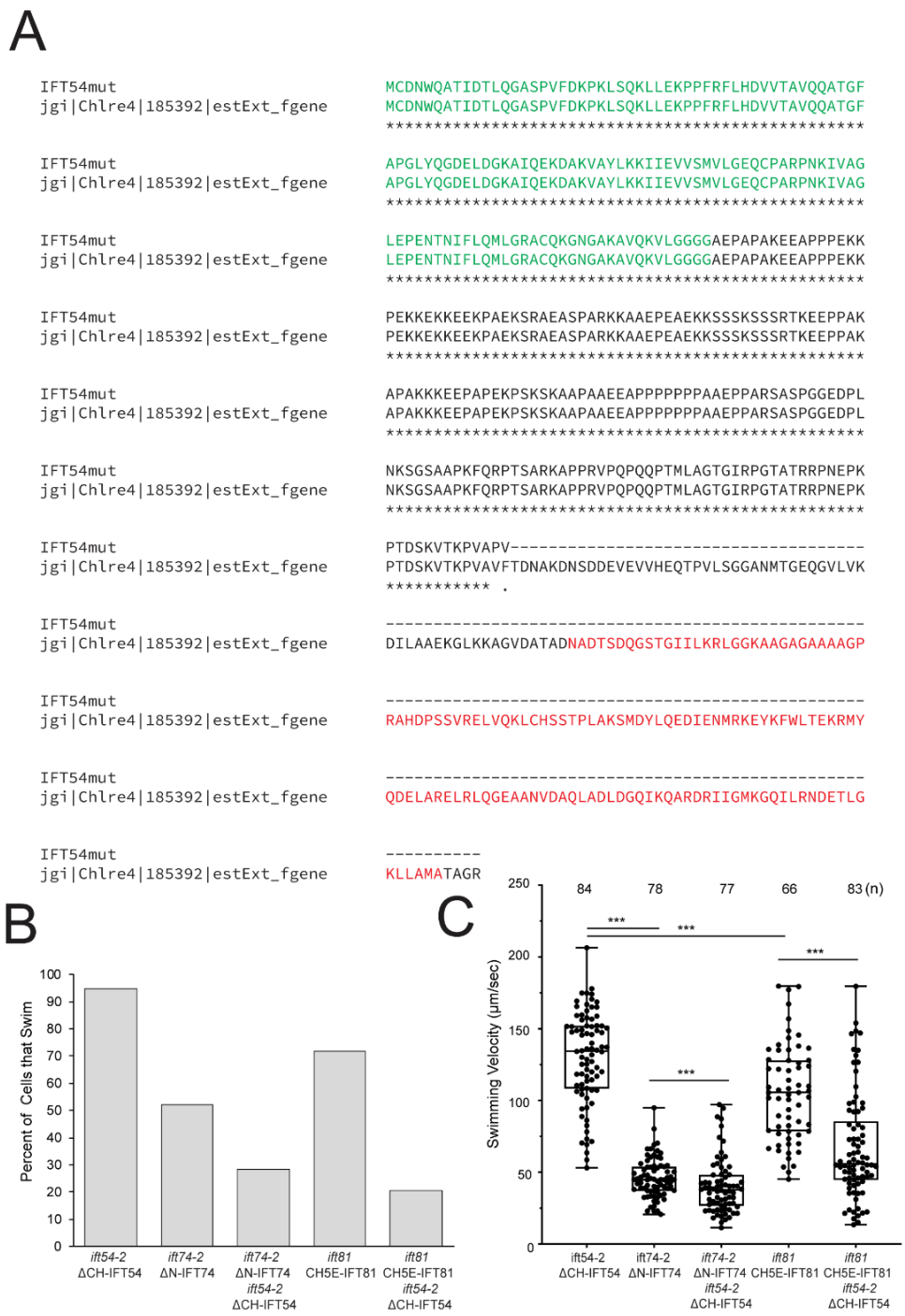

Figure 4.2-figure supplemental 1. A Map of IFT54 and mutant cell motility.

A)Alignment (Clustaw 2.1) of predicted peptide sequences of IFT54ΔCC and wild-type IFT54 (jgi|Chlre4|185392|estExt_fgene). Green amino acids correspond to the CH-domain which is present in both the mutant and wild-type IFT54 and the red amino acids correspond to the coil-

coil domain, which is absent in IFT54mut sequence (termed ift54-ΔCC). **B)** The percent of cells that swim for *ift54-2* ΔCH-IFT54, *ift74-2* ΔN-IFT74, and *ift81* CH5E-IFT81 parental strains and the *ift54-2* ΔCH-IFT54 *ift74-2* ΔN-IFT74, *ift81* CH5E-IFT81 *ift54-2* ΔCH-IFT54 double mutants. The percent of cells that swim, indicative of the percent of flagellated cells, was significantly lower for *ift54-2* ΔCH-IFT54 *ift74-2* ΔN-IFT74 compared with *ift54-2* ΔCH-IFT54 and *ift74-2* ΔN-IFT74; and for *ift81* CH5E-IFT81 *ift54-2* ΔCH-IFT54 compared with *ift81* CH5E-IFT81 and *ift54-2* ΔCH-IFT54. **C)** The swimming velocity for *ift54-2* ΔCH-IFT54, *ift74-2* ΔN-IFT74, and *ift81* CH5E-IFT81 parental strains and the *ift54-2* ΔCH-IFT54 *ift74-2* ΔN-IFT74, *ift81* CH5E-IFT81 *ift54-2* ΔCH-IFT54 double mutants. The swimming velocity was significantly slower for *ift54-2* ΔCH-IFT54 *ift74-2* ΔN-IFT74 compared with *ift54-2* ΔCH-IFT54 and *ift74-2* ΔN-IFT74; and for *ift81* CH5E-IFT81 *ift54-2* ΔCH-IFT54 compared with *ift81* CH5E-IFT81 and *ift54-2* ΔCH-IFT54. n=60 or more cells. ***p-value<0.001

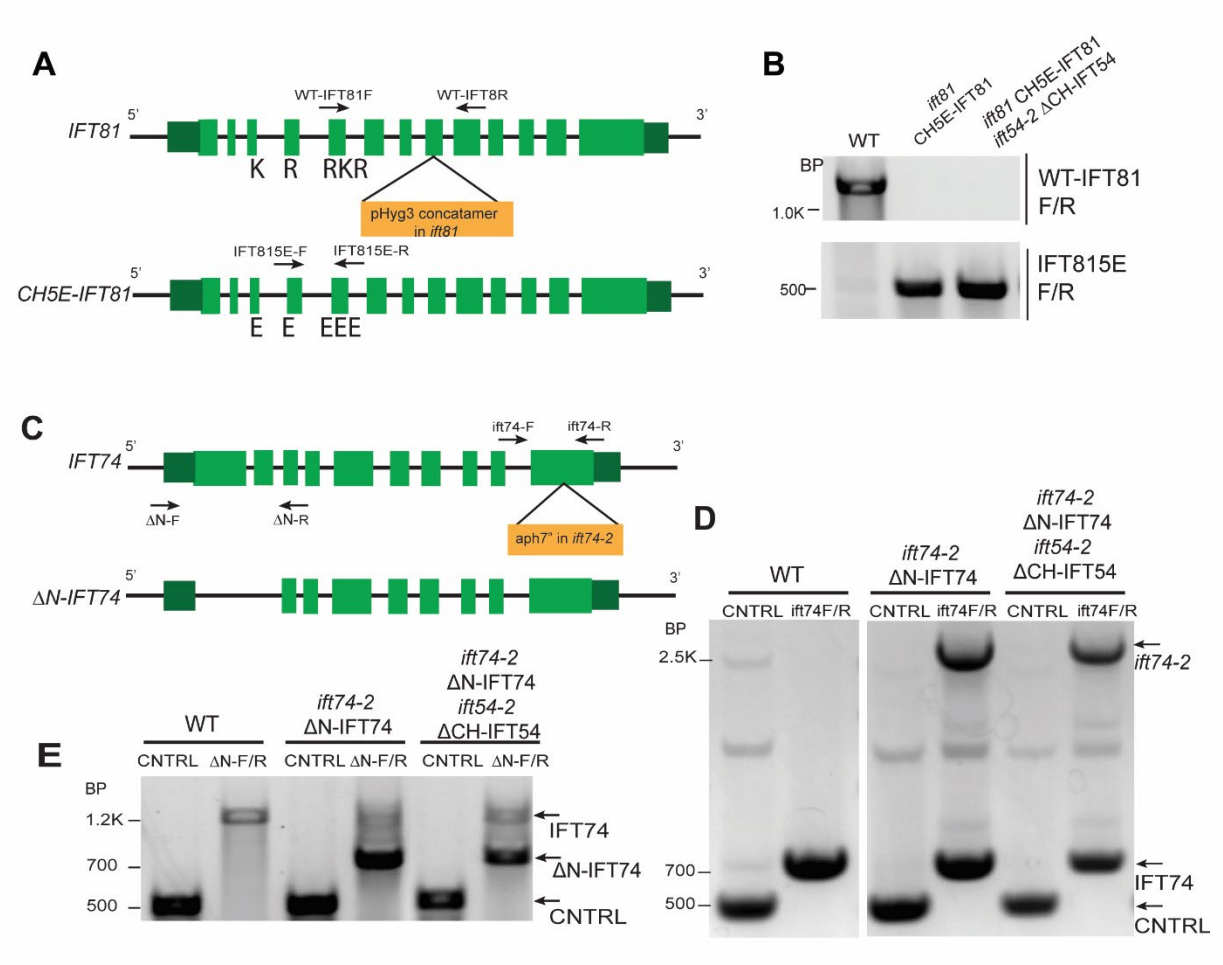

Figure 4.2-figure supplemental 2. PCR data for identification of *ift54-2* ΔCH-IFT54 *ift81-1* CH5E-IFT81 and *ift54-2* ΔCH-IFT54 *ift74-2* ΔN-IFT74.

A) top: Map of *IFT81* with pHyg3 in *ift81*. WT residues (K73, R75, R85, K112 and R113) which were altered to glutamate (E) in CH5E-IFT81 are indicated. WT-IFT81F/R primers will amplify a 1209bp fragment in WT IFT81 and a ~5kbp fragment in *ift81*. bottom: Map of CH5E-IFT81. IFT815E primers amplify a 508bp fragment in strains with CH5E-IFT81 insert but will not anneal to the endogenous *IFT81*. **B)** PCR analysis of genomic DNA isolated from a single progeny obtained by mating *ift81* CH5E-IFT81 to the *ift54-2* ΔCH-IFT54 and determined to be an *ift81* mutant and possess the altered CH5E-IFT81 insert. **C)** Map of the ift74-2 and ΔN-IFT74 and the approximate location of where the primers anneal. **D)** PCR revealing a progeny from the

ift54-2 ΔCH-IFT54 X *ift74-2* ΔN-IFT74 mating to be mutant for ift74. **E)** PCR showing the progeny from B to contain the ΔN-IFT74 insertion.

Strain	*ift74-2* ΔN-IFT74	*ift81* CH5E-IFT81	81N/74N	*ift54-2* ΔCH-IFT54	74N/54N	81N/54N	*ift81* L-ΔCH-IFT81	*ift81* IFT54CH-L-ΔCH-IFT81	*ift81* IFT81CH-L-ΔCH-IFT81
	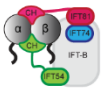		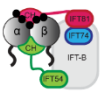	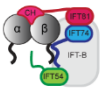	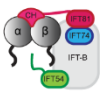	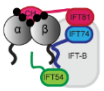			
Cilia length (μm)	↓ 8.43 ± 1.01	= 9.09 ± 1.59	↓ <2**	= 10.98 ± 2.74	↓ 7.00 ± 2.35	↓ 6.34 ± 2.04	↓ 6.45 ± 1.93	↓ 6.57 ± 2.30	= 8.47 ± 1.37
Cilia growth (t1/2 min)	↓ ~200*	↓ 30 ± 2	N.A.	= 22 ± 2	N.A.	↓ 45 ± 2	↓ 35 ± 2	= 20 ± 2	= 22 ± 2
Cells with cilia	↓ 52%	↓ 82.1%	N.A.	= 93.5%	↓ 28.4%	↓ 23.6%	N.A.	N.A.	N.A.

Figure 4.5- figure supplemental 1. Summary of IFT74, IFT81, and IFT54 data. Arrows indicate a significant decrease compared to wild-type, equal sign indicates a non-significant difference. N.A. indicates data not available. * from (Brown et al., 2015). ** from (Kubo et al., 2016b).

4.10 METHODS

Strains and culture conditions

The C. reinhardtii strains used were wild-type (cc124 [g1]), ift74-2 IFT74Δ130 (Brown et al., 2015), *ift81-1* CH5E-IFT81 (Kubo et al., 2016b) and *ift140-1* sfGFP-IFT140 (Picariello et al., 2019b). Cells were cultured in liquid minimal (M) medium (Sager and Granick, 1954) and aerated with 5% CO2 or grown on Tris-acetate-phosphate (Gorman and Levine, 1965) agar plates. Cells were maintained on a 14-10 h light-dark cycle.

Generation and identification of the ift54-2 insertional mutant

To generate insertional mutants, the cc124 strain was transformed with the 1.7-kb Hind III fragment of pHyg3, which confers hygromycin resistance (Berthold et al., 2002). Strains with palmelloid phenotypes – (ift54-2) – were selected and their insertion sites were determined by DNA sequencing of products amplified by RESDA-PCR (González-Ballester et al., 2005). ift54-2 was outcrossed once with wild-type strains (cc621) to decrease other potential pHyg3 insertions. Transformation of the resulting strain (ift54-2, mt+ and mt-, palmelloid) with the XbaI-KpnI fragment of pBR25-IFT54 (see next section) yielded transformants that can properly generate flagella with normal motility, confirming that the phenotype is due to the mutation of IFT54.

Generation of strains expressing modified proteins

A 3.3-kb fragment of genomic sequence including the IFT54 gene (Cre11.g467739, from the first ATG to the TAA stop codon) was amplified by PCR using specific primers (Table S1). The resulting PCR product was digested with Xho1 and EcoRI and then ligated into the pBR25

plasmid and sequenced (Rasala et al., 2013b). The PBR25 cassette containing zeocin-resistance and the IFT54 fragment was then excised by XbaI and KpnI and transformed into the ift54-2 mutant. To truncate the CH domain from IFT54, a new forward primer was designed starting in the fifth exon and was used to amplify genomic IFT54 lacking the CH domain. This fragment was amplified by PCR, followed by restriction enzyme digestion and ligation of the mutated DNA fragments into the original pBR25-IFT54 vector. All the constructed plasmids in Fig. S1 were digested with XbaI and KpnI-HF, and the resulting~8.6-kb fragments containing IFT81 genomic sequence with the zeocin-resistance cassette were used to transform ift81-1 by electroporation (Brown et al., 2012). Individual zeocin-resistant transformants were picked, screened for motility, and then analyzed by western blotting to select one strain for each construct in which the modified IFT81 is expressed at near wild-type levels.

Antibodies and Western Blotting.

Isolated whole cell, cell body, and flagella samples were incubated at 85 °C for 10 min in Laemmli SDS sample buffer. Protein samples were separated by SDS/PAGE using Precast Gels (Bio-Rad TGX) and transferred to PVDF membrane. Membranes were blocked in 4% nonfat milk and stained following standard procedures incubating the primary antibodies overnight at 4 °C and the secondary antibodies for ~90 min at room temperature. The following antibodies were used in this study: The polyclonal antibody to IFT54 (used 1:500) was raised against the peptide 1-136aa IFT54 in rabbit (Pocono Farms) and affinity-purified using the peptide linked to carrier protein immobilized on PVDF membrane. The mouse monoclonal antibody anti-IFT81 was diluted 1:200 (Cole et al., 1998a). Rabbit polyclonal anti-IFT74 (CAT no. 5993-100; CBiovision) was diluted 1:1,000. Secondary antibodies (anti–mouse or anti–rabbit IgG

conjugated to horseradish peroxidase; Invitrogen) were diluted 1:3,000, and FemtoGlow WesternPLUS (Michigan Diagnostics) was used for developing. A ChemiDoc MP imaging system and Image Lab software (Bio-Rad Laboratories) were used for documentation and quantification of signals.

TIRF microscopy of fluorescently tagged ß-tubulin and IFT140-sfGFP

To generate strains expressing IFT140-sfGFP, *ift140-1* IFT140-sfGFP was mated with and *ift54-2* ΔCH-IFT54 *ift81-1* CH5E-IFT81. Western blotting and PCR analysis was used to identify the *ift140-1* IFT140sfGFP *ift54-2* ΔCH-IFT54 strain and *ift140-1* IFT140-sfGFP *ift54-2* ΔCH-IFT54 *ift81-1* CH5E-IFT81 strain. TIRF microscopy was performed as a described in (Wingfield et al., 2017). To generate strains expressing fluorescently tagged tubulin cc124 cells were transformed with the XbaI/KpnI fragment of construct pBR25-sfGFP–βtubulin (Craft et al., 2015). Colonies of transformants were picked from Trisacetate-phosphate agar plates containing 10 µg/ml zeocin, and strains that had high expression levels of sfGFPβ-tubulin were selected. The cc124 sfGFPβ-tubulin strain was then mated to *ift54-2* ΔCH-IFT54, *ift81-1* CH5E-IFT81, and *ift54-2* ΔCH-IFT54 *ift81-1* CH5E-IFT81. Progeny were selected which expressed similar levels of sfGFPβ-tubulin in the corresponding 81/54N mutant parental background. For TIRF microscopy of tubulin transport, we used a custom-built TIRF/ epi-fluorescence structure-illumination microscope (TESM; Navaroli et al., 2012) with 100-mW diode lasers emitting at 491 nm and 561 nm, and equipped with a 525/50-nm emission filter. Cells were deflagellated by pH shock (Rosenbaum et al., 1969) and the cells with regenerating flagella were then allowed to rest on coverslips (Warner Instruments, MA; #1.5 thickness, 25-mm diameter). The experiments were carried out at room temperature. Flagella attached to the coverslip were partially photobleached

by using a 491-nm epifluorescence beam of ~3.3 nm diameter. Images were recorded at 10 images/s for 60 s (photobleach occurred 5 s after the onset of the recording) and analyzed by ImageJ as described in Lechtreck (2013). To increase the contrast by ImageJ, 'Brightness/Contrast' of all movies was adjusted identically; the value of 'Maximum' was decreased from 255 to 185.

IFT81 and IFT54 in vitro competition assay

The *C. reinhardtii* IFT81ΔN-GST/74ΔN/His6-27/25ΔC complex was expressed and purified as described in Bhogaraju et al. (2013). The IFT54CH(1-134)-GST domain was expressed and purified as described in Taschner et al. (2016b). GST was removed from the IFT54-CH by incubation with a TEV protease. GST beads were first incubated with 4 µM IFT81ΔN-GST/74ΔN/His6-27/25ΔC in BRB80 buffer. Then 4 µM tubulin and increasing amounts IFT54CH (see fig) was added simultaneously to the GST beads with IFT81 allowed to incubate for 1 hour at 4℃ (Input sample taken prior to incubation). GST beads and the associated proteins were spun down, washed and eluted with Glutathione. Eluates were loaded as Pulldown.

Measurement of flagellar length and assessment of swimming velocity

To determine flagellar regeneration kinetics, cells were deflagellated by pH shock (Rosenbaum et al., 1969). Subsequently, aliquots of cells were removed and fixed with 1% glutaraldehyde at 15-30min intervals up to 180 min after deflagellation, and observed by using an inverted microscope. One flagellum each on at least 60 cells was measured in each experiment and the average flagella length was calculated. The velocities and frequencies of IFT particles were determined by DIC microscopy as described previously (Kubo et al., 2015).

Swimming velocity was measured by tracking images of moving cells recorded by means of bright-field microscopy using a 40× objective, 5× eyepiece and a digital camera incorporating a charge-coupled device. Recorded movies were processed using ImageJ to obtain average swimming velocities.

4.11 REFERENCES

Ahmed, N.T., C. Gao, B.F. Lucker, D.G. Cole, and D.R. Mitchell. 2008. ODA16 aids axonemal outer row dynein assembly through an interaction with the intraflagellar transport machinery. *The Journal of cell biology*. 183:313-322.

Avidor-Reiss, T., A.M. Maer, E. Koundakjian, A. Polyanovsky, T. Keil, S. Subramaniam, and C.S. Zuker. 2004. Decoding cilia function: defining specialized genes required for compartmentalized cilia biogenesis. *Cell*. 117:527-539.

Banizs, B., M.M. Pike, C.L. Millican, W.B. Ferguson, P. Komlosi, J. Sheetz, P.D. Bell, E.M. Schwiebert, and B.K. Yoder. 2005. Dysfunctional cilia lead to altered ependyma and choroid plexus function, and result in the formation of hydrocephalus. *Development (Cambridge, England)*. 132:5329-5339.

Beales, P., and P.K. Jackson. 2012. Cilia - the prodigal organelle. *Cilia*. 1:1-1.

Berbari, N.F., J.S. Lewis, G.A. Bishop, C.C. Askwith, and K. Mykytyn. 2008. Bardet-Biedl syndrome proteins are required for the localization of G protein-coupled receptors to primary cilia. *Proceedings of the National Academy of Sciences of the United States of America*. 105:4242-4246.

Berthold, P., R. Schmitt, and W. Mages. 2002. An engineered Streptomyces hygroscopicus aph 7" gene mediates dominant resistance against hygromycin B in Chlamydomonas reinhardtii. *Protist*. 153:401-412.

Besschetnova, T.Y., B. Roy, and J.V. Shah. 2009. Imaging intraflagellar transport in mammalian primary cilia. *Methods Cell Biol*. 93:331-346.

Bhogaraju, S., L. Cajanek, C. Fort, T. Blisnick, K. Weber, M. Taschner, N. Mizuno, S. Lamla, P. Bastin, E.A. Nigg, and E. Lorentzen. 2013. Molecular basis of tubulin transport within the cilium by IFT74 and IFT81. *Science*. 341:1009-1012.

Bhogaraju, S., K. Weber, B.D. Engel, K.F. Lechtreck, and E. Lorentzen. 2014. Getting tubulin to the tip of the cilium: one IFT train, many different tubulin cargo-binding sites? *BioEssays : news and reviews in molecular, cellular and developmental biology*. 36:463-467.

Bizet, A.A., A. Becker-Heck, R. Ryan, K. Weber, E. Filhol, P. Krug, J. Halbritter, M. Delous, M.-C. Lasbennes, B. Linghu, E.J. Oakeley, M. Zarhrate, P. Nitschké, M. Garfa-Traore, F. Serluca, F. Yang, T. Bouwmeester, L. Pinson, E. Cassuto, P. Dubot, N.A.S. Elshakhs, J.A. Sahel, R. Salomon, I.A. Drummond, M.-C. Gubler, C. Antignac, S. Chibout, J.D. Szustakowski, F. Hildebrandt, E. Lorentzen, A.W. Sailer, A. Benmerah, P. Saint-Mezard, and S. Saunier. 2015. Mutations in TRAF3IP1/IFT54 reveal a new role for IFT proteins in microtubule stabilization. *Nature Communications*. 6:8666.

Blacque, O.E., M.J. Reardon, C. Li, J. McCarthy, M.R. Mahjoub, S.J. Ansley, J.L. Badano, A.K. Mah, P.L. Beales, W.S. Davidson, R.C. Johnsen, M. Audeh, R.H.A. Plasterk, D.L. Baillie, N. Katsanis, L.M. Quarmby, S.R. Wicks, and M.R. Leroux. 2004. Loss of C. elegans BBS-7 and BBS-8 protein function results in cilia defects and compromised intraflagellar transport. *Genes & development*. 18:1630-1642.

Bloodgood, R.A. 2010. Sensory reception is an attribute of both primary cilia and motile cilia. 123:505-509.

Brown, J.M., D.A. Cochran, B. Craige, T. Kubo, and G.B. Witman. 2015. Assembly of IFT trains at the ciliary base depends on IFT74. *Current biology : CB*. 25:1583-1593.

Buisson, J., N. Chenouard, T. Lagache, T. Blisnick, J.C. Olivo-Marin, and P. Bastin. 2012. Intraflagellar transport proteins cycle between the flagellum and its base. *J Cell Sci*.

Chien, A., S.M. Shih, R. Bower, D. Tritschler, M.E. Porter, and A. Yildiz. 2017a. Dynamics of the IFT machinery at the ciliary tip. *eLife*. 6:e28606.
Chien, A., S.M. Shih, R. Bower, D. Tritschler, M.E. Porter, and A. Yildiz. 2017b. Dynamics of the IFT machinery at the ciliary tip. *Elife*. 6.
Christensen, S.T., C.A. Clement, P. Satir, and L.B. Pedersen. 2012. Primary cilia and coordination of receptor tyrosine kinase (RTK) signalling. *The Journal of pathology*. 226:172-184.
Clement, C.A., K.D. Ajbro, K. Koefoed, M.L. Vestergaard, I.R. Veland, M.P. Henriques de Jesus, L.B. Pedersen, A. Benmerah, C.Y. Andersen, L.A. Larsen, and S.T. Christensen. 2013. TGF-beta signaling is associated with endocytosis at the pocket region of the primary cilium. *Cell reports*. 3:1806-1814.
Cole, D.G., D.R. Diener, A.L. Himelblau, P.L. Beech, J.C. Fuster, and J.L. Rosenbaum. 1998a. Chlamydomonas kinesin-II-dependent intraflagellar transport (IFT): IFT particles contain proteins required for ciliary assembly in Caenorhabditis elegans sensory neurons. *The Journal of cell biology*. 141:993-1008.
Cole, D.G., D.R. Diener, A.L. Himelblau, P.L. Beech, J.C. Fuster, and J.L. Rosenbaum. 1998b. Chlamydomonas Kinesin-II–dependent Intraflagellar Transport (IFT): IFT Particles Contain Proteins Required for Ciliary Assembly in Caenorhabditis elegans Sensory Neurons. *The Journal of cell biology*. 141:993-1008.
Cole, D.G., and W.J. Snell. 2009. SnapShot: Intraflagellar transport. *Cell*. 137:784-784.e781.
Corbit, K.C., P. Aanstad, V. Singla, A.R. Norman, D.Y. Stainier, and J.F. Reiter. 2005. Vertebrate Smoothened functions at the primary cilium. *Nature*. 437:1018-1021.
Craft, J.M., J.A. Harris, S. Hyman, P. Kner, and K.F. Lechtreck. 2015a. Tubulin transport by IFT is upregulated during ciliary growth by a cilium-autonomous mechanism. *The Journal of cell biology*. 208:223.
Craft, J.M., J.A. Harris, S. Hyman, P. Kner, and K.F. Lechtreck. 2015b. Tubulin transport by IFT is upregulated during ciliary growth by a cilium-autonomous mechanism. *J Cell Biol*. 208:223-237.
Dai, J., F. Barbieri, D.R. Mitchell, and K.F. Lechtreck. 2018. In vivo analysis of outer arm dynein transport reveals cargo-specific intraflagellar transport properties. *Mol Biol Cell*. 29:2553-2565.
Datta, P., C. Allamargot, J.S. Hudson, E.K. Andersen, S. Bhattarai, A.V. Drack, V.C. Sheffield, and S. Seo. 2015. Accumulation of non-outer segment proteins in the outer segment underlies photoreceptor degeneration in Bardet-Biedl syndrome. *Proceedings of the National Academy of Sciences of the United States of America*. 112:E4400-4409.
Dave, D., D. Wloga, N. Sharma, and J. Gaertig. 2009. DYF-1 Is required for assembly of the axoneme in Tetrahymena thermophila. *Eukaryotic cell*. 8:1397-1406.
Dawson, S.C., and S.A. House. 2010. Life with eight flagella: flagellar assembly and division in Giardia. *Curr Opin Microbiol*. 13:480-490.
Deane, J.A., D.G. Cole, E.S. Seeley, D.R. Diener, and J.L. Rosenbaum. 2001. Localization of intraflagellar transport protein IFT52 identifies basal body transitional fibers as the docking site for IFT particles. *Current biology : CB*. 11:1586-1590.
Dentler, W. 2005. Intraflagellar transport (IFT) during assembly and disassembly of Chlamydomonas flagella. *The Journal of cell biology*. 170:649-659.

Eichele, G., E. Bodenschatz, Z. Ditte, A.K. Gunther, S. Kapoor, Y. Wang, and C. Westendorf. 2020. Cilia-driven flows in the brain third ventricle. *Philosophical transactions of the Royal Society of London. Series B, Biological sciences*. 375:20190154.

Gonçalves, J., and L. Pelletier. 2017. The Ciliary Transition Zone: Finding the Pieces and Assembling the Gate. *Mol Cells*. 40:243-253.

González-Ballester, D., A. de Montaigu, A. Galván, and E. Fernández. 2005. Restriction enzyme site-directed amplification PCR: A tool to identify regions flanking a marker DNA. *Analytical Biochemistry*. 340:330-335.

Gudis, D.A., and N.A. Cohen. 2010. Cilia dysfunction. *Otolaryngologic clinics of North America*. 43:461-472, vii.

Habbig, S., M.P. Bartram, R.U. Muller, R. Schwarz, N. Andriopoulos, S. Chen, J.G. Sagmuller, M. Hoehne, V. Burst, M.C. Liebau, H.C. Reinhardt, T. Benzing, and B. Schermer. 2011. NPHP4, a cilia-associated protein, negatively regulates the Hippo pathway. *The Journal of cell biology*. 193:633-642.

Han, Y.G., B.H. Kwok, and M.J. Kernan. 2003. Intraflagellar transport is required in Drosophila to differentiate sensory cilia but not sperm. *Current biology : CB*. 13:1679-1686.

Haycraft, C.J., B. Banizs, Y. Aydin-Son, Q. Zhang, E.J. Michaud, and B.K. Yoder. 2005. Gli2 and Gli3 localize to cilia and require the intraflagellar transport protein polaris for processing and function. *PLoS genetics*. 1:e53.

Hirano, T., Y. Katoh, and K. Nakayama. 2017. Intraflagellar transport-A complex mediates ciliary entry and retrograde trafficking of ciliary G protein-coupled receptors. *Mol Biol Cell*. 28:429-439.

Hirokawa, N., Y. Tanaka, and Y. Okada. 2009. Left-right determination: involvement of molecular motor KIF3, cilia, and nodal flow. *Cold Spring Harb Perspect Biol*. 1:a000802-a000802.

Hou, Y., G.J. Pazour, and G.B. Witman. 2004. A dynein light intermediate chain, D1bLIC, is required for retrograde intraflagellar transport. *Mol Biol Cell*. 15:4382-4394.

Hou, Y., H. Qin, J.A. Follit, G.J. Pazour, J.L. Rosenbaum, and G.B. Witman. 2007. Functional analysis of an individual IFT protein: IFT46 is required for transport of outer dynein arms into flagella. *The Journal of cell biology*. 176:653-665.

Hsu, Y., J.E. Garrison, G. Kim, A.R. Schmitz, C.C. Searby, Q. Zhang, P. Datta, D.Y. Nishimura, S. Seo, and V.C. Sheffield. 2017. BBSome function is required for both the morphogenesis and maintenance of the photoreceptor outer segment. *PLoS genetics*. 13:e1007057-e1007057.

Hua, K., and R.J. Ferland. 2018. Primary cilia proteins: ciliary and extraciliary sites and functions. *Cellular and molecular life sciences : CMLS*. 75:1521-1540.

Huang, B., G. Piperno, and D.J. Luck. 1979. Paralyzed flagella mutants of Chlamydomonas reinhardtii. Defective for axonemal doublet microtubule arms. *The Journal of biological chemistry*. 254:3091-3099.

Huangfu, D., A. Liu, A.S. Rakeman, N.S. Murcia, L. Niswander, and K.V. Anderson. 2003. Hedgehog signalling in the mouse requires intraflagellar transport proteins. *Nature*. 426:83-87.

Hunter, E.L., K. Lechtreck, G. Fu, J. Hwang, H. Lin, A. Gokhale, L.M. Alford, B. Lewis, R. Yamamoto, R. Kamiya, F. Yang, D. Nicastro, S.K. Dutcher, M. Wirschell, and W.S. Sale. 2018. The IDA3 adapter, required for intraflagellar transport of I1 dynein, is regulated by ciliary length. *Mol Biol Cell*. 29:886-896.

Iomini, C., V. Babaev-Khaimov, M. Sassaroli, and G. Piperno. 2001. Protein particles in Chlamydomonas flagella undergo a transport cycle consisting of four phases. *The Journal of cell biology*. 153:13-24.

Ishikawa, H., and W.F. Marshall. 2011. Ciliogenesis: building the cell's antenna. *Nature Reviews Molecular Cell Biology*. 12:222-234.

Jenkins, P.M., D.P. McEwen, and J.R. Martens. 2009. Olfactory cilia: linking sensory cilia function and human disease. *Chem Senses*. 34:451-464.

Jiang, Y.Y., K. Lechtreck, and J. Gaertig. 2015. Total internal reflection fluorescence microscopy of intraflagellar transport in Tetrahymena thermophila. *Methods Cell Biol*. 127:445-456.

Jordan, M.A., D.R. Diener, L. Stepanek, and G. Pigino. 2018. The cryo-EM structure of intraflagellar transport trains reveals how dynein is inactivated to ensure unidirectional anterograde movement in cilia. *Nat Cell Biol*. 20:1250-1255.

Kanie, T., K.L. Abbott, N.A. Mooney, E.D. Plowey, J. Demeter, and P.K. Jackson. 2017. The CEP19-RABL2 GTPase Complex Binds IFT-B to Initiate Intraflagellar Transport at the Ciliary Base. *Dev Cell*. 42:22-36.e12.

Khanna, H. 2015. Photoreceptor Sensory Cilium: Traversing the Ciliary Gate. *Cells*. 4:674-686.

Kobayashi, T., K. Gengyo-Ando, T. Ishihara, I. Katsura, and S. Mitani. 2007. IFT-81 and IFT-74 are required for intraflagellar transport in C. elegans. *Genes to cells : devoted to molecular & cellular mechanisms*. 12:593-602.

Koefoed, K., I.R. Veland, L.B. Pedersen, L.A. Larsen, and S.T. Christensen. 2014. Cilia and coordination of signaling networks during heart development. *Organogenesis*. 10:108-125.

Kozminski, K.G., P.L. Beech, and J.L. Rosenbaum. 1995. The Chlamydomonas kinesin-like protein FLA10 is involved in motility associated with the flagellar membrane. *The Journal of cell biology*. 131:1517-1527.

Kozminski, K.G., K.A. Johnson, P. Forscher, and J.L. Rosenbaum. 1993. A motility in the eukaryotic flagellum unrelated to flagellar beating. *Proc Natl Acad Sci U S A*. 90:5519-5523.

Kubo, T., J.M. Brown, K. Bellve, B. Craige, J.M. Craft, K. Fogarty, K.F. Lechtreck, and G.B. Witman. 2016a. The IFT81 and IFT74 N-termini together form the major module for intraflagellar transport of tubulin. *J Cell Sci*.

Kubo, T., J.M. Brown, K. Bellve, B. Craige, J.M. Craft, K. Fogarty, K.F. Lechtreck, and G.B. Witman. 2016b. Together, the IFT81 and IFT74 N-termini form the main module for intraflagellar transport of tubulin. *Journal of cell science*. 129:2106-2119.

Kubo, T., M. Hirono, T. Aikawa, R. Kamiya, and G.B. Witman. 2015. Reduced tubulin polyglutamylation suppresses flagellar shortness in Chlamydomonas. *Mol Biol Cell*. 26:2810-2822.

Lechtreck, K.F., E.C. Johnson, T. Sakai, D. Cochran, B.A. Ballif, J. Rush, G.J. Pazour, M. Ikebe, and G.B. Witman. 2009. The Chlamydomonas reinhardtii BBSome is an IFT cargo required for export of specific signaling proteins from flagella. *The Journal of cell biology*. 187:1117-1132.

Lechtreck, K.F., I. Mengoni, B. Okivie, and K.B. Hilderhoff. 2018. In vivo analyses of radial spoke transport, assembly, repair and maintenance. *Cytoskeleton (Hoboken)*. 75:352-362.

Lefebvre, P.A. 1995. Flagellar amputation and regeneration in Chlamydomonas. *Methods Cell Biol*. 47:3-7.

Lehti, M.S., and A. Sironen. 2017. Formation and function of sperm tail structures in association with sperm motility defects†. *Biology of Reproduction*. 97:522-536.
Lewin, R.A., and K.W. Lee. 1985. Autotomy of algal flagella: electron microscope studies of Chlamydomonas (Chlorophyceae) and Tetraselmis (Prasinophyceae). *Phycologia*. 24:311-316.
Liang, Y., Y. Pang, Q. Wu, Z. Hu, X. Han, Y. Xu, H. Deng, and J. Pan. 2014. FLA8/KIF3B Phosphorylation Regulates Kinesin-II Interaction with IFT-B to Control IFT Entry and Turnaround. *Dev Cell*. 30:585-597.
Liew, G.M., F. Ye, A.R. Nager, J.P. Murphy, J.S. Lee, M. Aguiar, D.K. Breslow, S.P. Gygi, and M.V. Nachury. 2014. The intraflagellar transport protein IFT27 promotes BBSome exit from cilia through the GTPase ARL6/BBS3. *Dev Cell*. 31:265-278.
Ling, L., and D.V. Goeddel. 2000. MIP-T3, a novel protein linking tumor necrosis factor receptor-associated factor 3 to the microtubule network. *J Biol Chem*. 275:23852-23860.
Liu, A., B. Wang, and L.A. Niswander. 2005. Mouse intraflagellar transport proteins regulate both the activator and repressor functions of Gli transcription factors. *Development (Cambridge, England)*. 132:3103-3111.
Liu, P., and K.F. Lechtreck. 2018. The Bardet-Biedl syndrome protein complex is an adapter expanding the cargo range of intraflagellar transport trains for ciliary export. *Proceedings of the National Academy of Sciences of the United States of America*. 115:E934-e943.
Liu, Z., H. Tu, Y. Kang, Y. Xue, D. Ma, C. Zhao, H. Li, L. Wang, and F. Liu. 2019. Primary cilia regulate hematopoietic stem and progenitor cell specification through Notch signaling in zebrafish. *Nature Communications*. 10:1839.
Ludington, W.B., K.A. Wemmer, K.F. Lechtreck, G.B. Witman, and W.F. Marshall. 2013. Avalanche-like behavior in ciliary import. *Proc Natl Acad Sci U S A*. 110:3925-3930.
Lv, B., L. Wan, M. Taschner, X. Cheng, E. Lorentzen, and K. Huang. 2017a. Intraflagellar transport protein IFT52 recruits IFT46 to the basal body and flagella. *Journal of cell science*. 130:1662-1674.
Lv, B., L. Wan, M. Taschner, X. Cheng, E. Lorentzen, and K. Huang. 2017b. Intraflagellar transport protein IFT52 recruits IFT46 to the basal body and flagella. *J Cell Sci*.
Marshall, W.F., and J.L. Rosenbaum. 2001. Intraflagellar transport balances continuous turnover of outer doublet microtubules: implications for flagellar length control. *The Journal of cell biology*. 155:405-414.
Mijalkovic, J., B. Prevo, F. Oswald, P. Mangeol, and E.J. Peterman. 2017. Ensemble and single-molecule dynamics of IFT dynein in Caenorhabditis elegans cilia. *Nat Commun*. 8:14591.
Mijalkovic, J., J. van Krugten, F. Oswald, S. Acar, and E.J.G. Peterman. 2018. Single-Molecule Turnarounds of Intraflagellar Transport at the C. elegans Ciliary Tip. *Cell reports*. 25:1701-1707.e1702.
Mönnich, M., L. Borgeskov, L. Breslin, L. Jakobsen, M. Rogowski, C. Doganli, J.M. Schrøder, J.B. Mogensen, L. Blinkenkjær, and L.M.J.C.r. Harder. 2018. CEP128 localizes to the subdistal appendages of the mother centriole and regulates TGF-β/BMP signaling at the primary cilium. 22:2584-2592.
Morga, B., and P. Bastin. 2013. Getting to the heart of intraflagellar transport using Trypanosoma and Chlamydomonas models: the strength is in their differences. *Cilia*. 2:16.

Mueller, J., C.A. Perrone, R. Bower, D.G. Cole, and M.E. Porter. 2005. The FLA3 KAP subunit is required for localization of kinesin-2 to the site of flagellar assembly and processive anterograde intraflagellar transport. *Mol Biol Cell*. 16:1341-1354.

Müller, O.F., and O. Fabricius. 1786. Animalcula infusoria fluviatilia et marina que detexit, systematice descripsit et ad vivum delineari curavit Otho Fridericus Müller sistit opus hoc posthumum quod cum tabulis Aeneis L. in lucem tradit vidua ejus nobilissima cura Othonis Fabricii. Typis N. Mölleri, Hauniae :.

Mykytyn, K., R.F. Mullins, M. Andrews, A.P. Chiang, R.E. Swiderski, B. Yang, T. Braun, T. Casavant, E.M. Stone, and V.C. Sheffield. 2004. Bardet-Biedl syndrome type 4 (BBS4)-null mice implicate Bbs4 in flagella formation but not global cilia assembly. *Proceedings of the National Academy of Sciences of the United States of America*. 101:8664-8669.

Nachury, M.V.J.C.o.i.c.b. 2018. The molecular machines that traffic signaling receptors into and out of cilia. 51:124-131.

Nakayama, K., and Y. Katoh. 2018. Ciliary protein trafficking mediated by IFT and BBSome complexes with the aid of kinesin-2 and dynein-2 motors. *J Biochem*. 163:155-164.

Nechipurenko, I.V., C. Berciu, P. Sengupta, and D. Nicastro. 2017. Centriolar remodeling underlies basal body maturation during ciliogenesis in Caenorhabditis elegans. *Elife*. 6.

Nishijima, Y., Y. Hagiya, T. Kubo, R. Takei, Y. Katoh, and K. Nakayama. 2017. RABL2 interacts with the intraflagellar transport-B complex and CEP19 and participates in ciliary assembly. *Mol Biol Cell*. 28:1652-1666.

Okada, Y., S. Nonaka, Y. Tanaka, Y. Saijoh, H. Hamada, and N. Hirokawa. 1999. Abnormal Nodal Flow Precedes Situs Inversus in iv and inv mice. *Molecular Cell*. 4:459-468.

Orozco, J.T., K.P. Wedaman, D. Signor, H. Brown, L. Rose, and J.M. Scholey. 1999. Movement of motor and cargo along cilia. *Nature*. 398:674.

Ott, C., and J. Lippincott-Schwartz. 2012. Visualization of live primary cilia dynamics using fluorescence microscopy. *Curr Protoc Cell Biol*. Chapter 4:Unit 4 26.

Pazour, G.J., N. Agrin, J. Leszyk, and G.B. Witman. 2005. Proteomic analysis of a eukaryotic cilium. *The Journal of cell biology*. 170:103-113.

Pazour, G.J., B.L. Dickert, Y. Vucica, E.S. Seeley, J.L. Rosenbaum, G.B. Witman, and D.G. Cole. 2000. Chlamydomonas IFT88 and its mouse homologue, polycystic kidney disease gene tg737, are required for assembly of cilia and flagella. *The Journal of cell biology*. 151:709-718.

Peabody, J.E., R.-J. Shei, B.M. Bermingham, S.E. Phillips, B. Turner, S.M. Rowe, and G.M. Solomon. 2018. Seeing cilia: imaging modalities for ciliary motion and clinical connections. *Am J Physiol Lung Cell Mol Physiol*. 314:L909-L921.

Pedersen, L.B., S. Geimer, and J.L. Rosenbaum. 2006. Dissecting the Molecular Mechanisms of Intraflagellar Transport in Chlamydomonas. *Current Biology*. 16:450-459.

Peixoto, E., S. Richard, K. Pant, A. Biswas, and S.A. Gradilone. 2020. The primary cilium: Its role as a tumor suppressor organelle. *Biochemical Pharmacology*. 175:113906.

Perrone, C.A., D. Tritschler, P. Taulman, R. Bower, B.K. Yoder, and M.E. Porter. 2003. A Novel Dynein Light Intermediate Chain Colocalizes with the Retrograde Motor for Intraflagellar Transport at Sites of Axoneme Assembly in Chlamydomonas and Mammalian Cells. *Mol Biol Cell*. 14:2041-2056.

Picariello, T., J.M. Brown, Y. Hou, G. Swank, D.A. Cochran, O.D. King, K. Lechtreck, G.J. Pazour, and G.B. Witman. 2019a. A global analysis of IFT-A function reveals

specialization for transport of membrane-associated proteins into cilia. *Journal of cell science*. 132:jcs220749.
Picariello, T., J.M. Brown, Y. Hou, G. Swank, D.A. Cochran, O.D. King, K. Lechtreck, G.J. Pazour, and G.B. Witman. 2019b. A global analysis of IFT-A function reveals specialization for transport of membrane-associated proteins into cilia. *Journal of cell science*. 132.
Picariello, T., M.S. Valentine, J. Yano, and J. Van Houten. 2014. Reduction of meckelin leads to general loss of cilia, ciliary microtubule misalignment and distorted cell surface organization. *Cilia*. 3:2.
Piperno, G., E. Siuda, S. Henderson, M. Segil, H. Vaananen, and M. Sassaroli. 1998. Distinct mutants of retrograde intraflagellar transport (IFT) share similar morphological and molecular defects. *The Journal of cell biology*. 143:1591-1601.
Prevo, B., P. Mangeol, F. Oswald, J.M. Scholey, and E.J. Peterman. 2015. Functional differentiation of cooperating kinesin-2 motors orchestrates cargo import and transport in C. elegans cilia. *Nat Cell Biol*. 17:1536-1545.
Qin, H., D.R. Diener, S. Geimer, D.G. Cole, and J.L. Rosenbaum. 2004a. Intraflagellar transport (IFT) cargo: IFT transports flagellar precursors to the tip and turnover products to the cell body. *The Journal of cell biology*. 164:255-266.
Qin, H., D.R. Diener, S. Geimer, D.G. Cole, and J.L. Rosenbaum. 2004b. Intraflagellar transport (IFT) cargo: IFT transports flagellar precursors to the tip and turnover products to the cell body. *The Journal of cell biology*. 164:255-266.
Qin, H., Z. Wang, D. Diener, and J. Rosenbaum. 2007a. Intraflagellar transport protein 27 is a small G protein involved in cell-cycle control. *Curr Biol*. 17:193-202.
Qin, H., Z. Wang, D. Diener, and J. Rosenbaum. 2007b. Intraflagellar transport protein 27 is a small G protein involved in cell-cycle control. *Current biology : CB*. 17:193-202.
Raidt, J., C. Werner, T. Menchen, G.W. Dougherty, H. Olbrich, N.T. Loges, R. Schmitz, P. Pennekamp, and H. Omran. 2015. Ciliary function and motor protein composition of human fallopian tubes. *Human Reproduction*. 30:2871-2880.
Rasala, B.A., D.J. Barrera, J. Ng, T.M. Plucinak, J.N. Rosenberg, D.P. Weeks, G.A. Oyler, T.C. Peterson, F. Haerizadeh, and S.P. Mayfield. 2013a. Expanding the spectral palette of fluorescent proteins for the green microalga Chlamydomonas reinhardtii. *Plant J*.
Rasala, B.A., D.J. Barrera, J. Ng, T.M. Plucinak, J.N. Rosenberg, D.P. Weeks, G.A. Oyler, T.C. Peterson, F. Haerizadeh, and S.P. Mayfield. 2013b. Expanding the spectral palette of fluorescent proteins for the green microalga Chlamydomonas reinhardtii. *The Plant journal : for cell and molecular biology*. 74:545-556.
Reck, J., A.M. Schauer, K. VanderWaal Mills, R. Bower, D. Tritschler, C.A. Perrone, and M.E. Porter. 2016. The role of the dynein light intermediate chain in retrograde IFT and flagellar function in Chlamydomonas. *Mol Biol Cell*. 27:2404-2422.
Richey, E.A., and H. Qin. 2012a. Dissecting the sequential assembly and localization of intraflagellar transport particle complex B in Chlamydomonas. *PLoS One*. 7:e43118.
Richey, E.A., and H. Qin. 2012b. Dissecting the sequential assembly and localization of intraflagellar transport particle complex B in Chlamydomonas. *PLoS One*. 7:e43118-e43118.
Rogowski, M., D. Scholz, and S. Geimer. 2013. Electron microscopy of flagella, primary cilia, and intraflagellar transport in flat-embedded cells. *Methods in enzymology*. 524:243-263.

Rosenbaum, J.L., and F.M. Child. 1967. Flagellar regeneration in protozoan flagellates. *The Journal of cell biology*. 34:345-364.
Rosenbaum, J.L., J.E. Moulder, and D.L. Ringo. 1969. Flagellar elongation and shortening in Chlamydomonas. The use of cycloheximide and colchicine to study the synthesis and assembly of flagellar proteins. *The Journal of cell biology*. 41:600-619.
Sarpal, R., S.V. Todi, E. Sivan-Loukianova, S. Shirolikar, N. Subramanian, E.C. Raff, J.W. Erickson, K. Ray, and D.F. Eberl. 2003. Drosophila KAP interacts with the kinesin II motor subunit KLP64D to assemble chordotonal sensory cilia, but not sperm tails. *Current biology : CB*. 13:1687-1696.
Satir, P. 1995. Landmarks in cilia research from Leeuwenhoek to us. *Cell motility and the cytoskeleton*. 32:90-94.
Shah, A.S., Y. Ben-Shahar, T.O. Moninger, J.N. Kline, and M.J. Welsh. 2009. Motile Cilia of Human Airway Epithelia Are Chemosensory. 325:1131-1134.
Slep, K.C., and R.D. Vale. 2007. Structural basis of microtubule plus end tracking by XMAP215, CLIP-170, and EB1. *Mol Cell*. 27:976-991.
Soares, H., B. Carmona, S. Nolasco, L. Viseu Melo, and J. Goncalves. 2019. Cilia Distal Domain: Diversity in Evolutionarily Conserved Structures. *Cells*. 8.
Stasiulewicz, M., S.D. Gray, I. Mastromina, J.C. Silva, M. Björklund, P.A. Seymour, D. Booth, C. Thompson, R.J. Green, E.A. Hall, P. Serup, and J.K. Dale. 2015. A conserved role for Notch signaling in priming the cellular response to Shh through ciliary localisation of the key Shh transducer Smo. 142:2291-2303.
Stepanek, L., and G. Pigino. 2016. Microtubule doublets are double-track railways for intraflagellar transport trains. *Science*. 352:721-724.
Taschner, M., A. Lorentzen, A. Mourao, T. Collins, G.M. Freke, D. Moulding, J. Basquin, D. Jenkins, and E. Lorentzen. 2018a. Crystal structure of intraflagellar transport protein 80 reveals a homo-dimer required for ciliogenesis. *eLife*. 7.
Taschner, M., A. Lorentzen, A. Mourão, T. Collins, G.M. Freke, D. Moulding, J. Basquin, D. Jenkins, and E. Lorentzen. 2018b. Crystal structure of intraflagellar transport protein 80 reveals a homo-dimer required for ciliogenesis. *eLife*. 7:e33067.
Taschner, M., and E. Lorentzen. 2016. The Intraflagellar Transport Machinery. *Cold Spring Harb Perspect Biol*. 8.
Taschner, M., K. Weber, A. Mourao, M. Vetter, M. Awasthi, M. Stiegler, S. Bhogaraju, and E. Lorentzen. 2016a. Intraflagellar transport proteins 172, 80, 57, 54, 38, and 20 form a stable tubulin-binding IFT-B2 complex. *EMBO J*. 35:773-790.
Taschner, M., K. Weber, A. Mourão, M. Vetter, M. Awasthi, M. Stiegler, S. Bhogaraju, and E. Lorentzen. 2016b. Intraflagellar transport proteins 172, 80, 57, 54, 38, and 20 form a stable tubulin-binding IFT-B2 complex. *The EMBO Journal*. 35:773-790.
Taschner, M., K. Weber, A. Mourão, M. Vetter, M. Awasthi, M. Stiegler, S. Bhogaraju, and E. Lorentzen. 2016c. Intraflagellar transport proteins 172, 80, 57, 54, 38, and 20 form a stable tubulin-binding IFT-B2 complex. *The EMBO Journal*. 35:773-790.
Toropova, K., R. Zalyte, A.G. Mukhopadhyay, M. Mladenov, A.P. Carter, and A.J. Roberts. 2019. Structure of the dynein-2 complex and its assembly with intraflagellar transport trains. *Nature Structural & Molecular Biology*. 26:823-829.
van Dam, T.J., M.J. Townsend, M. Turk, A. Schlessinger, A. Sali, M.C. Field, and M.A. Huynen. 2013. Evolution of modular intraflagellar transport from a coatomer-like

progenitor. *Proceedings of the National Academy of Sciences of the United States of America*. 110:6943-6948.
Vannuccini, E., E. Paccagnini, F. Cantele, M. Gentile, D. Dini, F. Fino, D. Diener, C. Mencarelli, and P. Lupetti. 2016. Two classes of short intraflagellar transport train with different 3D structures are present in Chlamydomonas flagella. *Journal of cell science*. 129:2064-2074.
Wagner, M.K., and H.J. Yost. 2000. Left–right development: The roles of nodal cilia. *Current Biology*. 10:R149-R151.
Wallingford, J.B., and B. Mitchell. 2011. Strange as it may seem: the many links between Wnt signaling, planar cell polarity, and cilia. *Genes & development*. 25:201-213.
Waters, A.M., and P.L. Beales. 2011. Ciliopathies: an expanding disease spectrum. *Pediatric nephrology (Berlin, Germany)*. 26:1039-1056.
Williams, C.L., J.C. McIntyre, S.R. Norris, P.M. Jenkins, L. Zhang, Q. Pei, K. Verhey, and J.R. Martens. 2014. Direct evidence for BBSome-associated intraflagellar transport reveals distinct properties of native mammalian cilia. *Nat Commun*. 5:5813.
Wingfield, J.L., and K.-F. Lechtreck. 2018. Chlamydomonas Basal Bodies as Flagella Organizing Centers. *Cells*. 7:79.
Wingfield, J.L., I. Mengoni, H. Bomberger, Y.Y. Jiang, J.D. Walsh, J.M. Brown, T. Picariello, D.A. Cochran, B. Zhu, J. Pan, J. Eggenschwiler, J. Gaertig, G.B. Witman, P. Kner, and K. Lechtreck. 2017. IFT trains in different stages of assembly queue at the ciliary base for consecutive release into the cilium. *eLife*. 6.
Wood, C.R., and J.L. Rosenbaum. 2014. Proteins of the ciliary axoneme are found on cytoplasmic membrane vesicles during growth of cilia. *Curr Biol*. 24:1114-1120.
Wren, K.N., J.M. Craft, D. Tritschler, A. Schauer, D.K. Patel, E.F. Smith, M.E. Porter, P. Kner, and K.F. Lechtreck. 2013a. A differential cargo-loading model of ciliary length regulation by IFT. *Current biology : CB*. 23:2463-2471.
Wren, K.N., J.M. Craft, D. Tritschler, A. Schauer, D.K. Patel, E.F. Smith, M.E. Porter, P. Kner, and K.F. Lechtreck. 2013b. A differential cargo-loading model of ciliary length regulation by IFT. *Curr Biol*. 23:2463-2471.
Zhang, R., G.M. Alushin, A. Brown, and E. Nogales. 2015. Mechanistic Origin of Microtubule Dynamic Instability and Its Modulation by EB Proteins. *Cell*. 162:849-859.
Zhu, B., X. Zhu, L. Wang, Y. Liang, Q. Feng, and J. Pan. 2017a. Functional exploration of the IFT-A complex in intraflagellar transport and ciliogenesis. *PLoS genetics*. 13:e1006627-e1006627.
Zhu, B., X. Zhu, L. Wang, Y. Liang, Q. Feng, and J. Pan. 2017b. Functional exploration of the IFT-A complex in intraflagellar transport and ciliogenesis. *PLoS Genet*. 13:e1006627.
Zhu, X., Y. Liang, F. Gao, and J. Pan. 2017c. IFT54 regulates IFT20 stability but is not essential for tubulin transport during ciliogenesis. *Cellular and molecular life sciences : CMLS*. 74:3425-3437.
Zhu, X., Y. Liang, F. Gao, and J. Pan. 2017d. IFT54 regulates IFT20 stability but is not essential for tubulin transport during ciliogenesis. *Cell Mol Life Sci*.

CHAPTER 5

CONCLUSIONS AND FUTURE DIRECTIONS

5.1 SUMMARY OF DISSERTATION

The work in this dissertation studies the journey of IFT trains as they emerge from the ciliary base, become loaded with tubulin, traffic to the ciliary tip, remodel into retrograde trains, and traffic back to the base. We find that trains form in a stepwise manner, with IFT-A arriving at the ciliary base first, followed by IFT-B, and then kinesin. IFT dynein and tubulin are loaded briefly before the trains exit the cell body; dynein lays across rows of IFT-B (Toropova et al., 2019), and tubulin binds onto the IFT54/74/81 site of IFT-B. Once these trains reach the tip, kinesin and tubulin dissociate (Chien et al., 2017), and the rest of the train fragments into smaller 'train cars', with IFT-A, IFT-B and dynein still associated. Train cars from multiple anterograde trains will recombine to become retrograde trains and undergo trafficking to the base once dynein is activated. Once at the base, the components of the train separate, IFT-A and dynein will return to the cell body pool and a portion of IFT-B will be immediately reused on retrograde trains. How these conclusions were made are summarized below.

IFT train assembly at the ciliary base.

IFT trains have a clear ultrastructure within the cilium but are unrecognizable at the ciliary base from where they emerge, and there is limited knowledge on how trains assemble. In a pioneering study, Buisson et al. (2013) used IFT52-GFP (an IFT-B protein) and a fluorescence recovery after photobleaching (FRAP) approach to study the dynamics of IFT in *Trypanosoma*

brucei at it the ciliary base. After photobleaching the pool of IFT52-GFP at the ciliary base, there was a brief absence in florescent anterograde IFT, indicative of bleached trains leaving the pool. The fluorescence intensity at the pool partially recovered, and the brightness of anterograde traffic was decrease, implying that photobleached proteins, returning from the cilia, re-enter the pool and are immediately recycled on IFT trains. This led to the proposal of a closed IFT system in which the IFT proteins continuously cycle within the flagellum and the basal body pool with minor exchange of proteins between the basal body pool and that of the cell body.

To further examine both the assembly of IFT trains and the degree of exchange between the cell body and basal body pool of IFT, we used a collection of eight fluorescent protein (FP)-tagged IFT proteins, representative of IFT-A, IFT-B1, IFT-B2, and the IFT motors. The FP-tagged proteins were expressed to rescue the corresponding mutant phenotype (except for IFT27 (IFT-B1) and the kinesin subunit, KAP), ensuring that all the proteins present were fluorescently labeled. We used a focused laser beam to photo-bleach one of the two basal body pools, using the other as a control to normalize for fluorescence loss due to the continuous TIRF illumination. The fluorescence intensity of pools for all eight proteins recovered, on average, in three to ten seconds, to 60% of the signal or more. Repeated bleaching of the pool still allowed for signal recovery, suggesting that the basal body pool is much smaller than the cell body pool. Furthermore, we noted that different proteins recovered at different rates, with the KAP-GFP signal recovering faster than the IFT-A and IFT-B proteins. Therefore, IFT proteins in the bb-pool exchange at different rates.

We next wanted to determine the source of the fluorescence recovery as unbleached material could come from the cell body pool or the flagella. To do so, we eliminated the flagella

source of unbleached trains with a fluorescence loss in photobleaching (FLIP) approach. We placed the bleaching laser at the tip of one of the two flagella (the experimental flagella) and set it to blink on and off with a duty ratio that photobleached trains as they pass by, ensuring retrograde trains were bleached. We reasoned that if the pool was derived from recycled trains, the signal at the base would decrease; however, if the pool was made of material from the cell body, the signal would remain stable. Interestingly, we observed both scenarios. The basal body signal decreased significantly, ~50%, for the IFT-B proteins analyzed (with IFT27 as the exception) while the signal remained much more constant for the motors and IFT-A. This data suggests that while most of IFT-B reenters the basal body pool, IFT27, IFT-A, and the IFT motors do not.

Next, we sought to determine if IFT-B that reenters the pool is directly reused on anterograde trains. We focused our analysis on NG-IFT54 because of its bright and stable signal. If the proteins are reused, then we would expect to observe the signal strength of anterograde trains to progressively decrease the longer we use the FLIP laser to the point of no longer being able to see unbleached trains in the experimental flagellum. Even after more than a minute of FLIP we saw anterograde traffic of IFT in the experimental flagellum with a frequency similar to that of the control. However, these trains were dimmer than those in the control flagellum. The data reveal that a portion (~50%) of the IFT-B protein NG-IFT54 in anterograde IFT trains is directly derived from retrograde IFT.

Our data indicate that *Chlamydomonas* has a primarily ‘open’ system with little reuse of IFT material, which conflicts with the data from *T. brucei* that suggests a ‘closed’ system for IFT. To examine if our findings are generalizable to other organisms or specific to *Chlamydomonas*,

we examined IFT in the primary cilia of IMCD cells expressing IFT88-YFP (IFT-B) and the motile cilia of the ciliate *Tetrahymena thermophila* expressing GFP-Dyf-1 (IFT70, IFT-B). Neither IMCD3 or Tetrahymena are amenable to the FLIP approach we used in *Chlamydomonas*, so instead, we used a FRAP approach where we photobleached the entire cilium and basal body pool and then measured fluorescence recovery. In IMCD3 cells, the basal body signal recovered to 60-95% in ~16.8 seconds with the first unbleached anterograde train entering the cilium in ~18.1 seconds, indicative of an open system. In *Tetrahymena* cells, the basal body pool recovered to a maximum of ~74% the prebleach intensity in ~29 seconds with first unbleached anterograde train entering the flagellum after ~17.1 seconds, suggesting IFT70-GFP is continuously recruited from the cell body to the basal bodies for assembly into IFT trains. Therefore, open and semi-open IFT systems are present not just for *Chlamydomonas* but also IMCD3 or *Tetrahymena* cells.

We next sought to determine how long it takes to assemble an anterograde IFT train. To do so, we measured the interval between the bleaching of one basal body pool and the departure of the first unbleached train into the attached flagellum. Typically, after we bleached the basal body, there was a break in the traffic of fluorescent anterograde IFT in the experimental flagellum; we call this period 'the gap.' This gap suggests that IFT trains containing the bleached proteins exit the basal body pool before new trains assemble from unbleached proteins. The timing of the gap varied significantly for the different IFT proteins analyzed and ranged from ~7 s [IFT140-sfGFP (IFT-A)] to ~2.5 s [D1bLIC-GFP (Dynein)]. The differences in the duration of the gap between each of the two IFT-A, -B1, and -B2 proteins as well as those between the IFT-A and -B2 proteins were not significant, while those between IFT-A and -B1 and the motors were. These observations suggest that different parts of the IFT trains need different amounts of time to shift

from being in the basal body pool to being released into the flagellum as part of an anterograde train.

To verify that the differences in gap times were biologically relevant and not a consequence of using different strains, we generated a double mutant for an IFT-A protein and kinesin subunit, rescued with the FP- tagged versions of those proteins (*fla3* KAP-GFP *ift140* IFT140-mCherry). In the vast majority of experiments, an anterograde train with unbleached KAP-GFP preceded a train marked by both KAP-GFP and IFT140-mCherry. Additionally, the gap times for both proteins were similar to those in the single-tag strain. We propose that IFT trains are assembled by sequential addition of distinct IFT proteins/subcomplexes and that trains in different states of assembly are lined up at the basal bodies to be successively dispatched into the flagellum upon completion.

Lastly, we examined when an axonemal cargo, tubulin, is loaded onto trains. Previous studies suggest that tubulin may be pre-loaded onto IFT complexes, in post-Golgi vesicles, before the complexes enter the basal body pools (Wood and Rosenbaum, 2014). Alternatively, tubulin could load onto trains at the ciliary base in the later stages of train assembly. If the latter is correct, we would expect that there would be a long gap time, similar to the IFT-proteins, while if the former is true, the gap time should be short, like IFT dynein. By performing the FRAP analysis described above in regenerating cilia, which have much more frequent sfGFP-tubulin IFT traffic, we observed a ~2.1 second gap between photo-bleaching the basal bodies and the departure of the first sfGFP-tubulin IFT track. Based on these data, we propose that sfGFP-tubulin and the anterograde cargo- IFT dynein, associate to IFT trains at the flagellar base briefly before departure into the cilium.

IFT train remodeling at the ciliary tip.

After examining how trains assemble at the ciliary base, we analyzed how trains remodel at the ciliary tip, which encompasses both the disassembly of anterograde trains and the assembly of retrograde trains. At the ciliary tip, IFT trains convert from highly ordered anterograde structures, consisting of distinct layers or IFT-A, IFT-B, and dynein, to more amorphous retrograde structures in the ~2 seconds they remain at the tip (Jordan et al., 2018). Based on models of IFT cycling in reviews and primary literature, the field assumes that IFT-A, IFT-B, dynein, and kinesin separate at the tip before remodeling and activating dynein for retrograde transport, despite little evidence for this. Here, to better understand IFT train remodeling, we performed *in vivo* imaging on IFT proteins in *Chlamydomonas*.

We first wanted to determine the size of the pool of IFT at the tip in terms of anterograde train equivalents. To do so, we photobleached the tip of the cilium and quantified how long and how many anterograde trains arrived at the tip to recover the signal to near prebleach levels. We did these experiments in a double mutant double tagged IFT-A IFT-B strain (*ift54-2* mSc-IFT54 *ift140-1* IFT140-sfGFP) to additionally test if there were differences in the relative amount of IFT-A and IFT-B at the tip. We found the signals for IFT-A and IFT-B at the tip recovered in 3.6 seconds and 3.5 seconds, respectively; during this time, an average of 4.2 anterograde trains, for IFT-A and 4.1 for IFT-B, arrived at the tip. Therefore, IFT-A and IFT-B are present at the tip in similar amounts, and the pool at the tip is equivalent to approximately four anterograde trains.

We next sought to analyze how long the various parts of the trains dwell at the ciliary tip as this encompasses both the disassembly of anterograde trains and the assembly of retrograde trains. This analysis was accomplished by photobleaching the tip of the cilium and measuring the

time between the arrival of the first anterograde IFT train and the departure of the first retrograde train, we termed this the 'minimum tip dwell time.' While the first retrograde train could derive from material from an anterograde train arriving after the first anterograde train, we find this an appropriate method to determine the average length of time IFT proteins dwell at the tip. The minimum tip dwell time varied somewhat for a given IFT protein between experiments and the various strains analyzed. The average tip dwell time ranged from ~1.3 s to ~2.3 s. We wondered if the variability was biologically relevant or a consequence of performing the experiments without tight regulation of temperature. To test this, we imaged a subset of FP-tagged IFT proteins at 15.5, 21, and 27 °C and found temperature significantly affected both the speed of IFT and the length of the dwell time, with higher temperatures increasing the speed and decreasing the dwell time and vice versa for colder temperature. Therefore, the data suggest that the variations in minimum tip dwell time are likely caused by variations in imaging conditions and strain background rather than being representative of distinct tip dwell times of the different IFT proteins. We conclude that all IFT proteins pause at the tip and require at least ~1.5 s to transition from anterograde into retrograde trains.

The ciliary tip is where the BBSome, an IFT adaptor, often interacts with its membrane-protein cargoes before exporting them out of the cilia (Liu and Lechtreck, 2018; Nachury, 2018). To explore the behavior of the BBSome at the ciliary tip, we used the *bbs4-1* BBS4-mNG strain, which has low expression of BBS4-mNG, enabling us to image individual BBSomes without FRAP analysis. In contrast to IFT proteins that appear stationary at the tip, BBS4-mNG particles often diffuse around near the tip for ~ 3 seconds before undergoing retrograde transport. The data suggest both that BBSomes often dissociate from IFT at the tip and that IFT particles are somehow secured from moving during the pause.

In the above analyses, there are multiple florescent anterograde trains present at the tip, making it impossible to explore the journey of a single anterograde train. To overcome this limitation, we used the PhotoGate approach developed by Chien et al. (2017), which allows the transport of a single fluorescent anterograde train to be examined while other anterograde trains are photobleached before they reach the ciliary tip. We used this technique on strains expressing two IFT-A proteins, two IFT-B protein, and the dynein subunit, D1bLIC. In addition to confirming that anterograde trains of IFT-B and dynein fragment at the tip (Chien et al., 2017), we found that IFT-A (IFT140-sfGFP) fragmented as well. On average, one anterograde train gave rise to ~3.1 retrograde trains with the exception of IFT43-YFP (a peripheral IFT-A protein), which could in parts result from the low photostability of YFP. As noted in Chien et al. (2017), one anterograde train becoming three retrograde trains does not agree with the establish anterograde: retrograde IFT ratios (1:1.4). This discrepancy is best explained by train fragments from multiple anterograde trains recombining to form a single retrograde train. We conclude that the IFT-A, IFT-B, and dynein motor layers of the anterograde IFT trains fragment with similar patterns, i.e., a similar number of breakage points, and mix with material from other anterograde trains before undergoing retrograde trafficking.

Lastly, we examined whether or not IFT-A, IFT-B, and dynein remain together during train fragmentation. To do so, we generated a double mutant double tagged IFT-A IFT-B strain (*ift54-2* mSc-IFT54 *ift140-1* IFT140-sfGFP) and a double mutant double tagged IFT-B IFT dynein strain (*ift54-2* mSc-IFT54 *d1blic* D1bLIC-GFP). FRAP and PhotoGate analysis of *ift54-2* mSc-IFT54 *ift140-1* IFT140-sfGFP revealed IFT-A and IFT-B dwelled at the tip for the same length of time, and IFT-A and IFT-B colocalized on retrograde trains during anterograde train fragmentation. Additionally, IFT-A and IFT-B fragmented with similar patterns of fluorescence

intensities on retrograde trains. These data strongly suggest IFT-A and IFT-B remain together during fragmentation. FRAP and PhotoGate analysis of *ift54-2* mSc-IFT54 *d1blic* D1bLIC-GFP revealed that D1bLIC-GFP and mSc-IFT54 have similar tip dwell times and are primarily found (~80%) colocalized on the first retrograde leaving the tip after PhotoGate. Interestingly, ~11% of the time, we saw the first retrograde train only carried mSc-IFT54, and ~9% of the time, the first retrograde only carried D1bLIC-GFP. This small variance is likely due to differences in the photostability and brightness of GFP and mScarlet rather than a biological principle. Together, these and the above data support a model where IFT-A, -B, and dynein remain together as train cars during IFT turnaround.

The tubulin binding site on IFT

In our earlier study, we found that IFT trains are loaded with tubulin briefly before entering cilia, where and how IFT trains bind tubulin is still unclear. In vitro studies revealed that the IFT-B proteins IFT81 and IFT74 form a tubulin-binding module: IFT81 binds the dimer via its calponin homology (CH) domain and the basic N-terminal domain of IFT74 interacts with the acidic C-terminus of β-tubulin (Bhogaraju et al., 2013). In vivo studies in Chlamydomonas reinhardtii revealed that strains lacking either the N-terminal domain of IFT74 (ΔN-IFT74) or carrying mutations incapacitating the CH-domain of IFT81 (CH5E-IFT81) build near full-length flagella albeit at a slower rate. ift81 CH5E-IFT81 ift74-2 ΔN-IFT74 double mutants, however, largely fail to assemble cilia with a subset of cells possessing stumpy flagella. This suggests that IFT81/74 appears to form the major tubulin binding site on IFT trains. However, not all species that build cilia possess IFT81/74, and CH of IFT54 has been shown to bind to tubulin in vitro.

To address the question of whether IFT54 contributes to tubulin transport, we characterized an insertional mutant in the *IFT54* gene, *ift54-2*. The *ift54-2* mutant expresses a C-terminally truncated non-functional IFT54 protein and completely lacks flagella. The mutant phenotype is rescued by both full-length and truncated CH-less IFT54 (ΔCH-IFT54); the *ift54-2* ΔCH-IFT54 strain assembles full-length, fully motile cilia at a normal rate, arguing against an essential role of IFT54 CH in tubulin transport, similar to findings by Zhu et al. (2017).

Impairments in the tubulin-binding domains of IFT74 and IFT81 only has a minor impact on ciliary assembly and length. Thus, we wondered if the CH domain of IFT54 could make an obscure contribution to tubulin transport by IFT, which is not apparent in the ΔCH-IFT54 single mutant. To examine this possibility, we crossed our *ift54-2* ΔCH-IFT54 with *ift81-1* CH5E-IFT81 and identified the *ift54-2* ΔCH-IFT54 *ift81-1* CH5E-IFT81 double mutant strain (referred to as ΔCH54 CH5E81) with PCR and Western blotting. We used a similar approach to obtain an *ift54-2* ΔCH-IFT54 *ift74-2* ΔN-IFT74 strain (referred to as ΔCH54 ΔN74).

We found that the majority (80%) of ΔCH54 CH5E81 cells did not have cilia. The few cells that did grow cilia possessed short cilia, often with bulbous tips, and mostly remained entrapped within the mother cell wall. Failure to hatch from the mother cell wall is often observed for strains with paralyzed flagella, however, both ciliated ΔCH54 CH5E81 and the 54N/74N cells were motile (Huang et al., 1979). These cells swam with reduced velocity, likely due to the short length of their cilia. Additionally, we examined the ultrastructure of the ΔCH54 CH5E81 axonemes and found it to be normal, as revealed by TEM. However, we noticed that many of the cilia of the double mutant terminated in a membranous tubule characteristic for ciliary stumps briefly after flagellar abscission (Lewin and Lee, 1985). These ultrastructural data

suggest that the cilia of the ΔCH54 CH5E81 double mutant, for reasons unknown, might be less stable and prone to breakage and abscission. After cilia amputation by a pH shock, the ΔCH54 CH5E81 cells grow their flagella at a rate much slower than either of the parental strains.

We made similar findings in the ΔCH54 ΔN74 double mutant. The majority (~70%) of cells lacked flagella, and the rest of the cells grew short cilia with bulbous ends. Notably, these cilia were shorter than either parental strain. TEM analysis of ΔCH54 ΔN74 showed that short cilia appeared of normal ultrastructure but often terminated with an elongated blebbed membrane tube comparable to ΔCH54 CH5E81. Thus, ciliogenesis in the 54N/74N and ΔCH54 CH5E81 double mutants was more severely affected that in either parental strain. These observations suggest that the CH-domain of IFT54 contributes to ciliogenesis in situations when an intact 74N/81N module is absent.

The ciliogenesis defects in these strains 54N/74N and ΔCH54 CH5E81 double mutants could be due to an impaired IFT system or defects in tubulin transport. We focused our more detailed analysis of ciliogenesis on the 81N/54N strain as the CH domains likely confer specificity for the binding of tubulin. To visualize IFT, we crossed sfGFP-IFT140 into the *ift54-2* ΔCH-IFT54 and *ift54-2* ΔCH-IFT54 *ift81-1* CH5E-IFT81 backgrounds and used TIRF microscopy to analyze IFT. The velocities and frequencies of anterograde and retrograde IFT in the 54N single and the 54N/81N double mutants were similar to those observed in the *ift140-1* sfGFP-IFT140 control strain. Thus, IFT appeared to be unaffected by the manipulations of the CH IFT54/81.

We next examined the effect of the loss of the IFT54 CH domain on tubulin transport. To do so, we generated a 54N GFP-β-tubulin, an 81N GFP-β-tubulin, and an 81N/54N GFP-β-

tubulin strain, by mating 81N/54N to a wild-type strain expressing GFP-β-tubulin. We then measured tubulin transport frequencies in regenerating cilia of approximately half their steady-state length, as tubulin transport is significantly increased during ciliogenesis (Craft et al., 2015). The frequency of tubulin transport by anterograde IFT in the 81N/54N double mutant was significantly less than that observed in the 54N and 81N parental strains. From these data, we conclude that CH domain of IFT54 participates in tubulin transport by IFT in Chlamydomonas and that the ciliogenesis defects of the 81N/54N strain and likely the 74/54N strain, are due to defects in tubulin transport.

Both IFT54 and IFT81 bind tubulin via their CH domains, thus we wondered if the IFT54 can substitute for the CH domain of IFT81. We did not test if the CH domain of IFT81 can replace that of IFT54 as the loss of the CH of IFT54 has no discernible phenotype on its own. (Taschner et al., 2016b). To test this, we replaced the CH domain of IFT81 with that of IFT54, resulting in the ift81-1 IFT54CH-L-ΔCH-IFT81 strain. We also generated an ift81 L-ΔCH-IFT81 strain, which completely lacks a CH-domain, and an ift81-1 IFT81CH-L-ΔCH-IFT81 strain, which has the IFT81 backbone and its original CH domain separated by a flexible linker. The novel ift81 L-ΔCH-IFT81 deletion strain had shorter cilia (~5μm) than the previously described ift81 CH5E-IFT81 strain (~10μm), suggesting that the CH5E, despite being unable to bind tubulin in vitro, has some capacity in ciliogenesis in vivo. The average length of cilia in the ift81-1 IFT54CH-L-ΔCH-IFT81 strain was shorter than in ift81-1 IFT81CH-L-ΔCH-IFT81 rescue, but longer than the ift81 L-ΔCH-IFT81 deletion strain. Additionally, ift81-1 L-ΔCH-IFT81 regrew cilia slowly while ift81-1 IFT81CH-L-ΔCH-IFT81 and ift81-1 IFT54CH-L-ΔCH-IFT81 regrew cilia at wildtype kinetics. Further, IFT velocity in the three linker strains was normal except for a slight reduction in the velocity of retrograde IFT in the ift81 CH5E-IFT81.

Together, these data demonstrate that the 54CH domain can partially replace the CH domain of IFT81, suggesting that both domains fulfill similar functions in ciliogenesis.

The CH domains of IFT54 and IFT81 have very similar structures, but each possess a distinct distribution of the charged residues that likely mediate the interaction with tubulin (Taschner et al., 2016b). To test whether the IFT54 and IFT81 CH domains interfere with each other when binding to tubulin, we used an in vitro competition assay with equimolar amounts of tubulin and IFT81(within a recombinant IFT-B1 complex) and increasing amounts of IFT54-CH. Even with a 50-fold excess of the IFT54-CH vs. the IFT81-CH, IFT81 could still bind the same amount of tubulin it did without IFT54-CH present. This suggests the CH domains of IFT54 and the IFT81 bind to distinct sites of tubulin dimers. Thus, the two CH-domains could interact with the same tubulin dimer during transport rather than forming two independent tubulin-binding sites. We propose that IFT54, IFT74, and IFT81 form a tripartite binding site for tubulin on the IFT trains.

5.2 FUTURE DIRECTIONS

Regulation of a tripartite site

If IFT54/74/81 indeed form a tripartite tubulin binding site, it raises questions about how its loading could be regulated. IFT54 is part of the IFT-B2 complex, while IFT81 and IFT74 stabilize each other via their coiled-coiled domains on IFT-B1 (Taschner and Lorentzen, 2016). As both IFT-B1 and IFT-B2 come together on IFT trains to form the 'IFT-B complex' IFT54 and IFT81/74 may be directly next to each other on a fully assembled IFT train. The cell may even utilize this differential compartmentalization of the tubulin binding site to regulate tubulin loading; trains of growing cilia could have IFT54 and IFT81/74 positioned in close proximity to

optimize tubulin binding, while trains of steady-state cilia could position IFT54 and IFT81/74 farther apart. Vannuccini and colleagues used electron tomography to analyze the structure of IFT trains in steady-state and growing cilia (Vannuccini et al., 2016). They found that growing cilia had an overall increase in train number, and an increase in 'long' trains over 'short' trains, which had two classes, wide and narrow. According to data from Stepanek et al. 2016, who used electron tomography in combination with TIRF microscopy, these 'long' trains are likely stalled, expanded IFT trains, rather than a specialized class of IFT devoted to growing cilia. Nevertheless, the EM data clearly shows that IFT trains can exist in different conformations. Furthermore, IFT trains examined by cryo-EM, revealed that steady-state trains have almost no available spaces on IFT-B for cargo to bind; suggesting that trains in growing cilia must exist in a different conformation to accommodate the multitude of cargoes they bring in (Jordan et al., 2018). Further studies analyzing the conformation of IFT in steady-state vs. growing cilia will help inform if this kind of regulation is possible.

Additionally, the relative positions of the tubulin-binding domains of IFT54 and IFT81/74 in steady-state and growing cilia could be examined with a Bioluminescence Resonance Energy Transfer (FRET) approach. In brief, BRET relies on a donor luciferase to transfer energy to an acceptor fluorophore following oxidation of the luciferase substrate; if the donor and acceptor tagged protein are within <10nm of each other, the acceptor will be excited and emit fluorescence (Dale et al., 2019). This technique has advantages over FRET as it does not rely on an excitation laser for the donor, which is sometimes enough to cause fluorescence of the acceptor, even without FRET. To use BRET to study the proximity of the CH-domains on IFT54 and IFT81, one could tag the N-terminal domains of IFT54 and IFT81 with a donor and acceptor BRET pair and express them to rescue the corresponding mutant backgrounds. For

example, these strains could be *ift54-2* mNeonGreen-IFT54 and *ift81* Nanoluc-IFT81. These strains would then need to be mated to produce an *ift54-2* mNeonGreen-IFT54 *ift81* Nanoluc-IFT81 strain were BRET could be examined in regenerating cilia. A positive BRET strain should be generated to verify BRET can be imaged on IFT trains by attaching the Nanoluc construct with a flexible linker to the mNeonGreen-IFT54, resulting in *ift54-2* Nanoluc-L-mNeonGreen-IFT54. If our hypothesis is true, that the CH domains of IFT54 and IFT81 are closer in regenerating cilia and farther apart in steady-state cilia we would expect to see emission from NeonGreen in growing cilia after the addition of the Nanoluciferase substrate while in steady-state cilia we would only see emission of Nanoluciferase. Additionally, if this is the mechanism which regulates tubulin loading we would expect continuous BRET in the *lf2-1* mutant, which has continuously high levels of tubulin transport frequencies and low BRET in the *shf-2* mutant, which has low tubulin transport frequencies (Craft et al., 2015). If BRET is never seen, and the possibility of BRET was verified with the positive control, then this suggests that the CH domains IFT54 and IFT81 are farther than 10 nm apart on IFT trains, disproving our tripartite tubulin binding site model. If strong BRET is seen in both regenerating and steady-state cilia, then IFT54 and IFT81 CH domains are always near each other, supportive of a tripartite model. This also suggests that another mechanism, such as post-translational modifications regulate tubulin loading on to IFT. Lastly, there may be BRET in steady-state cilia and no BRET in regenerating cilia. This observation would suggest that if the CH domains of IFT54 and IFT81 are close together, tubulin loading is inhibited, and IFT trains require the CH domains to be farther apart, potentially ensuring the loading of tubulin oligomers onto IFT trains.

5.3 REFERENCES

Bhogaraju, S., L. Cajanek, C. Fort, T. Blisnick, K. Weber, M. Taschner, N. Mizuno, S. Lamla, P. Bastin, and E.A.J.S. Nigg. 2013. Molecular basis of tubulin transport within the cilium by IFT74 and IFT81. 341:1009-1012.

Buisson, J., N. Chenouard, T. Lagache, T. Blisnick, J.C. Olivo-Marin, and P. Bastin. 2013. Intraflagellar transport proteins cycle between the flagellum and its base. *Journal of cell science*. 126:327-338.

Chien, A., S.M. Shih, R. Bower, D. Tritschler, M.E. Porter, and A. Yildiz. 2017. Dynamics of the IFT machinery at the ciliary tip. *eLife*. 6:e28606.

Craft, J.M., J.A. Harris, S. Hyman, P. Kner, and K.F. Lechtreck. 2015. Tubulin transport by IFT is upregulated during ciliary growth by a cilium-autonomous mechanism. *The Journal of cell biology*. 208:223.

Dale, N.C., E.K.M. Johnstone, C.W. White, and K.D.G. Pfleger. 2019. NanoBRET: The Bright Future of Proximity-Based Assays. 7.

Huang, B., G. Piperno, and D.J. Luck. 1979. Paralyzed flagella mutants of Chlamydomonas reinhardtii. Defective for axonemal doublet microtubule arms. *The Journal of biological chemistry*. 254:3091-3099.

Jordan, M.A., D.R. Diener, L. Stepanek, and G. Pigino. 2018. The cryo-EM structure of intraflagellar transport trains reveals how dynein is inactivated to ensure unidirectional anterograde movement in cilia. *Nat Cell Biol*. 20:1250-1255.

Liu, P., and K.F. Lechtreck. 2018. The Bardet-Biedl syndrome protein complex is an adapter expanding the cargo range of intraflagellar transport trains for ciliary export. *Proceedings of the National Academy of Sciences of the United States of America*. 115:E934-e943.

Nachury, M.V.J.C.o.i.c.b. 2018. The molecular machines that traffic signaling receptors into and out of cilia. 51:124-131.

Taschner, M., and E. Lorentzen. 2016. The Intraflagellar Transport Machinery. *Cold Spring Harb Perspect Biol*. 8.

Toropova, K., R. Zalyte, A.G. Mukhopadhyay, M. Mladenov, A.P. Carter, and A.J. Roberts. 2019. Structure of the dynein-2 complex and its assembly with intraflagellar transport trains. *Nature Structural & Molecular Biology*. 26:823-829.

Vannuccini, E., E. Paccagnini, F. Cantele, M. Gentile, D. Dini, F. Fino, D. Diener, C. Mencarelli, and P. Lupetti. 2016. Two classes of short intraflagellar transport train with different 3D structures are present in Chlamydomonas flagella. *Journal of cell science*. 129:2064-2074.

Wood, C.R., and J.L. Rosenbaum. 2014. Proteins of the ciliary axoneme are found on cytoplasmic membrane vesicles during growth of cilia. *Current biology : CB*. 24:1114-1120.

Zhu, X., Y. Liang, F. Gao, and J. Pan. 2017. IFT54 regulates IFT20 stability but is not essential for tubulin transport during ciliogenesis. *Cellular and molecular life sciences : CMLS*. 74:3425-3437.